Low-order Methodology for the Design of Propellers with Serrated Trailing Edges

by

Jorge Hernan Santamaria Osorio

THESIS PRESENTED TO ÉCOLE DE TECHNOLOGIE SUPÉRIEURE
IN PARTIAL FULFILLMENT FOR THE DEGREE OF
DOCTOR OF PHILOSOPHY
Ph.D.

MONTREAL, DECEMBER 17, 2025

ÉCOLE DE TECHNOLOGIE SUPÉRIEURE
UNIVERSITÉ DU QUÉBEC

BOARD OF EXAMINERS

THIS THESIS HAS BEEN EVALUATED

BY THE FOLLOWING BOARD OF EXAMINERS

Mme. Marlène Sanjosé, Thesis supervisor
Department of Aerospace Engineering at École de Technologie Supérieure

M. Stéphane Moreau, Thesis Co-Supervisor
Department of Mechanical Engineering at Université de Sherbrooke

M. Georges Ghazi, Chair, Board of Examiners
Department of Systems Engineering at École de Technologie Supérieure

M. Patrick Germain, Member of the Jury
Department of Aerospace Engineering at École de Technologie Supérieure

M. Jovan Nedić, Member of the Jury
Department of Mechanical Engineering at McGill University

M. Sivakumaran Nadarajah, Member of the Jury
Department of Mechanical Engineering at McGill University

M. Benjamin Cotté, External Independent Examiner
Institute of Mechanical Sciences and Industrial Applications at ENSTA Paris

THIS THESIS WAS PRESENTED AND DEFENDED

IN THE PRESENCE OF A BOARD OF EXAMINERS AND THE PUBLIC

ON DECEMBER 8, 2025

AT ÉCOLE DE TECHNOLOGIE SUPÉRIEURE

ACKNOWLEDGEMENTS

It takes a village to raise a child, or so the saying goes. The same can be said about the process of transforming a student into a researcher. This work would not have been possible without the guidance, collaboration, and support of many people.

Marlene, Ma directrice, thank you for considering me for your research group and for inviting me to Montreal. I could stay for another 4 years and still have a lot to learn from you. Stephane, my sincere gratitude goes to you for believing in me from the first time we met and recommending me to Marlene. I have achieved more than I would have thought possible during my PhD, and it is all due to your support, patience, and encouragement. It is usually stated on most academic websites that the PhD program prepares students to conduct independent research. Still, that would do little justice to all the lessons I am taking with me after working by your side. You have led by example and supported me in difficult times, allowing me to become independent by trusting me with responsibility. Merci beaucoup!

Engineering is a collaborative endeavor in which theory, simulation, and testing support each other toward a common objective. I am pleased to have taken part in all these facets of engineering practice thanks to the collaboration with incredibly talented professionals. My sincere gratitude to Dr. Romain Gojon and Mr. Sylvain Belliot for their support during the propeller manufacturing and testing. Additionally, I would like to thank Prof. Benshuai Lyu and his students for the interesting discussions and insights during the development of analytical models. Lastly, thank you, Prof. Jovan Nedić and Prof. Siva Nadarajah, for our discussions and feedback during the early stages of the program.

To the GRENTE team (I still think greatETS was a better name!), thanks for the company during my PhD adventure. To Dr. Bamba and Mr. Ralph Pouhe, thank you for all the interesting discussions and for all the afternoons on the futsal court. I will never cease to be amazed by the power of the beautiful game to unite people all over the world. A special thanks to Dr. Arnaud Le'floch and Dr. Kathrin Stahl for sharing the office during the first year. It was good to have people close to the finish line early in this journey. My sincere gratitude to Mr. Teddy Garnier

and Mr. Andre Bierrenbach-Lima for your collaboration on some of the tedious work. Thanks for always being in the best of dispositions. To my foster home at UdeS, thanks for hosting me on multiple occasions. It was a pleasure to share the unforgettable 2024 conference with you. Special thanks to Mr. Jose for the support during the airfoil experimental campaign.

To my dear wife, thank you for believing in us despite all the adversities we faced to be together in Montreal. Your support on and offline is one of the main reasons I was able to finish this work. Thanks for your patience during the nights I was absent during the last mile. Spasibo bol'shoye, Min sine âratam. To my mother, thanks for teaching me to always do my work with love, and to my Father, thanks for teaching me that anything is possible with discipline. To my sister, my role model, thanks for always being there despite the distance. Thanks to my Grandma for encouraging me to play music; many lonely nights passed by to the lovely sound of a heavily distorted guitar. ¡Mil gracias, familia! To my friends in Montreal, especially Diego and Juan, thanks for your support all these years.

Méthodologie d'ordre réduit pour la conception d'hélices à bords de fuite dentelés

Jorge Hernan Santamaria Osorio

RÉSUMÉ

L'essor rapide de la mobilité aérienne avancée, et en particulier des véhicules sans pilote ou drones, soulève des enjeux d'acceptation sociale du fait de la pollution sonore engendrée par ces engins lors du survol de zones urbaines. Parmi les différentes sources de bruit de ces véhicules, le bruit de bord de fuite constitue une composante majeure du bruit à large bande émis par leurs hélices en vol stationnaire. Ce bruit peut être atténué grâce à l'utilisation de dentelures de bord de fuite. Toutefois, les méthodes numériques aéroacoustiques pour le calcul de bruit des hélices nécessitent des ressources de calcul trop élevées. En phase de conception, il est donc nécessaire de recourir à une approche rapide permettant d'estimer les gains acoustiques potentiels des dentelures. Certaines approches analytiques destinées aux bords droits ou dentelés requièrent comme donnée essentielle la densité spectrale des fluctuations de pression pariétale, qui peut être reconstruite à partir de données issues de simulations peu coûteuses de type Reynolds-Averaged Navier-Stokes (RANS). Dans le cadre de ces travaux, une méthodologie s'appuyant sur de tels modèles est proposée pour prévoir la réduction de bruit associée à l'emploi de dentelures de bord de fuite sur des hélices.

Le modèle théorique d'Ayton permet d'estimer le bruit généré par un écoulement turbulent sur le bord de fuite dentelé d'une plaque infiniment mince. Li et Lee en ont proposé une extension. Ils ont introduit un modèle heuristique tridimensionnel applicable à des pales de rotor d'envergure finie. Cette extension permet de mettre en évidence les avantages de la dentelure en créneau par rapport à la forme en dents de scie. Cette thèse propose une nouvelle approche s'appuyant sur l'analogie de Curle pour étendre le modèle d'Ayton et de pallier certaines limites du modèle de Li et Lee. Des considérations mathématiques limitent pour le moment cette approche aux bords de fuite en créneau. Une campagne expérimentale a été réalisée dans la soufflerie anéchoïque de l'Université de Sherbrooke afin de mesurer le bruit émis par un profilé NACA0012 soumis à des flux d'air dont les nombres de Reynolds sont représentatifs des conditions de fonctionnement typiques des hélices de drone. Trois géométries ont été testées : bord droit, bord en dents de scie et bord en créneau. Jusqu'à 5 dB de réduction ont pu être observés, et les dentelures en créneau se sont révélées plus efficaces que les dents de scie. Les estimations théoriques sont raisonnablement en accord avec les résultats expérimentaux. En particulier, le modèle proposé est plus précis et prévoit une meilleure directivité que le modèle de Li et Lee.

Le modèle de Li et Lee a été étendu aux pales en rotation, selon l'approche de Schlinker et Amiet. En faisant tendre l'amplitude des dentelures vers 0, son évaluation est en accord avec les prévisions du modèle d'Amiet, en particulier aux hautes fréquences, tant pour les profils fixes que pour les éléments de pale en rotation. La méthodologie couplée (RANS + modèle) a ensuite été confrontée, en termes d'aérodynamique et d'acoustique, à des mesures réalisées à l'ISAE sur une hélice de drone basée sur le profil NACA0012, pour différentes vitesses de rotation. L'analyse comparative des performances de l'hélice entre les calculs et les données

expérimentales a permis de démontrer l'importance de raffiner de manière adéquate le maillage autour des tourbillons d'extrémité de l'hélice et d'utiliser une modélisation de la turbulence avancée prenant en compte la transition. La densité spectrale des fluctuations de pression pariétale a été modélisée à l'aide d'informations issues des simulations RANS, et l'acoustique en champ lointain de l'hélice a été calculée à l'aide du code interne PyFanNoise dans lequel le modèle de Li et Lee a été implémenté.

Les prévisions acoustiques concordent assez bien avec les mesures expérimentales, en particulier à des vitesses de rotation élevées, lorsque les écoulements secondaires sont plus faibles que la couche limite au bord de fuite est pleinement turbulente. Le modèle de Li et Lee est ensuite utilisé pour comparer les réductions de bruit de différentes formes de dentelures. L'approche analytique prévoit que les bords de fuite en créneau permettent une réduction de bruit plus importante que les formes en dents de scie ou sinusoïdales, et ce, pour toutes les fréquences et tous les angles d'observation. Ce phénomène est particulier aux petites pales d'hélice, généralement utilisées dans les drones. Cependant, pour les pales à corde plus grande habituellement utilisées pour les ventilateurs carénés, les combinaisons de dentelures en dents de scie et sinusoïdales offrent de meilleures réductions de bruit.

Une dernière étape de ces travaux a consisté à valider la méthodologie couplée par une approche expérimentale. Il a toutefois fallu tenir compte des effets de l'installation et de la fabrication des dentelures, qui sont ignorés dans l'approche analytique. Plusieurs hélices ont été imprimées en 3D par fabrication additive, puis testées en chambre anéchoïque dans les installations de l'ISAE afin de mesurer le bruit en champ lointain et les performances aérodynamiques. La signature acoustique de la configuration de référence (à bord de fuite droit) démontre l'existence d'une instabilité de la couche limite laminaire. Les dentelures intégrées ou en appendices atténuent ce mécanisme de bruit. Pour éviter ce mécanisme de transition laminaire-turbulente à la surface des pales, une rugosité de surface a été ajoutée afin de déclencher la turbulence. Les dentelures intégrées génèrent un bruit supplémentaire d'échappement tourbillonnaire caractérisé par un nombre de Strouhal basé sur l'épaisseur à la racine de la dentelure. Les dentelures en appendice, plus minces, évitent cette source additionnelle et permettent d'atteindre une réduction de bruit. Les dentelures en créneau n'ont pas permis d'obtenir la réduction de bruit anticipée par le modèle. La réduction de bruit prévue par le modèle pour les dents de scie suit globalement la tendance des mesures, même si elle la surestime. De plus, les résultats expérimentaux démontrent que les dentelures constituent une méthode efficace pour contrôler le bruit de bord de fuite à basse vitesse de rotation, lorsque le bruit à large bande prédomine sur le bruit tonal. D'autre part, les dents de scie installées en appendice, combinées à un dispositif de transition, présentent la meilleure concordance avec les prédictions théoriques, soulignant ainsi l'importance des choix de fabrication dès la phase de conception.

Mots-clés: drone, hélice, aéroacoustique, dentelures de bord de fuite, modélisation

Low-order Methodology for the Design of Propellers with Serrated Trailing Edges

Jorge Hernan Santamaria Osorio

ABSTRACT

The exponential increase in applications where UAVs or drones are used raises concerns about potential noise pollution in large cities. Trailing edge noise is a significant broadband noise source of hovering UAV propellers, which can be reduced by employing bio-inspired trailing edge serrations. The high computational cost of high-fidelity CFD simulations put them at the end of the design cycle rather than at the beginning. Therefore, propeller designers need a fast method for predicting noise reductions. Analytical models for straight and serrated edges need as essential input the single-point wall-pressure fluctuations spectrum. This can be modeled using low-cost Reynolds-Averaged Navier-Stokes simulations. A low-order methodology is proposed to estimate the potential noise reductions resulting from trailing edge serrations using RANS simulations for a representative drone propeller based on a NACA0012 airfoil with constant pitch and constant chord.

Ayton's theoretical model provides predictions for serrated trailing edge noise generated by a fully turbulent flow over an infinitesimally thin plane. The extension of Ayton's model, proposed by Li and Lee, provides a heuristic three-dimensional model for a finite span applicable to rotor blades. This model reveals the potential benefits of using a square wave serration compared to the traditional sawtooth serration. This thesis addresses the limitations of Li and Lee's model by deriving a new model for the square wave using Ayton's model and Curle's analogy. Measurements of a NACA0012 airfoil at low-Reynolds numbers, typical of small drones, were performed in an anechoic chamber at the Université de Sherbrooke, for straight, sawtooth, and square wave edges. Noise reductions of up to 5 dB are measured, with the square wave outperforming the sawtooth serration. Theoretical predictions are in reasonable agreement with the experimental results.

Li and Lee's model is then extended to rotating blades using Schlinker and Amiet's model. The model is verified in the limit of zero serration amplitude finding good agreement at high frequencies and high observer angles. Single-blade passage RANS simulations of the NACA0012 propeller are performed, and aerodynamic validation is made with experimental data. The results highlight the importance of adequately refining the mesh around the propeller tip vortices and using transitional turbulence modeling. The wall-pressure fluctuations spectrum was modeled based on the RANS results, and the propeller far-field acoustics were calculated using the in-house code PyFanNoise.

The acoustic predictions agree fairly well with experimental measurements, especially at high rotational speeds, where secondary flows are weaker and the onset of turbulence matches more favorably with the fully turbulent k- SST model used in the RANS. Li and Lee's model is then used to study the sensitivity of noise reductions to different shapes. The square wave serration is shown to outperform the sawtooth and sinusoidal shapes for all frequencies and observer angles, particularly for small propeller blades typically used in drones. However, for larger chord blades

typically used for ducted fans, combinations of sawtooth and sinusoidal serrations provide better noise reductions.

The methodology is validated by considering the effects of serration installation and manufacturing. Several propellers were 3D printed and tested in an anechoic chamber, where far-field noise and aerodynamic performance were measured. The baseline configuration exhibits clear evidence of laminar boundary-layer instability noise. Cut-in and add-on serrations alleviate this noise mechanism. Similarly, to overcome the influence of the laminar-to-turbulent transition over the blade surface, some propellers also include additional surface roughness to trigger turbulence. Cut-in serrations experience additional vortex-shedding noise characterized by a Strouhal number based on the serration root thickness. The results show that serrations are a viable method for controlling trailing edge noise at low RPM, where broadband noise dominates over tonal noise, and that add-on serrations with a trip are in better agreement with the theoretical results, thus highlighting the importance of the manufacturing method during the design phase.

Keywords: drone, propeller, aeroacoustic noise, trailing edge serrations, modeling

TABLE OF CONTENTS

Page

LIST OF TABLES

LIST OF FIGURES

LIST OF ABBREVIATIONS

BVP	Boundary Value Problem
CFD	Computational Fluid Dynamics
DNS	Direct Numerical Simulation
LES	Large Eddy Simulation
LBL	Laminar Boundary Layer
LBM	Lattice Boltzmann Method
NACA	National Advisory Committee for Aeronautics
OASPL	Overall Sound Pressure Level
OASWL	Overall Sound Power Level
PSD	Power Spectral Density
RANS	Reynolds-Averaged Navier Stokes
SPL	Sound Pressure Level
SWL	Sound Power Level
TBL	Turbulent Boundary Layer
TEN	Trailing Edge Noise

LIST OF SYMBOLS AND UNITS OF MEASUREMENTS

c Airfoil chord [m]

C_T Thrust coefficient [–]

C_Q Torque coefficient [–]

C_{m_n} Modal expansion coefficients for serrated airfoil strip model [–]

FM Propeller Figure of Merit [–]

h Serration amplitude [m]

k Acoustic wavenumber [m^{-1}]

k_x, k_y Streamwise and spanwise aerodynamic wavenumbers [m^{-1}]

l_y Spanwise correlation length [m]

L Airfoil or blade strip span [m]

Q Propeller torque [N m]

R Propeller radius [m]

r_0 Corrected distance for convection effects [m]

SPL Far-field acoustic pressure PSD [dB/Hz]

T Propeller thrust [N]

U_∞ Free-stream velocity [m/s]

U_c Convection velocity [m/s]

U_{75} Blade relative velocity at 75% of the span [m/s]

(x, y, z) Observer coordinates in the blade strip frame [m]

	Observer coordinates in the rotor frame [m]
=	Free-stream to convection velocity ratio [–]
$_{eff}$	Effective angle of attack [rad]
	Geometric angle of attack [rad]
^{2}=1 ^{2}	compressibility factor, Prandtl-Glauert Transform [–]
	Azimuthal angle on the rotor plane [rad]
	Observer angle in the blade strip frame [rad]
	Observer angle in the rotor frame (elevation from the rotor plane) [rad]
	Input to the modal expansion coefficients [–]
	Serration wavelength [m]
$_0$	Streamwise-integrated wavenumber spectra of wall-pressure fluctuations [–]
	Wall-pressure fluctuations PSD [dB/Hz]
	Angular frequency [s ^{1}]
	Propeller angular velocity [rad/s]

INTRODUCTION

Since the early days of aviation, propellers have been a cornerstone of the propulsion systems of various types of aircraft. Whether it is the main rotor of a helicopter, the turboprops of regional aircraft, the piston-driven propeller of general aviation planes, the gigantic propellers of a Hercules C-130, or the tiny plastic rotors of recreational drones, rotary wings have played a pivotal role in the development of aviation. Even though high-bypass-ratio turbofans are the preferred engine choice for present and near-future long-range aircraft, advances in battery and motor technology, are helping to open new markets for electrically powered aircraft.

On the one hand, the initiative known as Urban Air Mobility (UAM) aims to use large propeller-driven Vertical Take-Off and Landing (VTOL) vehicles to alleviate traffic congestion in densely populated metropolises, transport critical goods, and respond to emergencies. On the other hand, small[1], multi-rotor Unmanned Aerial Vehicles (UAVs), commonly known as drones, have made their way into cities, aiding in surveillance, construction, terrain mapping, landscape planning, infrastructure inspection, and television and cinema applications (Watkins *et al.*, 2020).

The use of drones in urban environments poses numerous challenges, including communication jamming and interference[2], privacy concerns, limited battery range, potential collisions with other aircraft, or impact with people or structures on the ground. However, as noted by Watkins *et al.* (2020), the greatest challenge to the widespread use of drones is their acceptance and integration by society. A comprehensive study by Rizzi (2020) suggests that there is the potential that new populations will routinely be exposed to aircraft noise because UAM vehicles and drones are expected to fly in much greater numbers than helicopters. Historically, changes in noise levels over populated areas have been met with resistance, the same author notes.

---

[1] For some perspective, drones less than 250 g do not require a pilot license to fly but may require registration depending on the country. Drones weighing up to 25 kg require registration and a pilot license

[2] Most drones require a direct line of sight radio link in the 900 MHz, 2.4 GHz or 5.8 GHz bands for command, control and video data. These are the same frequencies used by WiFi.

According to Schäffer, Pieren, Heutschi, Wunderli & Becker (2021) and Gwak, Han & Lee (2020), drone noise is substantially more annoying than road traffic or aircraft noise due to special acoustic characteristics such as pure tones and high-frequency broadband noise. Continuous noise exposure not only creates auditory system problems (Le Prell, 2019), but it has been linked to cardiovascular disease, sleep disorders, and depression as noted by Passchier-Vermeer & Passchier (2000). Drone noise stems mainly from the propellers or from the interaction of the propellers with the airframe. Therefore, the development of quieter propellers is essential for future UAM and drone projects to take off.

Propellers consist of (usually[3]) evenly spaced blades whose cross-section is an airfoil. The chord and pitch of the airfoil section are functions of the radial position, generally decreasing in the outboard direction. A basic control volume analysis (known as Momentum Theory) can be used to demonstrate that propellers generate thrust by accelerating a relatively big mass of air by a small velocity. An unavoidable consequence of the relative motion between the blade and the air, is the generation of acoustic waves that are perceived as sound[4]. Similar to other bladed machinery, propeller noise can be divided into tonal and broadband components. The former is deterministic and localized at the Blade Passing Frequency (BPF) and its harmonics, whereas the latter is stochastic and spreads over a large frequency range. These noise characteristics are illustrated in the noise spectra in Figure 0.1(b) for a DJI 9443 propeller with a diameter of 25 cm at a rotational speed of 5400 RPM (Zawodny *et al.*, 2016). Note the prominent peak at 180 Hz corresponding to the BPF. At frequencies beyond 1000 Hz the spectra is dominated by the broadband component of the signal.

Tonal noise is a function of the blade velocity, blade geometry, and thickness, and of its aerodynamic loading (Thrust). In contrast, broadband noise is a consequence of the interaction

[3] Inspired by some automotive engine cooling fans designs, some propeller manufacturers have proposed unevenly spaced blade designs to reduce propeller noise.

[4] It is worth noting that marine propellers suffer from the same ailment as their air counterparts, plus the non-desirable effect of cavitation that compromises the blade integrity

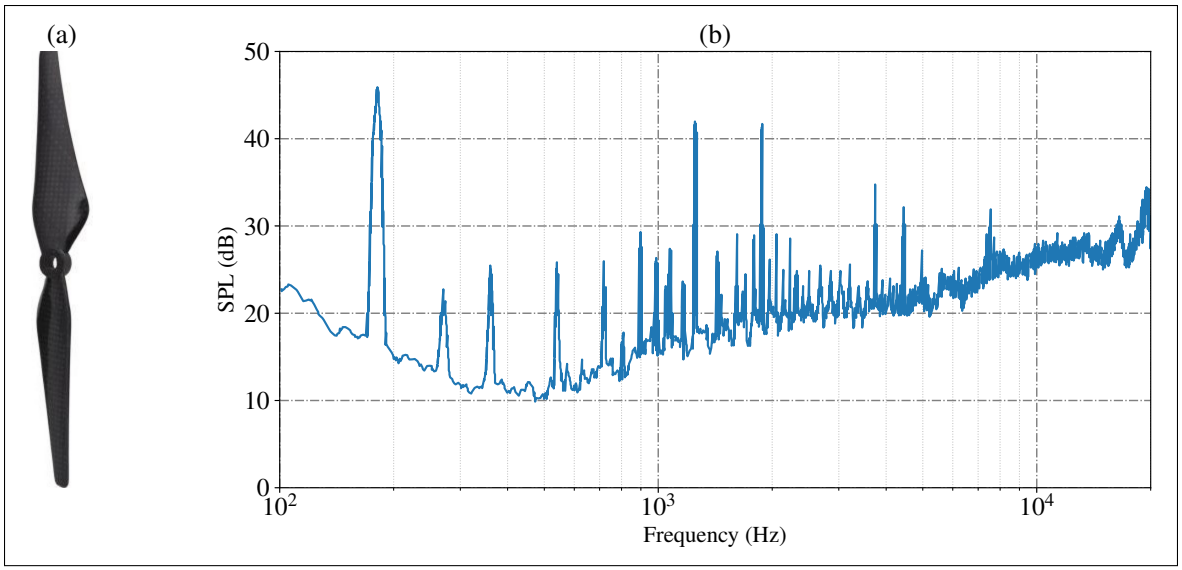

Figure 0.1 (a) DJI 9443 propeller and (b) its noise spectrum measured at 1.9 m and 45 degrees below the rotational plane.
Taken from Zawodny *et al.* (2016)

of turbulence with the blade. The turbulence may be generated in the atmosphere or as a consequence of the propeller ingesting the wake of an adjacent rotor or a structural component. When turbulence interacts with the blade leading edge, distorted eddies radiate sound into the far field, producing turbulence interaction noise (TIN). Turbulence may also be generated as the boundary layer develops along the blade surface. The interaction of the turbulent boundary layer at the trailing edge is known as trailing edge noise (TEN) or airfoil self-noise and represents the minimum achievable noise level by a propeller operating in turbulence-free flow. In either case, the broad range of spatio-temporal scales implies that the acoustic energy is spread in a large frequency range. The process of turbulent boundary layer noise production is illustrated in Figure 0.2. It is noticed that there is a scale disparity between the eddies close to the trailing edge and the corresponding acoustic wavelength .

The mechanism of turbulent boundary layer noise production is illustrated in Figure 0.2. The turbulent boundary layer develops over the airfoil as it moves in a uniform flow field with velocity

. Close to the trailing edge, the boundary layer thickness is , and contains a wide range of scales, or eddies, with a characteristic lengthscale, . A minute fraction of the turbulent kinetic energy contained in the eddies is converted to acoustic energy as the boundary layer meets the trailing edge. The acoustic waves with wavelength, , are propagated into the far-field for distances many times greater than the airfoil chord. Although the boundary layer has been enlarged for clarity, the scale disparity between acoustic and aerodynamic fields is evident. While hovering, and assuming that no unsteady flow is ingested into the propeller, trailing edge noise is a dominant broadband noise source given the human ear's frequency response in the 2 to 5 kHz range.

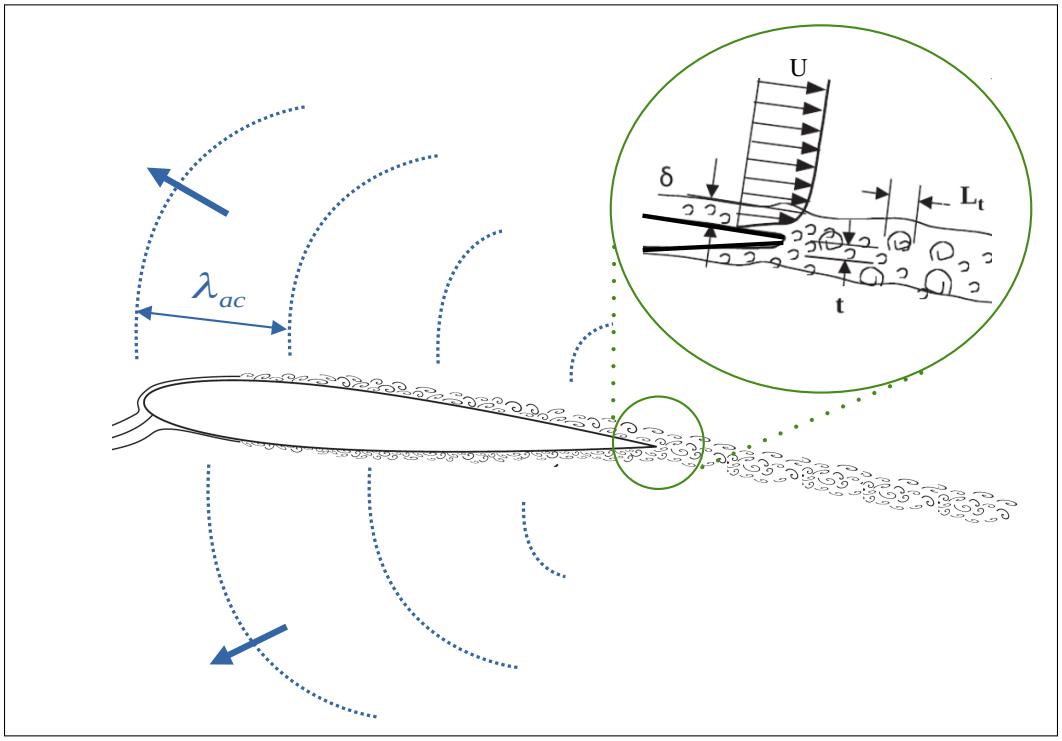

Figure 0.2 Schematic of turbulent boundary layer trailing edge noise mechanism. Taken from Colonius & Lele (2004)

While it is technically feasible to use Direct Numerical Simulations (DNS) to obtain both the aerodynamic and acoustic fields, the calculations are usually prohibitively long for use in propeller design. To put things in perspective, a single DNS simulation of the flow over an airfoil

(with the span a small percentage of the chord) at a relevant Reynolds number can take over 100 hours of wall time, using around 1000 cores of state-of-the-art computing power. For propeller design at an industrial scale, it is necessary to decouple the aerodynamic and acoustic fields. The acoustic analogy serves this purpose by using results from incompressible simulations to calculate far-field acoustics. For example, Large Eddy Simulation (LES) can be done to predict more complex flows, such as a propeller flow field, by limiting the resolution of the smallest turbulence scales. Then, the wall pressure over the blade can be used to obtain the acoustic information. Nevertheless, LES is still computationally intensive, and its place is at the end of the design cycle rather than at the beginning. The Reynolds-Averaged Navier-Stokes (RANS) equations model the effects of turbulence on the mean flow. While the very nature of turbulence has been eliminated in this process, the simulations are fast and can be used in conjunction with semi-analytical acoustic models to obtain broadband noise predictions.

Acoustic models for the two broadband edge noise mechanisms, i.e., TIN and TEN, were proposed by Amiet (1975, 1976) using the Linearized Euler Equations and simplifying the airfoil as a flat plate. Both models follow an excitation-response-propagation formulation, where the response or aeroacoustic transfer function relates the noise source (aerodynamic) to the far-field (acoustic) pressure. Despite the similarities in the mathematical formulation, the noise sources for TIN and TEN are essentially different. For the former, the random velocity field ahead of the leading edge alters the instantaneous angle of attack seen by the airfoil, leading to unsteady lift. Thus, the transfer function between excitation and response for TIN is tightly linked to the unsteady lift spectrum. For trailing edge noise, the transfer function relates the acoustic far-field to the wall-pressure fluctuations spectrum just upstream of the trailing edge. The wall-pressure spectrum is then an essential input to model TEN and can be obtained from RANS simulations (Sanjosé & Moreau, 2018).

Inspired by the owl's silent predatory capabilities, the use of serrations for trailing edge noise mitigation has been demonstrated for a variety of applications, with the noise reductions observed particularly at high frequencies (Lee *et al.*, 2021). Howe (1991) pioneered the analytical modeling for a semi-infinite flat plate with a sawtooth edge. The analytical results suggest that sharper serrations are more effective at mitigating trailing edge noise. However, the model overpredicted noise reductions. (Gruber, 2012; Moreau, Sanjosé, Lyu & Ayton, 2019). More recently, other models have been formulated in an attempt to improve the agreement with experiments. For example, Lyu, Azarpeyvand & Sinayoko (2016) used a serration model that combined Amiet's method with Fourier Series, resulting in a physically accurate but lengthy iterative method to evaluate the far-field noise. Using a different approach, Ayton (2018); Lyu & Ayton (2020) obtained a modal expansion that requires few modes to evaluate the far-field acoustics. Nevertheless, the model is strictly two-dimensional and cannot be directly applied to rotating blades. Lastly, all the airfoil models for both straight and serrated edges can be adapted to rotating blades using the model in Schlinker & Amiet (1981).

In this Thesis, a representative drone propeller based on the NACA0012 airfoil and with abundant experimental and numerical data available for validation (Gojon *et al.*, 2021; Rendon, Moreau, Gojon & Bauerheim, 2024; Vittal-Shenoy, 2023), is chosen to develop a low-order methodology for the design of propellers with serrated trailing edges. The following specific objectives are proposed:

- Validate Amiet's straight edge model for small-scale propellers.
- Extension of Ayton's model to include the effects of a finite chord.
- Develop a RANS-based design methodology for propellers with serrated trailing edges.
- Conduct an experimental validation of the designed propellers, taking into consideration the influence of serration manufacturing.

The Thesis is divided as follows: the first chapter describes the aerodynamics and aeroacoustics of small-scale propellers. Thus, it serves as a literature review. The physics and analytical methods for modeling trailing edge noise for straight and serrated trailing edges are presented in the second chapter. In the third chapter, an experimental campaign on airfoils is conducted, along with a comparison with analytical models. The RANS-based design methodology is presented in Chapter four, along with shape considerations for the serrated edges. This is followed in chapter five by the manufacturing of several serrated propellers to validate the design methodology. The thesis conclusions and recommendations are presented in the sixth and last chapter. The roadmap below summarizes the contents of this work, with the contributions outlined in the side boxes.

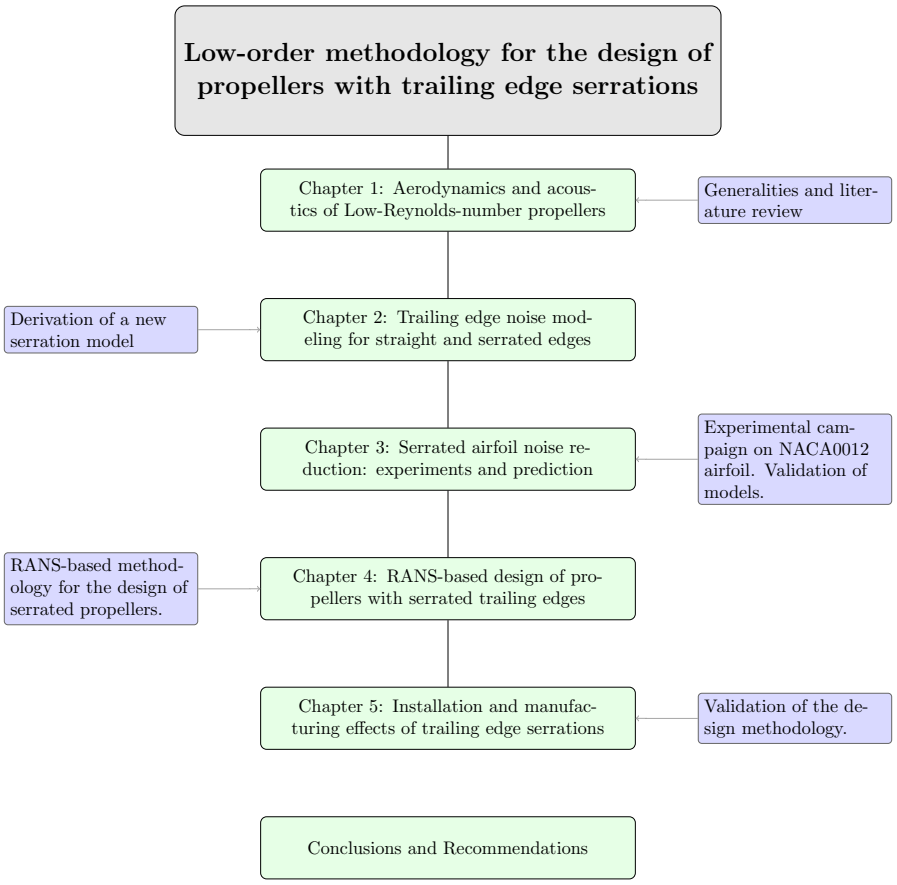

The following journal paper and articles in conference proceedings were published during the development of this Thesis and have been adapted or extended in the Chapters mentioned:

- Santamaria, J., Sanjose, M., Gojon, R., Belliot, S. & Moreau, S. Noise Generation Mechanisms in Propellers with Trailing Edge Serrations due to Installation and Manufacturing. Under review by the Journal of Sound and Vibration. *Chapter 5*
- Santamaria, J., Bierrenbach-Lima, A., Sanjosé, M. & Moreau, S. (2025). Shape Considerations for the Design of Propellers with Trailing Edge Serrations. Journal of Sound and Vibration, 595, 118771. doi: 10.1016/j.jsv.2024.118771. *Chapters 3,4*
- Santamaria, J., Bierrenbach-Lima, A., Sanjosé, M. (2025) Mesh Sensitivities for the RANS Simulations of Low-Reynolds number propellers. Proceedings of the FAN 2025 Conference *Chapters 3, 4*
- Santamaria, J., Sanjose, M., Gojon, R., Belliot, S. & Moreau, S. (2024). Installation and Manufacturing Effects of Propeller Trailing Edge Serrations. 30th AIAA/CEAS Aeroacoustics Conference (2024), (Aeroacoustics Conferences). doi: 10.2514/6.2024- 3322. *Chapter 5*
- Santamaria, J., Sanjose, M. & Moreau, S. (2023). Fast Broadband Noise Prediction of Serrated UAV Rotors in Hover. AIAA SCITECH 2023 Forum. doi: 10.2514/6.2023-0618. *Chapter 4*

CHAPTER 1

AERODYNAMICS AND ACOUSTICS OF LOW-REYNOLDS-NUMBER PROPELLERS

"What I cannot create, I cannot understand."

— Richard P. Feynman

December 17, 1903, Kitty Hawk, North Carolina, United States of America. After four successful powered, manned, and controlled flights in a heavier-than-air aircraft, the Wright brothers launched human civilization on a journey that would take them to the moon and their spacecraft to the edge of the solar system. A year prior to this milestone, Wilbur Wright took the task of designing and fabricating the wood propeller to drive their already working glider, while his brother worked on the "lightweight" gasoline engine that powers the propeller. Initially, Wilbur expected to find a detailed theory and calculation procedures based on the water-screws that had propelled steamships for over a century (Wolko & Anderson, 1987); instead, he found a compendium of empirical relations unfit for the demands of the aeronautical application. Building upon the knowledge extracted from their wind tunnel data, where several airfoils were designed and tested, Wilbur likely developed what is the first airplane propeller theory (Wolko & Anderson, 1987) in history. He recognized first that the propeller was essentially a twisted, rotating wing that generates lift in the forward direction and second that the propeller sections follow a helical path.

Propellers drove almost all the planes during the two World Wars, transitioning from fragile wooden blades that would easily delaminate and crack, to aluminum alloys that could withstand the higher speeds and high torques of supercharged piston engines. More blades were added to take advantage of the excess power available, and propeller aviation dominated the skies. The theory also became more refined through the understanding of lift following the results from Joukowski, Prandtl, Glauert, and Lanchester, among others. Circulation, blade element theory,

and finite wing corrections were available at the end of the Second World War, and propeller theory was largely completed by then.

Parallel to the theoretical developments in propeller aerodynamics, the sound generated by the blades was being studied. The first theory that matched experimental measurements was proposed by Gutin (1936). Gutin leveraged the periodicity of the rotating blade elements to formulate a frequency-domain theory, allowing for the prediction of noise due to the aerodynamic forces exerted by the propeller on the surrounding air, i.e., loading noise. Around the same time, Deming (1938) and Ernsthausen (1937) independently derived an analytical model for the noise caused by air displacement from the blade, known as thickness noise. The latter author highlighting the important effect on the noise field due to obstacles in the proximity of the blades.

Following World War II, another significant leap in aviation was made, as helicopter technology matured to the point where it allowed for vertical take-off and landing, hovering, and excellent maneuverability. While a helicopter rotor is mechanically, aerodynamically, and structurally more complex than a propeller, the principle of operation remains the same. Initially, helicopter noise was not a primary concern, as designers were mainly occupied with control and stability (F. Farassat & Brentner, K, 1994). However, it became important in the late 1960s, particularly with the replacement of piston engines with gas turbines to drive the rotors. The development of aeroacoustics through the Ffwocs-Williams and Hawking (FW-H) analogy resulted in a better understanding of the complex mechanisms behind helicopter noise. The following decades witnessed exponential growth in research on propeller and helicopter rotor noise, accompanied by the identification, characterization, and modeling of broadband noise sources.

While jet engines became the preferred method for propulsion during the second half of the 20th century, propellers are still used significantly in military and short-range civilian applications, mainly driven by turboprop engines. Modern propellers differ from older ones primarily in their shape and the materials used to construct them. Towards the top of the blade, high sweeps are used to avoid the drag rise associated with transonic flow; this additionally reduces the noise

emitted from the propeller. The development of composite materials allowed for stronger and lighter blades, giving propeller designers a larger design space.

Significant developments in materials, control, batteries, and electric motors, among other technologies, during the turn of the XX century sparked yet another revolution in aeronautics. Although Unmanned Aerial Vehicles (UAVs) have been designed and tested previously, their use was previously limited to recreational applications, such as radio-controlled airplanes and highly specialized military operations, where fixed-wing UAVs are used routinely.

Although a proof of concept was successfully demonstrated over a century ago by the Breguet brothers, it was not until the mid-2010s that the miniaturization of components allowed the quadcopter to become the civilian drone staple. Its maneuverability, versatility, and relative ease of control allow the quadcopter to permeate many industries. Quadcopters are now routinely used for complex tasks such as dam inspection, terrain mapping, agricultural monitoring, and surveillance. Additionally, they are used in search and rescue operations during disaster management. Delivery services is a market where drones are slowly being introduced and may see significant growth in the upcoming years. Propeller-driven drones are also at the forefront of planetary exploration. NASA's Ingenuity, a helicopter driven by counter-rotating propellers, was the first aircraft to flight outside the Earth, completing 72 flights in Mars' atmosphere, providing scientists with unique footage of the Martian surface. Projected to launch by 2028 and arriving to Saturn's largest moon, Titan, in 2034, Dragonfly is an eight-rotor drone currently being developed in a quest for answers on the origin of life on Earth.

Back on the pale blue dot, ambitious projects aim at upscaling drone technology to transport passengers and cargo in cities with heavy traffic. The aircraft designed for such purposes are called Urban Air Mobility (UAM) vehicles and aim to have a range of less than 100 km, thus creating a new market rather than competing with more traditional aviation. Companies such as Joby Aviation, Beta Technologies and Archer in the United States, Lilium and Volocopter in Germany, Vertical in the United Kingdom, and EHang in China are in a race towards certification. The UAM vehicles can be of hybrid design, featuring tilt-rotors and a fixed-wing for cruising,

such as Joby's S4 eVTOL. Other aircraft have dedicated propellers for the take-off and cruise phases, such as Archer's Midnight. However, some are purely VTOL, e.g., the EHang 216. Nevertheless, they all have in common the use of electric motors and propellers. Taking as a reference the restrictions on helicopter flights in the cities, the propeller noise signature of UAM vehicles is expected to be a crucial certification hurdle.

Compared to their historical predecessors, small drones and UAM propellers operate at lower Mach and Reynolds numbers as shown in Figure 1.1 where the y-axis corresponds to the tip blade Mach number while the x-axis is the Reynolds number based on the chord and the relative velocity seen by the blade at 75% span. A significant benefit of flying under these conditions is the elimination of noise sources associated with compressibility, such as shock waves. However, new challenges arise as historically, most propellers never operated in the range of modern ones, thus posing the question of whether the available aerodynamic and acoustic tools are adequate for the design of UAV propellers (Zawodny *et al.*, 2016)

Propellers were the cornerstone of early aviation propulsion, and, together with electrification and artificial intelligence, are driving aviation into a new era where drones are expected to become part of everyday life. The regulatory hurdles are more stringent given the proximity to people and range from safety to noise annoyance. According to Schäffer *et al.* (2021) drone noise is perceived as more annoying compared to road traffic or aircraft noise due special acoustic characteristics such as pure tones and high-frequency broadband noise. With increase drone traffic, noise regulations pertinent to these vehicles are expected to become more stringent over time, and it is of paramount importance to understand, model, and predict noise from propellers, as they will be the dominant noise sources. Moreover, the widespread and accessibility of additive manufacturing, particularly of 3D printing, is enabling more novel designs that can comply with the regulations while maintaining performance. This chapter describes the aerodynamic and acoustic characteristics of low-Reynolds-number propellers commonly found in quadcopters.

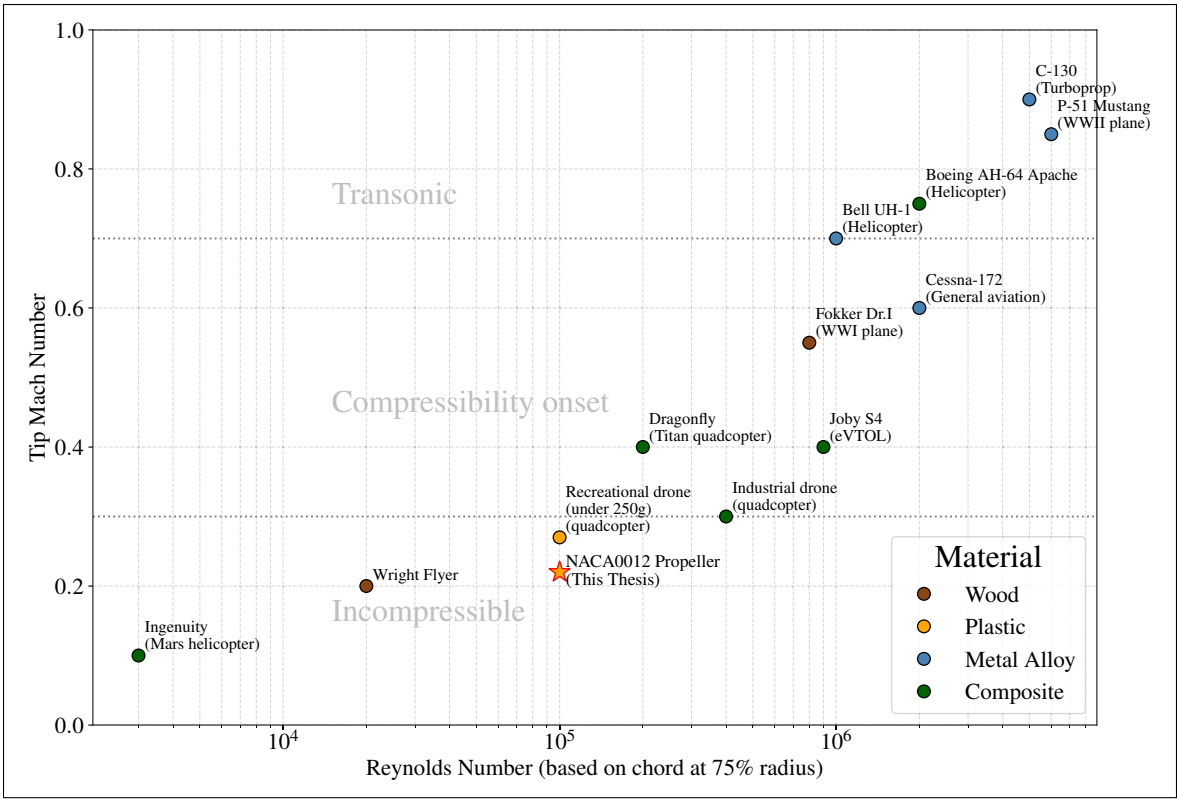

Figure 1.1 Propeller applications in terms of Mach and Reynolds number. Tip Mach numbers were calculated assuming sea-level conditions. Cruise velocities have been used for propeller-driven aircraft, whereas hover conditions were utilized for UAVs and helicopters.

1.1 Propeller Aerodynamics

1.1.1 Momentum theory

Almost half a century before the Wrights made their pioneering flight, Rankine (1865) and later Froude (1889) developed what is now known as momentum theory, providing a simple yet intuitive explanation of how ship propellers create thrust at the time. They recognized that the mass accelerated through the circular area swept by the propeller blade results in an opposite reaction that propels the vessel forward. The same principle can be applied to other bladed machinery such as airplane and drone propellers, helicopter rotors, and wind turbines.

Taking one isolated propeller from a drone in hover, a control volume is defined as shown in Figure 1.2(a). The propeller can be assumed to have an infinite number of blades of zero thickness, i.e., an actuator disk of area, , that supports the thrust, . Assuming steady, incompressible, and inviscid flow, a momentum balance can be done and in conjunction with Bernoulli's principle allows to find a relationship between the pressure in the disk and the thrust. The velocity and pressure evolution along the flow direction are shown in Figure 1.2(b). Notice that the pressure decreases upstream from the disk and increases downstream from it. This pressure difference is accompanied by an increase in flow velocity, resulting in the flow moving with induced velocity, . Notice that during ascending or descending phases of flight, the velocity can be taken into account by adding or subtracting from the induced velocity.

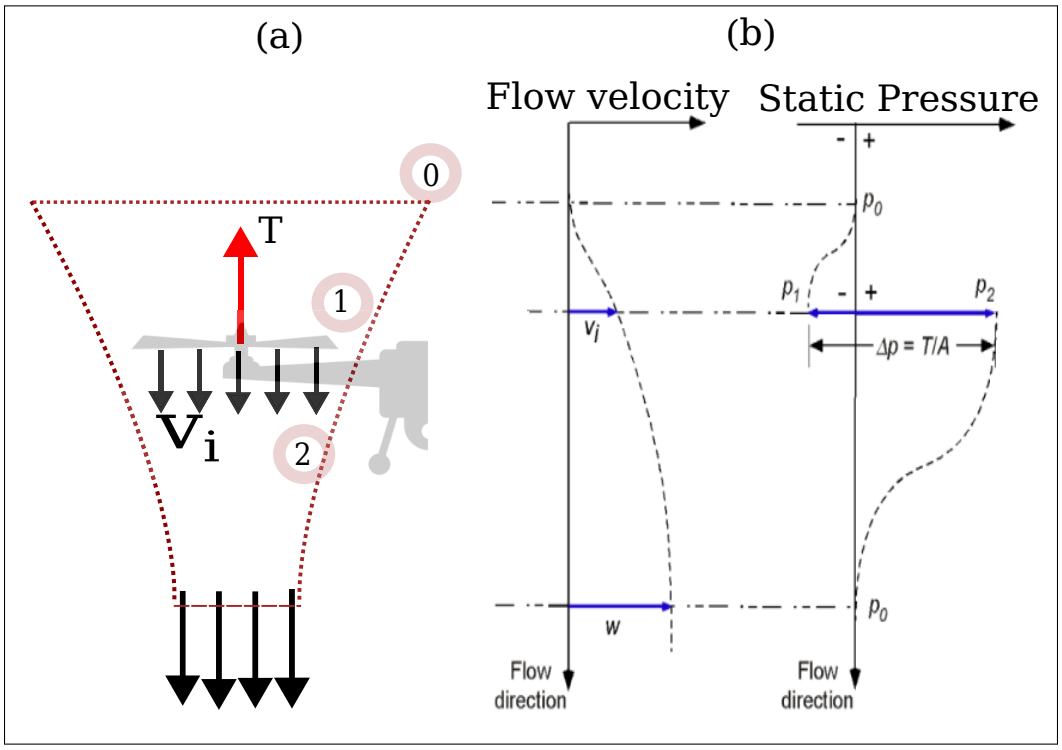

Figure 1.2 (a) Control volume for application of Momentum theory on an isolated propeller in hover (b) Velocity and pressure distribution along the axial direction
Taken from Leishman (2023)

Using momentum theory (Leishman, 2023) it can be shown that in hover, a drone propeller or a helicopter rotor accelerates a mass of fluid downwards and as a result, a pressure difference is

induced in the propeller disk area. Thrust is then the result of this pressure difference and equals to:

$$2 \quad {}^{2}\,{}^{2} \tag{1.1}$$

Where is the propeller radii and is the induced velocity in the disk. The ideal hovering power is then given by:

$$2 \quad {}^{2}\,{}^{3} \tag{1.2}$$

The above result partly justifies the large blades characteristic of all helicopters, as the power required to hover scales with the cube of the induced velocity. Notice that the assumptions in the actuator disk theory imply that the thrust distribution along the blade linearly increases from the hub towards a maximum value at the tip (Leishman, 2023). The simple momentum theory provides an intuitive model for quick estimates of propeller performance, but the geometry of the blade has not been taken into account, and all viscous losses have been ignored. To account for these effects, blade element theory is employed.

1.1.2 Blade element theory

A propeller blade consists of a few airfoil sections stacked on top of each other, usually at different pitch angles, , measured from the rotational plane, as illustrated in Figure 1.3. In blade element theory, each airfoil section is considered as independent of the others where the lift and drag of each section corresponds to the isolated airfoil section.

The isolated airfoil section shows the velocity triangle. The relative velocity being the vector sum of the inflow velocity and the blade velocity. While hovering, the inflow velocity corresponds to the induced velocity. The sectional lift experienced by a blade element of width d and chord with lift coefficient is given by:

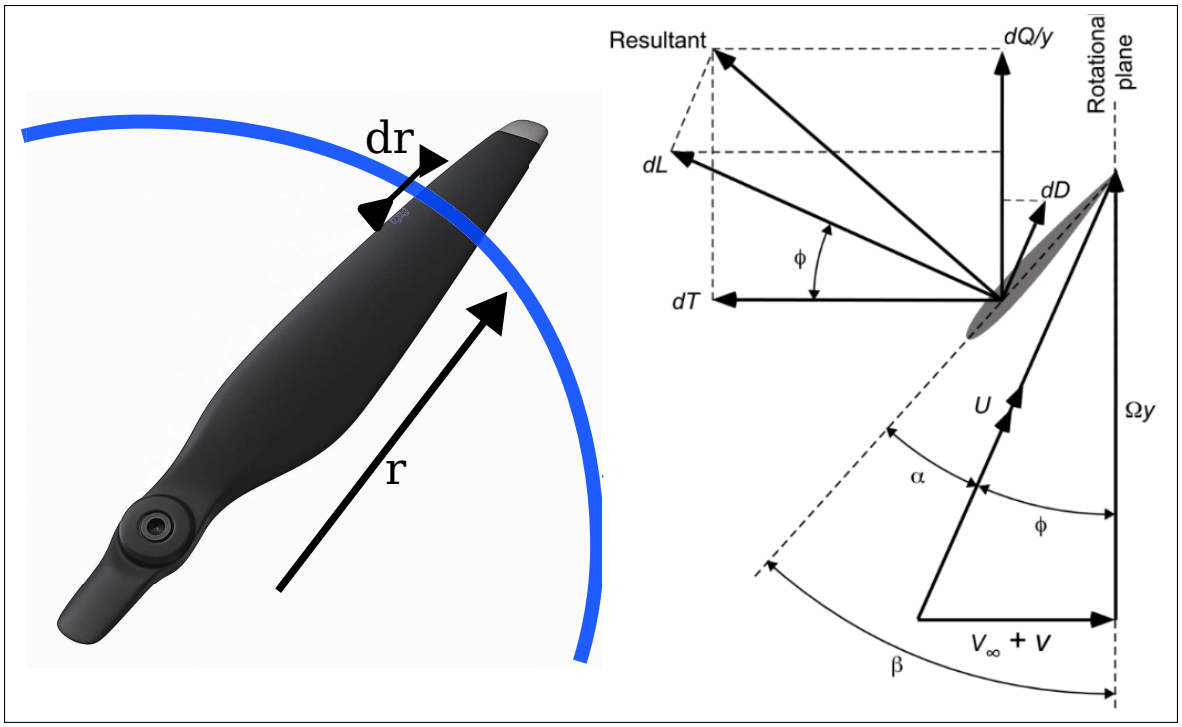

Figure 1.3 Propeller blade and airfoil section with velocities triangle.
Taken from Leishman (2023)

$$\frac{1}{2} \quad ^2 \tag{1.3}$$

Similarly, the sectional drag is given by:

$$\frac{1}{2} \quad ^2 \tag{1.4}$$

Where is the section drag coefficient.

The projection of the resultant aerodynamic force in the direction perpendicular to the rotational plane is the section contribution to the propeller thrust given by:

$$\cos \qquad \sin \tag{1.5}$$

The aerodynamic torque per unit span, , is similarly obtained as:

$$\sin \qquad \cos \tag{1.6}$$

In practice, the integrated thrust and torque are obtained by discretizing the blade into between 30 and 100 segments (Leishman, 2023) and using look up tables for the sectional lift and drag coefficients. Alternatively, a 2D viscous panel method such as XFOIL (Drela, 1988) can be used. Notice that the former quantities are a function of the local Reynolds and Mach number and thus knowledge of the induced velocity distribution is essential. To circumvent this issue, combined blade element and momentum theory (BEMT) are used in an iterative manner.

Propeller performance is commonly assessed using the following non-dimensional coefficients

- Advance ratio

$$\frac{}{} \tag{1.7}$$

- Thrust coefficient

$$\frac{}{\qquad 2 \qquad 2} \tag{1.8}$$

- Torque coefficient

$$\frac{}{\qquad 3 \qquad 2} \tag{1.9}$$

A common metric of hovering efficiency is the figure of merit defined as the ideal-to-actual hovering power ratio. Using Eq. (1.2) yields:

$$\frac{}{} \quad \frac{2 \qquad ^{2} \; ^{3}}{} \quad \frac{^{3} \; ^{2}}{\overline{2 \qquad ^{2}}} \tag{1.10}$$

1.1.3 Computational methods overview

While powerful, the BEMT method has certain limitations. First, it does not account for any rotor unsteadiness. Second, it assumes that the flow is radially balanced, with no velocity component along the span. Lastly, it limits the analysis to the rotor near-field, without any information on the wake. The development of powerful computers during the last quarter of the 20th century allowed for computational methods to be part of the propeller/rotor design process. Some of these methods are briefly described next.

1.1.3.1 Vortex lattice method

The wake of a propeller is a complex flow field bounded by the vortices shed from the propeller tip as shown in Figure 1.4 for a helicopter rotor in hover.

Figure 1.4 Tip vortex made visible through condensation of water vapor inside the vortex core of a Bell 214B-1 helicopter. Taken from http://www.airliners.net

In the Vortex Lattice Method (VLM), Laplace's equation is solved in a bounded domain with the blade surface discretized with two-dimensional panels. The flow is assumed, irrotational, incompressible and inviscid. Similarly to finite wing theory where a circulation distribution is solved by assuming that the wing sheds a vortex sheet, the Biot-Savart law can be used for propellers to relate the propeller wake to the blade circulation, and thereby the propeller thrust (Stepniewski & Keys, 1984). Nonlinearities can be added to the VLM by calculating effective sectional angles of attack and using airfoil look-up tables to include viscous effects as done by Jo, Jardin, Gojon, Jacob & Moschetta (2019). Given the mutual dependency between induced velocities and blade section circulation, the calculation proceeds in an iterative manner until force convergence is reached.

1.1.3.2 Computational fluid dynamics

While some non-linear effects due to viscosity can be coupled with the methods reviewed previously and therefore provide reasonable estimates of thrust and torque, there are a few factors that are left to empirical results and may not apply in particular cases. In other words, none of the methods reviewed so far deal directly with the governing equations of fluid flow. The use of computers to obtain solutions to the Navier-Stokes equations on discrete grids or meshes grew exponentially from in-house research codes in the 1980s to a billion-dollar industry that permeates almost all areas of science and engineering. Simulation of turbulent and transitional boundary layers, detached flow, unsteady pitching airfoil flow, combustion, flow-induced noise and vibrations are only a handful of the applications where Computational Fluid Dynamics is the only numerical tool available to study the problem. At the core of modern CFD is the oldest unsolved problem in classical physics, turbulence.

Chaotic flow is found in most natural and man-made flows. In them, a broad range of spatio-temporal scales continuously transfer energy from the largest to the smallest scales, where kinetic energy is ultimately converted into heat. There are different approaches to disentangle the myriad of scales contained in turbulent flows. On the most computationally intensive side, direct numerical simulation (DNS) solves all scales in the NS equations, extending to the Kolmogorov

scales responsible for the dissipation of turbulence kinetic energy into heat. A single DNS simulation for the flow over an airfoil at moderate Reynolds number can take on the order of months. While computational power is making DNS more accessible, directly solving the aerodynamic and acoustic field is still challenging for a variety of reasons (Sandberg & Sandham, 2008): firstly, the extent of the acoustic field is considerably larger than the relevant flow field, and there is an important disparity between the size of the scales in each one. Secondly, the acoustic field energy is orders of magnitude smaller than that of the aerodynamic field, which requires costly numerical schemes with low dissipation.

The most modeling-intensive approach, yet most friendly from the computational cost perspective, attempts to model the effects of turbulence on the average flow. In the Reynolds Averaged Navier-Stokes (RANS) equations, the flow field is decomposed into a mean and fluctuating part and then time-averaged. This effectively filters the fluctuating component but introduces additional stresses that must be modeled. In all RANS approaches, additional transport equations are introduced to close the resulting system of equations.

1.1.4 Low-Reynolds number aerodynamics

Propellers generally found on small airplanes, UAVs, and drones, operate in flow regimes characterized by Reynolds numbers based on the blade sectional chord at 75% radius, typically on the order of 10^5 (See Figure 1.1). In this regime, the blade sectional drag values are higher than at chord Reynolds numbers above 10^6, which significantly impacts the thrust and lowers the overall propulsive efficiency of the propeller. As the Reynolds number decreases below one million, the effects of viscosity begin to outweigh inertia effects in the flow, and the lift and drag characteristics of airfoil sections undergo profound changes. These considerations are essential for propeller applications to most UAVs and drones, which can expect maximum propulsion efficiencies of between 50% and 60% rather than 80% or higher for “full-scale” propellers (Leishman, 2023).

Figure 1.5 illustrates the flow characteristics over airfoils for different low-Reynolds number regimes. Just above = 500,000, the laminar flow experiences a high adverse pressure gradient (APG), which results in detachment due to the low energy levels in the laminar boundary layer. A laminar separation bubble (LSB) appears as a consequence, and the flow reattaches as a turbulent boundary layer. At Reynolds numbers between 50,000 and 100,000, the contribution of viscous forces increases, resulting in larger LSBs, up to 40% of the chord, and thicker turbulent boundary layers. With increasing angle of attack, the separation and re-attachment points tend to fluctuate, and force measurements carry large uncertainty bands. For yet lower Reynolds numbers, in the order of 10,000, the boundary layer remains laminar for most of the airfoil, and once it detaches, it remains in this condition; thus, the airfoil primarily operates in trailing-edge stall.

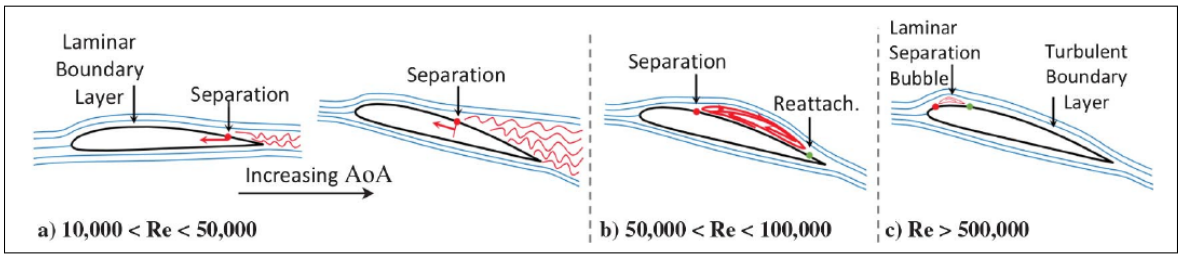

Figure 1.5 Flow over airfoil at transitional Reynolds number.
Taken from Winslow *et al.* (2018)

From the preceding discussion it is clear that a typical quadcopter propeller operates in a regime where the formation of LSB and the transitional flow play a key role in the propeller performance. High-fidelity CFD methods have been used to model propeller aerodynamics at this challenging regime. For example, Casalino, Grande, Romani, Ragni & Avallone (2021) used the Lattice Boltzman Method (LBM) to predict aerodynamics and acoustics of a small propeller, finding good agreement in the thrust for high advance ratios but some disagreement at hover conditions. Vittal-Shenoy (2023) and Rendon *et al.* (2024) used LES and LBM respectively for a representative drone propeller. Thurman, Boyd Jr., Buning, Reboul & Benoit (2024) compared smooth and rough 3D printed rotors with LBM simulations finding discrepancies of up to 10% and 5% for the smooth and rough propellers respectively, highlighting the importance

of the manufacturing method when comparing with numerical results. Carreño Ruiz, Scanavino, D'Ambrosio, Guglieri & Vilardi (2022) obtained results within 3% of experimental results for a small-scale rotor using RANS with transitional modeling. Overall, the challenges of low-Reynolds number performance prediction are still being addressed. RANS transitional modeling is an area of ongoing research with the industry-oriented codes implemented in the last 10 years and subjected to continuous verification. Nonetheless, it is still the most viable alternative to rapidly evaluate the performance of new prototypes.

1.2 Low-Reynolds number propeller noise

While many noise sources are shared between helicopters and drones, their relative importance in terms of human ear response differs. One of the characteristic noise signatures from a helicopter is the loud "thump-thump" often heard in forward flight. This complex acoustic mechanism is partly due to the high blade tip speeds and the interaction of the blade with preceding blade tip vortices. This mechanism is not present in standard quadcopters as the tip Mach number is not high enough. However, other noise sources are present in quadcopters. For example, aerodynamic and acoustic interactions between the propellers may result in beating phenomena (Tinney & Sirohi (2018)) due to slight differences in rotational speed. Furthermore, interaction of the propeller with the quadcopter arms may result in increased noise levels (Gojon, Parisot-Dupuis, Mellot & Jardin (2023)). Lastly, during turning maneuvers, noise increase has been reported (Zamponi *et al.* (2025)). Given all the complex acoustic interactions, propellers can be studied in isolation to get insight into the noise source mechanisms.

The power spectral density(PSD) of the acoustic pressure measurements in an anechoic chamber for an APC 11x7.4 propeller (Gojon *et al.*, 2021) is shown in Figure 1.6 for two observer positions and at 6000 RPM, with corresponding shaft rotational frequency of 100 Hz. The commercial 2-bladed low-Reynolds-number propeller has a diameter of 28 cm, with Eppler E63 and Clark-Y airfoils. The total spectrum shows high noise levels between 10 and 100 Hz, corresponding to background noise. The motor noise shows peaks at the shaft rotational frequency and a few narrowband humps at frequencies around 10 kHz. The well-defined peaks at the Blade Passing

Frequency (BPF) and its harmonics, and at the shaft rotational frequency and its harmonics are the propeller tonal noise. For frequencies above 1000 Hz, the acoustic energy spreads across a broad frequency range, resulting in broadband noise. Notice the difference in the acoustic energy distribution for the two different observers, i.e, the noise directivity. On the rotational plane (cyan spectra), the tonal noise is significantly higher at the BPF, while the broadband component is lower compared to the observer at 60 degrees (red spectra). As discussed in the next Chapter, because broadband noise radiation is symmetric about the rotational plane, it is a dominant noise source for overhead drones in hover. The sources of tonal and broadband noise are discussed in the following section.

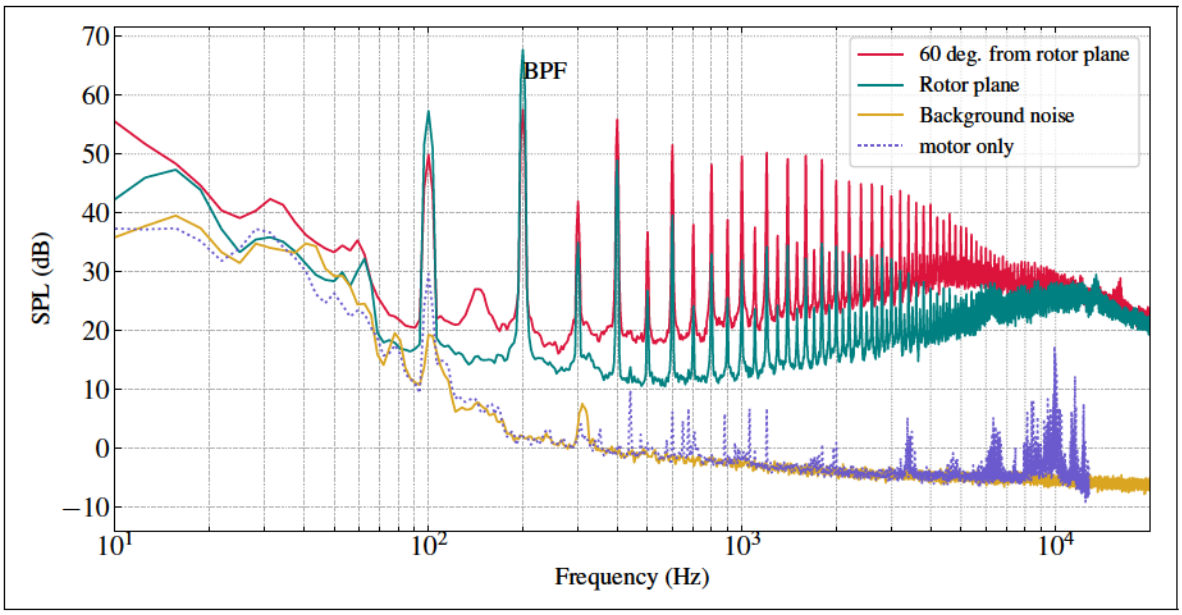

Figure 1.6 APC 11x4.7 spectra with background and motor noise
Reproduced with permission from Gojon *et al.* (2021)

1.2.1 Tonal noise

As a blade rotates, it displaces air and the rapid displacement of the air volume emits noise as a consequence. The intensity of this sound depends exclusively on the geometry and the speed of the blade section, and it is labeled as thickness noise. The thrust and torque exerted on the surrounding air by the rotor blades also result in sound emission, known as loading noise. Time

and frequency domain approaches can be used to predict tonal noise. The time-domain method is based on Farassat (1976) integral solution to the Ffwocs-Williams and Hawkings analogy, detailed in the next chapter. The time-domain approach requires time sequences of the near-field variables and estimation of the retarded time is done in the integral solutions. In contrast, the frequency domain method mainly developed by Hanson & Parzych (1993) leverages the noise sources periodicity and provides a formulation using Fourier series expansion coefficients at the BPF and its harmonics.

Time-domain approaches are convenient when transient phenomena are expected, for example for helicopters blade-vortex interaction. Frequency domain methods are preferred for statistically stationary phenomena and are commonly employed for small-scale propellers. To illustrate the different geometrical and flow parameters influencing tonal noise, Zhong *et al.* (2020) simplified analysis for propellers in hover, based on Hanson & Parzych (1993) frequency-domain model, is presented.

Consider a propeller with equally spaced blades, each with a surface area. . The source (i.e., propeller) coordinates are given by **y** $_1$ $_2$ $_3$ $_1$ cos sin , where is the azimuthal angle in the propeller rotational plane, and is the initial phase angle. Please note that throughout this Thesis, bold symbols represent vector quantities. The point in space where the acoustic pressure is calculated is given by the observer position coordinates, **x** $_1$ $_2$ $_3$. The acoustic pressure at an observer, **x**, due to thickness, **x** , and loading **x** noise is given by:

$$\mathbf{x} \quad \frac{0}{2} \quad {}^{2} \quad \frac{}{} \quad {}_{1} \quad \hat{}_{0} \tag{1.11}$$

$$\mathbf{x} \quad \frac{}{2} \quad {}^{2} \quad \frac{\hat{}_{0}}{} \tag{1.12}$$

where $_0$ is the undisturbed medium density, is the propeller angular velocity, and is the mean axial flow velocity in the $_1$ direction. The noise is calculated at the BPF and its harmonics

given by where is an integer. $\hat{}_0$ is the frequency-domain free-field Green's function, i.e, the impulse response function of the homogeneous wave equation in three dimensions, defined as:

$$\hat{}_0 \ \mathbf{x}\ \mathbf{y} \quad \frac{\mathbf{x}\ \mathbf{y}}{4\ \mathbf{x}\ \ \mathbf{y}} \tag{1.13}$$

The source terms in Eq. (1.11) and Eq. (1.12) are and for thickness and loading noise respectively. The former represents the volume displaced per unit time by the area element due to the motion of the blade. The latter contains contributions from the axial, radial and azimuthal components of the force on the blade. For propellers, the radial component is usually ignored. Considering that the flow contains unsteady but periodic components in the -direction, the source terms are commonly represented as Fourier series over n modes, with the 0 mode representing the mean loading. Note that the velocity and force distributions over the blade can be obtained from the aerodynamic methods discussed in the previous section, i.e., BEMT, RANS, LES. Additionally, upon evaluation of the free-field Green's function, the resulting integrals are expressed in terms of Bessel functions of the first kind of order m.

Under ideal conditions, such as a uniform and steady inflow, the propeller tonal noise signature will be concentrated at the BPF. However, that is rarely the case. Rotor dynamic unbalance and recirculation are common sources of variation of blade loading during isolated rotor testing, the latter being critically avoided in anechoic room measurements (Stephenson, Weitsman & Zawodny, 2019). Due to these factors, the axial and azimuthal forces contain not only the mean loading but also its harmonics. The effect is illustrated for an APC 9x5 propeller in hover conditions in Figure 1.7(a) for 3600 and (b) 7200 RPM. The loading coefficients were obtained using BEMT (Zhong *et al.*, 2020). Notice that the mean loading contributes mainly to the BPF and its first few harmonics, while all other loading harmonics (0) contribute to the remaining harmonics.

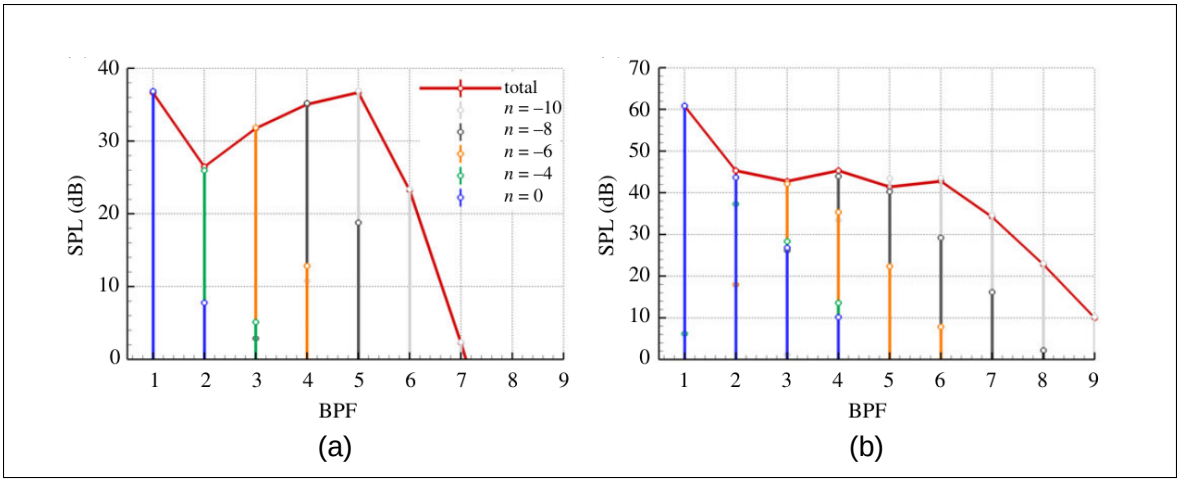

Figure 1.7 The influence of unsteady motion in the sound produced at the BPF and its harmonics at (a) 3600 RPM and (b) 7200 RPM.
Taken from Zhong *et al.* (2020)

1.2.2 Broadband noise

Noise sources that randomly fluctuate in time are responsible for broadband noise. For the typical low-Mach numbers found in quadcopter propellers, the turbulent eddies, modeled as a quadrupolar source, are inefficient sound radiators. However, the presence of the blades leading and trailing edges significantly increases the acoustic radiation efficiency. Typical spectra for leading and trailing edge noise are shown in Figure 1.8. The former tends to dominate at low non-dimensional frequencies while the latter does so at high frequencies. Interaction of the rotor blades edges with incoming or self-generated turbulence results in acoustic waves being emitted in a broad range of frequencies

The interaction of the blade leading edge with incoming turbulence results in random lift fluctuations, which can be modeled as a dipole source following the analogy of Curle (1955). This results in turbulence interaction noise, also known as TIN. Such turbulence might be the result of atmospheric disturbances, wake of other flying vehicles or the wake of structures upstream from the propeller.

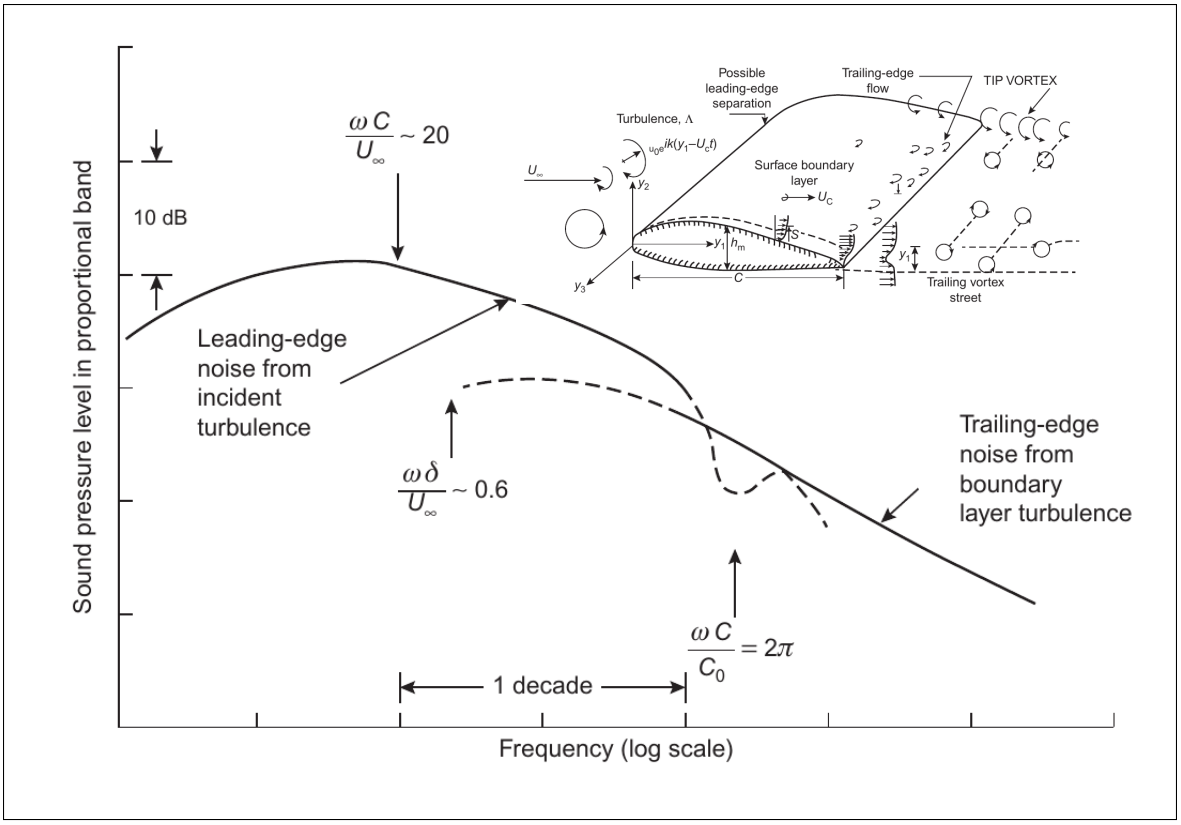

Figure 1.8 Edge noise mechanisms for an airfoil in a turbulent flow.
Taken from Blake (2017)

Assuming homogeneous and steady inflow into the rotor, the only broadband noise sources are due to self-generated turbulence in the blade boundary layer. A minute fraction of the turbulence kinetic energy is converted into acoustic energy and radiated as noise due to the scattering of the boundary layer at the trailing edge. Thus, trailing edge noise (TEN) represents the minimum achievable noise level for a propeller or any turbomachine. TEN has directivity as shown in Figure 1.6, where the broadband levels for the upstream observer are higher than the ones at the rotational plane. Given the human ear sensitivity in the frequency range between 1-5 kHz, TEN is a dominant noise source for small propellers, particularly while hovering (Zawodny *et al.* (2016); Intaratep, Alexander, Devenport, Grace & Dropkin (2016); Tinney & Sirohi (2018)).

The sound emitted from either the interaction of a leading edge with upstream turbulence or the interaction of a trailing edge with the surface boundary layer turbulence is fundamentally a

scattering[1] phenomenon in which a high-wave-number aerodynamic disturbance incident on the edge, generates a low-wave-number propagating acoustic pressure. Following the steps in Lighthill (1952) seminal work, Curle (1955); Powell (1959) showed that the acoustic power PSD scales between the fourth and fifth power of the flow velocity for edge generated noise. During the 1970s, Williams & Hall (1970), Howe (1978) and Amiet (1976) derived analytical models from first principles to predict trailing edge noise. Common to all models is the solution of a boundary value problem (BVP) based on the convected Helmholtz equation with mixed boundary conditions. All models agree with the aforementioned scaling and yield a dipole-type directivity pattern. Brooks, Stuart & Marcolini (1989) (BPM) then proposed a simpler empirical model to calculate airfoil self-noise, including TEN. The BPM model is based on scaling laws for TEN and empirical fitting using several measurements on NACA0012 airfoils at different operating parameters (Bertagnolio *et al.*, 2023). The main drawback of the method is its application to airfoils that differ significantly from the NACA0012 shape (Lee *et al.*, 2021).

Amiet (1976) model uses the Linearized Euler Equations, recast into a canonical wave equation, to solve a scattering problem and obtain an aeroacoustic transfer function. The aeroacoustic transfer function relates the noise source, i.e., the wall-pressure fluctuations near the trailing edge, to the far-field acoustic pressure. Direct measurement of the former is difficult for any rotating machinery (Neal, 2010). Thus, a key step in predicting propeller trailing edge noise is modeling the wall-pressure fluctuation spectrum. Later, Roger & Moreau (2005) extended Amiet's model to include the effects of back-scattering from the leading edge, which are important at small non-dimensional frequencies.

Schlinker & Amiet (1981) proposed a strip-theory-based method to use Amiet's model for helicopter rotors, which was later successfully applied to low-speed fans (Sanjosé & Moreau, 2018; Rozenberg, Roger & Moreau, 2010), to wind turbines (Tian & Cotté, 2016) and more recently to large propellers (Lallier-Daniels *et al.*, 2020). The blade strip moves in a local rectilinear motion, thus neglecting the acceleration effects due to rotation. Additionally, the

[1] In the context of trailing edge noise, scattering and diffraction are usually used interchangeably. These two terms are borrowed from acoustics and often refer to the interaction of an acoustic wave with an object, where the wavelength of the former is approximately the same size as the latter.

rotor frequency is much smaller when compared to the turbulence frequency, and the noise is blade-to-blade uncorrelated. Lastly, the noise from one blade strip can be obtained by a weighted average over one strip revolution, with the weight factor accounting for the Doppler effect for the emission frequency.

Besides the edge noise mechanisms, the low-Reynolds number operating conditions may result in noise emission from the interaction of instabilities in the laminar boundary layer with the trailing edge. During the laminar-to-turbulent transition, Kelvin-Helmholtz instabilities are convected towards the trailing edge resulting in the scattering of acoustic waves. The acoustic waves in turn travel upstream and reinforce the instabilities, thus creating a feedback-loop as shown in Figure 1.9. Noise due to the acoustic feedback loop can be heard in helicopters during the slowing down of the rotor after landing (Wright, 1976) and was intensively studied both in airfoil (Paterson, Vogt, Fink & Munch, 1973b) and low-speed fans (Longhouse, 1977) during the 1970s.

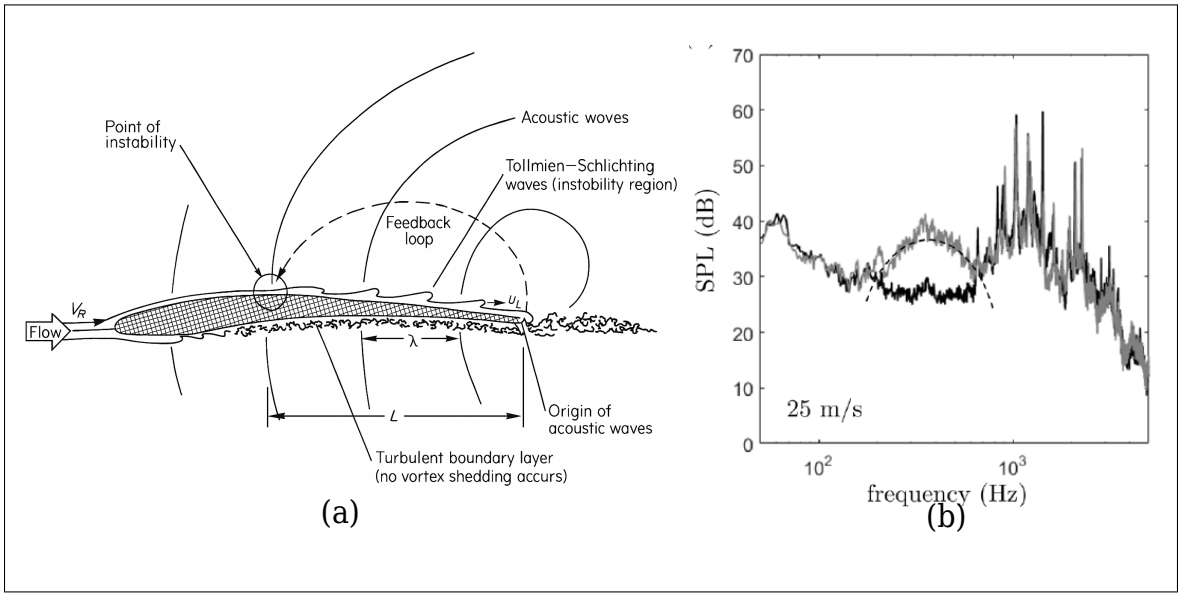

Figure 1.9 (a) Aeroacoustic feedback loop mechanism. Taken from Longhouse (1977), and (b) far-field noise spectrum on a NACA0012 at low-Re number. Taken from Yakhina *et al.* (2020)

1.2.3 Propeller noise control

Tonal noise control can be achieved through geometry modifications, such as chord and pitch distributions, which may influence thickness and loading noise, respectively (Li Volsi *et al.*, 2024). Additionally, with synchrophasing, the relative phase angle of the propellers can be manipulated to create destructive interference in the far-field at specific frequency (Patterson *et al.*, 2020; Pagliaroli, Candeloro, Duchetto, Rossignol & Yin, 2025). In large propellers, the most used noise control method stems from the avoidance of critical Mach numbers at the blade tip, resulting in high blade sweeps.

For broadband noise control, active and passive techniques are employed to control edge noise. The former requires an external mechanism to act on the airfoil, whereas in the latter, the edge geometry or the airfoil itself is modified. Active noise control includes the suction or blowing of the boundary layer or plasma actuation. Boundary layer suction upstream from the trailing edge has two main effects, as noted by Szőke, Fiscaletti & Azarpeyvand (2020): first, the boundary layer height is reduced, and second, the energy content is reduced mainly in the logarithmic layer. These two effects result in lower wall-pressure fluctuations, which in turn yield lower trailing-edge noise. While effective, active noise control methods are invasive, costly, and their implementation in a rotating environment is complicated.

Alternatively, passive edge treatments can be used to mitigate the acoustic scattering. Designers have drawn inspiration from the stealth capabilities of certain owl species. Owls rely on several evolutionary adaptations to succeed in the challenging task of hunting in quiet and dark forests. Among these adaptations are a disproportionate eyes-to-face ratio, bi-aural hearing, an almost freely rotating head, and, notably, serrated feathers. According to Lilley (1998), this last adaptation was first noted by Graham (1934), who suggested three main structures that helped Owls to capture prey while being unnoticed or giving them too short a time to escape. The first one are leading-edge comb-like serrations, the second one, trailing-edge comb-like serrations, and lastly very soft upper and lower wing surfaces. These structures are shown in Figure 1.10 (a). Figure 1.10 (b) shows the scaled spectra of in-flight measurements of three birds of prey, the

barn owl, the Harris's hawk, and the Common kestrel performed by Sarradj, Fritzsche & Geyer (2011). The barn owl's noise signature is remarkably lower in the 1.6 to 6.3 kHz frequency range, noting that the acoustic array could not resolve the signal past the latter frequency. In an extensive experimental investigation by Kroeger & Helvey (1971), some noise suppression mechanisms were suggested that could explain the morphology of the Owls' wings. Among them, vortex sheet generators guaranteed attached laminar flow on the outboard part of the wing, reduced velocity gradients at the trailing edge, and a shift towards lower frequencies compared to solid surfaces.

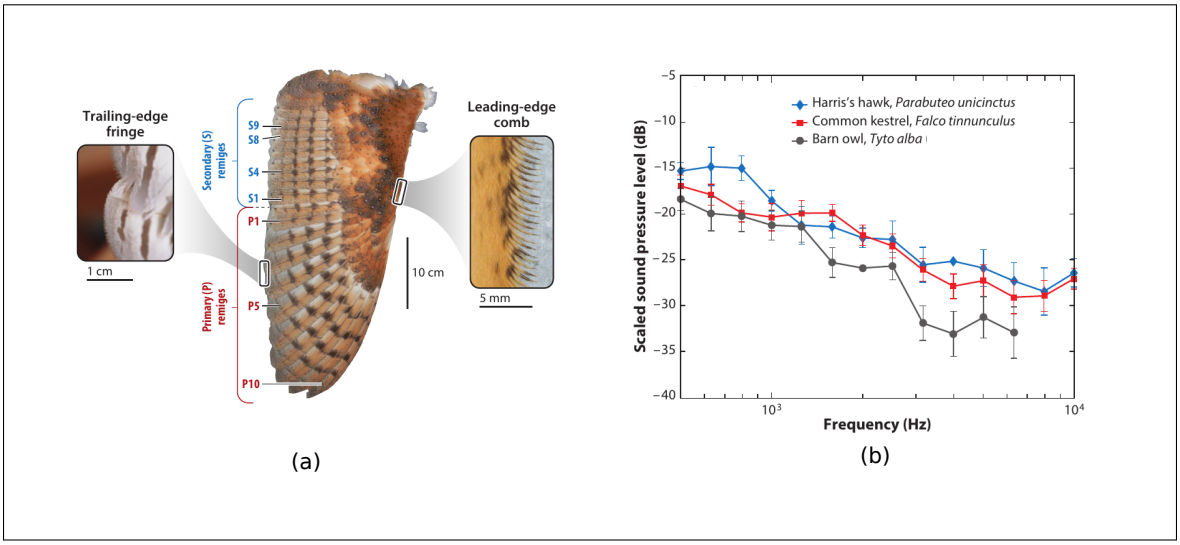

Figure 1.10 (a)Barn's owl wing morphology and (b) noise spectrum from three birds of prey.
Taken from Jaworski & Peake (2020)

As pointed out by Jaworski & Peake (2020), the mechanisms behind the owl's silent flight are still an intensive field of research and understanding of the basic physics involved are desired in order to be adapted to aerospace applications. Despite the lack of understanding into the essential mechanisms, serrations have already shown to be an effective noise control method.

Oerlemans, Fisher, Maeder & Kögler (2009) installed serrations in a full-scale, 94 m diameter wind turbine. Noise reductions of 2-3 dB were achieved at low frequencies, accompanied by a slight increase in noise at higher frequencies. Gruber, Joseph & Chong (2010) investigated the

effect of serration wavelength, , and amplitude, 2 , on far-field noise using a NACA65(12)-10 airfoil as shown in Figure 1.11 (a). The experimental campaign demonstrated that serrations can be utilized for airfoil TEN mitigation at non-dimensional frequencies, given by 1, Figure 1.11 (b), where is the boundary layer thickness and is the convection velocity of eddies within the boundary layer. Noise increase was found for non-dimensional frequencies above 1, as shown in Figure 1.11 (c). Narrower serrations characterized by a smaller serration wavelength, , showed better noise reduction performance. Later, Chong, Vathylakis, Joseph & Gruber (2013) investigated the effect of non-flat serrations at a moderate Reynolds number on a NACA0012 airfoil. They found that the serrations were able to suppress airfoil tonal noise on the one hand, and were responsible for vortex-shedding noise due to the thickness at the serration root on the other hand.

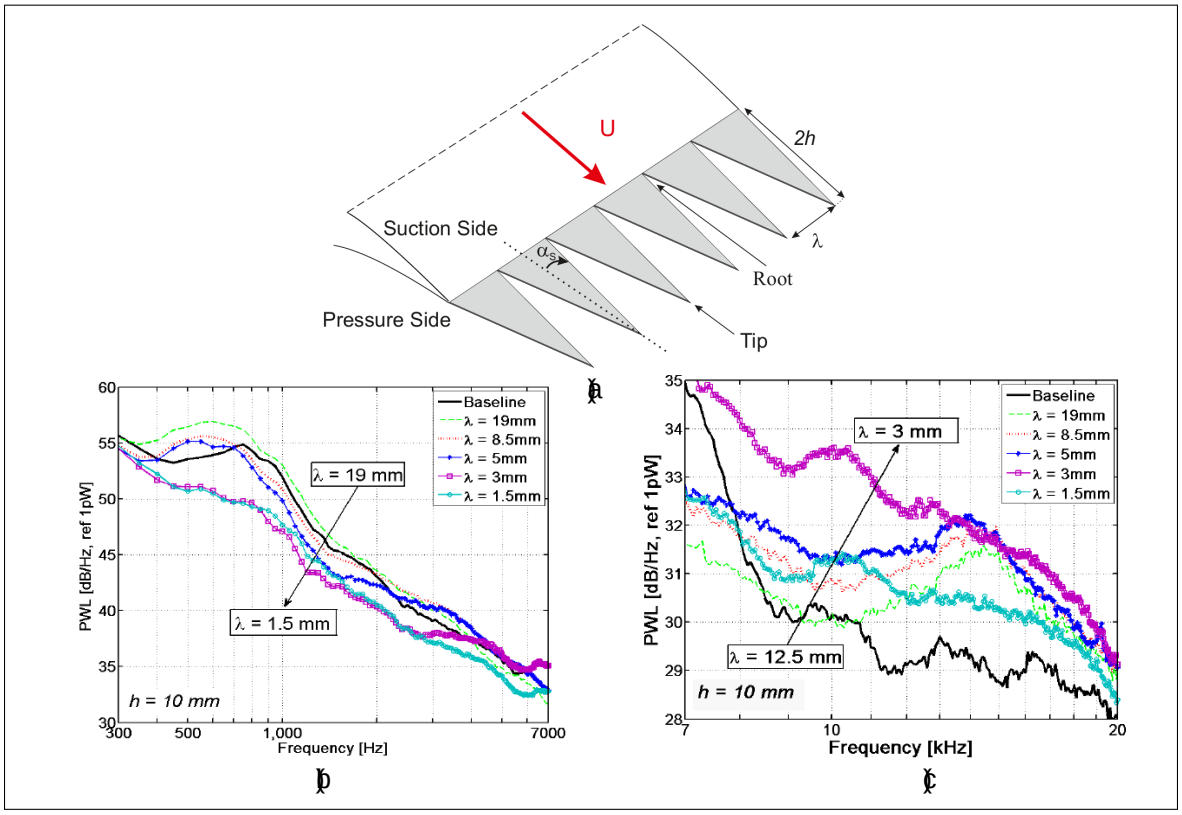

Figure 1.11 Comparison of baseline airfoil with serrated ones.(a) Airfoil with trailing edge serrations, (b) noise spectrum from 300 to 7000 Hz, and (c) noise spectrum from 7000 to 20000 Hz.
Taken from Gruber (2012)

Arce León, Ragni, Pröbsting, Scarano & Madsen (2016) performed far-field acoustics and particle image velocimetry (PIV) measurements of the flow through serrations added to a NACA0018 airfoil at a Reynolds number of 2 6 10^5. The effect of the serration angle with respect to the trailing edge, as in a flap, was investigated. Noise reductions of up to 6 dB were measured between 1-5 kHz for aligned serrations, whereas noise reduction was followed by noise increase for the misaligned ones. In the same configuration, Avallone, Pröbsting & Ragni (2016) used PIV to characterize the flow over the serrations and the near wake. The results showed that upstream of the trailing edge, the flow is mildly affected by the serrations. Downstream, the flow pattern is complex and characterized by a pair of counter-rotating streamwise-oriented vortical structures.

Direct Numerical Simulations (Sanjose *et al.*, 2014; Jones & Sandberg, 2012; Moreau *et al.*, 2019) have shown that the far-field noise reduction achieved by serrations is caused by the scattering process, i.e., tip-root interference rather than a change in the turbulence statistics. This minimal change in turbulence statistics between straight and serrated edges can be exploited by modeling the wall-pressure spectrum only once and using analytical models to account for the scattering differences between straight and serrated edges

While several studies focused on airfoil TEN control with serrations, only a handful of investigations looked at small propeller TEN reduction. For example, Ning, Wlezien & Hu (2017) measured the noise reductions from a small propeller with sawtooth serrations of different amplitudes with one microphone located on the rotation axis, upstream from the propeller. They concluded that sharper serrations are better at reducing TEN. Additionally, the study found no difference in thrust between straight and serrated edges at hover. Similarly, Pang, Cambray, Rezgui, Azarpeyvand & Showkat Ali (2018) investigated the far-field acoustics of small serrated propellers using a directivity antenna that covered the upstream direction. The results showed that serrations can reduce broadband noise, particularly for low rotational velocities. Lee *et al.* (2019) experimented with serrations with a flat tip (chopped peak) and with rectangular patterns in a small anechoic chamber. In the former case, noise reduction was achieved at most RPM and observer positions, whereas in the latter, noise reduction was observed only at one RPM.

Yang, Wang, Liu, Hu & Li (2020) investigated different ways to add serrations to a propeller blade. They studied the influence of adding versus cutting the serrations on the blade. They also varied the portion of the blade span that is serrated. Looking at forward flight, they found that add-on serrations increased thrust compared to the baseline configuration at the same rotational speed (RPM). The opposite behavior was found for cut-in serrations. Both serrated designs showed reduced power consumption. The noise reductions measured for blades with full-span or half-span serrations were similar. Wei *et al.* (2021) compared the performance of conventional sawtooth serrations with rounded ones in a narrow RPM range (2000-3000). They concluded that both methods are effective and noted an increase in thrust generated, attributing the performance improvement to the added area of the baseline propeller. More recently, Candeloro, Nargi, Grande, Ragni & Pagliaroli (2021) tested rotors with sawtooth serrations of different amplitudes and wavelengths in hover and forward flight. They showed that the serrations seem to be more effective during forward flight and that the reductions are greater closer to the rotor plane. Moreover, a reduction in thrust compared to the baseline was observed. Lastly, Wei *et al.* (2024) combined a cicada's wing shape with serrations, resulting in better noise and aerodynamic performance. Their design, along with other serrated propellers, is shown in Figure 1.12

Given the vast creative space that serrations provide to propeller designers, a physical model capable of capturing the essential mechanism of noise attenuation is desired during early design phases. Howe (1991) pioneered the analytical modeling of serrated trailing edges. The methodology follows the use of Green's functions. The far-field leading order approximation, as explained by Lee *et al.* (2021), states that for a serrated edge with height-to-wavelength ratio 1 the spectrum is given by $_0$ 2 , where $_0$ is the straight-edge spectrum, resulting in less noise than the corresponding straight edge. Gruber (2012) experiments tested Howe's model concluding that it overpredicted the noise reductions by over 10 dB at certain frequencies.

Later, Lyu *et al.* (2016) leveraged Amiet's solution for the straight-edge problem, and assumed the solution as a Fourier expansion, yielding a system of coupled PDEs. The coupled system of PDEs must be solved iteratively, and approximation of different orders can be obtained, with the second-order solution giving reasonable convergence (Lyu *et al.*, 2016; Akila, Marinus & Larbi,

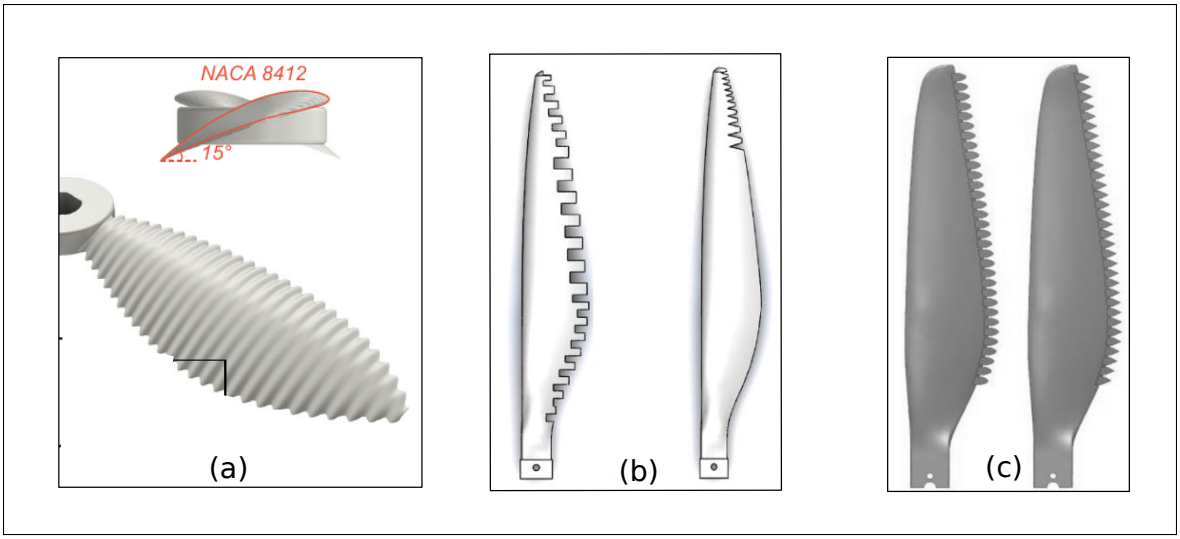

Figure 1.12 Bio-inspired propeller designs (a) Cicada wing shape with chordwise 3D serrations. Taken from Wei *et al.* (2024), (b) rectangular and flat tip serrations. Taken from Lee *et al.* (2019), and (c) sawtooth and rounded serrations. Taken from Wei *et al.* (2021)

2018). While accurate, Lyu's model evaluation is computationally intensive. To circumvent the long computational time, Ayton (2018) employed the Wiener-Hopf method[2] to derive a closed-form solution to the serrated edge problem. Ayton application of the Wiener-Hopf method, resulted in an eigenfunction expansion for the spanwise direction (serrated edge) in transformed Fourier-space, where the expansion coefficients are determined by the serration shape. Ayton then applied the method of steepest descent (or stationary phase) to approximate the inverse Fourier Transform. This latter approximation implies that the model is strictly 2D and valid only in the geometrical far-field, i.e., when the observer distance to the trailing edge is much larger than the acoustic wavelength. Lastly, Ayton's original model required a double-sum and integral over infinite spanwise wavenumbers.

[2] The Wiener-Hopf method is a mathematical technique that exploits the properties of Fourier-transformed complex-analytical functions to find solutions to PDEs with mixed boundary conditions.

Lyu & Ayton (2020) noted that the integral and the sums, could be reduced to a single sum for the case of sharp serrations, thus yielding faster computations. Nevertheless, the model remained 2D, and its radiation cylindrical rather than spherical, rendering its application to rotating blades questionable. To circumvent this, Li & Lee (2022) heuristically modified the rapid model to match finite span and spherical radiation conditions. More recently, Lyu (2023) found a complete 3D analytical solution to Ayton's model without using the steepest descent approximation. Lyu noted that the assumptions used in the Wiener-Hopf factorization may limit the method's validity to high frequencies.

1.3 Critical review of the literature

Given the low tip Mach number at which quadcopters operate, propeller trailing-edge noise has been recognized as a dominant noise source, and it is particularly significant due to the human ear's frequency response. Amiet (1976) model has been validated in numerous applications and can therefore be used to calculate the far-field acoustic pressure for a blade after it has been discretized into spanwise strips. The key to accurate trailing-edge noise predictions is modeling the wall-pressure fluctuation spectrum near the trailing edge. Small propellers operate in a regime where viscous effects play a large role in the aerodynamic and acoustic fields. High-fidelity simulations require a substantial amount of computational time, and further improvements are needed to achieve better agreement with experimental data. Amiet's theory is developed on the assumption of a fully turbulent boundary layer, which might not be the case for quadcopter blades; thus, its applicability must be assessed and its limitations established.

Bio-inspired serrations have shown potential for reducing trailing-edge noise. However, the plethora of possible combinations between serration shape, wavelength, and height demands a thorough understanding of the basic scattering mechanism behind the noise reduction. Additionally, propeller designers need a fast method to account for potential noise reductions in the early design stages. Although significant progress has been made in serration acoustic models, their implementation and validation for low-Reynolds-number propellers is scarce. A fast serration model, such as Li & Lee (2022) extension of Ayton's model, is desirable from

a design perspective. Nevertheless, the heuristic assumptions made for its extension must be assessed, and its applicability for small scale propellers defined.

While Ayton's original model provides a fast way to evaluate the far-field acoustics, the near-field effects, such as the surface pressure distribution on the serration, are not available. Starting from the original model by Ayton (2018), a first step towards a 3D model is proposed by solving the square wave which presents less mathematical complexities compared to the sawtooth.

Accurate wall-pressure spectrum modeling is an essential input to the acoustic models. As noted by Moreau *et al.* (2019) the fact that most of the far-field noise reduction comes from the acoustic interference between the tip and root of the serrations, low-cost RANS simulations can be used to generate the input data required by wall-pressure spectrum models (Sanjosé & Moreau, 2018) by considering simulations with only straight edges. As a first building block in the methodology, the next Chapter presents the mathematical formulation for straight and serrated edge acoustic models.

CHAPTER 2

TRAILING EDGE NOISE MODELING FOR STRAIGHT AND SERRATED EDGES

"The scientist describes what is; the engineer creates what never was and in the middle, we try to understand turbulence."

— Anonymous, inspired by Theodore von Kármán

Lighthill (1952) seminal work demonstrated that turbulence emits sound by converting a minute fraction of turbulence kinetic energy into acoustic waves. For example, a jet discharging into a stationary fluid produces noise despite the absence of any solid boundary. Lighthill proposed the concept of an acoustic analogy to address such scenarios where free turbulence radiates sound. Lighthill rearranged the Navier-Stokes equations to obtain an inhomogeneous wave equation where a finite volume of turbulent fluid contains the noise sources. In the case of free turbulence, the sound can be modeled as an equivalent distribution of static quadrupole sources in an otherwise undisturbed medium. Using the derived equations and scaling arguments, Lighthill demonstrated that the acoustic intensity scales with the eight power of the flow velocity, concluding that turbulence itself is an inefficient sound radiator at low Mach numbers. Following Lighthill's work, Curle (1955) demonstrated that the presence of solid surfaces increases the effective radiation of sound, since the equivalent noise sources can be modeled as dipoles.

Perhaps the most widely studied flow-surface interaction is that of a Turbulent Boundary Layer (TBL), as noted by Blake (2017). This stems from fundamental turbulence research on one hand, and from practical engineering purposes on the other. Any vehicle, ranging from submarines to space launch vehicles, will develop a turbulent boundary layer on its surface. Aerodynamically generated noise results from the interaction of the pressure fluctuations within the boundary layer with edges, such as the wings of an airplane or the side mirrors of an automobile. At sufficiently high Mach numbers, the turbulence itself becomes a significant sound radiator. The pressure

fluctuations also induce vibrations in the vehicle's panel structure that are transmitted to the interior. According to Panda, Roozeboom & Ross (2019), the transmitted pressure fluctuations are responsible for the interior acoustic environment of an automobile, the cabin of an aircraft, and the payload and crew-compartment of a space vehicle. Equally important, knowledge of these flow-induced vibrations is required during the design phase to ensure structural integrity of the vehicles.

Turbulent boundary layers play a role in everyday life as a mechanism that produces certain sounds, such as the fricative consonant 's' when speaking (Howe & McGowan, 2005). Additionally, TBLs are fundamental to the sound generating mechanism of reed-driven wind instruments, such as saxophones, clarinets, or oboes (Fabre, Gilbert, Hirschberg & Pelorson, 2012). The airflow from the player's mouth induces turbulent flow over the reed walls, which in turn radiate sound using the instrument as a waveguide. The final sound resulting from the complex vibro-acoustic coupling of the reed with the instrument. It is noted that in this Thesis all vibro-acoustic effects are not considered, even though the source of aerodynamic noise and flow-induced vibrations is the same.

This chapter starts with the introduction of Curle's analogy, a powerful mathematical tool in aeroacoustics used in the derivation of trailing edge noise models. This is followed by a description of the turbulent boundary layer as the trailing edge noise source. Then, Amiet's model for straight edges is derived. The subsequent section will derive Ayton's model for serrated edges and its various extension and limitations. The chapter concludes with a novel approach to extend the square wave serration to finite chord using Curle's analogy.

2.1 Curle's Acoustic Analogy

Curle (1955) followed Lighthill footsteps to derive scaling laws for trailing edge noise. Here, the approach in Glegg & Devenport (2024) is used to illustrate the application of the analogy to obtain a scaling between the acoustic intensity and the flow as the latter interacts with a surface. Figure 2.1 shows a turbulent boundary layer developing over the surface of an airfoil with

normal vector . The noise source location at the trailing edge is given by **y** and the observer is at **x**. Thus, the emission and reception times are and ,respectively. Following Curle's analogy, Eq.(2.1), the density fluctuations at the receiver, **x** , are given by:

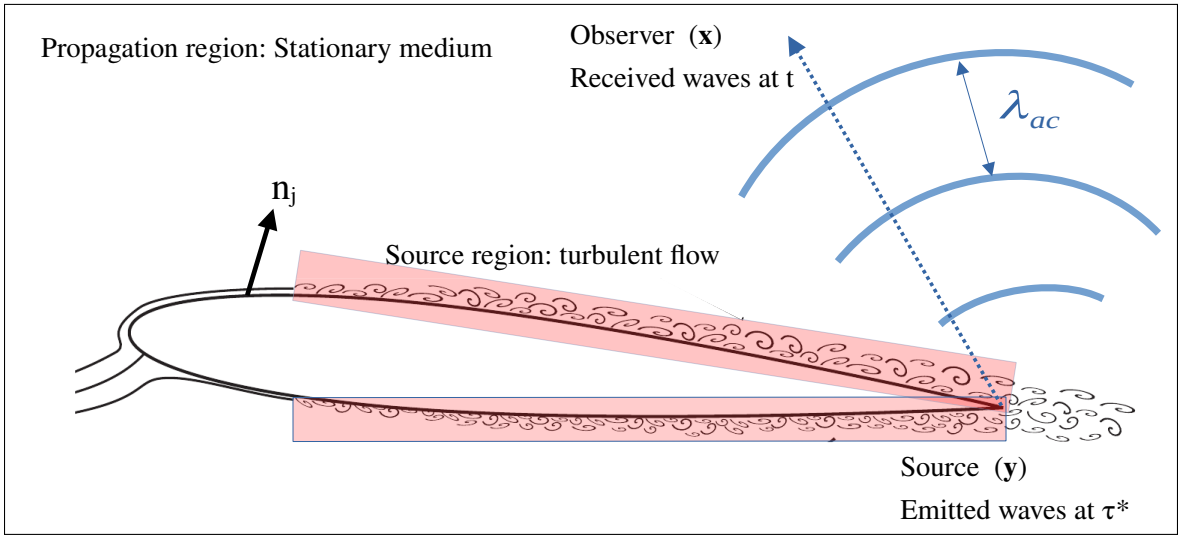

Figure 2.1 Acoustic waves emitted from the trailing edge for reference in Curle's analogy Taken from Merino Martinez (2018)

$$\mathbf{x} \quad \frac{2}{0} \qquad \frac{\qquad}{\qquad} \quad 0 \qquad \mathbf{y}$$

monopole term

$$\frac{}{} \qquad\qquad 0 \qquad \mathbf{y}$$

Dipole (loading) term

$$\frac{2}{\qquad} \qquad \mathbf{y} \quad 0 \quad \mathbf{y}$$

Volume quadrupole term

(2.1)

where is the normal component of the velocity and represents the mass flux across the surface. is the unsteady force (loading) exerted on the surface of the airfoil by the fluid. is Lighthill's stress tensor that for incompressible and homentropic flow equals to (Glegg & Devenport, 2024) and $_0$ is time-domain free-field Green's function given by:

$$_0\,\mathbf{x}\quad\mathbf{y}\qquad\frac{\mathbf{x}\quad\mathbf{y}\quad_0}{4\quad\mathbf{x}\quad\mathbf{y}} \tag{2.2}$$

The sources are integrated for a finite period of time 2 resulting in:

$$\mathbf{x}\quad\begin{matrix}2\\0\end{matrix}\qquad\frac{\qquad}{\qquad}\qquad\frac{\mathbf{y}}{4\quad\mathbf{x}\quad\mathbf{y}}$$
$$\frac{}{}\qquad\qquad\frac{\mathbf{y}}{4\quad\mathbf{x}\quad\mathbf{y}} \tag{2.3}$$
$$\frac{2}{\qquad}\qquad\mathbf{y}\qquad\frac{\mathbf{y}}{4\quad\mathbf{x}\quad\mathbf{y}}$$

In the above solution, the source terms are evaluated at the source or retarded times. The surfaces are stationary so **y** is independent of . This formulation implies that source fluctuations occurring at the same time will contribute to the observer signal at **x** at different reception times. Note that if the source regions is sufficiently small, the retarded times can be ignored (i.e., the time delay at the observer is close to zero) and the integrals can be evaluated at a fixed time. Since the goal is to obtain a proportionality between the noise and the flow over the surface, some simplifications can be made. The monopole term equals to zero in this case as the surface is considered impermeable and thus 0. Moreover, the quadrupole term scaling is known from Lighthill's eight power law. Thus, the derivation focuses on the dipole term related to the surface loading:

$$\mathbf{x}\quad\begin{matrix}2\\0\end{matrix}_{\text{dipole}}\qquad\frac{}{}\qquad\mathbf{y}\quad\frac{1}{4\quad\mathbf{x}\quad\mathbf{y}} \tag{2.4}$$

the space derivative is evaluated with the chain rule:

$$\frac{\qquad}{}\qquad\frac{}{}\qquad\frac{\qquad}{} \tag{2.5}$$

Since $\frac{\mathbf{x}\quad\mathbf{y}}{_0}$, it follows that:

$$\frac{}{\mathbf{x}\quad\mathbf{y}_{0}}\qquad(2.6)$$

Therefore, an alternate form of the dipole term is:

$$\mathbf{x}\quad{}^{2}_{0\,\text{dipole}}\quad\frac{}{{}_{0}\,\mathbf{x}\quad\mathbf{y}}\quad\frac{}{4\quad\mathbf{x}\quad\mathbf{y}^{2}\,{}_{0}}\quad\mathbf{y}\qquad(2.7)$$

Since the surface is impermeable, then 0, and the only significant term is the loading term . For most scenarios, it is the far-field what is of interest, so the second term in the square brackets becomes less important as the observer moves away from the source region, **x** **y** . Therefore, the far-field approximation for a rigid stationary surface simplifies to:

$$\mathbf{x}\quad{}^{2}_{0\,\text{dipole}}\quad\frac{}{4\quad\mathbf{x}^{2}\,{}_{0}}\quad\frac{}{}\quad\mathbf{y}\qquad(2.8)$$

Furthermore, assuming that the surface is acoustically compact such that the chord is much smaller than the acoustic wavelength, , retarded time effects can be neglected:

$$\mathbf{x}\quad{}^{2}_{0\,\text{dipole}}\quad\frac{}{4\quad\mathbf{x}^{2}\,{}_{0}}\quad\frac{}{}\qquad(2.9)$$

with

$$\mathbf{y}\qquad(2.10)$$

If the surface applies a net force to the fluid, the sound radiation has the characteristics of a compact dipole oriented in the direction of the force. The force typically scales as $_{0}{}^{2}$, and the time derivative as $\frac{}{}\,{}_{0}{}^{3}$. Thus, the far-field acoustic intensity is given by:

$$\frac{2}{0\ 0} \qquad \frac{2\ 2}{0\ 0} \tag{2.11}$$

and scales as:

$$\frac{0^{\ 6\ 2}\sin^2}{4\ \mathbf{x}^{\ 2\ 3\ 2}_{\ 0}} \tag{2.12}$$

where is the observer angle relative to the free-stream direction when the lift force is considered as shown in Figure 2.2.

The scaling results show two important characteristics of dipole-type sources: first, that far-field acoustic intensity from a compact dipole source scales with the sixth power of the mean flow velocity, and second, that noise levels are higher with higher elevation angles from the trailing edge. Notice that the above analysis uses a compact assumption. In the case that the source characteristic length, in this case the chord, is on the same order of magnitude as the acoustic wavelength, one obtains a non-compact source and thus an acoustic intensity scaling with the fifth power of the flow velocity, as demonstrated by Williams & Hall (1970). The directivity is equally affected due to the source non-compactness, and transitions from a dipole to a cardioid shape as schematically shown in Figure 2.2.

2.1.1 Moving surfaces and the Ffwocs-Williams and Hawkings analogy

Curle's analogy is valid for stationary surfaces in a uniform flow; if the surfaces positions are changing with time, as is the case with a propeller blade, a generalization of the analogy is required. Ffowcs Williams, Hawkings & Lighthill (1969) extended Curle's results by exploiting the concept of generalized derivatives to include the effect of surfaces in arbitrary motion. In the Ffwocs-Williams and Hawkings (FW-H) analogy, the volume and surface integrals must be evaluated over moving surfaces, which adds a new layer of complexity, as the sources are

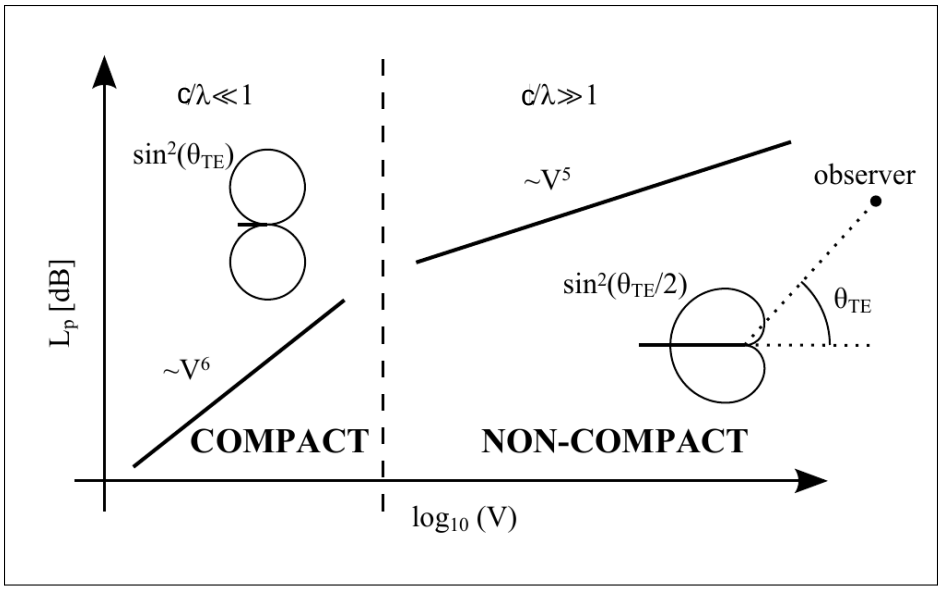

Figure 2.2 Directivity radiation and flow velocity dependency for compact and non-compact trailing edge noise sources
Taken from Merino Martinez (2018)

moving relative to the observer, so both **y** and the propagation distance between the source and the observer will change with emission time.

According to Glegg & Devenport (2024), in the FW-H analogy for a propeller, there are three terms of importance for the far-field noise. The first is the quadrupole term, whose strength depends on , and corresponds to the sound radiated by both turbulence and flow distortions, such as shock waves associated with the blades. The second is the dipole source term, controlled by the surface loading . Finally, there is an additional term in the monopole source that depends only on the blade surface velocity and the density at the observer. This is a volume displacement source and is only nonzero if the observer 'sees' a time-varying surface velocity at emission time. This source is zero for an object in linear motion traveling toward the observer, but it is nonzero for a rotating blade that continuously changes direction relative to the observer. For typical low-tip-Mach-number drone propellers, the quadrupole term is not significant. As discussed in Chapter 4, when considering broadband noise sources, such as TEN, the effects of rotation (source acceleration) as captured in the FW-H can usually be neglected, particularly for

low-Mach-number applications. Thus, Curle's analogy can be used to model trailing-edge noise, provided that statistics of the turbulent flow field beneath the boundary layer are available.

Curle's Analogy——————————————————Summary

- Curle's analogy allows relating unsteady forces over a surface to the far-field acoustic pressure. This noise source is usually called a dipole source.
- The acoustic intensity of compact and non-compact dipole noise sources scales with the sixth and fifth power of the velocity, respectively.

2.2 Turbulent boundary layer Wavenumber-Frequency spectrum

In Curle's analogy, the dipole contribution is associated with steady or unsteady forces on a surface, e.g., a propeller blade. The unsteady forces are a result of the interaction of the surface with unsteady flow. The latter can be generated by bodies in front of the propeller, a common example being the hull of a ship in maritime applications or the intake of a turboprop engine in aeronautical applications. The unsteady flow may also be self-generated, as in a Turbulent Boundary Layer (TBL) over an airfoil surface.

The flow field beneath a TBL is characterized by partially correlated spatio-temporal scales in a continuous energy exchange, extracting energy from the free-stream and ultimately dissipating it by heat at the wall. Fundamental processes in the boundary layer, such as entrainment and vortical motions of different scales, are illustrated in Figure 2.3 for a spatially evolving zero-pressure-gradient turbulent boundary layer developing under a five metre-long flat plate towed through water (Lee *et al.*, 2012). The marks at the bottom of each frame show the downstream distance from the trip, which is close to the plate leading edge. The division between the vortical flow inside the boundary layer and the irrotational flow in the free-stream is not well-defined, and it is made irregular by large-scale eddies. As noted by Lee *et al.* (2012), in the more traditional laboratory frame of reference, in which fluid passes over a stationary body, it is difficult to observe the whole evolution and lifetime of turbulent coherent structures. An

equivalent experiment in a wind/water tunnel would require a camera and a laser that move with the flow, effectively 'chasing' eddies as they are convected downstream.

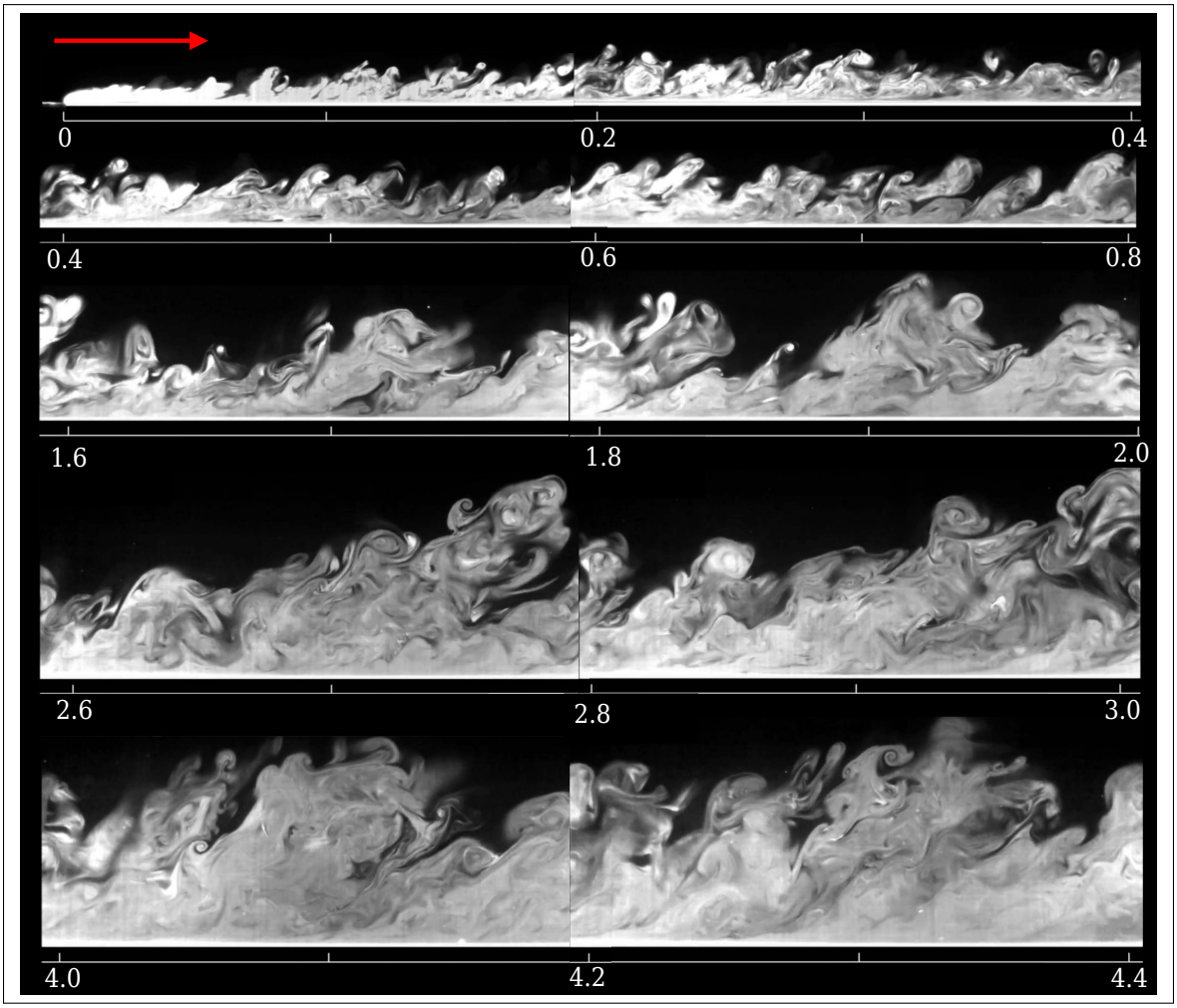

Figure 2.3 Evolution of a turbulent boundary layer on a flat plate at zero-pressure-gradient
Taken from Lee *et al.* (2012)

The very nature of turbulence dictates that even if an experiment is repeated with seemingly identical conditions and with exceptional care, the measurements of the velocity, pressure or any other field variable will be different. Moreover, and as noted by Smol'yakov & Tkachenko (1983), the turbulent fluctuations cannot be predicted for any point within the flow or for any instant of time. In other words, the only approach to study turbulence at the present time is through statistical methods.

Consider turbulent flow over a wall such that $_1$ is in the flow direction, $_2$ normal to the wall, and $_3$ is in the spanwise direction. Furthermore, with the common assumption that the field is homogeneous in space and statistically-stationary in time (Bull, 1996), it is possible to define space-time correlations as a function of the stream and spanwise separation of two points in the wall separated by a distance, $_1$ 0 $_3$ and at two times separated by

$$\quad 1 \quad 3 \qquad\qquad 1 \quad 3 \qquad\quad 1 \quad\; 1 \quad 3 \quad\; 3 \tag{2.13}$$

where $\quad _1 \quad _3$ is the fluctuating wall-pressure at the surface point ($_1$, $_3$) at time t, and the brackets < > represent the ensemble averaging. Taking the space and time Fourier transform of the correlation function yields the wavenumber-frequency spectrum of the wall-pressure fluctuations.

$$1 \quad 3 \qquad \frac{1}{2 \quad 3} \qquad\qquad 1 \quad 3 \qquad\quad {}^{1\ 1} \quad {}^{3\ 3} \qquad\quad 1 \quad 3 \tag{2.14}$$

With the angular frequency, and $_1$ and $_3$ the streamwise and spanwise wavenumbers, respectively. The Wavenumber-Frequency (WF) spectrum, $\quad _1 \quad _3 \quad$, contains a vast amount of information. Three, two, and one-dimensional representations of the WF spectrum are illustrated in Figure 2.4 (Zhao *et al.*, 2024). In the 3D representation, the spectrum consists of the aerodynamic and the acoustic components, with associated high and low wavenumbers, respectively. The peak at $\quad 0$ is the convective ridge, and it is the main characteristic of the aerodynamic component. For example, the large eddies in Figure 2.3 are responsible for this part of the spectrum. Taking a slice at a constant yields the wavenumber map, where once again the convective ridge is the dominant feature. The ridge alongside the subconvective region is, for example, the main contributor to cabin noise in aircraft and high-speed trains (Zhao *et al.*, 2024). Lastly, the viscous region is characterized by large wavenumbers where energy is dissipated as heat. Small eddies close to the wall in Figure 2.3 contribute to this part of the spectrum. The same regions are highlighted in the 1D (constant $_3$) representation.

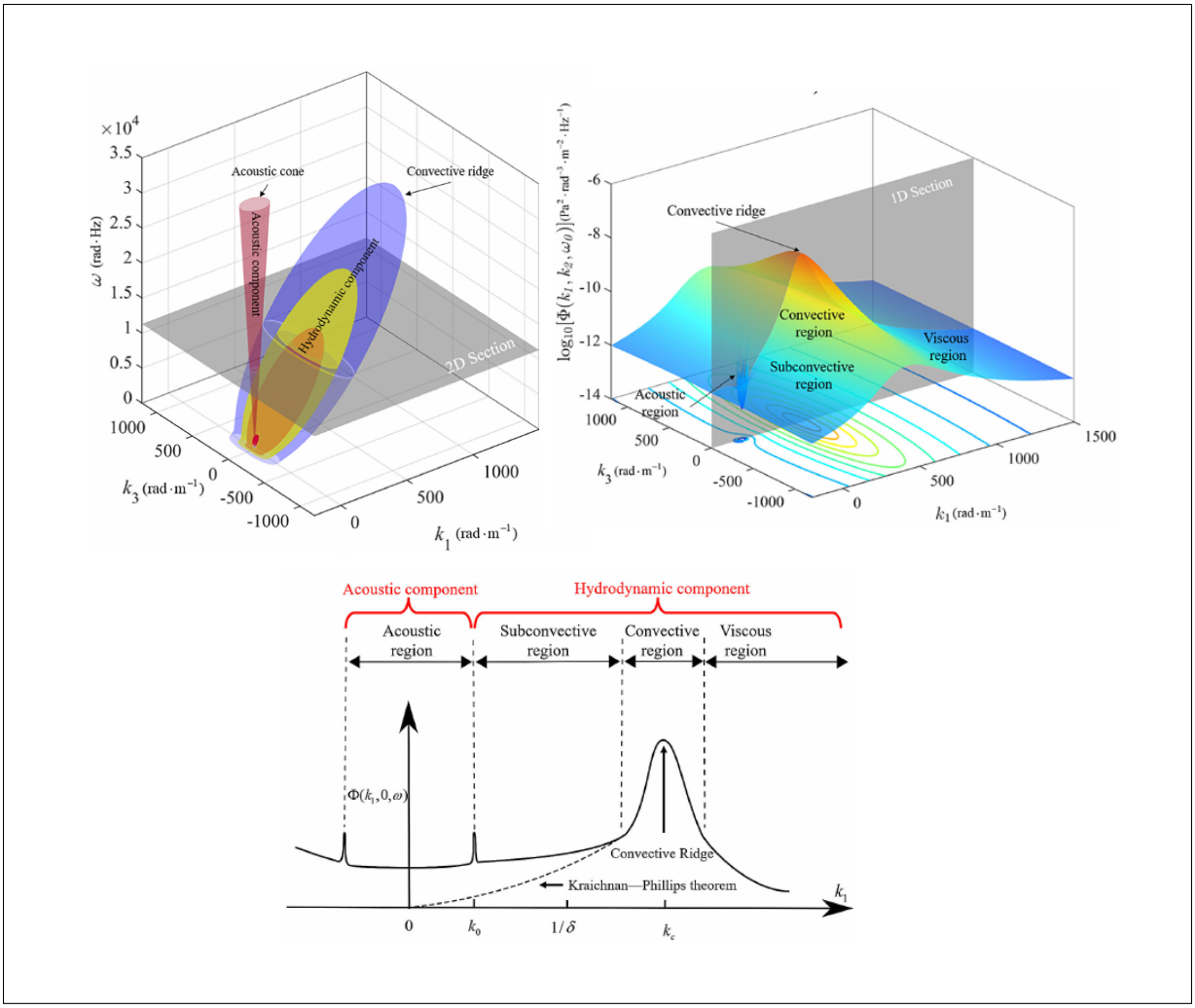

Figure 2.4 Representations of a TBL wavenumber-frequency spectrum: (a) 3D representation, (b) 2D representation(constant) and (c) 1D representation(constant $_3$)
Taken from Zhao *et al.* (2024)

Despite almost a century of research, the theoretical progress on the TBL spectrum has exclusively focused on the infinitely long and infinitesimally thin flat plate, as any deviation from this idealized geometry introduces excessive complexity. For example, for the flow over an airfoil, the curvature induces a streamwise pressure gradient. If the curvature favors flow acceleration, a Favorable Pressure Gradient (FPG) results. In contrast, if the curvature causes the flow to slow down the pressure gradient is Adverse (APG). Given the vast number of airfoils available, it is not feasible to obtain a one-fits-all model including the effect of the pressure gradient on the

WF spectrum. Moreover, in a laboratory setting, it is only possible to have a finite number of pressure sensors on the surface and thus the wavenumber-frequency spectrum is only estimated.

2.2.1 Wall-pressure fluctuations spectrum

According to Bull (1996) comprehensive measurement of the space-time correlation function or the wavenumber-frequency spectrum are difficult to make and for engineering applications some research has focused on the measurement of intermediate quantities. Among them, the single point spectrum has been extensively used for trailing edge noise calculations (Lee *et al.* (2021)). In an experimental setting, the single-point spectrum is measured by flush-mounted sensors on a wall or on the surface of an airfoil. The single point spectrum is related to the space-time correlation and the wavenumber-frequency via:

$$\frac{1}{2} \qquad 0\ 0 \qquad\qquad\qquad 1\quad 3 \qquad 1\quad 3 \tag{2.15}$$

Note that the mean pressure fluctuations, $\overline{\ \ ^2}$ can be obtained from the integration of the single-point wall-pressure spectrum across the frequency range:

$$\overline{\ \ ^2} \tag{2.16}$$

According to Glegg & Devenport (2024) the root-mean-square pressure fluctuations in an equilibrium turbulent boundary layer are in the order of 1% of the free stream dynamic pressure $1\ 2 \qquad ^2$ and approximately three times the wall-shear stress.

Analytical progress to relate the complete wavenumber-frequency spectrum to the single-point wall-pressure spectrum can be made using Corcos (1964) model with the caveat that it was proposed to fit measured data on a flat plate at zero pressure gradient (Roger & Moreau (2005)). Assuming that the turbulence is frozen and that the turbulent field convects at velocity allows to express the statistically homogeneous wall-pressure field using separation of variables as:

$$\Phi_{pp}(\omega, k_3) = \frac{\omega^2 \rho^2}{4\pi^2} \Phi_{ww}(\omega) \mathcal{B}(k_3 l_3) \mathcal{A}(k_1 l_1) \quad (2.17)$$

where $\mathcal{A}$ and $\mathcal{B}$ are decreasing functions of the separation distances l_1 and l_3 characterizing the streamwise and spanwise coherence lengths, respectively. In the original Corcos (1964) model they are exponential functions decreasing with increasing frequency and separation. This hypothesis has been put into question as the factorization leads to erroneous values of the model oblique wavenumber statistics. In other words, spanwise and streamwise separations cannot be considered as independent variables. A more general definition for the functions A and B is:

$$\mathcal{A}(k_1 l_1) = \frac{\Phi_{pp}(k_1, 0)}{\Phi_{pp}(0, 0)} \qquad \mathcal{B}(k_3 l_3) = \frac{\Phi_{pp}(0, k_3)}{\Phi_{pp}(0, 0)} \quad (2.18)$$

For straight edges, it is established that the chordwise statistics have no effect on trailing-edge noise (Roger & Moreau (2005)). However, the spanwise statistics are of major importance as they are distributed all over the span. A commonly used parameter characterizing the pressure field is the coherence between two points on the airfoil surface:

$$\gamma^2(k_1, \Delta x_3) = \frac{\left|\Phi_{pp}(k_1, \Delta x_3)\right|^2}{\Phi_{pp}^2} \quad (2.19)$$

The coherence is thus the squared streamwise or spanwise functions A, B when the separation l_1 or l_3 is set to zero. Integration of the coherence function yields the spanwise correlation length:

$$\Lambda_3 = \int_0^{\infty} \sqrt{\gamma^2(k_3)} \cos(k_3 \Delta x_3)\, d\Delta x_3 \quad (2.20)$$

In the special case of Corcos' model the spanwise correlation length simplifies to:

$$\mathcal{B}(k_3 l_3) = \frac{\Lambda_3}{\pi} \frac{k_3^2}{k_3^2 + \left(\frac{2}{l_3}\right)^2} \quad (2.21)$$

Further developments to obtain a relationship between the WF spectrum and the single-point wall-pressure spectrum are made in the derivation of the trailing edge noise model in the next section.

Following Bull (1996), the single point spectrum can broadly be divided into four regions and no universal scaling exist for the complete spectrum. In other words, each one of the four regions must be scaled by different flow variables to collapse results from different measurements. The regions are shown in Figure 2.5. For the lowest frequencies, the spectrum evolves with the square of the frequency and the corresponding time and pressure scales are, and $1\ 2^{2}$ respectively. At mid-frequencies the spectrum peaks and mixed scales can be used. The universal range is an overlap region between mid and high frequency regions. The size of these regions grows with Reynolds number as noted by Goody (2004). No agreement in the evolution of the spectrum has been reached in this region, with some theoretical results giving an ^{1} dependency (Bull, 1996; Blake, 2017) whereas Goody (2004) suggest evolution between $^{0\,7}$ and $^{0\,8}$. The highest frequency range is characterized by an ^{5} dependency and scaling by internal boundary layer variables, and ^{2} for the pressure and time respectively. Where is the wall shear stress, is the kinematic viscosity and $\overline{}$ is the friction velocity.

2.2.2 Wall-pressure fluctuations spectrum modeling

Based on the gathered experimental data on turbulent boundary layers in flat plates, some empirical wall-pressure models have been proposed. For example, Amiet (1976) used Willmarth & Roos (1965) data to propose an empirical model to be used alongside his trailing edge noise model. According to Lee (2018), Howe (1998) proposed a new model using theoretical derivations made by Chase (1980). The resulting model was able to predict the ^{2} and ^{1} portions of the spectrum, but failed in the others. More recently, Goody (2004) included the effects of Reynolds number, his model thus decaying with ^{5} at high frequencies. All earlier models, including Goody's one, were based on zero-pressure-gradient turbulent boundary layers and often disagreed by more than 10dB when used in airfoils. Rozenberg, Robert & Moreau (2012) was the first to include the effect of adverse pressure gradient(APG) by fitting experimental data.

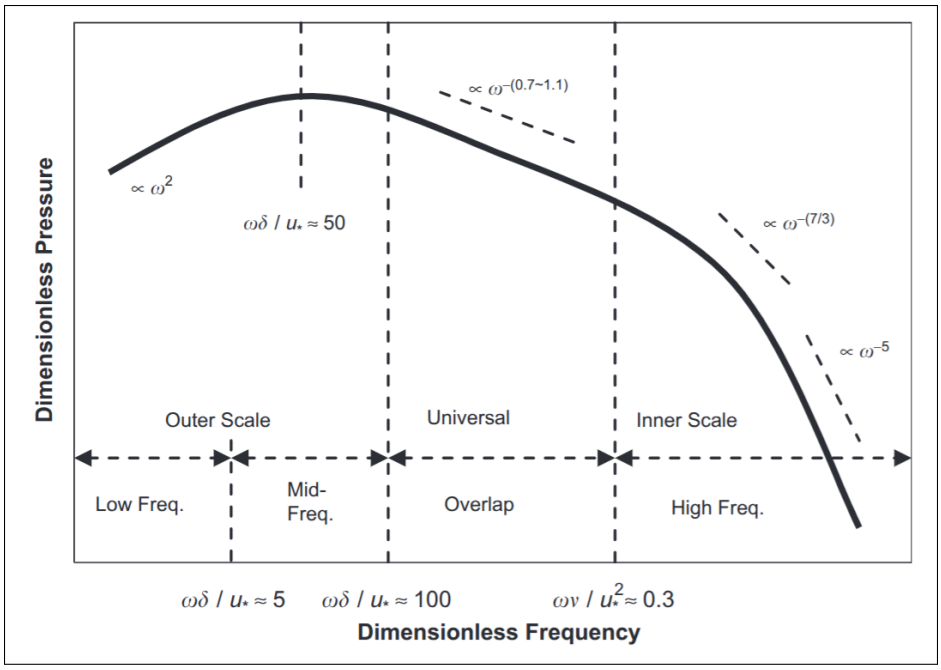

Figure 2.5 Frequency regions and characteristic slopes of the single-point wall-pressure fluctuations spectrum
Taken from Hwang *et al.* (2009)

Rozenberg's model is accurate for mild to moderate APGs but disagrees with zero pressure gradients. Later, Hu & Herr (2016) proposed a different scaling parameter to improve the agreement with experimental data from highly loaded airfoils. Building upon the aforementioned models, Lee (2018) proposed a universal wall pressure spectrum that could generalize the behavior at zero, adverse and favorable pressure gradients.

According to Catlett, Anderson, Forest & Stewart (2016), these models have proved valid only within specific ranges of the pressure gradient. Although rooted in the physics of the boundary layer, their derivation remains somewhat ad hoc and usually requires the data-driven calibration of several coefficients. More recently, and leveraging on one hand the increase in available data from wind tunnel and high-fidelity simulations (LES or DNS) and on the other the advances in Machine Learning, some authors have proposed data-driven/ models. Dominique, Van den Berghe, Schram & Mendez (2022) proposed a new empirical model based on Artificial Neural Networks (ANN) as an alternative to the semi-empirical models failure to predict wall-pressure

spectra for boundary layers under strong adverse pressure gradients. The neural network-base model provided a significant improvement over the semi-empirical models, with predictions within 1 dB/Hz for different flow cases. However, the model tends to feature a steeper decay at high frequencies due to the limited training data. Similarly, Fritsch *et al.* (2023) used Gene Expression Programming (GEP) with RANS and experimental data to obtain a model for the wall-pressure spectra. The results showed that the GEP models improve the accuracy of prediction considerably at all the different pressure gradient conditions as compared to the Hu model.

The models discussed so far are for attached boundary layers. In the case of separated boundary layers the wall-shear stress becomes zero, thus yielding a discontinuity if these models are used. Pargal, Yuan & Moreau (2024) demonstrated such limitations and proposed a new scaling for non-equilibrium boundary layers spectra. In addition, their model uses the mean velocity profile to input information on the local state of the boundary layer. Lastly, Arroyo Ramo, Moreau, Sandberg, Bauerheim & Jacob (2025) used ANN with a large database for a cambered, industrial Controlled Diffusion (CD) airfoil that includes transitional effects via LSB. The resulting model prediction outperforms the existing empirical models and is able of not only capture the general shape of the spectrum but also predicts tonal peaks. The historical evolution of the wall-pressure spectrum semi-empirical modeling is summarized in Figure 2.6

For the intended application of small-scale propellers in hover with no inflow distortion where attached boundary layers under moderated APG are expected, Lee (2018) universal model can be used given its proven accuracy (Lee *et al.*, 2021). The spectrum is given by:

(2.22)

Where is the ratio of timescales between the outer and inner boundary layer sides given by that characterized the Reynolds number effect. Other models may use the boundary layer displacement thickness instead of the boundary layer thickness . Additionally, is the boundary layer's edge velocity, is the kinematic viscosity and 2 is the

friction velocity with being the wall shear stress. SS and FS represent the spectrum scale factor and the frequency scale factor respectively.

As explained by Lee *et al.* (2021) the parameters are model-dependent and define the spectrum's shape. Parameter controls the spectrum's shape. Variables, and determine the slope of the spectrum at different frequencies. With controlling the low frequency slope, and defining the roll-off rate at middle frequencies and with and determining the high frequency slope. Lastly, parameter influences the position of the low frequency maxima. Tables 2.1 to 2.3 show the values of parameters for Goody's, Rozenberg's and Lee's models.

Table 2.1 Parameters a-c for empirical wall-pressure spectrum models

Model	**a**	**b**	**c**
Goody	3	2	0.75
Rozenberg	[2.82 ^{2} 6 13 $^{0\,75}$][4.2( )+1]	2	0.75
Lee	max(,(0.25 -0.52))	2	0.75

Table 2.2 Parameters d-g for empirical wall-pressure spectrum models

Model	**d**	**e**	**f**	**g**
Goody	0.5	3.7	1.1	-0.57
Rozenberg	4.76(1.4/ $^{0\,75}$ 0 375 1	3.7+1.5	8.8	-0.57
Lee	max(1,1.25)(0 5) or (0.5)	3.7+1.5	8.8	-0.57

Table 2.3 Parameter i and spectrum (SS) and frequency scaling(FS) factors for empirical wall-pressure spectrum models

Model	**h**	**i**	**SS**	**FS**
Goody	7	1	^{2}	
Rozenberg	min(3,19/ $\overline{\quad}$)+4	4.76	^{2}	
Lee	min(3,(0.139+3.1043))+7	4.76	^{2}	

To illustrate the capabilities of the different models, the wall-pressure fluctuations spectra measured close to the trailing edge of an industrial controlled-diffusion airfoil at an angle of attack of 8 and Re = 10^{5} are compared with Goody's, Rozenberg's and Lee's models. All the models inputs come from a RANS simulation where the effect of the wind tunnel jet deflection

on the airfoil loading was accounted for by modeling the tunnel nozzle (Moreau & Roger, 2005). The k- SST model was used for closure of the RANS equations, and the extracted values used to model the wall-pressure spectrum are shown in Table 2.4. As shown in Figure 2.7 the three models predict the correct general shape of the spectrum, Goody's model significantly underpredicts the levels at all frequencies. This is expected as a cambered airfoil at non-zero incidence experiences adverse pressure gradient. It is noted that under this flow conditions, Rozenberg's and Lee's model have identical results.

Table 2.4 Values extracted from RANS simulations to model the wall-pressure spectrum

Variable	Symbol	Value	Units
Boundary layer thickness		6.52E-03	m
Boundary layer Edge Velocity		1.68E+01	m/s
Boundary layer Disp thickness		2.30E-03	m
Momentum thickness		9.45E-04	m
Wall Shear Stress		3.40E-01	Pa
Air Density	0	1.23E+00	kg/m^3
Air Kinematic Viscosity		1.48E-05	m^2/s
Ratio of timescales		7.28E+00	-
Pressure Gradient	dP/dx	2.66E+03	Pa/m

Wall-pressure fluctuations spectrum——————————————Summary

- The complete WF spectrum contains a vast amount of information that is seldom required for engineering purposes.
- The wall pressure fluctuations spectrum, , and the spanwise correlation length, can be used to approximate the WF for source modeling.
- Lee's model will be used as it is the most tested and verified model for airfoils under loading, i.e., subjected to adverse pressure gradient.

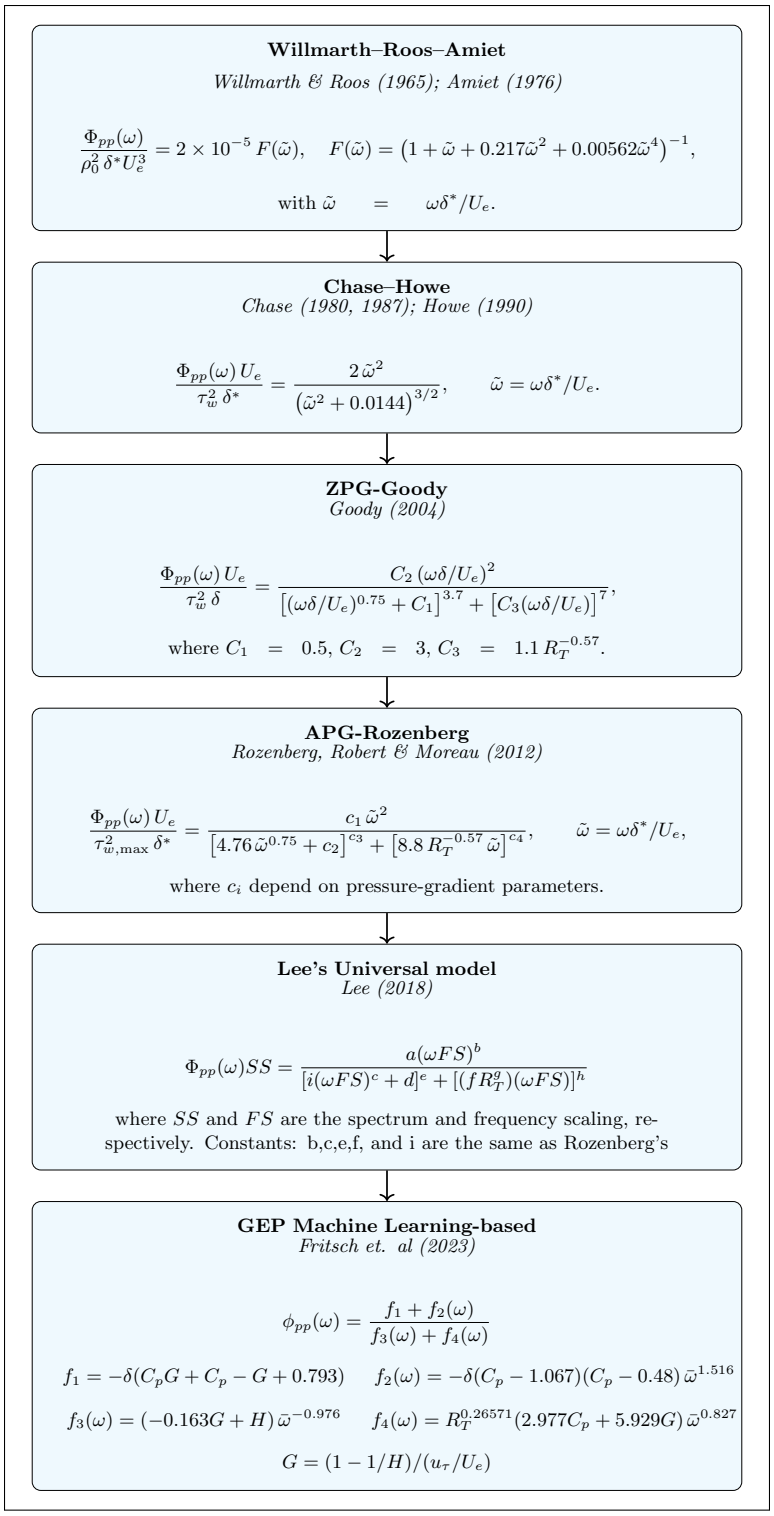

Figure 2.6 Historical evolution of wall-pressure spectrum models

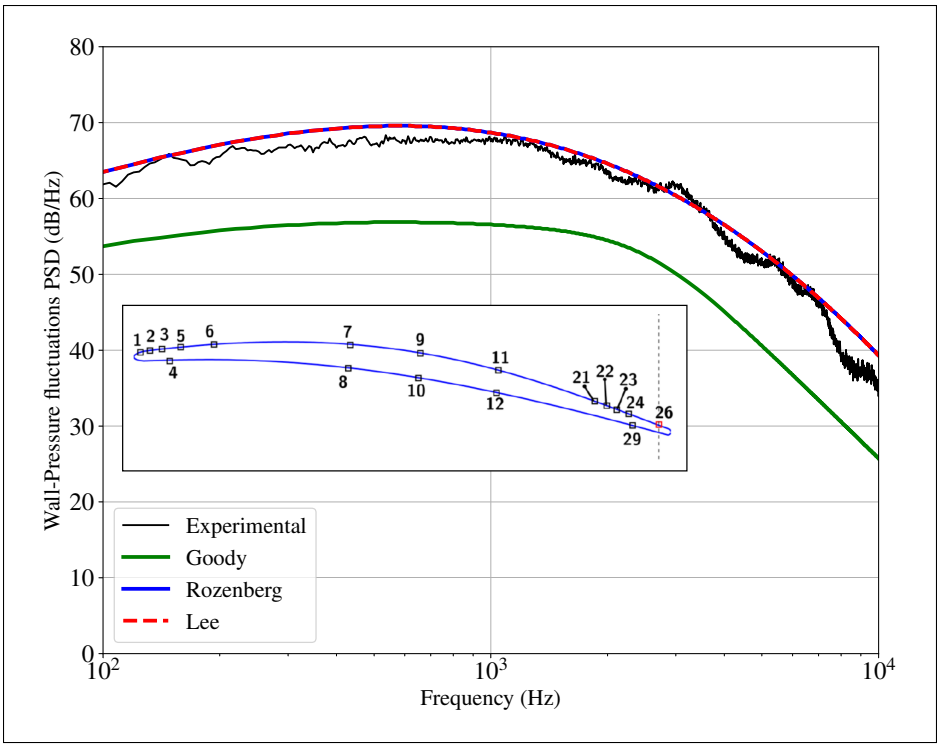

Figure 2.7 Comparison of experimental wall-pressure spectrum with different RANS-informed models at the trailing edge of a controlled-diffusion airfoil

2.3 Amiet's Trailing edge noise model

While several authors have proposed models to predict Trailing Edge Noise (TEN), Amiet (1976) model has arguably been applied the most in a variety of scenarios ranging from wind turbines to helicopter rotor noise. This is primarily because of its clear physical interpretation in the excitation (source), response, and propagation modeling. Amiet used the half-plane diffraction problem to derive an expression for the scattered pressure on the plane. This pressure acts as an equivalent dipole source and can then be propagated to the far-field via Curle's analogy (Sec. 2.1). Amiet's TEN model is based on his earlier work for turbulence interaction noise (Amiet, 1975) and follows the same methodology. The TEN model is derived next.

Common to most analytically tractable aerodynamic problems, Amiet models the airfoil as a flat plate of zero thickness at zero angle of attack. Following Roger & Moreau (2005), the plate is mathematically assimilated to a half-plane covering the negative x-direction and thus with its trailing edge at 0 as shown in Figure 2.8. An incident pressure gust, i.e., a plane wave, characterized by wavenumbers $_1$ and $_3$ in the streamwise and spanwise directions, respectively, is convected at velocity . That is, Taylor's frozen flow hypothesis is assumed valid, and the pressure fluctuations do not evolve and are convected downstream at uniform speed , usually assumed to be 0.6-0.8 of the free-stream velocity (Lee *et al.*, 2021). In this thesis, the free-stream-to-convection ratio is defined as . Therefore, the aerodynamic streamwise wavenumber is defined as $_1$

The incident pressure gust has magnitude and is given by:

$$ {}^{1} \quad {}^{3} \tag{2.23} $$

Under the assumptions of inviscid, irrotational and compressible flow, the Linearized Euler Equations can be rearranged into a convected Helmholtz equation:

$$^{2}\frac{^{2}}{^{2}} \quad \frac{^{2}}{^{2}} \quad \frac{^{2}}{^{2}} \quad 2 \quad — \quad ^{2} \quad 0 \tag{2.24}$$

with the acoustic wavenumber, $_{0}$ and the Prandtl-Glauert factor, ^{2} 1 ^{2}, where the free stream Mach number is assumed less than unity. The 2D problem is solved first for clarity.

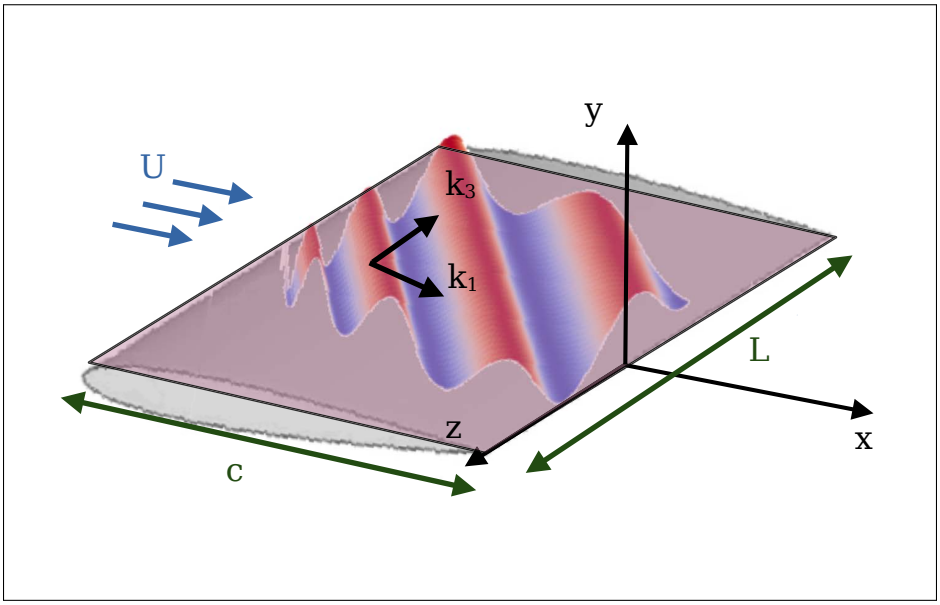

Figure 2.8 An incident pressure gust convecting towards the edge of a half-plane that models an airfoil

2.3.1 2D Solution

The 2D canonical Helmholtz equation can be obtained from Eq. (2.24) by introducing the following transformation:

$$^{2} \tag{2.25}$$

Yielding:

$$^{2}\frac{^{2}}{^{2}} \quad \frac{^{2}}{^{2}} \quad – \quad ^{2} \quad 0 \tag{2.26}$$

By using the half-chord length, , the following non-dimensional variables are obtained:

$$- \quad - \quad - \quad \frac{}{2} \quad 1 \quad 1 \tag{2.27}$$

and upon substitution in Eq. (2.26)

$$\frac{2}{2} \quad \frac{2}{2} \quad -2 \quad 0 \tag{2.28}$$

The domain of the problem is artificially extended to - in the x direction in order to obtain Amiet's solution. To solve Eq. (2.28) two boundary conditions are required. Since the plate is assumed to be rigid the no-flow-through condition applies on 0. The second boundary condition follows from the Kutta condition. This condition is applied to allow for viscous effects to be considered within equations that are inviscid. Physically, this means that the total pressure at the trailing edge must be zero and for this particular problem it follows that the incident pressure gust must be canceled at the trailing edge. Crighton (1985) and more recently Ayton, Gill & Peake (2016) have discussed the importance and validity of the Kutta condition for modeling gust-edge interaction problems. A consequence of the Kutta conditions is thus that the total field is the sum of an incident field, , and a scattered field, $_1$. This scattered filed can be found by solving the following Boundary Value Problem (BVP), involving the Helmholtz equation alongside the no-flow-through and Kutta conditions:

$$\begin{aligned} &\frac{2}{2}\frac{1}{} \quad \frac{2}{2}\frac{1}{} \quad -2 \quad {}_1 \quad 0 \\ &\frac{1}{} \quad 0 \quad 0 \quad 0 \\ &{}_1 \quad {}_1 - {}_2 \quad 0 \end{aligned} \tag{2.29}$$

It is worth pointing out that the Helmholtz Equation with the discussed boundary conditions is applicable for any type of wave, and thus it is valid for acoustic and electromagnetic waves.

In the latter case, Sommerfeld (1896) gave the first mathematically rigorous solution to the problem of diffraction by a half-plane in the context of optics. The solution equally applies to acoustic waves. Soon after, Schwarzschild (1901) formulated an iterative procedure to solve for the diffracted field by a slit (i.e., a gap between two half-planes). Amiet (1976) leveraged Schwarzschild (1901) method to find the solution on the half-plane:

$$\quad 1 \quad 0 \quad \frac{1}{-} \quad _0 \tag{2.30}$$

where

$$0 \quad \frac{}{} \quad \frac{}{} \tag{2.31}$$

and is the incident gust just upstream the trailing edge, which yields:

$$1 \quad 0 \quad \frac{1}{-} \quad _0 \quad \frac{}{} \quad \frac{}{} \quad _1 \; - \; _2 \tag{2.32}$$

which can be rearranged to give a more general formula

$$0 \quad \frac{}{} \quad _0 \quad \frac{}{} \quad \frac{}{} \tag{2.33}$$

The solution to the above integral is commonly tabulated. For example given by Gradštejn, Ryžik, Jeffrey & Zwillinger (2009):

$$_0 \quad \frac{}{} \quad \frac{}{} \quad 1 \quad \frac{}{-} \quad _0 \quad \frac{}{-} \tag{2.34}$$

$$_1 \quad 0 \quad - \quad 1 \quad 1 \tag{2.35}$$

where a factor of $\overline{2}$ has been introduced to simplify $\overline{2}^{\,4}\ 1$ and the following combination of Fresnel integrals is used:

$$_0\ \overline{\overline{2}}\ \ _2\ \ _2 \tag{2.36}$$

The final solution for the scattering pressure obtained by Amiet (1976) reads:

$$_1\ 0\ \ 1\ \ _1\ 1\ \ ^{-}\ \ 1\ \ ^{1} \tag{2.37}$$

The scattered pressure thus corresponds to the surface pressure distribution on a half-plane with the amplitude equal to the magnitude of Eq. (2.37). This is often referred also as the pressure jump.

2.3.1.1 Leading edge back-scattering correction

The surface pressure distribution given by Eq. (2.37) is valid in cases where the airfoil chord is much larger compared to the acoustic wavelength, i.e., 1. For cases where the chord is of the same order of magnitude as the wavelength a leading edge back-scattering correction, $_2$, is necessary. As mentioned in the previous section, Schwarzschild (1901) originally proposed an iterative approach to solve two coupled half-plane problems: the first considers a plate with no leading edge but with a trailing edge and thus satisfies the Kutta condition; the second one considers a plate with leading edge but without trailing edge and thus satisfies the upstream potential condition but not the Kutta condition. The iterative technique is illustrated in Figure 2.9

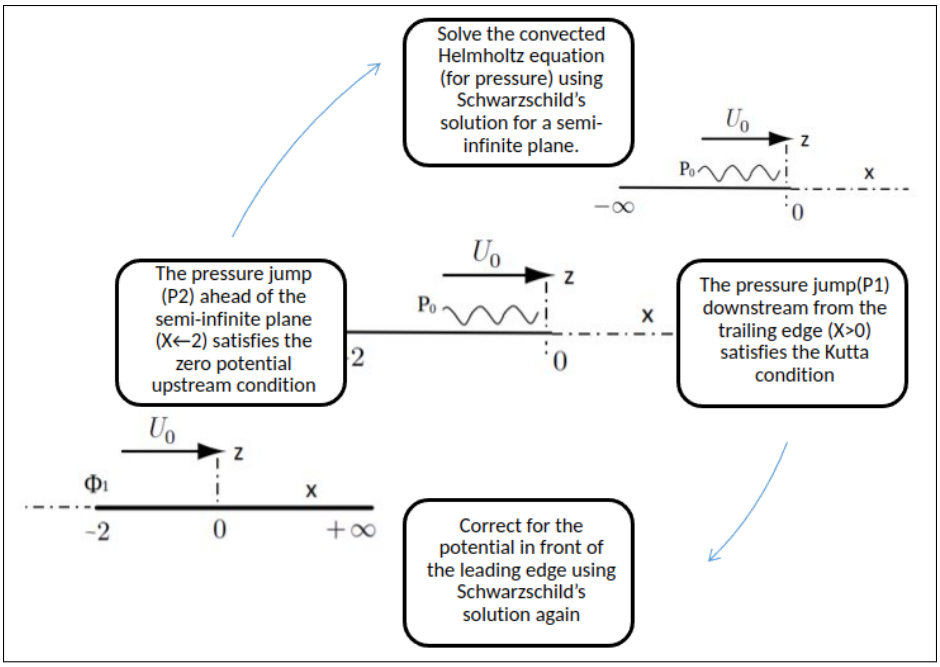

Figure 2.9 Iterative procedure to account for finite chord effects using the Schwarzschild method

Roger & Moreau (2005) applied such approach to obtain a closed form solution for the scattered pressure on a finite chord airfoil. The complete formulae are given in Appendix I. Figure 2.10 shows the effect of the back-scattering correction for two Mach numbers at low and high frequencies for two dimensionless gust parameter . The effect of the finite chord correction is important at low frequencies and/or low Mach number, whereas for high frequencies the effect of the correction is minimum. Thus, for drone propellers the use of the leading edge correction is necessary if accurate results are desired across the complete frequency range. For Underwater applications for example, where the speed of sound is five times that of air and thus the wavenumbers are one fifth of the ones in air, the leading edge correction is essential.

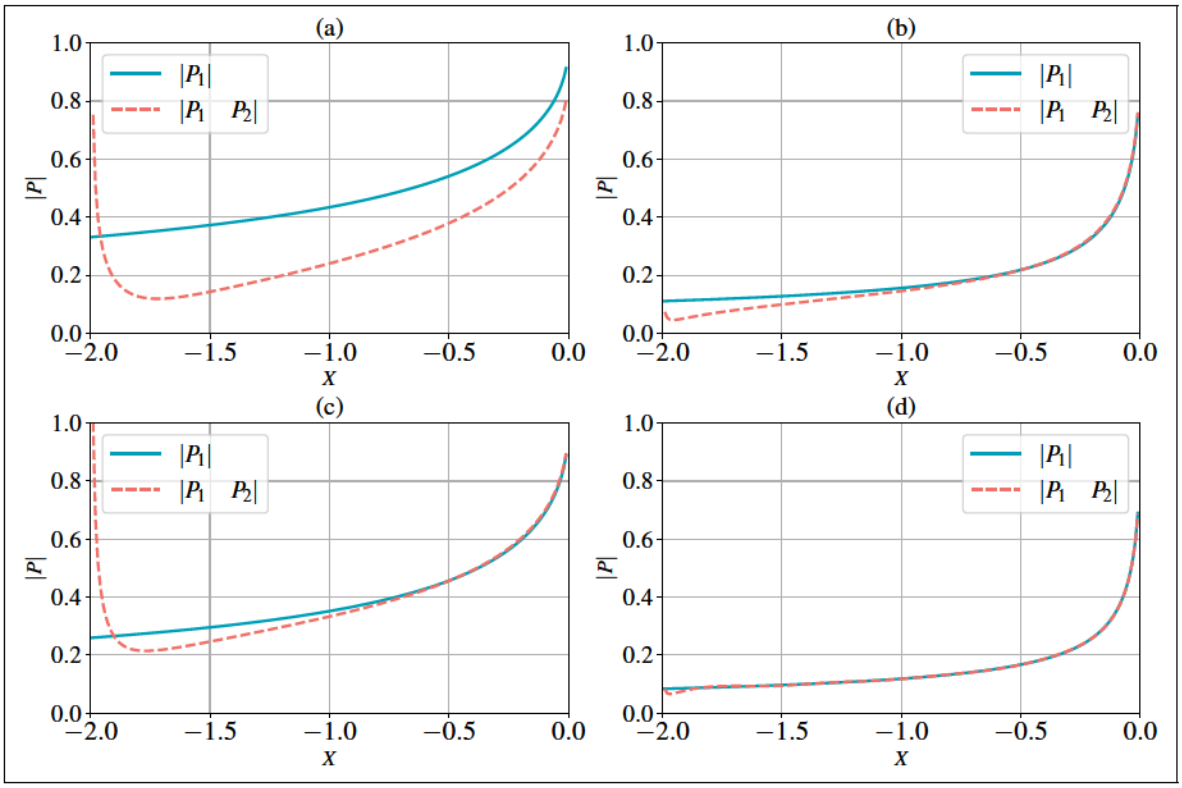

Figure 2.10 Magnitude of scattered pressure, P_1 and leading edge correction P_2 at (a) f=100 Hz, M=0.05, (b) f=1000 Hz, M=0.05, (c) f=100, M=0.5 and (d)f=1000 Hz, M=0.5

2.3.2 3D Solution

The previous section dealt with a parallel gust, or a gust characterized only by the streamwise-wavenumber $_1$. In this section a more general analysis is done by taking into account an oblique gust, characterized by dimensionless streamwise and a spanwise wavenumbers ($_1$ $_3$)(See Figure 2.8). This generalization is possible given that the trailing edge is taken as the edge of a half-plane in the z-direction and thus the spanwise dependency can be factorized. The 3D convective Helmholtz equation is given by:

$$\frac{^2}{^2} \quad \frac{^2}{^2} \quad ^{-2} \quad 0 \tag{2.38}$$

with

$$^{-2} \quad ^{-2} \quad \frac{^2}{^3} \tag{2.39}$$

All the derivations from the parallel gust solution are easily extended into 3D provided that $^{-2}$ is positive, in which case the gust is said to be supercritical and Eq. (2.38) is hyperbolic. The solution for the pressure jump, , is thus given by:

$$0 \quad 1 \quad _1 \quad ^- \quad ^- \quad 1 \quad ^1 \quad ^3 \tag{2.40}$$

If $^{-2}$ is negative, Eq. (2.38) is elliptic and labeled subcritical. For sufficiently large spans, subcritical gust do not radiate into the far-field but rather decay exponentially (Roger & Moreau (2005)). Nonetheless, the solution proceeds similarly.

2.3.3 Aeroacoustic transfer function

The preceding result, (Eq. (2.40)) gives the pressure distribution on the flat plate. Recalling Curle's analogy, Eq. (2.8), the pressure represents an equivalent dipole distribution that is to be integrated over the plate surface to obtain the far-field acoustic pressure. The broadband nature of the trailing edge noise suggests that it is easier to work in the frequency domain than in

the time domain. To frequency-domain version of Eq. (2.8), is obtained by taking its Fourier transform (Glegg & Devenport, 2024):

$$\mathbf{x} \qquad \frac{}{4 \quad \mathbf{x}^{2}{}_{0}} \quad \hat{} \quad \mathbf{y} \qquad \mathbf{y} \tag{2.41}$$

where $\hat{}$ $\mathbf{y}$ is the Fourier transform of the unsteady force, and $\mathbf{y}$ and $\mathbf{x}$ $_{1}$ $_{2}$ $_{3}$ are the source and observer coordinates respectively as shown in Figure 2.11.

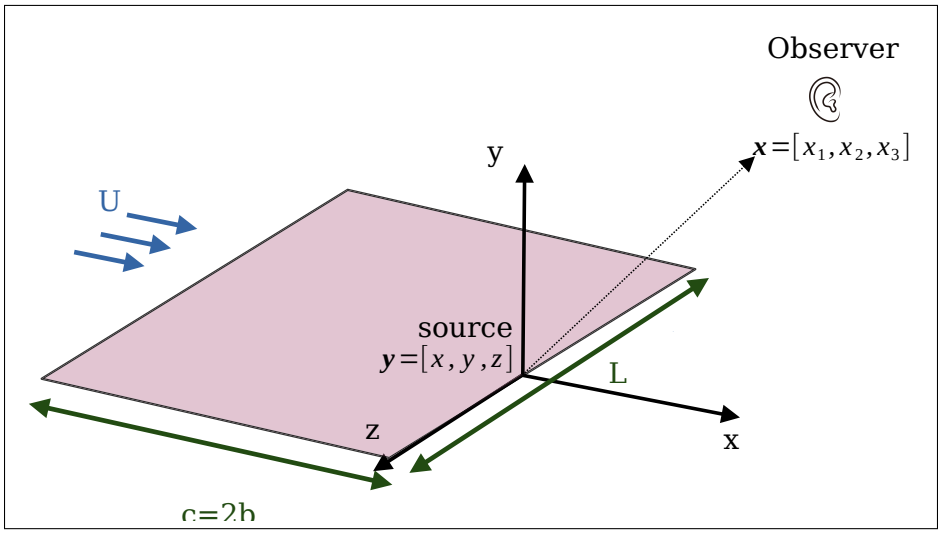

Figure 2.11 Radiation integral source and observer coordinates

Using the following far-field approximation $\mathbf{x}$ $\mathbf{x}$ $\mathbf{y}$ $\mathbf{x}$ and noting that the only surface of integration is given by the flat plate located at 0, yields:

$$\mathbf{x} \qquad \frac{}{4 \quad \mathbf{x}^{2}{}_{0}} \quad \begin{matrix} 0 & 2 \\ 2 & 2 \end{matrix} \qquad \mathbf{y} \tag{2.42}$$

where is the pressure jump (or scattered pressure) on the flat plate. Note that in the time-domain version of Curle's Analogy (Eq. (2.8)), the integral is evaluated at the corresponding emission time. In the case of a uniform flow over a flat plate this means that the source at the

trailing edge appears to be moving or in other words, the acoustic waves are convected by the mean flow. Due to Galilean invariance of the acoustic equations, a moving source in a stationary fluid is equivalent to a stationary source in a moving fluid.

To better understand the effects of a moving source, consider the situation in Figure 2.12 where a drone (modeled as a monopole source) is flying at constant velocity $_0$ overhead with respect to a stationary observer. A pulse is emitted from the source **y** at time and is heard by the observer at time . In the elapsed between emission and reception, the source has moved a distance and the observer cannot discern if the pulse came from a fixed source, **y**, moving with the flow or from a virtual source at **y** . In the frequency-domain version of Curle's analogy (Eq. (2.42)) the distance , known as the phase radius, accounts for the emission and reception time differences. To find , first let denote the modified distance between the source and the observer such that:

$$2 \quad 1 \quad 2 \quad 2 \quad 2 \quad 2 \quad 3 \quad 2 \tag{2.43}$$

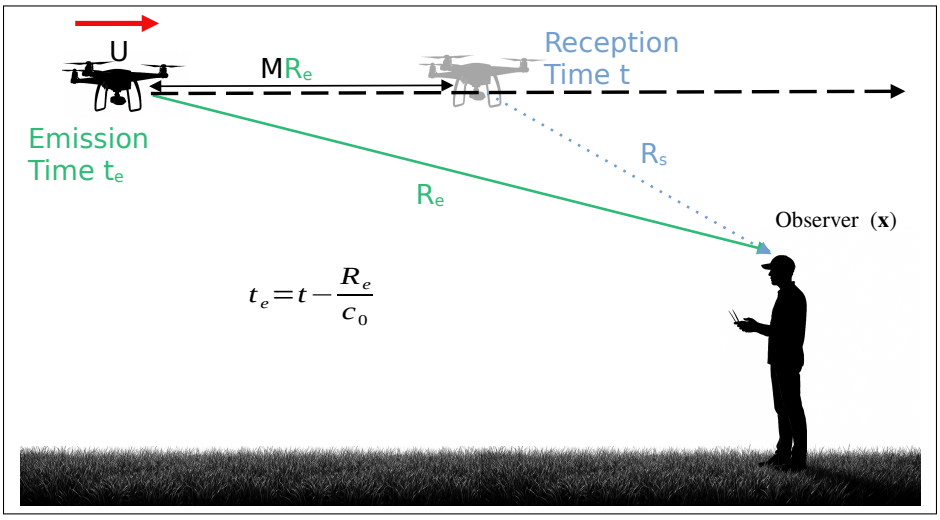

Figure 2.12 Effects of a moving source in emission and reception time

An implicit equation can be formulated for the emission distance in terms of the reception coordinates:

$$2 \quad 1 \quad 2 \quad 2 \quad 2 \quad 2 \quad 3 \quad 2$$
$$1 \quad 2 \quad 2 \quad 2 \quad 2 \quad 3 \quad 2 \tag{2.44}$$

For subsonic Mach numbers, the above equation results in two roots. The physical root is the one in which the causality condition is enforced, i.e., the wave at the observer was detected at a time . The root that satisfies this condition is given by:

$$1 \quad \overline{1 \quad 2 \quad 2 \quad 2 \quad 2 \quad 3 \quad 2} \quad 2$$
$$1 \quad 2 \tag{2.45}$$

Assuming far-field conditions, i.e., $_1 \quad _3$ and with 0 since all the sources are on the airfoil's surface, can be Taylor-expanded and approximated to first order by:

$$_0 \quad 1 \quad \frac{1 \quad 2 \quad 3}{2 \quad 0} \tag{2.46}$$

where $_0$ is given by:

$$\begin{matrix} 2 & 2 & 2 & 2 & 2 \\ 0 & 1 & & 2 & 3 \end{matrix} \tag{2.47}$$

After substitution of the phase radius, Eq. (2.45), in Eq. (2.42) the far-field acoustic pressure reads:

$$\mathbf{x} \quad \frac{2 \quad 2}{2 \quad 0 \quad 0^2} \quad \begin{matrix} 0 & 2 \\ 2 & 2 \end{matrix} \quad \overline{2} \quad 0 \quad \frac{1 \quad 2 \quad 3}{0} \quad 1 \tag{2.48}$$

Using the scattered pressure solution for the 3D gust in Eq. (2.40) allows to evaluate the X and Z integrals independently. The integral in Z is given by:

$$\int_{2}^{2} {}_{3} \; -\frac{3}{0} \qquad \frac{\bar{2} \qquad \bar{2}}{} \; 2\,\frac{\sin \bar{2}}{\bar{2}} \qquad \mathrm{sinc}\,\frac{}{2} \; {}_{3} \; -\frac{3}{0} \tag{2.49}$$

with $\bar{}$ and ${}_{3}\;\bar{}\;{}_{3}\;{}_{0}$. Substituting in the radiation integral yields:

$$\mathbf{x} \qquad \frac{3}{2\;{}_{0}\;{}^{2}_{0}} \; \mathrm{sinc}\,\frac{}{2} \; {}_{3} \; -\frac{3}{0} \qquad \bar{2} \;{}_{0}\; {}_{1} \int_{2}^{0} 1 \qquad 1 \tag{2.50}$$

where

$$ {}_{1} \; - \frac{1}{0} \tag{2.51}$$

$$ {}_{1} \; \bar{} \qquad \bar{} \tag{2.52}$$

The integral in Eq. (2.50) is usually called the radiation integral. Its calculation gives the aeroacoustic transfer function $\mathcal{L}$ that relates the far-field sound to the aerodynamic wall-pressure. The integral must be calculated for the main pressure term (Eq. (2.40)) and for the back-scattering correction for both supercritical and subcritical gusts. Starting with the former gives:

$$\mathcal{L}_{1} \int_{2}^{0} 1 \qquad \frac{1}{} \qquad \frac{2}{} \; 1 \; {}^{2} \; \frac{}{} \; 2 \qquad 1 \qquad 2 \; 1 \; {}^{2} \tag{2.53}$$

after integrating by parts.

This is the same as Eq.(5) in Amiet (1976) for parallel gusts, i.e., $\bar{}_3 \quad 0$. The leading-edge back-scattering is given by (details are given in Roger & Moreau (2005)):

$$\frac{1}{-}\mathcal{L}_2 \quad \frac{1}{-} \quad \begin{matrix}0\\ \\ 2\end{matrix} \quad {}_2 \qquad {}^{4\,-}\,1 \quad 1 \qquad 4^{-} \quad {}^{2} \qquad {}^{-} \qquad {}^{-} \tag{2.54}$$

with

$$\frac{1 \qquad {}^{4\,-}\,1 \qquad {}^{2}}{2 \quad - \; - \quad -} \qquad {}^{-} \quad {}^{-}{}_{1} \quad {}_{0}$$

$$1 \qquad {}^{2^{-}} \quad \mathrm{sinc} \quad 2^{-} \quad 1 \qquad {}^{2^{-}} \quad \mathrm{sinc} \quad 2^{-} \quad \frac{1 \quad 1}{2 \quad 2^{-}} \; {}^{4\,-} \quad 4^{-}$$

$$\frac{1 \quad 1}{2 \quad 2^{-}} \; {}^{4\,-} \quad 4^{-} \frac{{}^{2}}{2} \quad \overline{2^{-}} \quad 2 \quad \frac{1 \quad 1}{2^{-}} \quad \frac{1 \quad 1}{2^{-}} \tag{2.55}$$

The aeroacoustic transfer function for a supercritical gust is then:

$$\mathcal{L} \quad {}_1 \quad {}_3 \quad \mathcal{L}_1 \quad \mathcal{L}_2 \tag{2.56}$$

2.3.4 Far-field acoustic pressure power spectral density

All the efforts discussed so far have been aimed towards obtaining a relationship between an incident harmonic pressure gust with frequency, , and dimensional streamwise and spanwise wavenumbers, ${}_1$ and ${}_3$ respectively and its corresponding acoustic far-field pressure. Since a turbulent boundary layer contains a myriad of pressure scales, a statistical analysis is required to relate the wall-pressure statistics, discussed in Sec. 2.2.2, to the far-field acoustic pressure Power Spectral Density (PSD). The complete detailed procedure can be found in Nigro (2017), in this section only the main steps are outlined.

Following Roger & Moreau (2005) the PSD is found by integration over all gusts with 2D wavenumbers contributing to the frequency . However, the 2D integration over all the wavenumbers is usually simplified in the streamwise direction by assuming that most of the spectral energy is concentrated on the convective ridge where the streamwise wavenumber is 1 . Thus, the wavenumber-frequency spectrum can be also be written as:

$$0 \quad — \quad 3 \qquad\qquad 1 \quad 3 \qquad 1 \tag{2.57}$$

Therefore, only an integration over the spanwise wavenumbers is required. As discussed by Amiet (1975) the far-field acoustic pressure PSD, , due to the pressure fluctuations in the boundary layer is given by:

$$\frac{1}{} \qquad — \quad 3 \qquad — \quad 3 \qquad {}^{3} \quad 0 \quad — \quad 3 \quad 3 \tag{2.58}$$

where — 3 is related to the transfer function derived in the previous section and '*' denotes the complex conjugate. The streamwise dependency has been eliminated by assuming that the eddies are convected downstream at a constant velocity and with the distance between two points in the spanwise direction as

Using the results from the transfer function yields:

$$\mathbf{x} \qquad \frac{2}{2 \quad 0 \; \frac{2}{0}} \; \frac{1}{} \qquad \operatorname{sinc}^2 \frac{}{2} \quad 3 \quad - \frac{3}{0} \quad \mathcal{L} \quad — \quad 3 \quad 0 \quad — \quad 3 \quad 3 \tag{2.59}$$

As explained by Schlinker & Amiet (1981), the assumption of frozen turbulence allows to establish a direct relationship between the wavenumber spectrum and the frequency spectrum. Therefore, the wavenumber-frequency spectrum can be expressed as the product of the single-point wall-pressure fluctuations spectrum and the spanwise correlation length using Corcos' model(Eq. (2.21)) :

$$0 \;\text{—}\; 3 \quad \frac{1}{} \qquad 3 \tag{2.60}$$

which yields:

$$\mathbf{x} \qquad \frac{2}{2 \;\; 0 \;\; \frac{2}{0}} \;\; \frac{1}{} \qquad \text{sinc}^2 \;\; \frac{}{2} \;\; {}_{3} \;\; -\frac{3}{0} \quad \mathcal{L} \;\text{—}\; {}_{3} \;\; \frac{1}{} \qquad 3 \qquad {}_{3} \tag{2.61}$$

Assuming that the span is significantly larger than the chord, or that the characteristics aerodynamic scales close to the trailing edge are smaller than the chord the following important simplification can be made:

$$\text{sinc}^2 \;\; \frac{}{2} \;\; {}_{3} \;\; -\frac{3}{0} \qquad \frac{2}{} \qquad {}_{3} \;\; -\frac{3}{0} \tag{2.62}$$

Using the sifting property of the delta function gives:

$$\mathbf{x} \qquad \frac{2}{2 \;\; 0 \;\; \frac{2}{0}} \;\; 2 \quad \mathcal{L} \;\text{—}\; \frac{3}{0} \qquad \frac{3}{0} \tag{2.63}$$

Note than when the wall pressure spectrum model is used in conjunction with Amiet's model, it represents an incident wall pressure spectrum, which is not affected by a trailing edge. In other words, the acoustic models solve the scattering of this wall pressure spectrum by a trailing edge so that this wall pressure spectrum should not include the scattered part. However, it would be challenging in the measurement or in the compressible high-fidelity LES or DNS simulations to distinguish the incident wall pressure spectrum from the scattered wall pressure spectrum near the trailing edge (Lee *et al.*, 2021). Note that in the calculations in this Thesis, Eq. (2.63) is multiplied by a factor of 4 that accounts for a single-sided spectra, and for radiation from both

upper and lower surfaces of the plate. Eq. (2.63) is the fundamental result of this section, and it is the model used to calculate the trailing edge noise from straight edges.

Amiet's straight trailing edge model ——————————-Summary

- Amiet's model is derived from Linearized aerodynamic equations which can be interpreted also as a wave equation.
- The wall pressure fluctuations spectrum, , and the spanwise correlation length, are essential inputs that must be modeled.
- Using the frozen turbulence assumption the wall-pressure statistics upstream of the trailing edge can be used.
- The aeroacoustic transfer function $\mathcal{L}$ relates the wall-pressure fluctuations spectrum to the far-field acoustic pressure PSD.

2.4 Ayton's serrated trailing edge noise model

While experimental measurements demonstrated the effectiveness of serrated edges for trailing edge noise control, the prediction of such reductions is still elusive. From a mathematical point of view, the modeling is essentially unchanged compared to that of straight edges. The excitation is still a harmonic pressure gust (Eq.(2.23)) and the mixed boundary conditions still apply. However, the division between the no-flow-through and the Kutta conditions is now a function of the spanwise-coordinate, and this alone significantly increases the analytical treatment. This section explores the noise modeling from serrated trailing edges using Ayton (2018) approach, based on the Wiener-Hopf method.

Ayton (2018) model aimed to provide an alternative to Lyu *et al.* (2016) and Howe (1991) models. The former being too computationally demanding and the latter known to over-predict noise reduction by as much as 15 dB as noted by Gruber (2012). In contrast to Lyu's approach, based on the Schwarzschild technique, Ayton uses the Wiener-Hopf method. As noted by Noble (1958), the technique was originally intended to solve a specific integral equation, but during the Second World War, its potential to solve diffraction problems by semi-infinite planes. At its core,

the Wiener-Hopf method relies on the Fourier Transform of the partial differential equation and subsequent factorization of complex variable functions. It is worth noting that Huang (2017) also used the Wiener-Hopf technique, albeit in combination with a Fourier series expansion. Thus, the solution is not given in closed analytical form. The derivation of Ayton's model of serrated trailing edge noise is presented next.

2.4.1 Original Ayton's model

Consider an incoming pressure wave (Eq.(2.23)) on a semi-infinite plane convected towards an edge described by a periodic function . Figure 2.13 shows a sawtooth shape characterized by root-to-tip amplitude, 2 , and wavelength, . Nevertheless, Ayton's model allows the use of any periodic function, e.g., square wave, sinusoidal, chopped peak, among others. Mathematically, the serration shape is described by piecewise functions. Following Ayton's derivation, all lengths are made dimensionless by the serration wavelength, . Note that in the following derivation 2 is noted as 2 as Ayton did. In other words, all the lengths are implicitly non-dimensional by the serration wavelength.

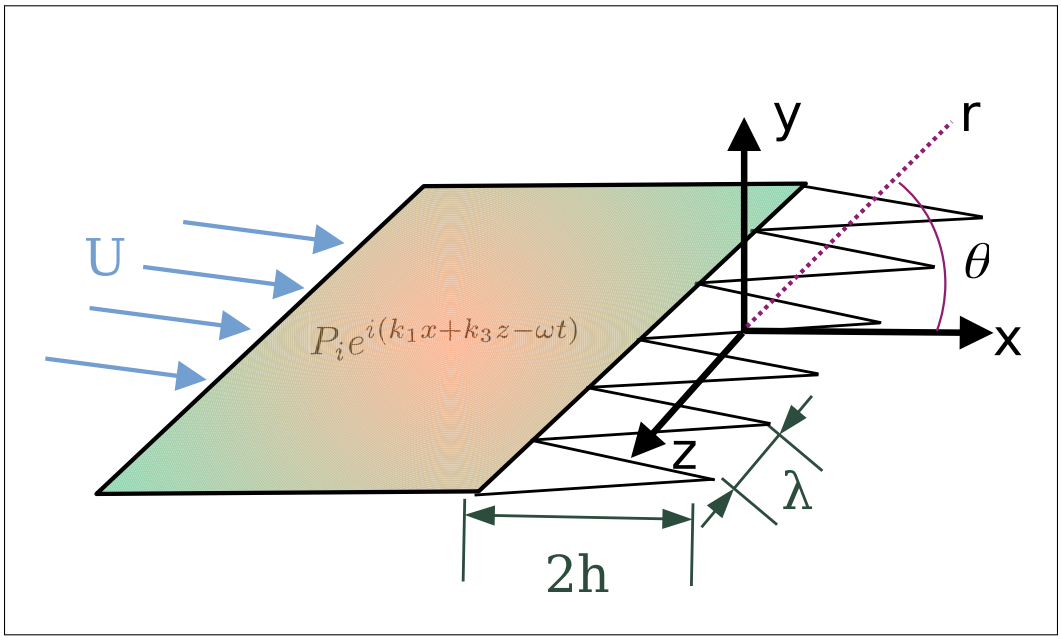

Figure 2.13 Coordinate system for the serrated trailing edge problem

The scattered field must satisfy the convective Helmholtz equation (Eq. (2.24)) subject to boundary conditions of zero normal velocity on the surface:

$$\frac{\partial}{\partial n_0} \qquad 0 \qquad 2 \tag{2.64}$$

and zero pressure jump across the wake downstream of the plate (the familiar Kutta condition):

$$0 \qquad 1 \quad 3 \qquad 2 \tag{2.65}$$

The problem is solved for one serration period only, and periodic boundary conditions are enforced in the spanwise-direction:

$$1 \qquad 0 \qquad 3 \qquad \frac{\partial}{\partial x_1} \qquad \frac{\partial}{\partial x_1} \qquad 0 \qquad 3 \tag{2.66}$$

A convective transform $\qquad\qquad 2$ is used to simplify the Helmholtz equation yielding:

$$2\frac{\partial^2}{\partial x_2^2} \quad \frac{\partial^2}{\partial x_2^2} \quad \frac{\partial^2}{\partial x_2^2} \quad - \qquad ^2 \qquad 0 \tag{2.67a}$$

$$\frac{\partial}{\partial n_0} \qquad 2 \tag{2.67b}$$

$$0 \qquad \tilde{1} \quad 3 \qquad 2 \tag{2.67c}$$

$$1 \qquad 0 \quad 3 \tag{2.67d}$$

$$\frac{\partial}{\partial x_1} \qquad \frac{\partial}{\partial x_1} \qquad 3 \tag{2.67e}$$

where $\tilde{1} \qquad 1 \qquad ^2$. Ayton proceeds by introducing a non-orthogonal coordinate transformation, arguing that this is necessary to allow a solution using separation of variables. However, Lyu (2023) demonstrated that the transformation is not strictly necessary. The transformation is made here for consistency with the original derivation. Thus introducing the

transformation:

$$- \quad 2 \tag{2.68a}$$

(2.68b)

(2.68c)

The following system of equations is obtained:

$$1 \quad 2 \; {}^{2} \quad {}^{2} \; \frac{2}{2} \; \frac{2}{2} \; \frac{2}{2} \; 2 \; 2 \quad \frac{2}{} \quad 2 \quad — \quad - \; {}^{2} \; 0$$

(2.69a)

$$— \quad {}_{0} \quad 0 \quad 0 \tag{2.69b}$$

$$0 \quad {}^{\sim}{}_{1} \; 2 \quad {}^{3} \quad 0 \tag{2.69c}$$

$$1 \quad 0 \; {}^{3} \tag{2.69d}$$

$$— \quad {}_{1} \quad — \quad {}_{0} \; {}^{3} \tag{2.69e}$$

where ${}^{\sim}{}_{1}$. Inspection of Eq. (2.69a) reveals that the coefficients of the derivatives are functions of the spanwise variable , this impedes the use of separation of variables method to solve the equation. As pointed out by Roger, Schram & Santana (2013), one way to by-pass this restriction is to Fourier Transform the coordinate only, such that:

$$\hat{} \tag{2.70}$$

The solution to $\hat{}$ can now be expressed as the product of two functions, Y and Z, such that:

$$\hat{} \tag{2.71}$$

with Y and Z being the solution of the following ordinary differential equations (ODE). The two functions are related by a separation constant :

$$-^{2} \quad ^{2} \quad ^{2} \quad 0 \tag{2.72}$$

and

$$2 \quad 2 \quad 2 \quad ^{2} \; 2 \; ^{2} \quad ^{2} \quad ^{2} \quad 0 \tag{2.73}$$

The -equation is a second order ODE with constant coefficients and the solution is given by:

$$\text{sgn} \quad ^{\overline{2 \quad 2}} \tag{2.74}$$

where sgn 0 = 0 and sgn = 1 when 0. Note that the Sommerfeld radiation condition (negative exponential) has been enforced. This ensures that the solution is an outgoing wave, radiating energy towards infinity and not the opposite. In addition:

$$^{2} \quad -^{2} \quad ^{2} \tag{2.75}$$

The -equation is a second order ODE with variable coefficients and requires the substitution ^{2} , where is a dummy-function, to eliminate the first-order term. The equation is then solved for and after transforming back gives:

$$^{2} \quad \cos \quad \sin \tag{2.76}$$

Imposing periodic boundary conditions to Eq. (2.76), allows one to eliminate or and find the following allowable modes:

$$^{2} \quad _{3} \; ^{2} \tag{2.77}$$

And a general solution in transformed space given by:

$$\hat{} \quad \overline{^{2} \; ^{2}} \tag{2.78}$$

where:

$$^{2} \quad - \; ^{2} \quad _{3} \; 2 \tag{2.79}$$

The derivation proceeds to solve for using the Wiener-Hopf Technique. Details are omitted for brevity. According to Ayton (2018), the boundary conditions (Eqs. (2.69c) and (2.69d)) are applied to find two holomorphic[1] functions. One function that is analytical in the upper half -plane and another one that is analytical in the lower half -plane.

A narrow strip enclosing the real axis is then considered, within which both analytic continuations coincide on the boundary. This equality implies that their difference defines a function analytic throughout the entire complex plane. By Liouville's theorem, such a function must be constant (or, in certain cases, a polynomial of finite degree). This constraint provides the closure condition required to uniquely determine the analytic function and hence solve for the coefficients .

The solution in the transformed space is given by:

$$\hat{} \quad \frac{\overline{\qquad}}{\overline{\qquad\qquad}} \; \text{sgn} \quad \overline{^{2} \; ^{2}} \tag{2.80}$$

[1] Holomorphic functions are complex-valued functions that are differentiable in a neighborhood of each point in a domain in the complex coordinate space

The solution in Eq. (2.80) presents a few alternatives. Ayton (2018) proceeded by approximating the inverse Fourier transform using the method of stationary phase, also known as method of the steepest descent. This yields a far-field (1) approximation and, as noted by Jones (1989), with additional limitations for observers at small angles (0) from the trailing edge. On the other hand, a complete solution in physical space may be attempted by completely evaluating the inverse Fourier transform. The inverse transform is mathematically involved and was performed by Lyu (2023) who also pointed out a limitation of the model, due to the factorization of the coefficients. A third approach consists in evaluating the inverse Fourier transform only on the plane surface (0). This removes one coordinate from the problem, and gives the surface pressure, which can then be used in Curle's analogy.

2.4.2 Rapid Lyu and Ayton's model

As noted before, application of the steepest descent method allows to evaluate the inverse Fourier transform of Eq. (2.80) in the far-field. At a glance, the steepest descent method (not to be confused with the gradient descent algorithm in optimization) exploits the rapid oscillatory behavior of the phase function, in integrals of the type:

$$I \tag{2.81}$$

The steepest descent method can be used, for example, to obtain large argument approximations of the Bessel functions among other functions of mathematical physics. Note that for sufficient large values of , the majority of the contribution to the integral will come from the neighborhood of the stationary points of . In the rest of the interval, the rapid oscillations will cancel each other out. Using a Taylor's expansion of the phase function, , about a saddle point $_0$ allows approximating I to first order:

$$I \quad _0 \quad \frac{2}{\quad _0} \quad ^0 \quad 1 \quad O \quad \frac{1}{-} \tag{2.82}$$

The method of the steepest descent still requires the specification of a contour. For the mixed boundary conditions problems like the straight or serrated edge, the contour is usually parameterized such that the imaginary part of the phase function ( ) remains constant. For the detailed definition of the contours, the reader is referred to Lyu, Ayton & Chaitanya (2019) and Hales (2024). After application of the steepest descent method, the solution of Eq. (2.80) yields, in cylindrical coordinates:

$$\frac{\cos \qquad \overline{\qquad}}{2 \qquad \cos} \sin \frac{}{2} \quad \frac{\qquad ^{4}}{\overline{\quad}} \tag{2.83}$$

where $\overline{\quad ^{2} \quad ^{2}}$ and is measured from the x-axis. Following Lyu & Ayton (2020), the PSD due to a convecting statistically stationary turbulent pressure field, is given by:

$$_{\text{A}} \qquad ^{2} \qquad _{3} \quad _{3} \tag{2.84}$$

Substituting Eq. (2.83) in the above equation gives:

$$
\begin{aligned}
_{\text{A}} \qquad & \frac{1}{4}\sin^{2}\frac{}{2} \qquad ^{3} \qquad \frac{\cos \qquad \overline{\qquad}}{\cos} \\
& \frac{\cos \qquad \overline{\qquad}}{\cos} \qquad _{3}
\end{aligned}
\tag{2.85}
$$

Since experimental evidence and theoretical results have shown that serrations are effective when they are narrow (2), Lyu & Ayton (2020) proposed the following simplifications to Eq. (2.85). First, it is only needed to investigate the case were both and are real, because otherwise the term causes the whole term to exponentially decay in the far-field. Since $\overline{\quad ^{2} \quad ^{2}}$ it is concluded that is real only when . It is then permissible to have:

$$\text{sgn} \tag{2.86}$$

where $\quad$ is the real part and $\quad$ is the Kronecker delta. Note that Eq. (2.86) shows that its right-hand side vanishes if $\quad$ is imaginary. This implies that:

$$\text{A} \qquad \frac{1}{4}\sin^2\frac{}{2} \qquad {}_3\,\frac{\cos\ \overline{\qquad}^{\,2}}{\cos}\ \text{sgn}\ {}_3 \tag{2.87}$$

Then, using the fact that $\quad$ is real only when $\qquad$ and that the serration wavelength is small, Lyu & Ayton (2020) conclude that the integrand does not vanish only when $2\ {}_3\ 2\ \ $ (using Eq. (2.79)). This allows one to take the ${}_3$ dependency out of the integral and to change the integration interval to $2\ \ $ to $2\ \ $, without causing significant errors. After doing so, Eq. (2.87) simplifies to:

$$\frac{\bar{}}{4\ ^2}\frac{\bar{}}{\bar{}\cos\ ^2}\sin^2\frac{}{2} \qquad \bar{}\cos\ ^2\ \ \frac{2}{} \tag{2.88}$$

where $\bar{}\ \ $. As explained by Lyu & Ayton (2020), the simplifications from the original model can be summarized in the following inequality, $\ 2\ $. To put things in perspective, for small scale propellers the serration wavelength is a fraction of the serration height which is itself a fraction of the chord. For a value of $\ 5$ mm the above inequality holds up to 68 kHz, well beyond the human hearing range. Using the same simplified model for the wavenumber-frequency spectrum, Eq. (2.60), as in Amiet's model yields:

$$\frac{\bar{\quad}}{4^{\ 2}}\frac{\bar{\quad}}{\bar{\cos}^{\ 2}}\sin^2\ \frac{}{2}\qquad\qquad \bar{\cos}^{\ 2}\qquad \frac{2}{\quad} \tag{2.89}$$

2.4.3 Li and Lee's extension of the rapid model

As a consequence of the steepest descent approximation, the rapid Lyu and Ayton model (Eq.(2.83)) decays as $1\quad \bar{}$ or, equivalently, its PSD (Eq.(2.89)) as $1\quad$. As noted by Tian & Lyu (2022), this decay is strictly two-dimensional and thus the direct use of Eq. (2.89) for a finite airfoil or a blade segment is questionable. To circumvent this issue, Li & Lee (2022) suggested several heuristic modifications to the model. First, they proposed to include the airfoil span, L, and to include an additional $1\quad$ to match the attenuation rate of the acoustic propagation. Secondly, they modified the spanwise wavenumber to include the effect of observers out of the mid-span plane, yielding $_3\quad 2\qquad\qquad _0$ instead of $_3\quad 2\quad$. Additionally, they included the observer spanwise position. Lastly, the same factor of 4 used in Amiet's model that accounts for a single-sided spectra and to account radiation from both upper and lower surfaces of the plate was included. The Li and Lee's extension of the rapid Lyu and Ayton's model then reads:

$$\text{LL}\qquad \frac{4\ \bar{\quad}}{4^{\ 2}\ \frac{2}{0}}\frac{\bar{\quad}}{\bar{\cos}^{\ 2}}\sin^2\ \frac{}{2}\qquad\qquad \bar{\cos}^{\ 2}\qquad _3 \tag{2.90}$$

2.4.4 Effect of serration shape

So far, the serration treatment has been general with no consideration of the serration shape. Note that in the rapid Lyu and Ayton model and in Li and Lee's extension, all the serration effects are contained in the modal expansion coefficients $\quad \bar{\cos}\quad$ given by Eq. (2.91). Thus, the

coefficients result from expanding the serration shape function, , in the orthogonal base found in Eq.(2.77) and are therefore shape dependent.

$$\int_0^1 2 \tilde{}_1 \bar{} \cos \quad 2 \tag{2.91}$$

The expansion coefficients of some common shapes are given next. The original shape functions proposed by Ayton (2018) are used. In them the serration root-to-tip amplitude are normalized to 1/2. Thus, for the sawtooth serration the expansion coefficients are:

$$_{st} \quad \frac{4}{4^{\,2}\,2 \quad 2} \sin \frac{1}{4} \quad 2 \tag{2.92}$$

For the square wave are:

$$_{sq} \begin{cases} \frac{1\ 2}{} \sin \frac{}{4} & \text{odd} \\ 0 & \text{even} \\ \cos \frac{}{4} & 0 \end{cases} \tag{2.93}$$

and for the sinusoidal shape:

$$\sin \quad 4 \tag{2.94}$$

Where $_1 \quad ^2 \cos 2$ and is the Bessel's function of the first kind of n order. While it is well-known that sharper (2h/ >1) serrations give better noise reductions (Kholodov & Moreau, 2021), the debate over the "best" serration shape is not settled, as less traditional shapes have been proposed, such as the iron shaped or the ogee (Lima Pereira,

Avallone, Ragni & Scarano, 2023). The results from the analytical modeling, however, can offer some insights regarding the shape performance.

The expansion coefficients, $E_n(s)$, dictate the noise reduction capabilities of each serration Ayton (2018). Since only a few modes are cut-on, based on the analysis of the previous section, the zeroth-order coefficient, $E_0(s)$, dictates the general behavior of the serration shape. Figure 2.14 shows the magnitude squared of the zeroth-mode expansion coefficient for the sawtooth, sinusoidal, slitted-V, and square wave serration, for an observer at 90° from the trailing edge. Firstly, it is observed that for sufficiently low values of s the square wave outperforms all other shapes. Secondly, for values of s close to 10, the square wave becomes ineffective, and the sinusoidal shape outperforms for a small range of values before the sawtooth overtakes. The minima alternate between sawtooth and sinusoidal shapes for larger values of s. Lastly, it is shown that the slitted-V outperforms the other shapes only over very narrow ranges of s.

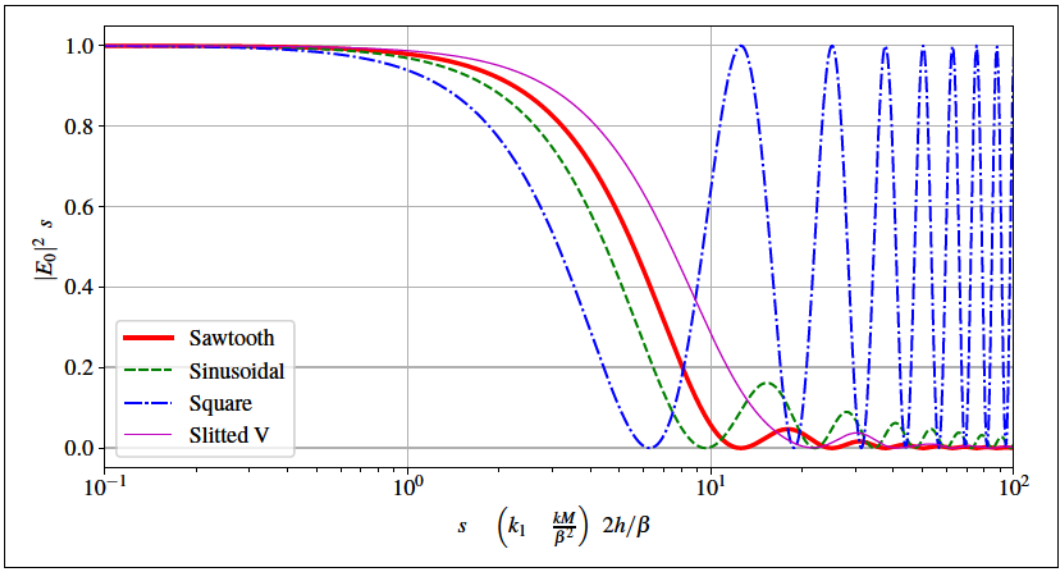

Figure 2.14 zeroth-mode modal expansion coefficients for different shapes

To give some perspective of the intended application, consider a typical quadcopter propeller, with a tip Mach number less than 0.3, as in the case of the NACA0012 propeller studied in this Thesis. For such low Mach numbers, the parameter, s, can be approximated by $s \approx k_1(2h) \approx \omega/U_c(2h)$. Considering the chord of the aforementioned propeller of 2.5 cm and assuming that the serrations

are about 20% of the chord gives values of s between 0.44 to 4.4 for frequencies between 1 and 10 kHz respectively. Therefore, for small scale propellers, the square wave should give better noise reductions than the other shapes, and it is chosen as the starting point to develop a 3D model based on the original Ayton's model.

Serrated Models ——————————————————————- Summary

- The original Ayton's model (Eq.(2.89)) is the result of an approximation using the steepest descent method as thus has a cylindrical (2D) decay in the far-field and it is limited to high non-dimensional frequencies.
- The heuristic extension by Li and Lee proposes a few modifications to alleviate the restrictions, yielding a correct 1/ (3D) decay, inclusion of the finite span and observer spanwise position effect.
- The expansion coefficients provide a simple way to assess the effect of each serration shape.
- A preliminary analysis based on the scattering properties of each serration shape, shows great potential for the square wave compared to other more traditional shapes, for drone applications.

2.5 Extension of the original Ayton's model for the square wave

The steepest descent approximation (Eq.(2.83)) used in the previous section allows to obtain a far-field solution to the serrated edge. Given the limitations discussed in the previous section, it is desirable to obtain an analytical model that does not require the steepest descent approximation or the heuristic extension from 2D to 3D. It is important to note that this approach is shape-dependent, unlike the original Ayton's model. For example, Lyu (2023) provides a complex analytical expression for the complete near-field of the sawtooth shape (and other linear functions). Zhang & Lyu (2024) used Lyu's results on the plate surface to evaluate the far-field acoustic pressure of the sawtooth via Curle's analogy.

This section presents a less mathematically intensive approach for the square wave, given its promising results for small-scale propellers. The main idea is to evaluate the Fourier transform of Eq.(2.80) only on the serrated plate to obtain the surface pressure. This surface pressure can then be used in Curle's analogy to obtain a closed-form solution without any approximation. Evaluating Eq.(2.80) for 0 then yields:

$$\hat{} \quad 0 \qquad \frac{\overline{\qquad}}{2\ \overline{\qquad}} \tag{2.95}$$

with inverse Fourier Transform:

$$0 \qquad \frac{1}{2} \qquad \hat{} \quad 0 \tag{2.96}$$

Which gives:

$$0 \qquad \frac{\overline{\qquad}}{2\ \overline{\qquad}} \tag{2.97}$$

Substituting Eq. (2.77) and using 2 gives:

$$0 \qquad \frac{}{2} \qquad \frac{\overline{\qquad}}{2\ \overline{\qquad}} \tag{2.98}$$

Using the following change of variables:

(2.99)

(2.100)

results in:

$$0 \qquad \frac{}{4} \qquad \frac{}{-} \tag{2.101}$$

2.5.1 Surface Pressure

Equation (2.101) is the starting point for the calculation of the surface pressure for the square wave. Due to the orthogonality of the modal expansion, each mode can be considered independently. Recalling that in the expansion coefficients for the square wave, Eq. (2.93), the even modes evaluate to zero, while the odd modes(2 1) are given by:

$$^{sq} \qquad \frac{1 \quad 2}{} \sin \frac{}{4} \qquad \frac{1 \quad 2}{} \frac{4 \qquad 4}{2} \qquad \text{for} \qquad 2 \quad 1 \tag{2.102}$$

with 2 $\tilde{}_1$ 2 $\tilde{}_1$. Substituting the above equation in Eq. (2.101) yields for the n^{th} odd mode:

$$0 \qquad \frac{}{-} \qquad \frac{4 \qquad 4}{2} \tag{2.103}$$

with

$$\frac{}{4} \frac{1 \quad 2}{} \tag{2.104}$$

Splitting the integral, substituting for and collecting the terms results in:

$$0 \qquad \frac{}{2} \quad \bar{2} \quad \tilde{1} \qquad \frac{}{-} \qquad 2$$
$$\bar{2} \quad \tilde{1} \qquad \frac{}{-} \qquad 2 \tag{2.105}$$

Before solving the preceding integrals, it is noted that since only the surface pressure on the plate is of interest, it is not necessary to compute the integral from to but rather from to 0, since in phase space the boundary between the plate and the wake corresponds to 0. The solution to the integrals is then given by the Schwarzschild technique, Eq. (2.34):

$$\frac{}{} \qquad 1 \quad \frac{}{} \qquad \text{erfc} \quad 1 \quad \frac{}{2} \tag{2.106}$$

where erfc(x)= 1-erf(x) is the complementary error function. Notice that the following relationship between the Fresnel integrals used in Eq. (2.34) and the complementary error function (Roger & Moreau, 2005) has been used :

$$1 \qquad 1 \quad \text{erfc} \quad 1 \quad \frac{}{2} \tag{2.107}$$

This allows for an easier implementation in Python using the special library scipy, and to better handle possible singularities when the function itself is divided by a value close to zero (Roger & Moreau, 2012). Substituting in Eq. (2.105) gives the square wave surface pressure odd modes as:

$$\begin{aligned} 0 \qquad \frac{}{2} \quad \frac{}{2} \quad \frac{}{1} \qquad & ^{2} \quad \text{erfc} \quad 1 \quad \frac{2}{2} \\ \frac{}{2} \quad \frac{}{1} \qquad & ^{2} \quad \text{erfc} \quad 1 \quad \frac{2}{2} \end{aligned} \tag{2.108}$$

Following the same logic, the solution for the zeroth-mode is:

$$_0 \quad 0 \qquad \frac{0}{2} \qquad \bar{2} \quad \tilde{1} \quad 0 \qquad\qquad ^2 \; ^0 \operatorname{erfc} \quad 1 \qquad \frac{\sqrt{\qquad\qquad 2 \quad 0}}{2}$$

$$\bar{2} \quad \tilde{1} \quad 0 \qquad\qquad ^2 \; ^0 \operatorname{erfc} \quad 1 \qquad \frac{\sqrt{\qquad\qquad 2 \quad 0}}{2} \tag{2.109}$$

with

$$0 \qquad \frac{^0 \quad ^0}{4} \tag{2.110}$$

Some important comments can be made upon inspection of Eq. (2.108) and Eq. (2.109). First, the square wave surface pressure distribution is equivalent to two straight edges, one at the serration root and one at the tip. Second, the solution for the odd modes and for the zeroth mode differ only in the sign between the main terms. Furthermore, in the limit of zero serration amplitude, 2 0, the two terms in Eq. (2.108) cancel each other, while the terms in Eq. (2.109) add each other, recovering the surface pressure in Amiet's model (Eq. (2.34)) for the case of parallel gusts, i.e., $_3 = 0$. The final expression for the surface pressure (or pressure jump) for the square wave thus reads:

$$0 \tag{2.111}$$

with

$$_0 \qquad \text{if} \qquad 0$$

$$\text{if} \qquad 2 \quad 1 \tag{2.112}$$

$$0 \qquad \text{if} \qquad 2$$

2.5.2 Radiation integral

The surface pressure distribution can now be used as an equivalent dipole source in Curle's analogy, Eq. (2.42). The plate is extended in the streamwise direction to and has a finite span from 2 to 2 as shown in Figure 2.15. The origin is at the middle of the tooth and the purple regions correspond to the integration surface for a single tooth. Notice that the teeth number, and the span are related by

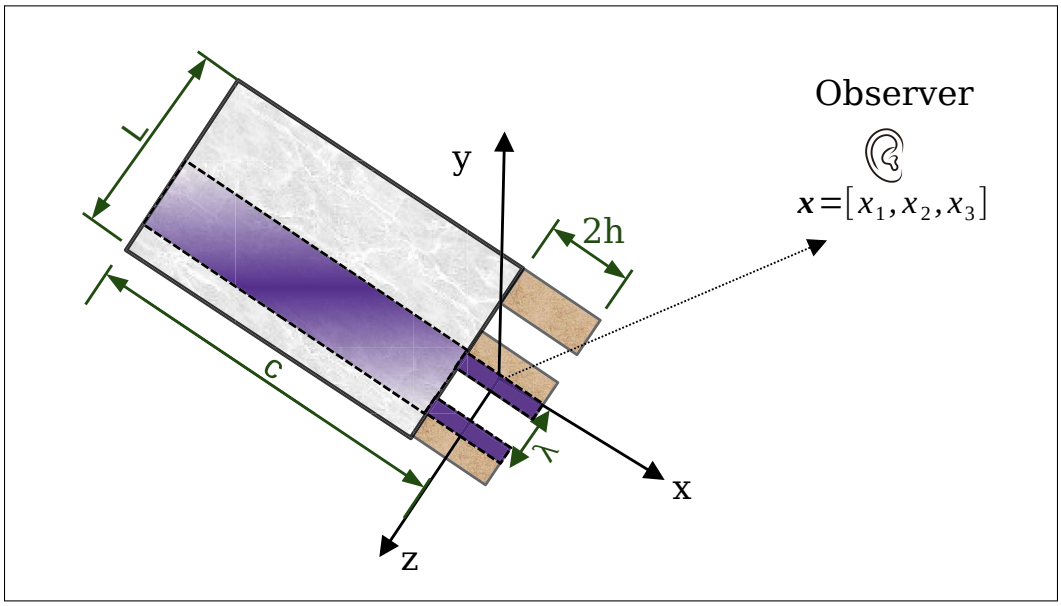

Figure 2.15 Coordinates for the square wave radiation integral. The purple zones correspond to the integration surface for a single tooth.

Since periodic boundary conditions are assumed in Eq. 2.67 the surface of integration corresponds to one wavelength only and the fluid region (white region between the two adjacent teeth in Figure 2.15) can be discarded. The radiation integral for a single mode, , over a single tooth, , and its adjacent plate surface is given by:

$$\mathbf{x} \qquad \frac{2}{4 \quad 0 \; \frac{2}{0}} \qquad \int_0^1 \qquad (2.113)$$

where is the source-observer distance accounting for convective effects given by Eq. (2.45) and where is the piecewise function defining the square wave in the original Ayton (2018) model given by:

$$\frac{1}{4} \qquad \begin{matrix} 0 \ \frac{1}{4} \\ \frac{1}{4} \ \frac{3}{4} \\ \frac{3}{4} \ 1 \end{matrix} \tag{2.114}$$

Note that in Ayton (2018), all the serration shapes were normalized to have a tip-to-root amplitude of 1/2 and can be arbitrarily scaled by 2 . The sharp boundaries of the square wave can be leveraged to discard the wake region (1 4 3 4) contribution to the surface integral. Additionally, since there is no explicit -dependency in , (Eq. (2.114)) the integral can be split into 3 regions:

The first one accounting for the pressure on the plate, from upstream, , to the serration root, 4:

$$^{1}\mathbf{x} \qquad \frac{2}{4 \quad 0 \ \frac{2}{0}} \qquad \begin{matrix} 4 & 2 \\ & 2 \end{matrix} \tag{2.115}$$

The second and third between the serration root, 4 and the serration tip, 4 with the former over the first quarter of the serration wavelength, (0 1 4) :

$$^{2}\mathbf{x} \qquad \frac{2}{4 \quad 0 \ \frac{2}{0}} \qquad \begin{matrix} 4 & 1 \ 4 \\ 4 & 0 \end{matrix} \tag{2.116}$$

and the latter, over the last quarter of the serration wavelength, (3 4 1)

$$^{3}\mathbf{x} \qquad \frac{2}{4 \quad 0 \ \frac{2}{0}} \qquad \begin{matrix} 4 & 1 \\ 4 & 3 \ 4 \end{matrix} \tag{2.117}$$

Following Zhang & Lyu (2024), it is possible to sum over all the teeth, , to obtain a finite span integral for a single mode, , given by:

$$^{2}\mathbf{x} \qquad \frac{2}{4 \quad 0 \; \frac{2}{0}} \qquad \begin{matrix} 4 \\ 4 \end{matrix} \qquad \begin{matrix} 1 & 4 \end{matrix} \tag{2.118}$$

and similarly:

$$^{3}\mathbf{x} \qquad \frac{2}{4 \quad 0 \; \frac{2}{0}} \qquad \begin{matrix} 4 \\ 4 \end{matrix} \qquad \begin{matrix} 1 \\ 3 & 4 \end{matrix} \tag{2.119}$$

Substituting (Eq. (2.104)) and (Eq. (2.45)) in the first radiation integral (Eq. (2.115)) gives:

$$^{1}\mathbf{x} \qquad \frac{2}{4 \quad 0 \; \frac{2}{0}} \quad 2 \qquad 2 \quad 2 \; \frac{}{4 \quad 2} \qquad 1 \quad 2$$

$$\overline{2} \quad \tilde{1} \qquad\qquad 2 \quad \text{erfc} \quad 1 \qquad \frac{\frac{}{\frac{2}{2}}}{}$$

$$\overline{2} \quad \tilde{1} \qquad\qquad 2 \quad \text{erfc} \quad 1 \qquad \frac{\frac{}{\frac{2}{2}}}{} \tag{2.120}$$

$$\frac{0 \quad 1}{2} \qquad \frac{1 \quad \frac{2}{0} \; 3}{2}$$

Inspection of the above equation reveals that the spanwise dependency of the integrals can be factorized outside the streamwise integral. Thus, after grouping the streamwise and spanwise terms the integral can be re-written as:

$$\mathbf{x} \qquad \frac{2}{4 \quad 0 \; \frac{2}{0}} \qquad \frac{}{2} \quad 0 \quad 1 \qquad \frac{2}{2}$$

$$\frac{2}{2} \; \tilde{} \; 1 \; 1 \qquad {}^{4}\mathrm{erfc} \quad 1 \qquad \frac{\sqrt{\frac{2}{2}}}{2} \tag{2.121}$$

$$\frac{2}{2} \; \tilde{} \; 1 \quad 1 \qquad {}^{4}\mathrm{erfc} \quad 1 \qquad \frac{\sqrt{\frac{2}{2}}}{2}$$

where the coefficients are defined as:

$$\frac{3}{0} \tag{2.122}$$

$$-\frac{1}{0} \tag{2.123}$$

The spanwise integral is straightforward and gives:

$$\frac{2}{2} \qquad \mathrm{sinc} \quad \frac{}{2} \tag{2.124}$$

Whereas integration by parts is used for the streamwise integral (details are given in Appendix II) yielding:

$$
\begin{aligned}
{}^{1}\mathbf{x} \quad & \frac{2}{4\ {}_{0}\ {}^{2}_{0}}\ \mathrm{sinc}\ \frac{}{2}\ \frac{3}{0}\ {}^{-}_{2}\ {}_{0}\ {}_{1}\ \frac{}{} \\
& {}^{-}_{2}\ {}^{\sim}_{1}\ {}_{1}\ \ \mathrm{erfc}\ \ 1\ \ \frac{\sqrt{\frac{2}{2}}}{2}\ - \\
& {}^{-}_{2}\ \ \frac{}{}\ \mathrm{erf}\ \ 1\ \ \frac{\sqrt{\frac{2}{2}}}{2} \\
& {}^{-}_{2}\ {}^{\sim}_{1}\ \ {}_{1}\ \ \mathrm{erfc}\ \ 1\ \ \frac{\sqrt{\frac{2}{2}}}{2}\ - \\
& {}^{-}_{2}\ \ \frac{}{}\ \mathrm{erf}\ \ 1\ \ \frac{\sqrt{\frac{2}{2}}}{2}\ {}^{-}_{4}
\end{aligned}
\tag{2.125}
$$

For the integration over the tooth the spanwise and streamwise integrals are given by:

$$
\begin{aligned}
{}^{2}\mathbf{x} \quad & \frac{2}{4\ {}_{0}\ {}^{2}_{0}}\ {}^{-}_{2}\ {}_{0}\ {}_{1}\ {}^{1}\ {}^{4} \\
& {}^{-}_{2}\ {}^{\sim}_{1}\ {}_{1}\ \ {}^{4}_{4}\ \mathrm{erfc}\ \ 1\ \ \frac{\sqrt{\frac{2}{2}}}{2} \\
& {}^{-}_{2}\ {}^{\sim}_{1}\ \ {}_{1}\ \ {}^{4}_{4}\ \mathrm{erfc}\ \ 1\ \ \frac{\sqrt{\frac{2}{2}}}{2}
\end{aligned}
\tag{2.126}
$$

and

$$
\begin{aligned}
{}^{3}\mathbf{x} \quad & \frac{2}{4\ {}_{0}\ {}^{2}_{0}}\ {}^{-}_{2}\ {}_{0}\ {}_{1}\ {}^{1}\ {}^{4} \\
& {}^{-}_{2}\ {}^{\sim}_{1}\ {}_{1}\ \ {}^{4}_{4}\ \mathrm{erfc}\ \ 1\ \ \frac{\sqrt{\frac{2}{2}}}{2} \\
& {}^{-}_{2}\ {}^{\sim}_{1}\ \ {}_{1}\ \ {}^{4}_{4}\ \mathrm{erfc}\ \ 1\ \ \frac{\sqrt{\frac{2}{2}}}{2}
\end{aligned}
\tag{2.127}
$$

Notice that Eq. (2.126) and Eq. (2.127) have the same common streamwise integral, and it is of the same form of that in Eq. (2.125). The spanwise integrals are given by:

$$\frac{1}{4}\left(1+\right)^{4} \tag{2.128}$$

$$\frac{1}{3}\left(1+\right)^{3}\left(4\right) \tag{2.129}$$

Substituting these results and adding $^{2}\mathbf{x}$ and $^{3}\mathbf{x}$ gives:

$$\begin{aligned}
^{2}\mathbf{x} \quad ^{3}\mathbf{x} \quad & \frac{2}{4}\left(\frac{2}{0}\right)^{2}\left(\frac{1}{0}\right)^{2}\left(1+\right)^{4}\left(3\right)\left(4\right) \\
& \left(\frac{1}{2}\right)\left(\frac{1}{2}\right)\left(1\right)\left(\frac{2}{2}\right)\left(\frac{2}{2}\right) \\
& \left(\frac{1}{2}\right)\left(\frac{1}{2}\right)\left(1\right)\left(\frac{2}{2}\right)\left(\frac{2}{2}\right) \\
& \left(\frac{1}{2}\right)\left(\frac{1}{2}\right)\left(1\right)\left(\frac{2}{2}\right)\left(\frac{2}{2}\right)\left(\frac{1}{4}\right) \\
& \left(\frac{1}{2}\right)\left(\frac{1}{2}\right)\left(1\right)\left(\frac{2}{2}\right)\left(\frac{2}{2}\right)\left(\frac{1}{4}\right)
\end{aligned} \tag{2.130}$$

Using the definition of the Dirichlet kernel:

$$\frac{\sin\left(2\right)\left(1\right)\left(2\right)}{\sin\left(2\right)} \tag{2.131}$$

gives:

$$\frac{\sin\left(\frac{2}{}\right)}{\sin\left(\frac{}{2}\right)}\quad\frac{\sin\left(\frac{2}{}\right)}{\sin\left(\frac{}{3}\frac{2}{}\right)}\quad\frac{1}{1}\frac{\sin\left(\frac{2}{}\right)}{\sin\left(\frac{}{3}\frac{2}{}\right)} \tag{2.132}$$

And upon substitution:

$$\begin{aligned}
&{}^{2}\mathbf{x}\quad{}^{3}\mathbf{x}\quad\frac{2}{4\ {}_{0}\frac{2}{0}}\ \overline{2}\ {}_{0}\ {}_{1}\\
&\frac{1}{}\ 1\quad{}_{4}\quad{}_{3}\quad{}_{4}\quad\frac{\sin\left(\frac{2}{}\right)}{\sin\left(\frac{}{0}\frac{2}{}\right)}\\
&\overline{2}\ \tilde{}_{1}\ 1\quad\operatorname{erfc}\left(1\quad\frac{2}{2}\right)\quad-\\
&\overline{2}\quad\operatorname{erf}\left(1\quad\frac{2}{2}\right)\\
&\overline{2}\ \tilde{}_{1}\ 1\quad\operatorname{erfc}\left(1\quad\frac{2}{2}\right)\quad-\\
&\overline{2}\quad\operatorname{erf}\left(1\quad\frac{2}{2}\right)\quad\overline{4}\\
&\qquad\qquad\qquad\qquad\qquad\qquad\qquad\qquad\qquad\qquad\overline{4}
\end{aligned} \tag{2.133}$$

While Eq. (2.115) and Eq. (2.133) are for the odd modes, 2 1, the same results can be used for the zeroth mode, 0, by changing the sign from negative to positive in the third main term. To obtain a closed form solution for the far-field acoustic pressure PSD, the infinite span (or large aspect ratio) assumption is used:

$$\lim\quad\frac{\sin\left(\frac{2}{}\right)}{\sin\left(\frac{}{0}\frac{2}{}\right)}^{2}\quad 2\qquad{}_{3}\quad\frac{3}{0}\quad 2 \tag{2.134}$$

where, , is the Dirac delta function. Then, by following the same statistical considerations as in Amiet's model (Sec. 2.3.4) results in:

$$\mathbf{x} \qquad \frac{2}{4 \quad 0 \quad \frac{2}{0}} \quad 2 \qquad \mathcal{L} \quad — \quad \frac{3}{0} \quad 2 \qquad 0 \qquad \frac{3}{0} \quad 2 \qquad (2.135)$$

where, , is odd or zero and $\mathcal{L}$ — $\frac{3}{0}$ 2 comes from the evaluation of the integration limits in Eq. (2.125) and Eq. (2.133) for the plate and the teeth respectively. Note that in the limit of zero serration amplitude (2 0), the teeth contribution to the far-field (Eq. (2.133)) is zero and the plate radiation integral (Eq. (2.125)) reduces to the radiation integral in Amiet's model (Eq.(2.50)).

3D square wave model ——————————————————————- Summary

- The new square wave model is found by evaluation of surface pressure distribution from Ayton's original model.
- The surface pressure is evaluated by using the Schwarzschild solution.
- The far-field radiation proceeds by using Curle's analogy.
- The new model agrees with Amiet's model in the limit of zero serration amplitude.

2.6 Conclusion

The mathematical formulae required to predict trailing edge noise from straight and serrated airfoils was derived in this Chapter. Assumptions and limitations were presented. Amiet's model is generally valid over the whole frequency range by using the back-scattering correction and for all observer positions, but it is limited to straight edges. In contrast, Ayton's model and Li and Lee's extension are valid at high non-dimensional frequencies and at high observer angles. Santamaria's model for the square wave does not present the aforementioned limitations, but it is only valid for square wave serrations. The equations for the far-field acoustic pressure PSD for each discussed model are summarized in Figure 2.16. All models, require accurate single-point wall-pressure spectrum to give useful engineering results. The models are put into test with

validation from experimental data for airfoils in the next Chapter. Lastly, both models can be extended to rotating blades as will be shown in Chapter 4.

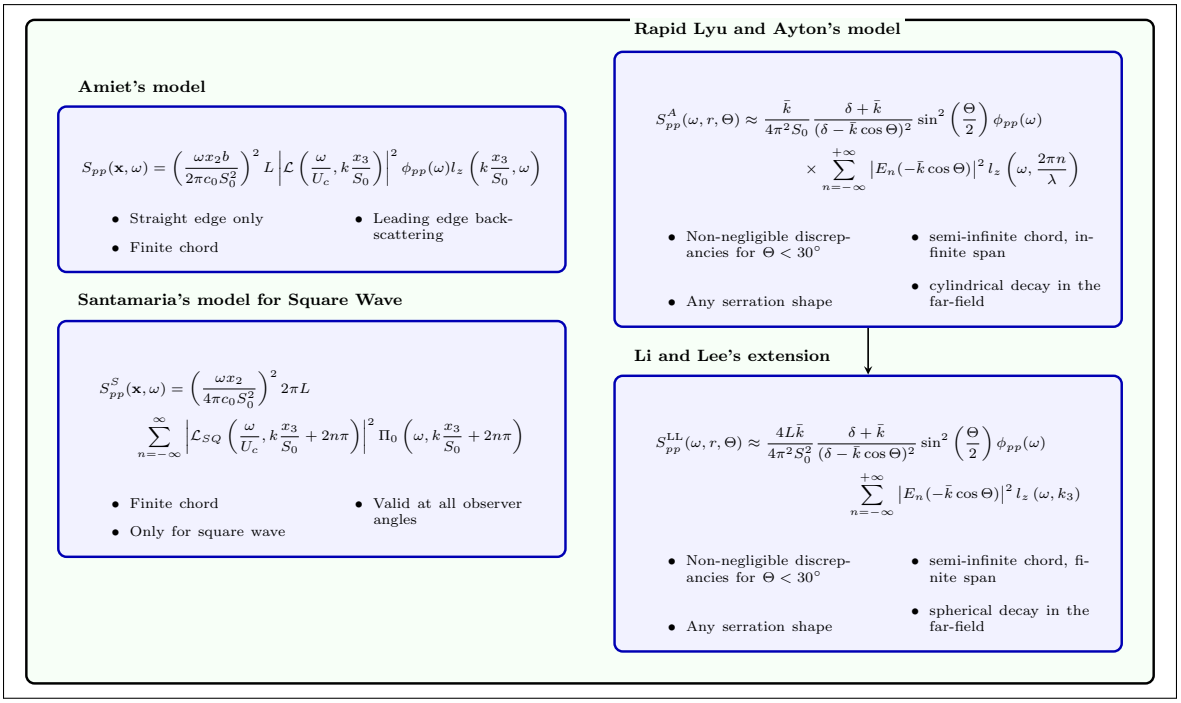

Figure 2.16 Summary of equations to calculate the far-field acoustic pressure PSD for straight and serrated edges

CHAPTER 3

SERRATED AIRFOIL NOISE REDUCTION:EXPERIMENTS AND PREDICTION

"... from so simple a beginning endless forms most beautiful and most wonderful have been, and are being, evolved"

— Charles Darwin

With the analytical tools at hand, this chapter presents some verification and validation examples of the straight and serrated edge models. Firstly, Li and Lee's extension of Ayton's model is compared in the limit of zero serration amplitude with Amiet's model. Then, noise reduction predictions are validated with measurements on a serrated controlled-diffusion airfoil, using the experimental wall-pressure spectra as input to the models. This is followed by a complete experimental campaign on a NACA0012 airfoil with Reynolds number and angle of attack representative of the NACA0012 propeller operating conditions. Two serrations geometries are evaluated, the conventional sawtooth, and the square wave, allowing thus verification and validation of the new square wave model. Comparisons between RANS-based predictions and experimental noise reductions are presented at the end of the Chapter.

3.1 Controlled-Diffusion airfoil

Controlled-Difussion (CD) airfoils are thin, highly cambered airfoils initially developed for compressor blades that have been the subject of extensive study during the past four decades by the turbomachinery community. As noted by Hobbs & Weingold (1984), CD airfoils were developed to control the momentum diffusion rate on the suction surface, in other words, to prevent boundary layer separation even at high incidences. Additionally, it was demonstrated by the same authors that blades with CD airfoils allowed transonic compressors to operate shock-free. The CD airfoil was again on the spotlight during the early 2000s (Moreau, Henner,

Iaccarino, Wang & Roger, 2003; Moreau & Roger, 2005) in the context of low-speed automotive engine cooling fans. More recently, high fidelity simulations have been done (Wang, Moreau, Iaccarino & Roger, 2009; Wu *et al.*, 2020), including a Lattice-Boltzmann method (LBM) with DNS resolution close to the wall on a CD airfoil with three-dimensional serrations by Sanjose *et al.* (2014). The vast database for the CD airfoil makes it ideal to validate trailing edge noise models.

Far-field acoustics, wall-pressure statistics, boundary layer, and wake profiles measurements were conducted at the anechoic wind tunnel at Université de Sherbrooke (Padois, Laffay, Idier & Moreau, 2015) and École Centrale de Lyon (Moreau & Roger, 2005) on the CD airfoil at angle of attack 8 and free stream velocity of 16 m/s. The airfoil has a chord of 0.135 m and a span of 0.3 m, with a Reynolds number based on the chord of 1 5 10^5. A modular mockup of the CD airfoil has been built to test different active and passive noise control techniques including: trailing edge serrations, a porous trailing edge and boundary layer suction (Moreau *et al.*, 2016). Noise reductions obtained using smooth three-dimensional sawtooth serrations of size 2 10 mm with an aspect ratio of 2 have been measured in the aforementioned flow conditions. Additionally, Moreau *et al.* (2019) compared the experimental noise spectra with the rapid Ayton's model finding a good agreement on the frequency range where the noise reductions occur. Figure 3.1(a) shows iso-countours of the swirling strength criterion superimposed on the divergence of the velocity field (representing density fluctuations) for the CD airfoil at 8 angle of attack from the DNS simulation of Wu *et al.* (2020). Figure 3.1(b) shows iso-contours of the $_2$-criterion colored by streamwise velocity from the simulation with serrations from Sanjose *et al.* (2014). Lastly, Figure 3.1(c) shows the serrated experimental mock-up used in Moreau *et al.* (2016).

Figure 3.2 compares experimental data from UdeS with: Amiet's model (including the back-scattering correction) given by Eq. (2.63), Ayton's rapid model given by Eq. (2.89), Li and Lee's extension given by Eq. (2.90), both in the limit of zero serration amplitude. The numerical predictions obtained from a Lattice-Boltzmann method simulation, with DNS resolution, coupled with the FW-H analogy (Sanjose *et al.*, 2014) are presented as well. In the present validation

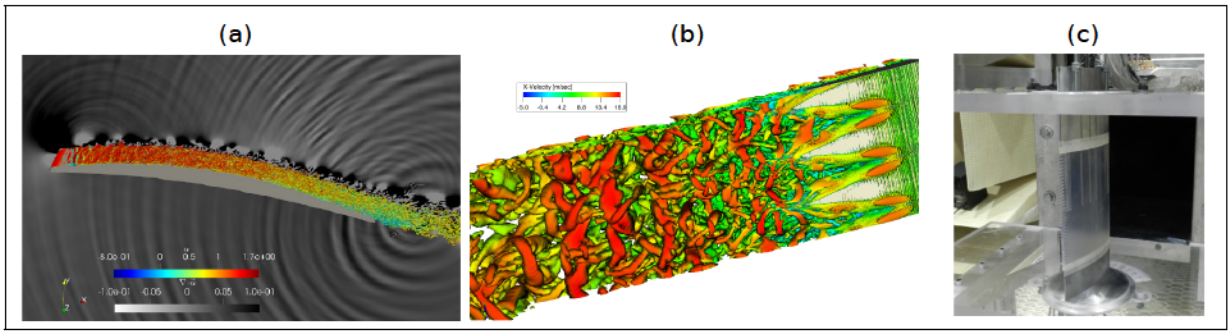

Figure 3.1 (a) Turbulent structures over the CD airfoil superimposed on the divergence of the velocities field. Taken from Wu *et al.* (2020) (b) Turbulent structures close to the trailing edge as seen from the pressure side. Taken from Sanjose *et al.* (2014) and (c) Serrated experimental mock-up. Taken from Moreau *et al.* (2016)

case, the measured wall-pressure statistics are directly used in analytical models. In Figure 3.2 (a), measured and predicted noise levels at 2 m from the trailing-edge in the $\Theta = 90°$ direction are shown for the baseline airfoil configuration with a straight trailing-edge. Figure 3.2 (b), shows the noise levels emitted by the airfoil with the serrated edge.

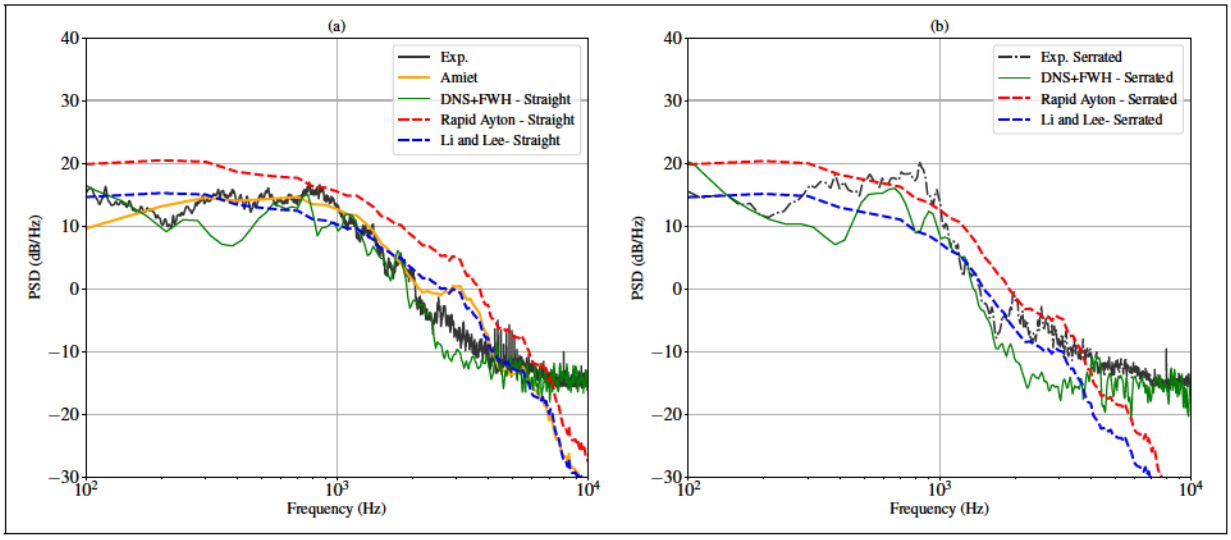

Figure 3.2 (a) Acoustic pressure PSD for an observer at 2 m and 90° from the trailing edge for a straight edge airfoil and (b) SPL reduction with the use of serrations.

Li and Lee's model is seen to match Amiet's model at all but low frequencies, which is expected given the half-plane assumption involved in the original Ayton's model (Ayton, 2018). Moreover,

Li and Lee's model improves the agreement between the rapid Ayton's model and Amiet's model, as it automatically accounts for the finite span and the three-dimensional noise radiation. All analytical models follow the trends of the experimental data at mid to high frequencies. Only at high frequencies, does the experimental PSD at UdeS level out, as an additional wake noise source contributes to this frequency range (Wu *et al.*, 2020).

To better visualize the results, the noise reductions from the experiments, the simulations and from the models are presented in Figure 3.3. The noise reduction is defined as:

$$\Delta\text{SPL} = 10\log_{10}\left(\frac{S_{pp}^{\text{straight}}(\omega, r, \theta)}{S_{pp}^{\text{serrated}}(\omega, r, \theta)}\right) \tag{3.1}$$

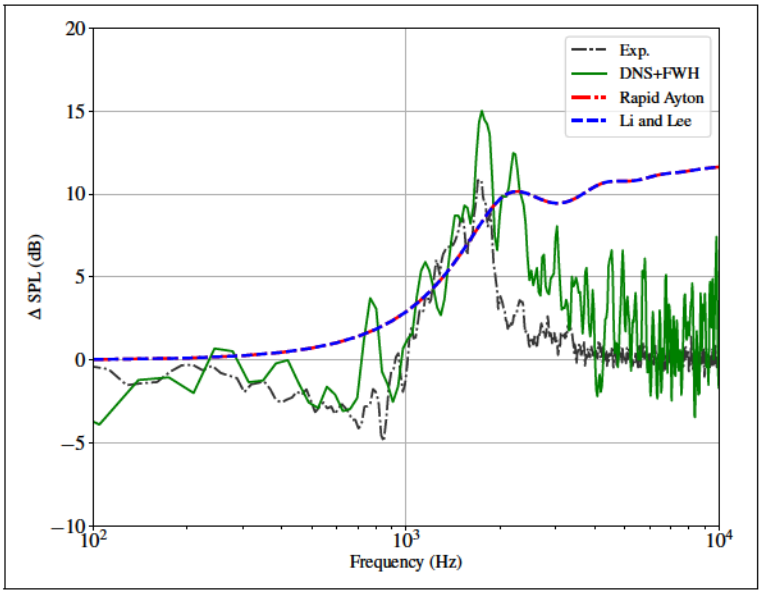

Figure 3.3 (a) Acoustic pressure PSD for an observer at 2 m and 90° from the trailing edge for a straight edge airfoil and (b) SPL reduction with the use of serrations.

Similar good trend of the noise reduction is observed for the serrated case. The difference seen beyond 4 kHz is again caused by the additional wake noise source. Li and Lee's model therefore provides excellent airfoil noise predictions for both straight and serrated cases at $\Theta = 90°$.

Figure 3.4 shows the directivity patterns for the CD airfoil using Amiet's model (Eq. (2.63)) and the Li and Lee's extension of Ayton's model (Eq. (2.90)) when the serration height, $2h$, approaches zero. The extended Ayton's model matches the well-known half-plane solution where finite chord effects are not included, and the source is acoustically compact as discussed in Sec. 2.1. Moreover, the patterns are in perfect agreement with the finite chord and half-plane patterns in Howe (2001) and Roger & Moreau (2005). Thus, it is expected that Li and Lee's model gives good predictions for observers at 90° from the trailing edge, and discrepancies are expected at other observer positions, particularly at low non-dimensional frequencies.

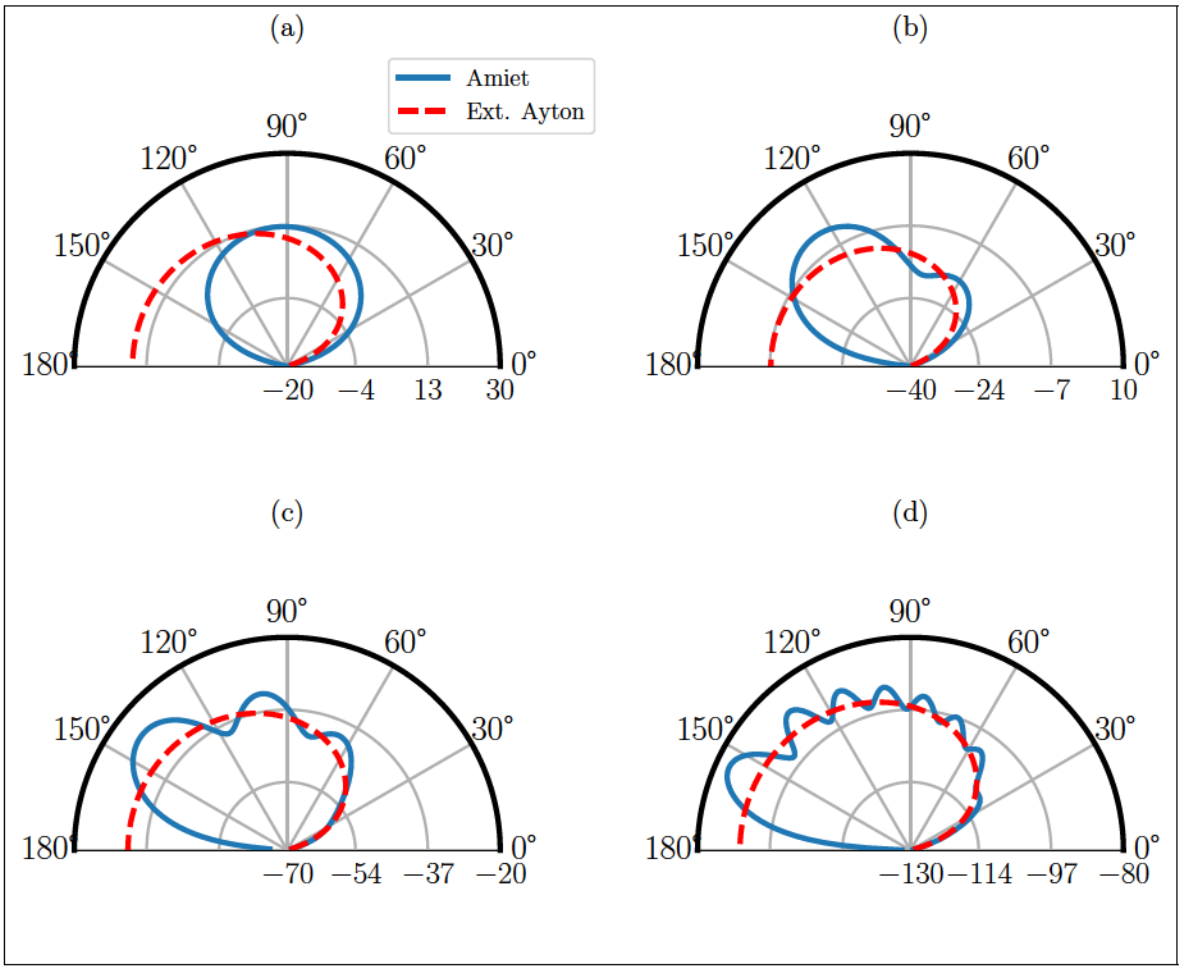

Figure 3.4 SPL directivity for the CD airfoil using Amiet's and the extended Ayton's models. (a) $kc = 1$,(b) $kc = 5$,(c) $kc = 10$ and (d) $kc = 25$. The flow is from left to right.

Airfoil trailing edge noise reduction with serrations——————————————Summary

- Noise reduction predictions are fairly well predicted by using an experimental wall-pressure spectrum.
- The frequency range where noise reductions occur is captured in the model, however it predicts constant noise reductions at high frequencies, which are not observed experimentally.
- Li and Lee's model predicted directivity pattern correspond to those of a half-plane scattering.

3.2 Trailing edge noise measurements on a NACA0012 airfoil with serrations

Since the main subject of study in this thesis is a propeller based on the NACA0012 airfoil, an experimental campaign was conducted at the anechoic open-jet wind tunnel at the Université de Sherbrooke on an airfoil based on the same profile. The objectives of the airfoil campaign were threefold. Firstly, to validate the findings in Chapter 2 for the square and sawtooth serrations, where potential benefits from the former were found. Secondly, to validate the new square wave model and compare with Li and Lee's predictions. Lastly, most experimental data for trailing edge noise have been recorded at moderate to high Reynolds numbers. Thus, aerodynamic and acoustic data for the Reynolds numbers where small propellers operate are scarce.

The anechoic room is the same one used for the CD airfoil measurements discussed in the previous section. The room dimensions are 7 5.5 4 m^3. The nozzle has an exit section of ( ) 30 50 cm^2 and operates in the velocity, , range between 5 and 50 m/s. The carbon fiber airfoil had a chord of 13 cm and a span, , of 30 cm with a blunt trailing edge of 1.57 mm. Pressure taps are installed along the mid-span for measuring the mean pressure. The taps were connected to two 16-port Scanivalve (DSA3217PTP) pressure scanners via plastic tubes. Detailed views of the installed airfoil at the exit of the nozzle are shown in Figure 3.5. The disks on the side plates allow modification of the airfoil geometric angle of attack in steps of 1 degree. For the far-field acoustic pressure measurements, six 1/2" PCB (378B02) microphones were located at the mid-span plane at a distance of 1.6 m from the trailing edge, as shown in Figure 3.6.

3.2.1 Test matrix

To select the wind tunnel free-stream velocity, , and the geometric angle of attack, , RANS simulations of the propeller in free-field conditions were used to match the airfoil chord-based Reynolds number. Since the velocity and angle of attack vary along the propeller span, data at 75% of the span were selected, as this is a common location to characterize propeller metrics. The details of the simulations are deferred to Chapter 4. From the RANS simulations, the

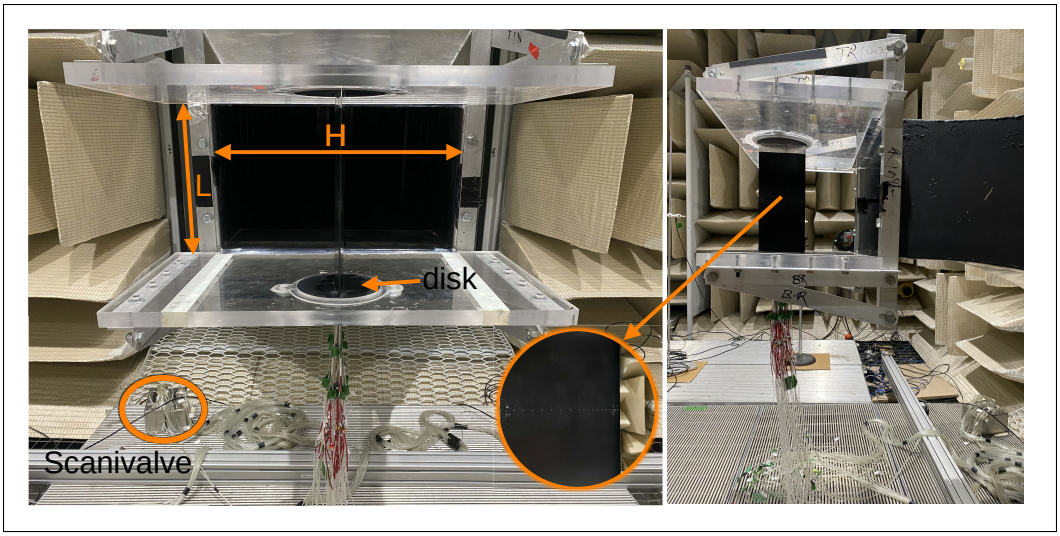

Figure 3.5 Wind tunnel nozzle and airfoil installed between side plates. (a) back view and (b) side view with detail showing pressure taps

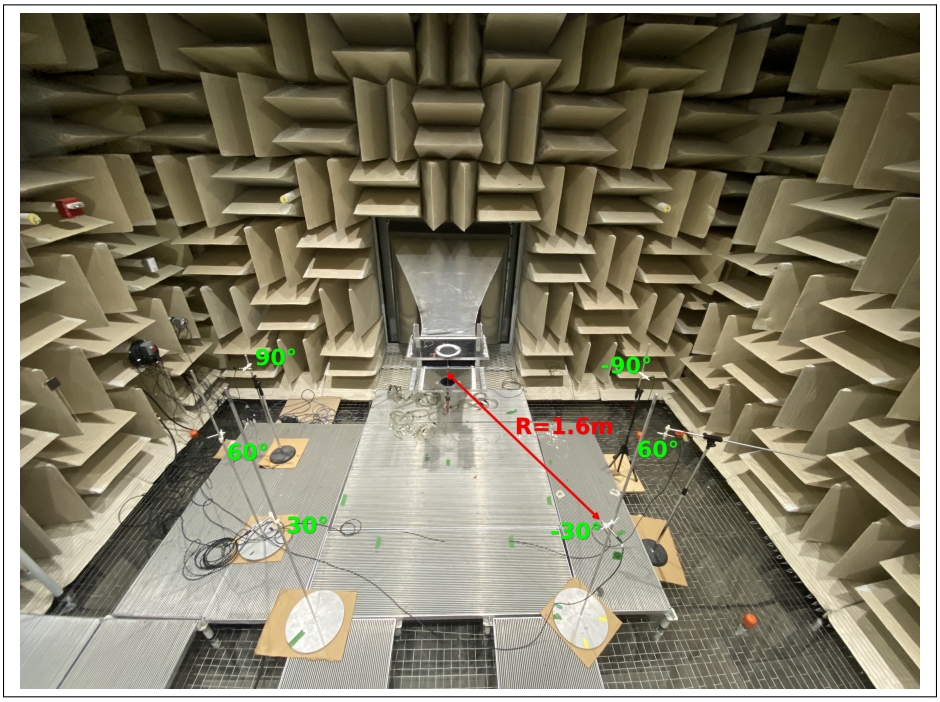

Figure 3.6 Experimental set-up at the anechoic wind tunnel with far-field microphones

relative velocity and effective angle of attack seen by the blade were estimated using a velocity triangle. Note that in hover conditions, the axial flow corresponds exclusively to the induced velocity generated by the propeller. The Reynolds number range corresponding to the RPM range from 4000 to 8000 is 66,000 to 132,000. The lowest Reynolds number corresponds to a wind tunnel velocity of 7.5 m/s and would not allow for the identification of trailing edge noise due to low noise levels. Therefore, the range was shifted and extended, resulting in the wind tunnel free-stream velocity range of 10 to 20 m/s. The effective angle of attack, $_{\text{eff}}$, in the RANS simulations varies between 2 and 5 degrees. The geometric angle of attack was calculated using the following wind tunnel correction by Brooks *et al.* (1989):

$$_{\text{eff}} \quad \frac{1 \quad 2 \quad ^{2} \quad \overline{12}}{\frac{^{2}}{48} \quad \frac{}{} \quad ^{2}} \tag{3.2}$$

where H is the tunnel width. The geometric angle of attack testing range was from 0 to 10 degrees, resulting in an effective angle of attack from 0 to 7 degrees. The Reynolds number range suggested that airfoil tonal noise due to transitional boundary layers might be present during the measurements, in line with the findings of Pröbsting *et al.* (2015). Thus, a means of forcing transition was needed to ensure a fully turbulent boundary layer at the trailing edge.

A 3D turbulator tape commonly used in gliders, and manufactured by Hansjorg-Streifeneder, was available in two thicknesses: 0.4 and 0.8 mm. The selection of the trip thickness is not trivial, as the goal is to force transition without excessively tripping the boundary layer and without significantly altering the airfoil loading. Therefore, the impact of the trip on aerodynamic performance was assessed by installing the tape on the suction side, the pressure side, or on both, with different thicknesses. The trip thicknesses were selected to be 0.4 mm and 0.8 mm on the suction and pressure sides, respectively. Details of the spectra under different tripping conditions can be found in Appendix III. The airfoil with the thickest trip is shown in Figure 3.7

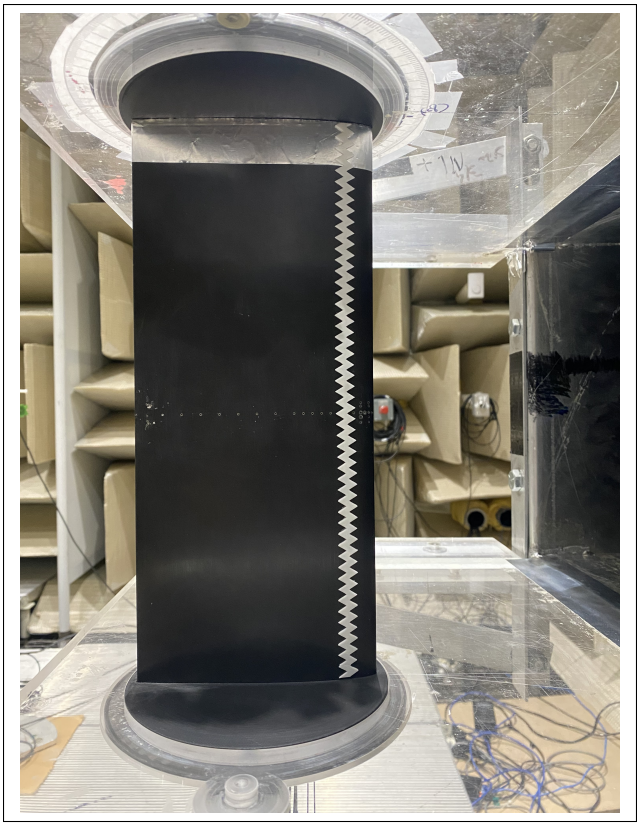

Figure 3.7 Airfoil pressure side
with 0.8 mm thick turbulator tape

To study the noise reduction due to trailing edge serrations, two serrated appendices were manufactured in acrylic (plexiglass) of the same thickness as the airfoil trailing edge. Based on the analysis from the previous chapter (Figure 2.14), the sawtooth and the square wave were selected as having the highest noise reduction potential at the low speeds tested. Following Gruber (2012), a trailing edge serration is effective when the serration amplitude is on the order of the boundary layer thickness (2). Therefore, the serration amplitude was determined from the boundary layer thickness extracted from 2D-RANS simulations at 10^5,representative of the propeller flow at around 6000 RPM, and set to 2 6mm. The serration wavelength was set to 3 mm following an optimal serration aspect ratio of 2 suggested by Kholodov & Moreau (2021). The serrations were secured to the airfoil trailing edge using double-sided tape, with

multiple runs showing no evidence of serration movement or detachment. Figure 3.8 shows the installed sawtooth and square wave serrations, the latter in the tripped configuration.

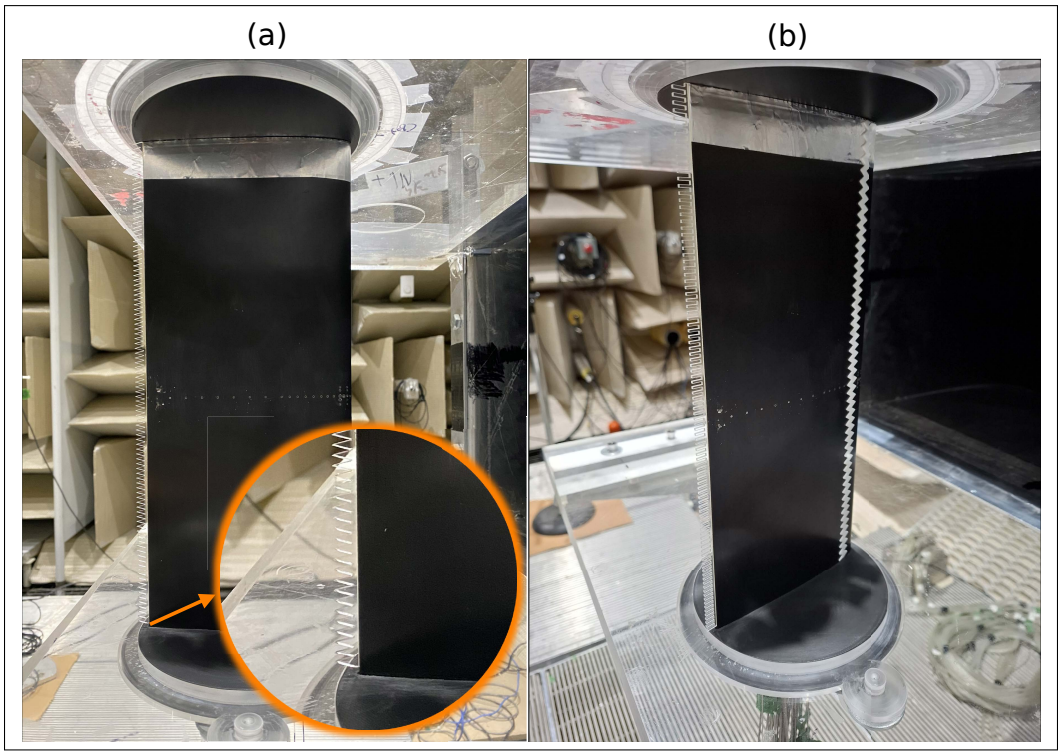

Figure 3.8 Trailing edge sawtooth serrations installed in the NACA0012 airfoil

Finally, the tests were run for the clean and tripped configurations with and without the serrations as summarized in Table 3.1

Table 3.1 Test matrix and designation for NACA0012 airfoil

Airfoil	**(m/s)**	**(deg.)**	**Designation**
Baseline	10,12,14,16,18,20	0,2,4,6,7,8,10	Baseline
Serrated-Sawtooth			Sawtooth
Serrated-Square Wave			Square
Baseline-tripped			Baseline(T)
Serrated-sawtooth-tripped			Sawtooth(T)
Serrated-square wave-tripped			Square(T)

Acoustic data sampling rate was 51.2 kHz and data were collected for 60 seconds. Whereas the mean pressure was sampled at 4 Hz for 25 seconds. Acoustic spectra were computed

using the Welch's periodogram method as implemented in the python library SciPy with a Blackman-Harris window. The windows size are optimally defined for the FFT algorithm to provide a 1 Hz resolution and include 10% of zero padding.

3.2.2 Results

The baseline results are discussed first. Figure 3.9 shows the spectra evolution with angle of attack for the 90-degree microphone. The anechoic room background noise is shown for reference. At all velocities, a wide hump at low frequencies is evident for angles of 0, 2, and 4 degrees. Humps of less amplitude appear at higher frequencies than the main hump for other angles of attack. For all humps, the amplitude and peak frequency increase with increasing velocity. Given the low-Reynolds-number conditions, these humps can be attributed to the scattering of large coherent structures at the trailing edge. As explained by Pröbsting & Yarusevych (2015) these structures are the result of the laminar-to-turbulent transition via a Laminar Separation Bubble (LSB) occurring on the suction, pressure, or both sides of the airfoil. LSBs often develop on airfoils operating at chord-based Reynolds number under 500,000 (Mueller & DeLaurier, 2003) as discussed in Sec. 1.1.4.

The humps observed in the baseline spectra are in line with the observations of Pröbsting *et al.* (2015) where at low angles of attack, and for Reynolds numbers below 10^5, it is expected that both the suction and pressure side boundary layers contribute to the humps in the spectra. The humps amplitude decreases with angle of attack with a noticeable change from 4 to 6 degrees at all Reynolds numbers. For the low-Reynold number investigated, it is expected that the LSB moves upstream as the angle of attack increases, thereby transitioning and reattaching as a TBL closer to the leading edge (Mueller & DeLaurier, 2003; Winslow *et al.*, 2018). Additionally, the background noise has no effect in the measured spectra. Lastly, note that the microphones reach their lower sensitivity threshold in all cases, and the signal is no longer detected for frequencies exceeding 5000 Hz in the highest speed case. Therefore, in the following results all the spectra shown will be limited to this frequency.

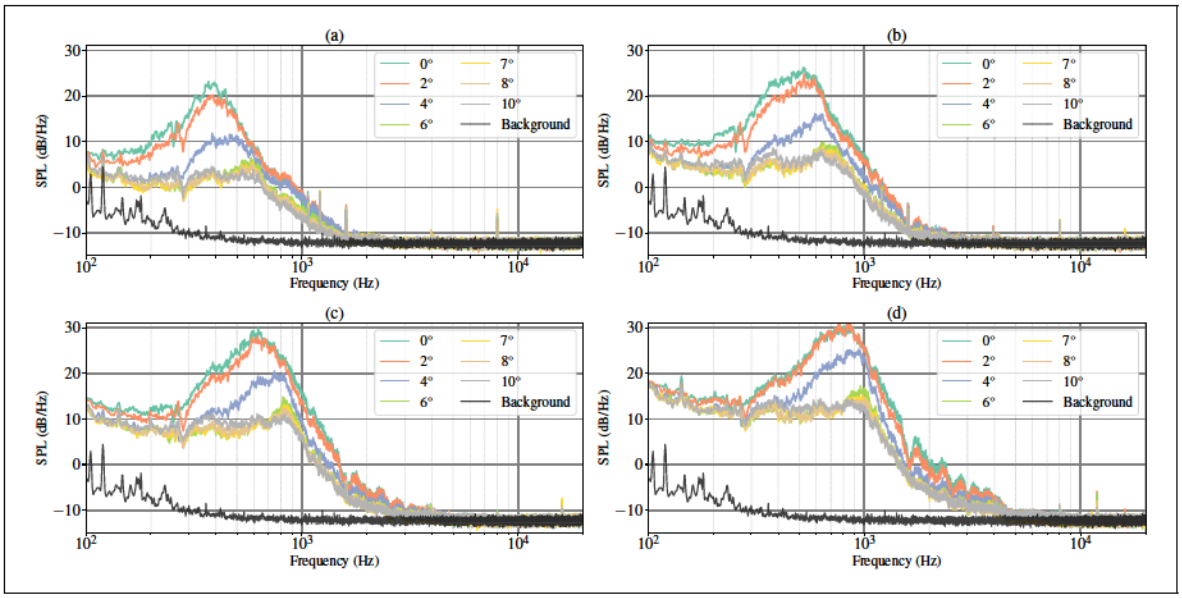

Figure 3.9 Baseline noise spectra for all angles of attack at (a) 10 m/s, (b) 12 m/s, (c) 16 m/s and (d) 20 m/s

A scaling of the humps frequencies with the free-stream velocity can be done to verify that the humps in the baseline spectra are due to laminar boundary layer instabilities. Thus, all the spectra are smoothed using a Savitzky & Golay (1964) filter, as implemented in the Python library SciPy. The application of the Savitzky-Golay filter with a window spanning 400 samples and a polynomial order of 2 allows to identify the hump peak frequency at all angles of attack for velocities between 10 and 16 m/s. At higher velocities, there is no clear identifiable peaks, therefore the 18 and 20 m/s spectra are not including in the scaling. The evolution of the humps peak frequency, f_{peak}, is shown in Figure 3.10 for all the angles of attack. Notice that the frequency depends on both the Reynolds number and the angle of attack, increasing with both parameters. The Figure also shows Paterson, Vogt, Fink & Munch (1973a) empirical scaling of the frequency with $V^{1.5}$. Good agreement with Patterson scaling is noted at the lowest angle of attack.

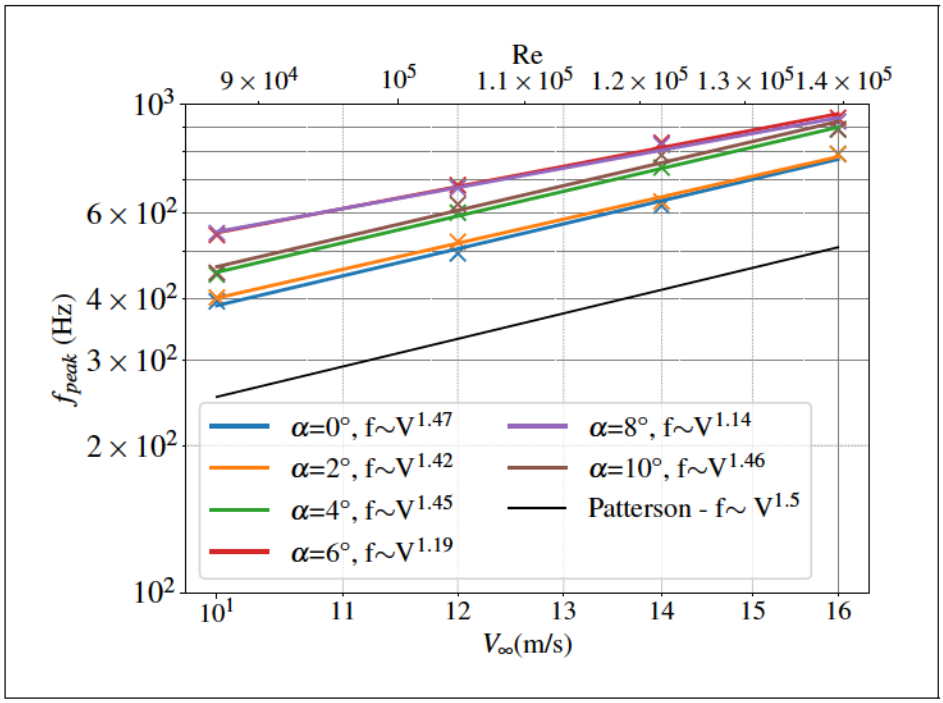

Figure 3.10 Evolution of the baseline humps peak frequency with velocity at different angles of attack

3.2.2.1 Effect of serrations

The effect of each serration shape on the far-field acoustics is shown in Figure 3.11 for α_g = 2 °, 6 ° and 10 ° and for velocities of 10, 16 and 20 m/s.

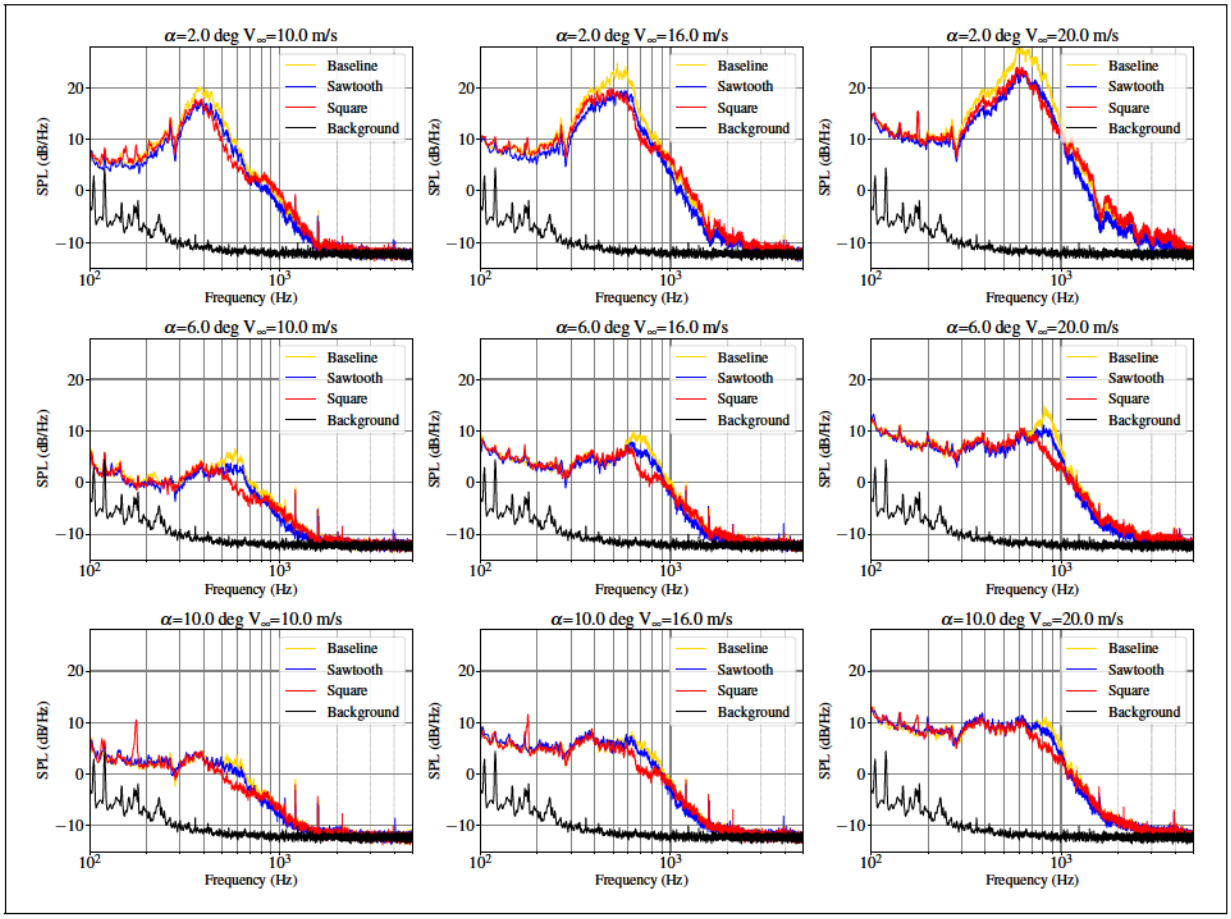

Figure 3.11 Comparison of baseline, sawtooth and square wave trailing edge noise at 90° for α_g = 2° (a)10 m/s, (b)16 m/s, (c)20 m/s, α_g = 6° (e)10 m/s, (f)16 m/s, (g)20 m/s and α_g = 10° (h)10 m/s, (i) 16 m/s, (j)20 m/s,

Overall, both the sawtooth and the square wave serrations are capable of reducing the main hump amplitude. The effect is evident at moderate angles of attack where the square wave serrations can give reductions of up to 10 dB. With increasing angle of attack, the serrations still reduce the noise but to a lesser degree. At large angles of attack, the main noise source is turbulent boundary layer trailing edge noise, which is expected as the LSB moves upstream and a TBL develops over most of the chord. Additionally, the square wave serrations give better

noise reductions at the hump-dominated part of the spectrum, while the sawtooth performs better at higher frequencies. Minor noise increase (2 dB) is observed for the square wave serrations at low angles of attack for all velocities at frequencies over 1 kHz.

Two ways in which the serrations may reduce the far-field noise due to the transitional boundary layers are hypothesized. Firstly, the presence of the serrations results in the large structures due to the transitional boundary layers decreasing their spanwise coherence. Secondly, the serrations act as a division between the flow fields from the pressure and suction sides, therefore weakening any potential coupling effect between both sides.

3.2.2.2 Effects of trip

While it has been demonstrated that the noise reduction capabilities of serrations are effective for transitional flows, the models presented in Chapter 2 assume fully turbulent boundary layers, and the noise due the scattering of small-scale structures at the trailing edge. Therefore, the second part of the results will focus on the cases where both airfoil sides were tripped. First, it is demonstrated that the trip can indeed eliminate the humps due to transitional boundary layers. The effect of the trip on the far-field acoustics is shown in Figure 3.12 for = 2 , 6 , and 10 and for velocities of 10, 16, and 20 m/s.

The trip effect is evident at low angles of attack and across all velocities. For = 2 , the trip trims the hump amplitude by about 20 dB and reduces noise beyond 1 kHz as well. For = 6 , the trip reduces the secondary hump amplitude by roughly 5 dB with minor noise increase past the hump frequency range. At the highest angle of attack, = 10 , the adverse pressure gradient has forced transition to turbulence on the clean airfoil suction side, resulting in very similar spectra for the clean and tripped configurations. A slight noise reduction is observed for the tripped configuration below specific velocity-dependent frequencies, and a slight noise increase occurs above these frequencies.

Recalling that trailing edge noise due to TBL scales with the fifth power of the flow velocity (Sec 2.1) it is possible to verify that indeed the trip has eliminated most of the noise from laminar

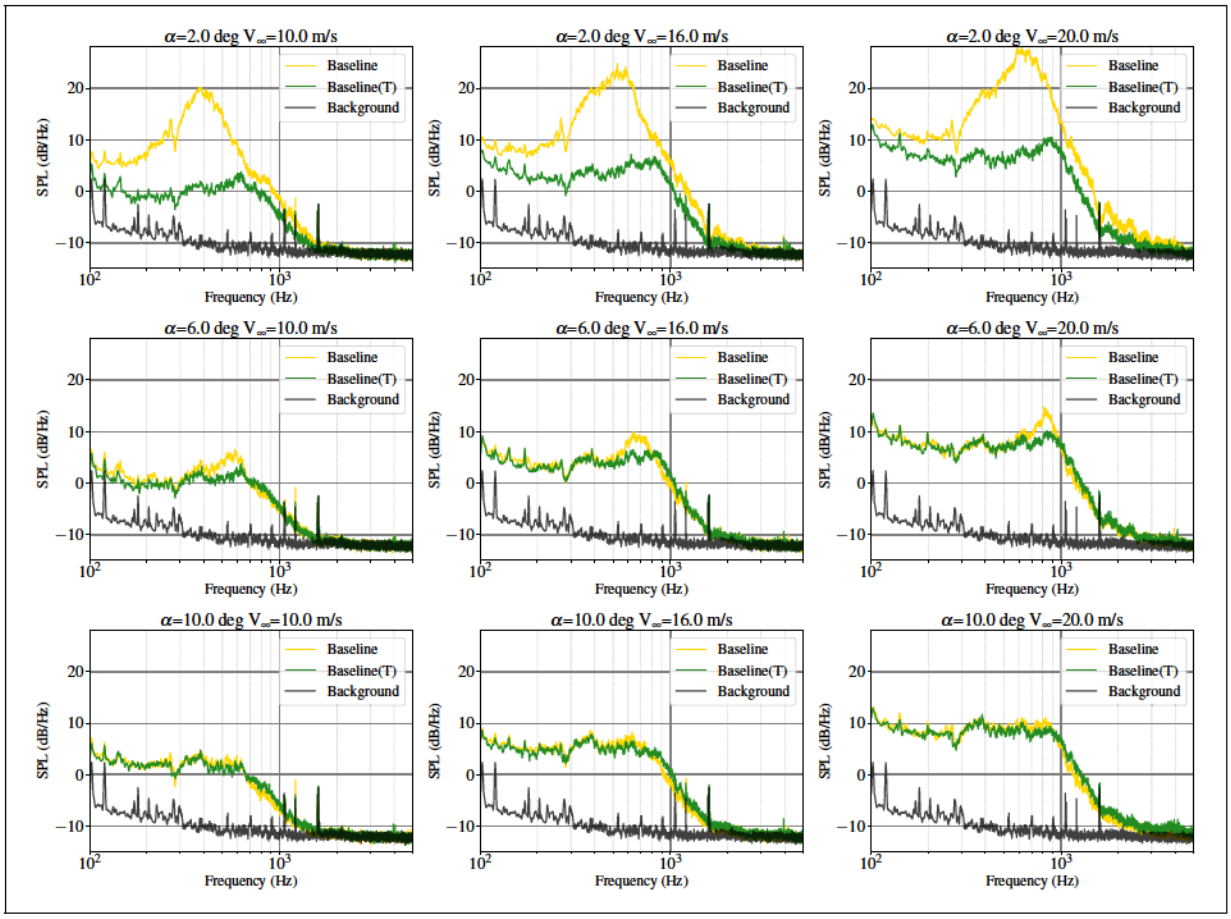

Figure 3.12 Comparison of baseline clean and with tripped trailing edge noise at 90° for $\alpha_g = 2°$ (a) 10 m/s, (b) 16 m/s, (c) 20 m/s, $\alpha_g = 6°$ (e) 10 m/s, (f) 16 m/s, (g)20 m/s and $\alpha_g = 10°$ (h) 10 m/s, (i) 16 m/s, (j) 20 m/s

boundary layer instabilities. Therefore, the tripped spectra are scaled to identify the regions where TBL trailing edge noise dominates. The scaling by the fifth power of the velocity is shown in Figure 3.13 for the lowest and highest angles of attack. It is noted that the spectra do not collapse for frequencies between 100 and 200 Hz, since this noise is due to the jet noise ($\approx V^7$) coming from the nozzle. For frequencies between 200 and 1000 Hz, the spectra collapses, particularly for the velocities between 14 and 20 m/s. Beyond 1500 Hz the spectra does not collapse and serves as an indicator that TBL trailing edge noise is no longer detected.

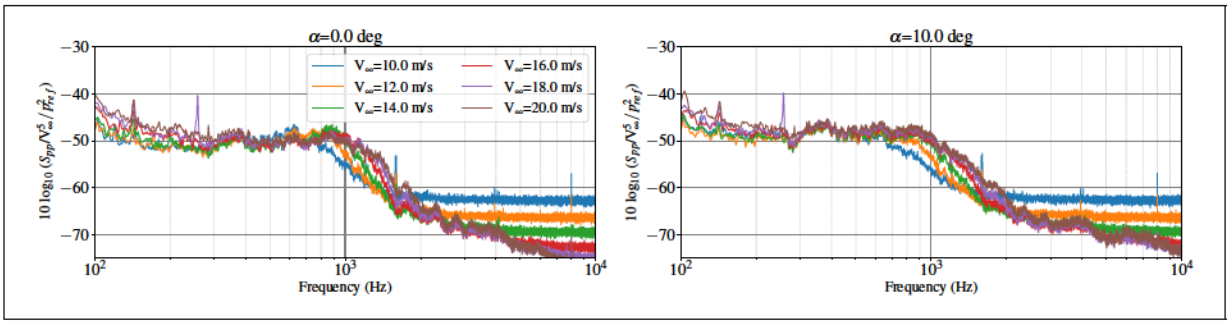

Figure 3.13 Scaling of spectra with the fifth power of the velocity for geometric angles of attack of 0 and 10 degrees

3.2.2.3 Effect of trip and serrations

With the certainty that the noise coming from the trailing edge is now exclusively due to turbulent boundary layer scattering, Figure 3.14 compares the spectra of the tripped baseline with the sawtooth and square wave serrations under the same tripped conditions for α_g = 2 °, 6 ° and 10 ° for velocities of 10, 16, and 20 m/s. Noise reductions are visible for all flow conditions. Similar to the clean cases, the square wave gives higher noise reductions at low frequencies while at higher frequency the sawtooth performs slightly better. The square wave can yield up to 5 dB reduction at low angles of attack.

Notably, the serration performance does not degrade significantly with increasing velocity for the same angle of attack. Recalling that the serrations were sized based on simulations with a chord-based Reynolds number of 10^5, which corresponds with the tunnel velocity of 12 m/s, it was expected that for increasing Reynolds numbers, the boundary layer thicknesses would be smaller. Thus, the serrations would still be beneficial, as their root-to-tip amplitude is always larger than the boundary layer thickness. This effect is somewhat competing with the thickening of the boundary layer due to adverse pressure gradient if the angle of attack is also varying. From the design point of view, it might be adequate to size the serrations for the operating point with the largest expected boundary layer thickness.

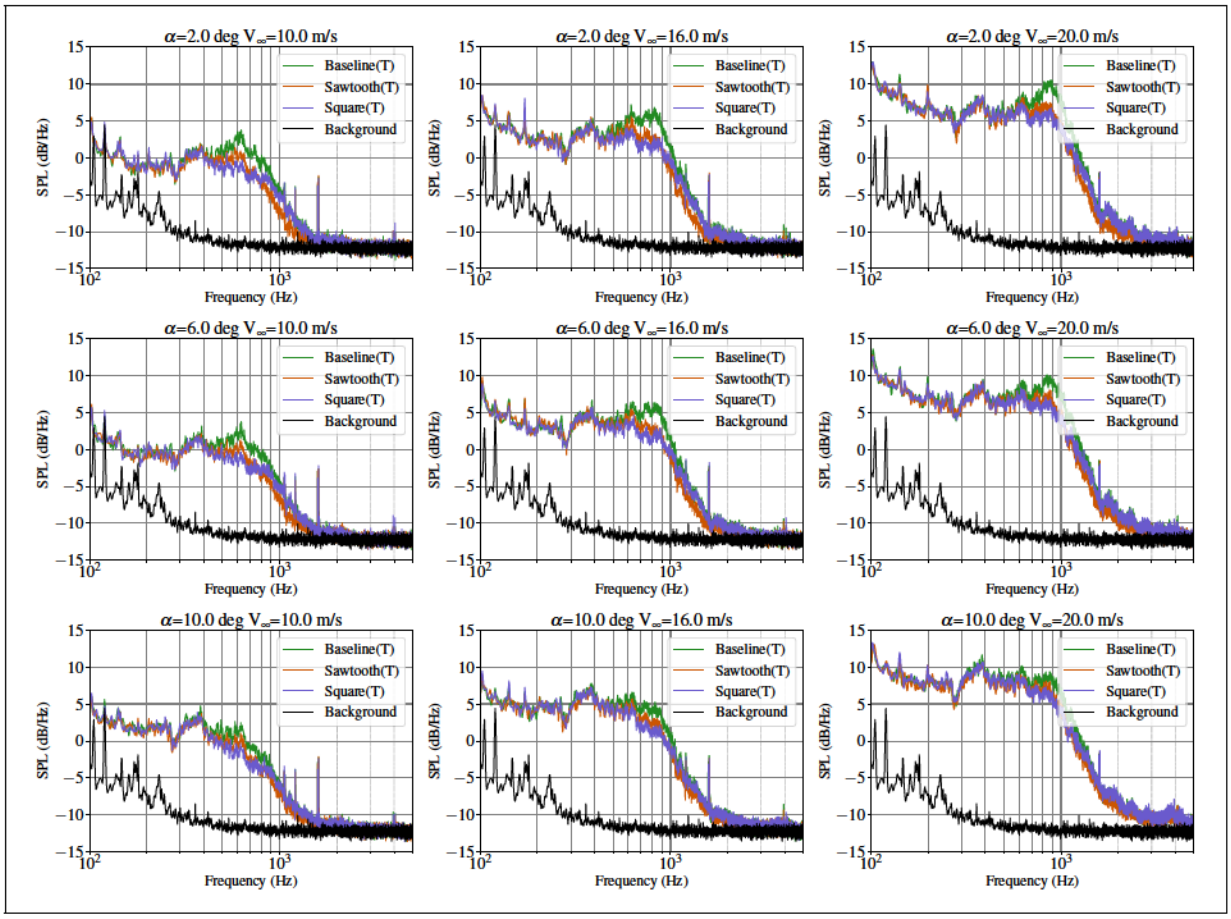

Figure 3.14 Comparison of baseline clean and with tripped trailing edge noise at 90° for α_g = 2° (a) 10 m/s, (b) 16 m/s, (c) 20 m/s, α_g = 6° (e) 10 m/s, (f) 16 m/s, (g)20 m/s and α_g = 10° (h) 10 m/s, (i) 16 m/s, (j)20 m/s

To conclude the experimental results section, it is worth verifying that the serrations are able to reduce trailing-edge noise at all microphone locations. This is shown in the Overall Sound Pressure Level (OASPL) directivity plots in Figure 3.15 for α_g = 2 °, 6 °, and 10 ° and for velocities of 10, 16, and 20 m/s . The OASPL is obtained by integrating each spectrum from 100 Hz to 5000 Hz. The lower limit corresponding to the anechoic room cut-off condition and the upper limit to the microphone lowest sensitivity frequency at the highest velocity. Both the square wave and the sawtooth serrations reduce noise for most operating conditions at all observer angles, with the former performing better than the latter.

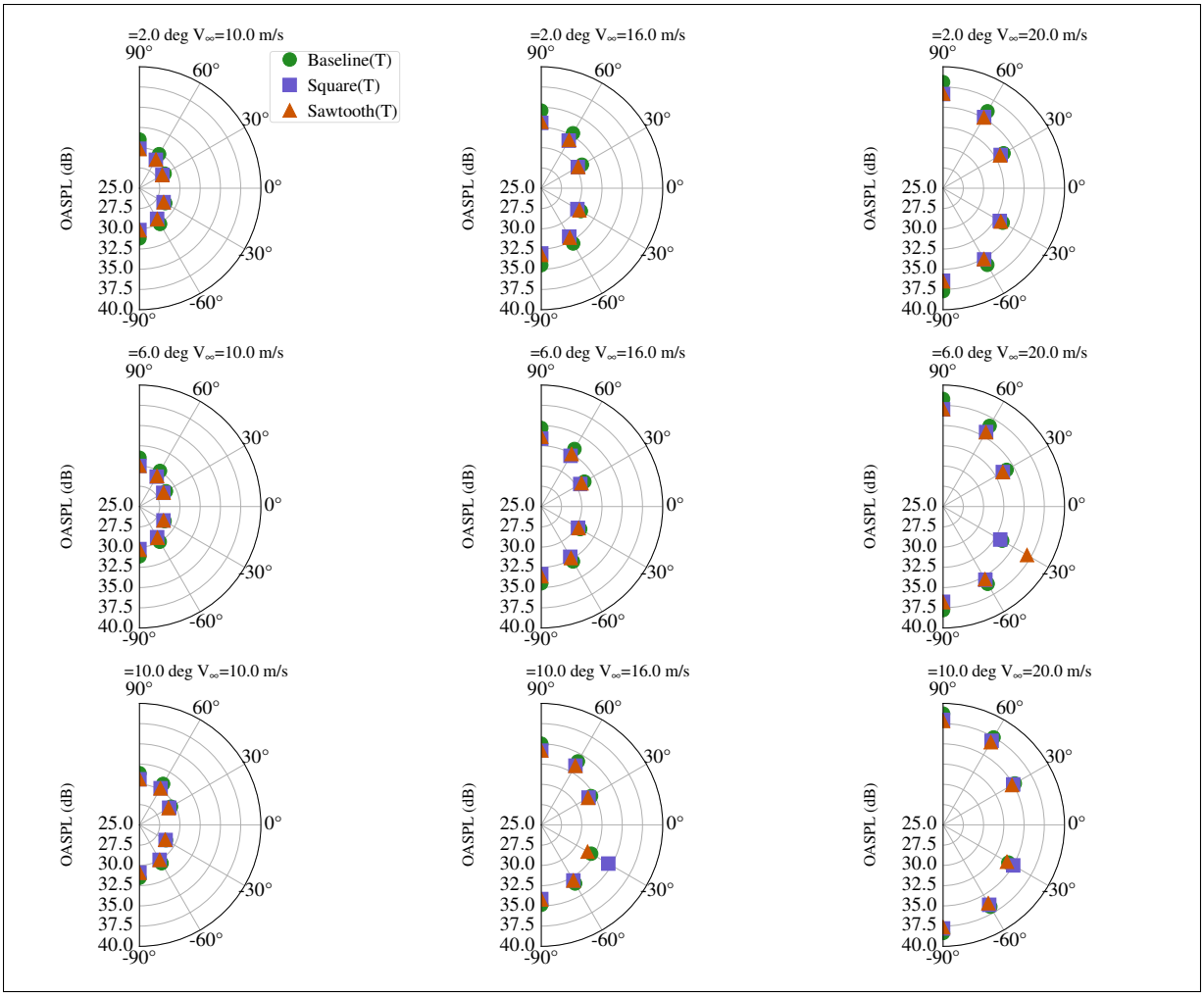

Figure 3.15 Comparison of baseline clean and with tripped trailing edge noise at 90 for = 2 (a)10 m/s, (b)16 m/s, (c)20 m/s, = 6 (e)10 m/s, (f)16 m/s, (g)20 m/s and = 10 (h)10 m/s, (i) 16 m/s, (j)20 m/s

Airfoil trailing edge noise reduction with serrations——————————————Summary

- Serrations are an effective way to mitigate trailing edge noise from both, transitional and fully-turbulent boundary layers.
- The square wave serration gives larger noise reductions at lower frequencies compared with the conventional sawtooth serration.
- For the tripped cases, TBL trailing edge noise dominates the spectra for frequencies between 200 and 1000 Hz.
- From the design point of view, it might be adequate to size the serrations for the operating point with the largest expected boundary layer thickness.

3.3 RANS-based trailing edge noise modeling

With the experimental results in hand, the next step is to apply the serrated models discussed in Chapter 2. The essential input of the models being the single-point wall-pressure spectrum upstream of the trailing edge. As discussed previously, RANS simulations are used to obtain the boundary layer information to model the spectra. Having the spectrum, the Li and Lee's extension of the rapid Lyu and Ayton's model is used to predict the noise due to the square wave and sawtooth serration. Additionally, the new square wave model is also compared with Li and Lee's model and the experimental data.

3.3.1 RANS simulations

The RANS simulations are performed in ANSYS-CFX using the k- SST model to compare with the experimental tripped cases. The domain is 3D, albeit with a small span, rendering the simulations effectively 2D with the use of periodic boundary conditions. The domain extends 10 chord lengths downstream from the trailing edge and 5 chord lengths upstream from the leading edge as shown in Figure 3.16. The hybrid mesh consists of prismatic layers close to the wall to capture the boundary layer evolution along the airfoil, whereas the rest of the domain consists of tetrahedral elements. A parametric study on the first layer thickness and the prismatic layer aspect ratio was performed to evaluate the impact of these parameters in the pressure and skin friction distributions. The parametric study and additional mesh details are presented in Appendix IV.

The effective angle of attack is calculated with Eq. (3.2) to recreate the wind tunnel conditions, and the same test matrix given in Table 3.1 is simulated for the tripped configurations. In all cases, the lift and drag coefficients are monitored to assess global convergence and the residuals fell below 10^{-6}. Starting with the aerodynamic results, the experimental pressure coefficient in the tripped configuration is compared with the RANS simulations for = 2 , 6 and 8 for the lowest and highest velocity in Figure 3.17

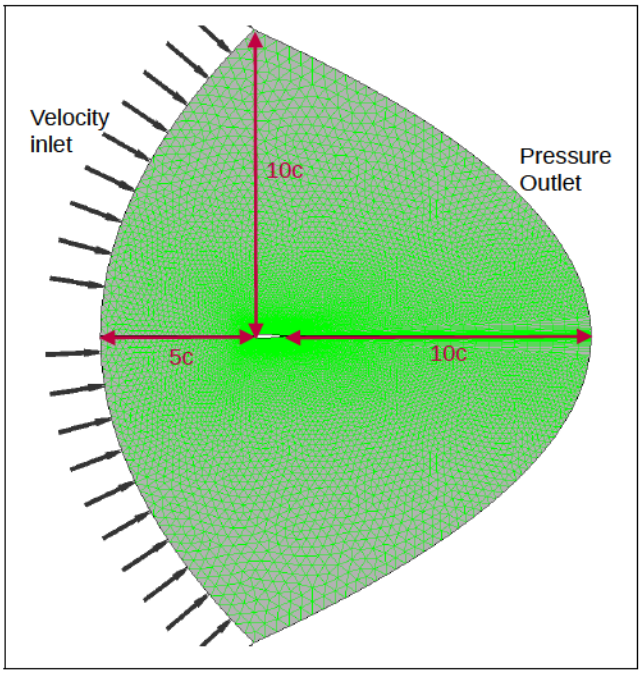

Figure 3.16 2D RANS simulation domain

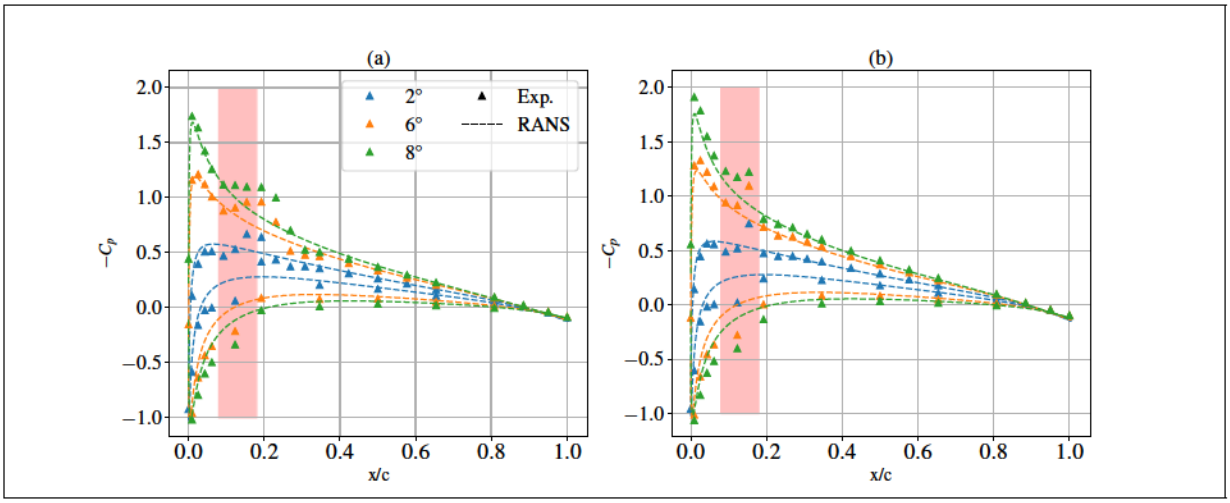

Figure 3.17 Experimental tripped and RANS computed pressure distribution with varying angle of attack at (a) 10 m/s and (b) 20 m/s. The red zone marks the area where the trip was installed

Firstly, note that the trip disturbs the pressure taps in its vicinity in both suction and pressure sides. This is shown by the red areas in Figure 3.17. The suction peak is captured at all angles

of attack for the lowest velocity and for all but 10 degrees for the highest one. Additionally, the pressure distribution is properly captured for the rest of the chord. The good agreement between the experimental and the RANS pressure coefficient, is a first-step to obtain trailing edge noise predictions for airfoils subjected to an adverse pressure gradient.

3.3.2 Trailing edge noise predictions

Following the RANS simulations, Python-based post-processing scripts were used to extract boundary-layer parameters for modeling the wall-pressure spectrum using Lee's model (Eq. 2.22). The required parameters are identical to those in Table 2.4. The extraction methodology follows that of Sanjosé & Moreau (2018) were the boundary layer parameters were extracted at 85% of the chord. A key value to extract is the boundary layer thickness, . Note, however, that this is not a straightforward process, as there are several difficulties in detecting the boundary-layer edge. For example, vorticity, turbulence kinetic energy, and total pressure all vary significantly within the boundary layer but attain constant values outside it, making them possible candidates for detecting the boundary layer edge. Additionally, consider that the non-uniformity of the mesh (particularly in 3D simulations, relevant to the propeller) makes it challenging to define a maximum along an extraction line (Sanjosé & Moreau, 2018). In summary, to detect the boundary layer edge, a Gaussian smoothing is applied to the extraction lines, and the first and second derivatives of the total pressure profiles are used to estimate .

Figure 3.18 shows the experimental and RANS-modeled far-field acoustics for angles of attack = 2 , 6 , and 10 and for velocities of 10, 16, and 20 m/s . The results are shown for an observer at 1.6 m for the 90 degree microphone using: Amiet's model, Eq. (2.63), Li and Lee's model, Eq. (2.90) and the new square wave model, Eq. (2.135), the latter two models evaluated at zero serration amplitude(2 0). Additionally, note that the boundary layers were extracted only on the suction side and equal radiation from the pressure side is assumed by including a factor of 2 in all the models.

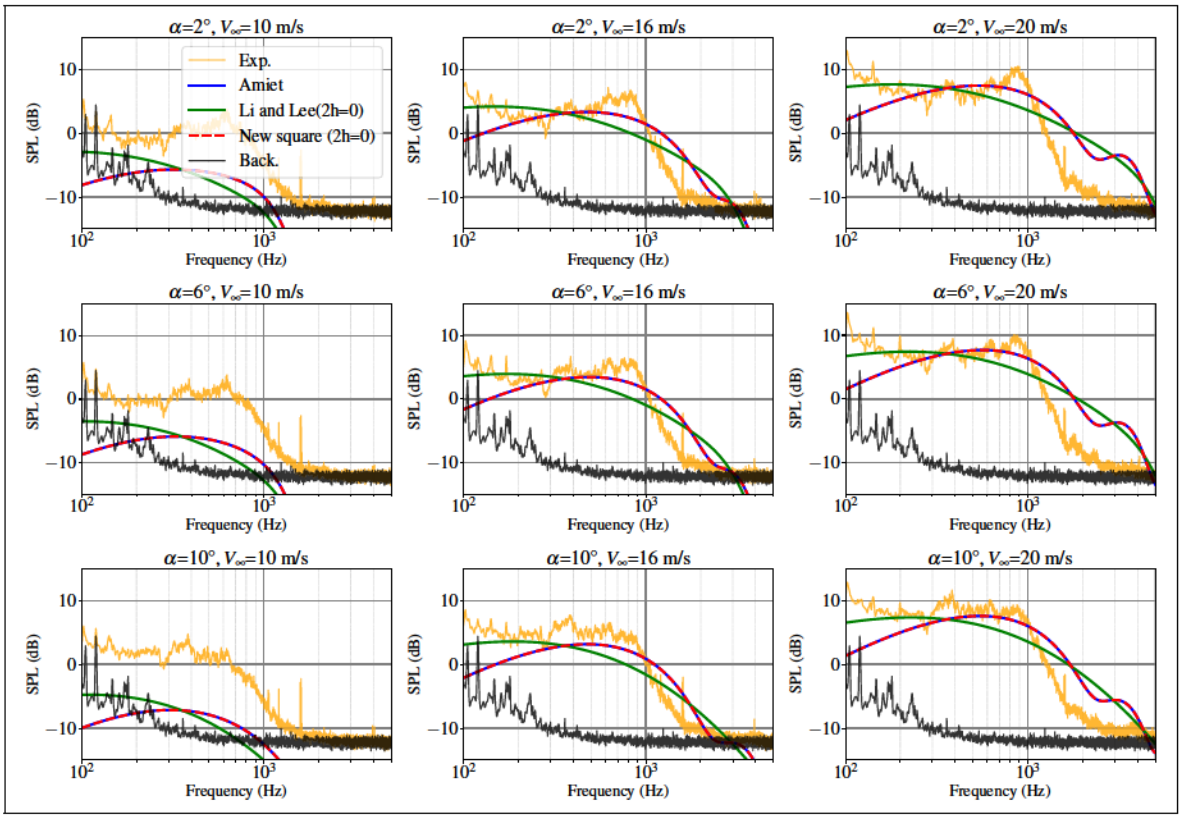

Figure 3.18 Experimental and RANS-modeled spectra for the tripped baseline at: α_g = 2° (a) 10 m/s, (b) 16 m/s, (c) 20 m/s, α_g = 6° (e) 10 m/s, (f) 16 m/s, (g) 20 m/s and α_g = 10° (h) 10 m/s, (i) 16 m/s, (j) 20 m/s

At the lowest speed, all models significantly underpredict the measured noise levels. This discrepancy can be partly attributed to the data used for calibrating the wall-pressure spectrum models, which are typically based on fully turbulent boundary layers at much higher Reynolds numbers. As the velocity increases, the agreement between predictions and experiments improves, and this trend is consistent across all angles of attack. Both Amiet's model and the new square-wave model yield nearly identical noise predictions, as expected from the findings in Chapter 2. Moreover, their results are in better agreement with the experimental data than those obtained using Li and Lee's model. At frequencies above 2000 Hz, none of the models can reproduce the trends of the experimental results. This limitation is attributed to the very low levels of trailing-edge noise in that range and is most likely linked to the wall-pressure model rather than to the acoustic models themselves.

The noise predictions for the tripped airfoil with square wave serrations are presented in Figure 3.19 for angles of attack α_g = 2 °, 6 °, and 10 ° and for velocities of 10, 16, and 20 m/s . The results are shown for an observer at 1.6 m for the 90 degree microphone using: Li and Lee's model, Eq. (2.90) and the new square wave model, Eq. (2.135). The two models evaluated with the serration amplitude of $2h$ = 6 mm.

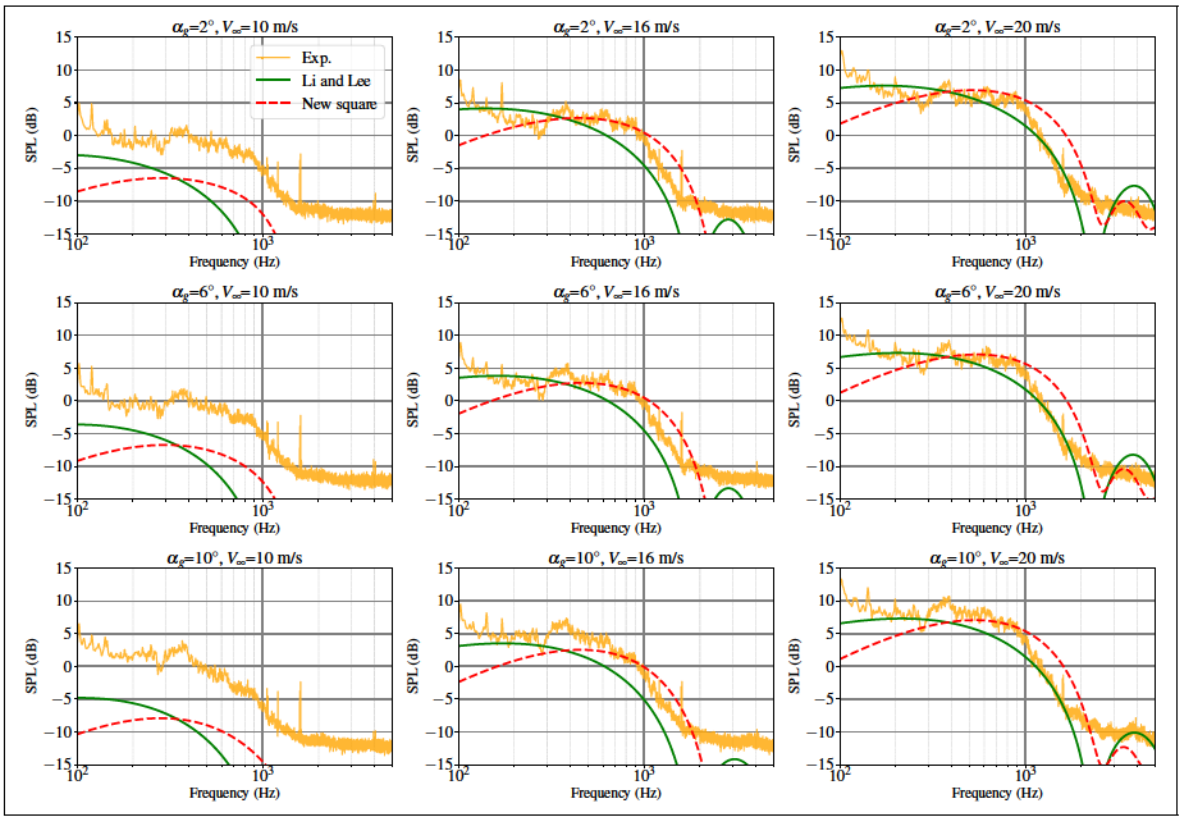

Figure 3.19 Experimental and RANS-modeled spectra for the tripped airfoil with square wave serrations at: α_g = 2° (a) 10 m/s, (b) 16 m/s, (c) 20 m/s, α_g = 6° (e) 10 m/s, (f) 16 m/s, (g) 20 m/s and α_g = 10° (h) 10 m/s, (i) 16 m/s, (j) 20 m/s

The same trends of the tripped baseline are found. This is expected, since the same wall-pressure fluctuations spectra model has been used for both straight and serrated edges. Notice that Li and Lee's model underpredict the noise levels at all operating conditions while the new square wave model overpredicts them. At the highest velocity, the latter model is in better agreement with the experimental data for frequencies below 1000 Hz, whereas Li and Lee's model agrees better

with the measured spectra at higher frequency. To improve the reliability of the new square wave model, further verification and validation cases are required.

To conclude this section on RANS-modeled predictions, a comparison between the experimental results and the noise predictions is made to assess Li and Lee's model capabilities to capture the differences in noise reduction due to serration shape. Figure 3.20 shows the noise reductions, calculated with Eq. (3.1), for the sawtooth and square wave serrrations for angles of attack α_g = 2 °, 6 °, and 10 ° and for velocities of 10, 16, and 20 m/s.

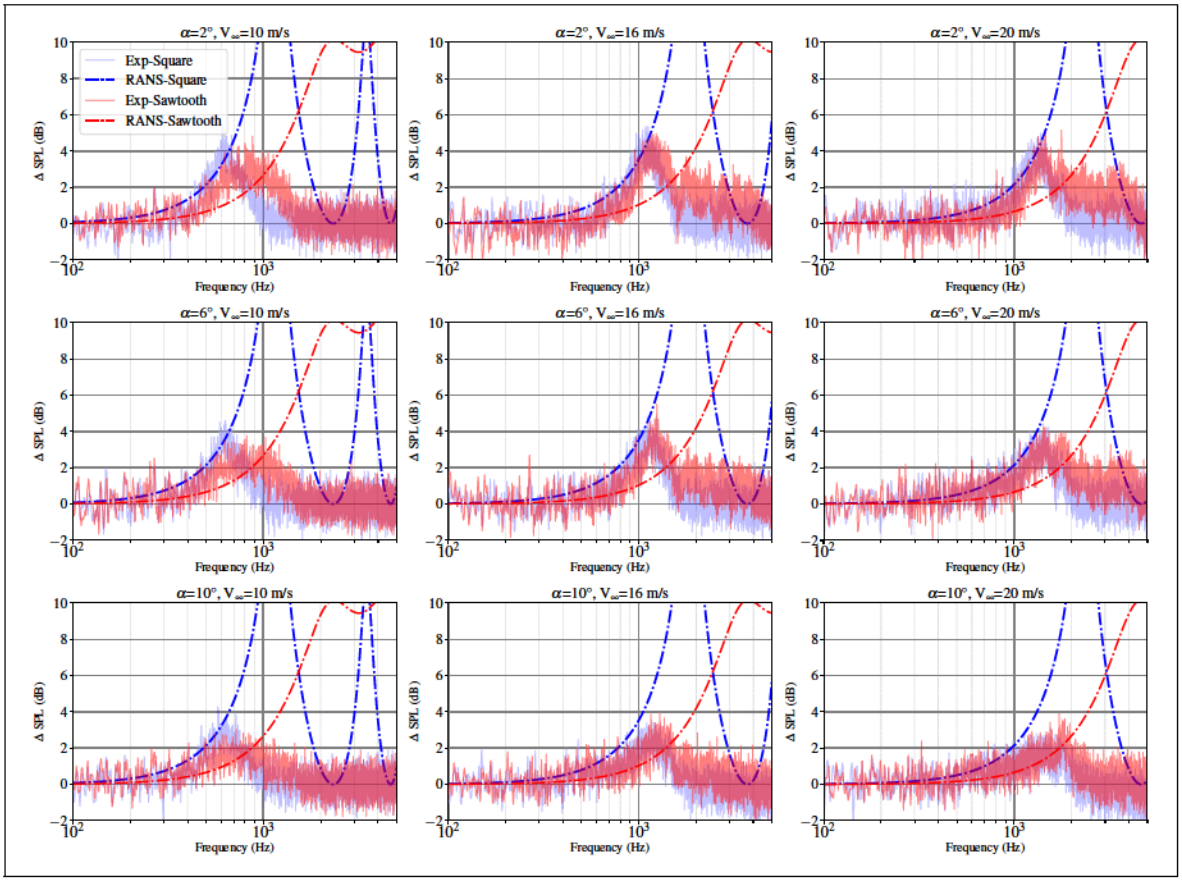

Figure 3.20 Experimental and RANS-modeled trailing edge noise reduction using Li and Lee's model at 90° for α_g = 2° (a)10 m/s, (b)16 m/s, (c)20 m/s, α_g = 6° (e)10 m/s, (f)16 m/s, (g)20 m/s and α_g = 10° (h)10 m/s, (i) 16 m/s, (j)20 m/s

Overall, Li and Lee's model captures the trend of noise reductions with increasing velocity. The modeled noise reductions are in good agreement with their experimental counterparts for both

serrations shapes. For the square wave noise reductions of up to 5 dB are noted at low speeds. Notice that the model is also able to capture the relative difference between the square wave and sawtooth serrations. For the experimental range where noise reductions are not observed, the model significantly overpredicts noise reductions. The oscillatory nature of the modal expansion coefficients for the square wave results in multiple peaks and troughs, whereas the sawtooth modeled noise reductions tend to stabilize at around 10 dB. The aforementioned behavior is in good agreement with the zeroth-mode expansion coefficient, $_0$, discussed in Sec 2.4.4. Therefore, the latter can be used for fast estimations of the frequency range of potential noise reductions.

RANS-based serrated airfoil noise predictions——————————————Summary

- Amiet's model and the new square wave model are in good agreement with the tripped baseline case, particularly at the highest velocities.
- The new square model and Li and Lee's model are better at predicting the serrated airfoil noise at low and high frequencies, respectively, with disagreements of up to 5 dB.
- Further validation is needed for the new square wave model.
- The noise reductions, SPL, calculated using Li and Lee's model, are in good agreement with the measurements for both sawtooth and square wave serrations.
- None of the models is able to capture the rapid decrease of TBL trailing edge noise for frequencies above 2000 Hz.

3.4 Conclusion

The models of Chapter 2 have been tested in the present Chapter for airfoils. Firstly, the noise reductions using a serrated Controlled-Diffusion airfoil were compared with experimental and numerical data using an experimental wall-pressure spectra. The results with Li and Lee's model are in fair agreement with the measurements. However, a directivity analysis showed that Li and Lee's model has a half-plane directivity and thus presents limitations at low dimensionless frequencies.

An experimental campaign on a NACA0012 airfoil was undertaken to further validate the models in the Reynolds number commonly found in drone propellers. The NACA0012 airfoil was adapted with trailing edge serrations and noise reductions were measured in the mid-span plane. Tripping was necessary to avoid transitional boundary layer noise. Square wave and sawtooth serrations were studied. The former was found to perform better at low frequencies and the latter at high frequencies, with a velocity-dependent cross-over frequency. Li and Lee's model and the new square wave model were compared with the measurements on the airfoil with square wave serrations. Each model performs better at different frequency ranges, with the new square wave model in better agreement for frequencies below 1000 Hz and the Li and Lee's model for higher frequencies.

Finally, Li and Lee's model is able to capture the trend of noise reductions due to different serration shapes. The model follows the noise reductions with velocity, and gives reasonable magnitude of them in the frequencies where they occur. However, outside this range, the model overpredicts the noise reductions. In the next Chapter, Li and Lee's model is extended to rotating blades and used to design serrations for the NACA0012 propeller.

CHAPTER 4

RANS-BASED DESIGN OF PROPELLERS WITH SERRATED TRAILING EDGES

"All models are wrong, some are useful"

— George Box

"If you want to find the secrets of the universe, think in terms of energy, frequency and vibration."

— Nikola Tesla

This chapter discusses how Schlinker & Amiet (1981) approximation for modeling rotating blades can be used in the context of serrated propeller blades, using Li and Lee's model. Rotating blade elements from a cooling fan and a wind turbine are used to verify Li and Lee's extension of Ayton's model in the limit of zero serration amplitude(2 0). A complete methodology to obtain the wall-pressure spectrum from RANS simulations is then presented. The RANS simulations are validated against the NACA0012 propeller experimental data with transitional and fully-turbulent modeling. Then, the effect of the serration shape is discussed for the NACA0012 propeller. General serration shape design considerations are given to conclude the chapter.

4.1 Propeller trailing edge noise

Schlinker & Amiet (1981) proposed a strip-theory-based method to use Amiet's results (Eq. (2.63)) for helicopter rotors, which was later successfully applied to low-speed fans (Roger, Moreau & Guedel (2006),Sanjosé & Moreau (2018)) and wind turbines (Tian & Cotté (2016)). Consider a blade strip (green segment) rotating in the XY plane as shown in Figure 4.1 at constant angular velocity . Note that flow direction is in the negative Z-direction.

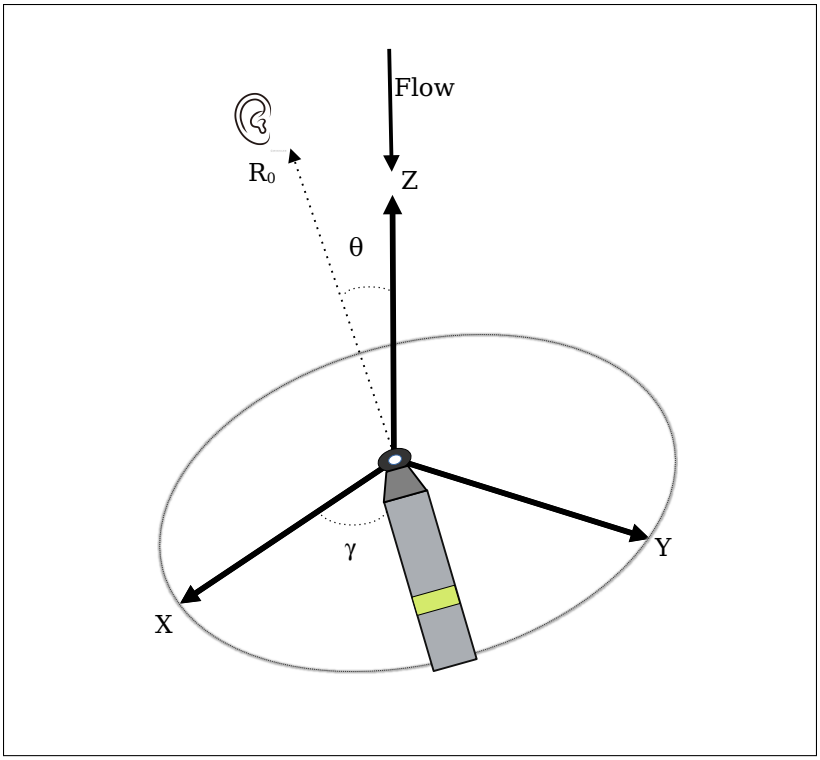

Figure 4.1 Propeller global coordinates

The blade strip moves in a local rectilinear motion, thus neglecting the acceleration effects due to rotation. Additionally, the rotor frequency is much smaller when compared to the turbulence characteristic frequency, and the noise is blade-to-blade uncorrelated. Sinayoko, Kingan & Agarwal (2013) derived a model for a blade segment in circular motion and investigated the effect of acceleration in the far-field sound. They demonstrated that it was negligible for low tip Mach numbers and found relatively small differences for high Mach numbers. Schlinker and Amiet proposed to use a blade segment far-field PSD and perform an azimuthal average over one revolution. Since there is a relative motion between the blade and the observer, the averaging is weighted by a Doppler factor, leading to the expression:

$$\text{rotor}\ \mathbf{R_o} \qquad \frac{}{2} \qquad {}_0^{\,0}{}^{\,2} \qquad \frac{}{} \qquad {}^{\,2}{}^{\,k}\ \mathbf{r_o} \qquad \mathrm{d} \qquad (4.1)$$

With the number of blades and the number of blade strips. The integration variable sweeps the angular shift of the observers over a whole revolution (0 2). The Doppler shift for a stationary rotor (e.g., a propeller in hover) is given by:

$$\frac{}{} \quad 1 \quad \frac{\sin \ \sin}{\overline{1 \quad \sin^{2}}} \tag{4.2}$$

Where and are the blade strip tangential and axial Mach number respectively, with and the polar and azimuthal angles determining the observer's position in the rotor frame of reference. The full blade rotor noise is obtained by adding the contributions of all blade segments calculated with either Amiet's model (Eq. (2.63)) or Li and Lee's model (Eq. (2.90)).

It must be noted that in the strip models, the sources are located at the trailing-edge. Therefore, Eq. (4.1) cannot be directly applied without a coordinate transformation that positions the source coordinates at the trailing edge of the considered blade segment. Several coordinate transformation operations are required to go from the global ( ) to the local (blade aligned) ( ). These transformations account for the geometry of the blade. The considered angles are, sweep ( ), pitch ( ) and lean ( ) as shown in Figure 4.2

The general form of a coordinate transformation, also called rotation, is given by:

$$\mathcal{M} \tag{4.3}$$

Where $\mathcal{M}$ is a rotation matrix that transforms the coordinate system ( ) into the system ( ). That is, from the fixed center of rotation to a moving system that is a function of the azimuthal angle . The rotation matrix is

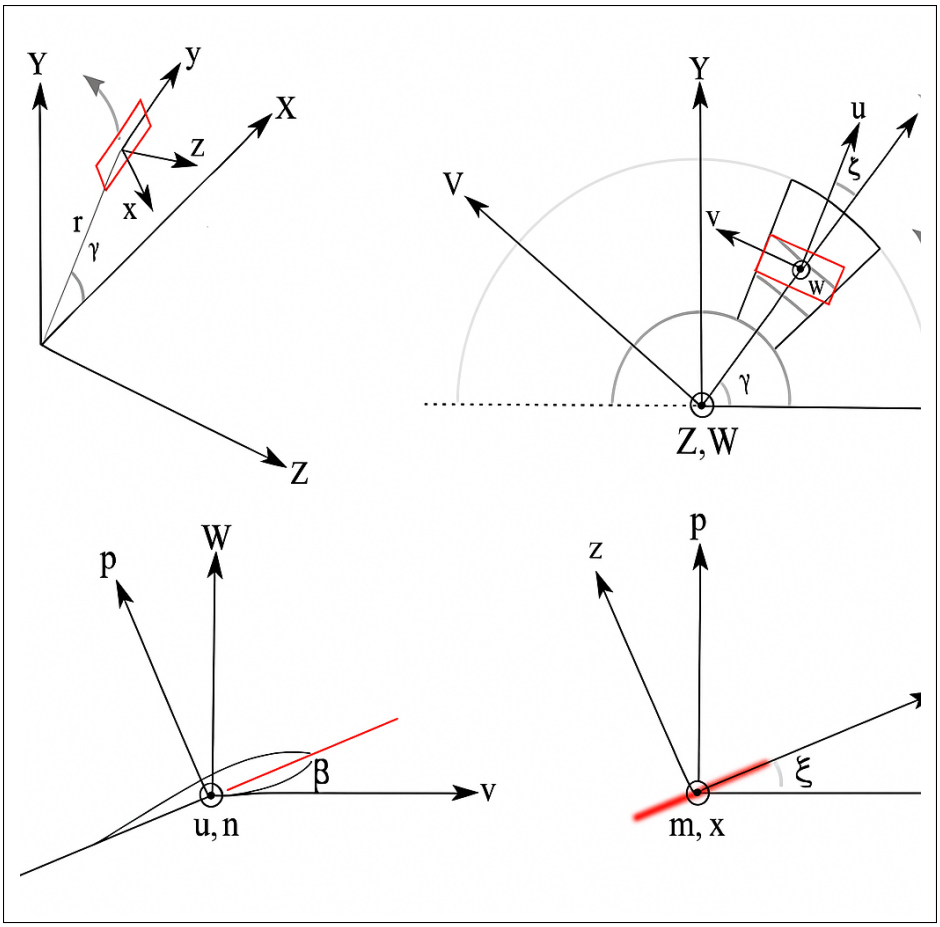

Figure 4.2 Rotation matrices to change from propeller (global) to strip (local) coordinates.
Taken from Kücükcoskun (2012)

$$\mathcal{M} \qquad \begin{matrix} \cos & \sin & 0 \\ \sin & \cos & 0 \\ 0 & 0 & 1 \end{matrix} \qquad (4.4)$$

The second rotation accounts for the sweep angle, , which is the deviation of the blade from the radial direction. The transformation is given by:

$$\mathcal{M} = \begin{matrix} \cos & \sin & 0 \\ \sin & \cos & 0 \\ 0 & 0 & 1 \end{matrix} \tag{4.5}$$

Next, to take into account the pitch angle, , measured with respect the rotor plane the transformation is and the associate rotation matrix is:

$$\mathcal{M} = \begin{matrix} 0 & \cos & \sin \\ 1 & 0 & 0 \\ 0 & \sin & \cos \end{matrix} \tag{4.6}$$

The minus sign appears since the streamwise component is defined from the blade strip center towards the trailing edge. Lastly, the lean angle is accounted by the transformation with the transformation matrix:

$$\mathcal{M} = \begin{matrix} 1 & 0 & 0 \\ 0 & \cos & \sin \\ 0 & \sin & \cos \end{matrix} \tag{4.7}$$

Now, the local coordinate system is aligned with the blade and thus Eq. (4.1) can be applied for a single blade strip. The present work approximates the integral in Eq. (4.1) numerically with the trapezoidal rule using 50 angular positions. The acoustic power radiated by the rotor can then be found by integrating Eq. (4.1) over a sphere $\mathcal{S}$ centered at the rotor hub center. In practice, a discrete number of observers is used. 360 observers are used in the meridional plane (XZ plane in Figure 4.1) and four observers in the azimuthal direction to obtain sufficient resolution without excessive computational time.

$$\mathcal{P} \quad \int_{\mathcal{S}} \frac{^{\text{rotor}}\ \mathbf{r_o}}{0\ \ 0}\, \mathrm{d} \tag{4.8}$$

with $_0$ $_0$ being the air impedance at rest. The sound power level (SWL) in dB is computed from $\mathcal{P}$ for a resolution of 1 Hz and with a reference power of $_{\text{ref}}$ 10^{-12} W:

$$\text{SWL} \quad 10 \log_{10} \frac{\mathcal{P}}{_{\text{ref}}} \tag{4.9}$$

The in-house turbomachinery noise code "PyFanNoise" was used in this Thesis to perform all the rotating blades calculations.

Schlinker and Amiet's blade trailing edge noise model ——————————-Summary

- Uses a strip-theory approach with each strip moving in rectilinear motion, thus neglecting the effect of source acceleration.
- It has been extensively validated in a variety of applications from Wind Turbines to automotive engine cooling fans.
- It can be used with any straight or serrated trailing edge model.

4.2 Verification of Li and Lee's model to rotating blades

Having established the directivity patterns of the extended Ayton's model for isolated blades in the previous chapter (Figure 3.4), this section presents results on the representative wind turbine and cooling fan blade elements, first presented by Blandeau & Joseph (2011) and later used by Sinayoko *et al.* (2013) and Tian & Lyu (2022) to verify Schlinker and Amiet's theory for rotating blades and for Lyu's serration model extension to rotating blades, respectively. The parameters of the blade elements are shown in Table 4.1. In both cases, Kim & George (1982) wall-pressure spectrum is used. The free stream-to-convection velocity ratio, , is assumed to be 1.25 and Corcos' constant, , 1.61 following Sinayoko *et al.* (2013).

Figure 4.3 shows the directivity results for the cooling fan and the wind turbine at a low and high Helmholtz number of, 0 5, and 50, respectively. The flow goes from right to left, so the rotational plane is at 90 . Firstly, it is noted that the implementation of Amiet's model is successful as the results are in good agreement with the directivity patterns in Sinayoko *et al.* (2013). Secondly, at high frequencies, it is clear that the extended Ayton's model matches

Table 4.1 Parameters of the blade elements

	Wind Turbine	Cooling Fan
	25 RPM	600 RPM
Span	7.25 m	0.1 m
Chord	2 m	0.13 m
Pitch	10	34
	7.5 10^6	1.8 10^5
	0.029	0.0354
	0.165	0.0525

Amiet's model for observers at high elevation angles from the rotational plane for both the cooling fan and the wind turbine, with the largest discrepancies occurring close to the rotational plane, as expected from the isolated airfoil directivity patterns from Figure3.4. In summary, it is expected that the extended Ayton's model will be valid for applications with sufficiently large chords (1), like wind turbines for all frequencies, whereas the validity for applications where the chord might be on the order of the acoustic wavelength (1) must be carefully assessed.

As discussed in Sec. 2.4.4, the modal expansion coefficients in Li and Lee's model govern the noise reduction capabilities of each serration shape. Given the behavior of zeroth-mode expansion coefficient (Figure 2.14), it is worth exploring how different shapes will perform for the representative cooling fan and wind turbine blade elements. Since detailed information on the boundary layer is not available for these cases, the largest serration amplitude considered is 20% of the chord to limit the impact on the aerodynamic performance. Figure. 4.4 shows the SPL reduction between straight edges and different serration shapes for the cooling fan and wind turbine elements. The serration amplitude-to-wavelength ratio (2) is fixed to 2, except for the cooling fan in Figure 4.4b where it is 2.5 to allow comparison with the results in Tian & Lyu (2022). For this case an observer at 45 is used, whereas for the other cases, the results are for an observer above the rotational plane (0) given the good agreement for straight edges in Figure 4.3 for both applications. The frequency range for the wind turbine is from 100 to 10000 Hz and from 1000 to 10000 Hz for the cooling fan.

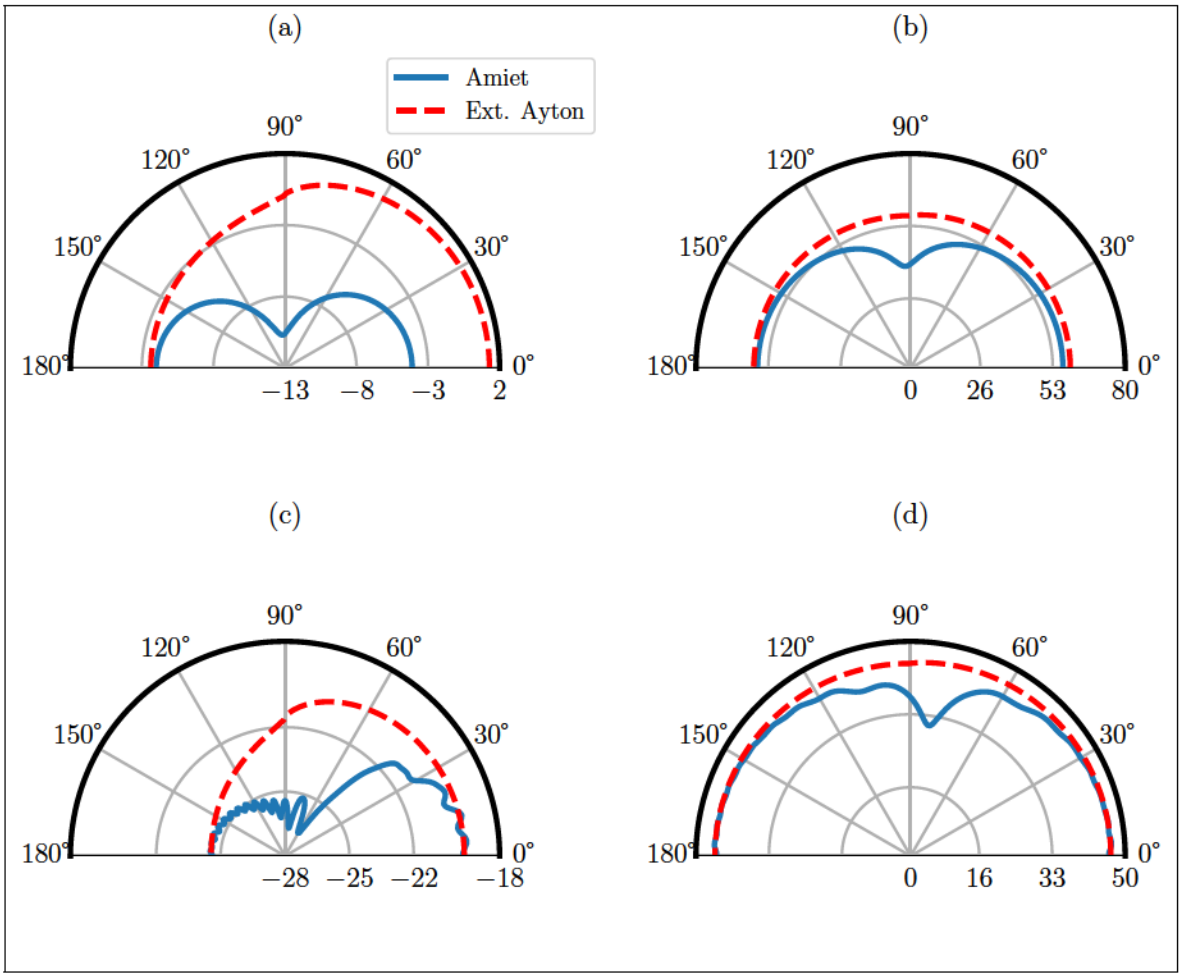

Figure 4.3 SPL directivities for blade elements using Amiet's and the extended Ayton's Model. (a) Cooling fan, $kc = 0.5$; (b) wind turbine, $kc = 0.5$; (c) cooling fan, $kc = 50$; and (d) cooling fan, $kc = 50$. The flow is from right to left.

It should be noted that the same conclusions from the zeroth-mode expansion coefficients in Figure 2.14 apply for all cases. The square wave, sinusoidal, and sawtooth shapes outperform each other in different frequency ranges, but for all cases the sawtooth provides more consistent noise reduction and dominates over the other shapes as the serration height increases. For the cooling fan with a serration height of 10% of the chord, it is noted that the sinusoidal and sawtooth serrations outperform each other in relatively close frequency ranges. Thus, it could be possible to use both shapes along the span to take advantage of their scattering properties. This arrangement will be investigated in the next sections. The large jump in the sawtooth case

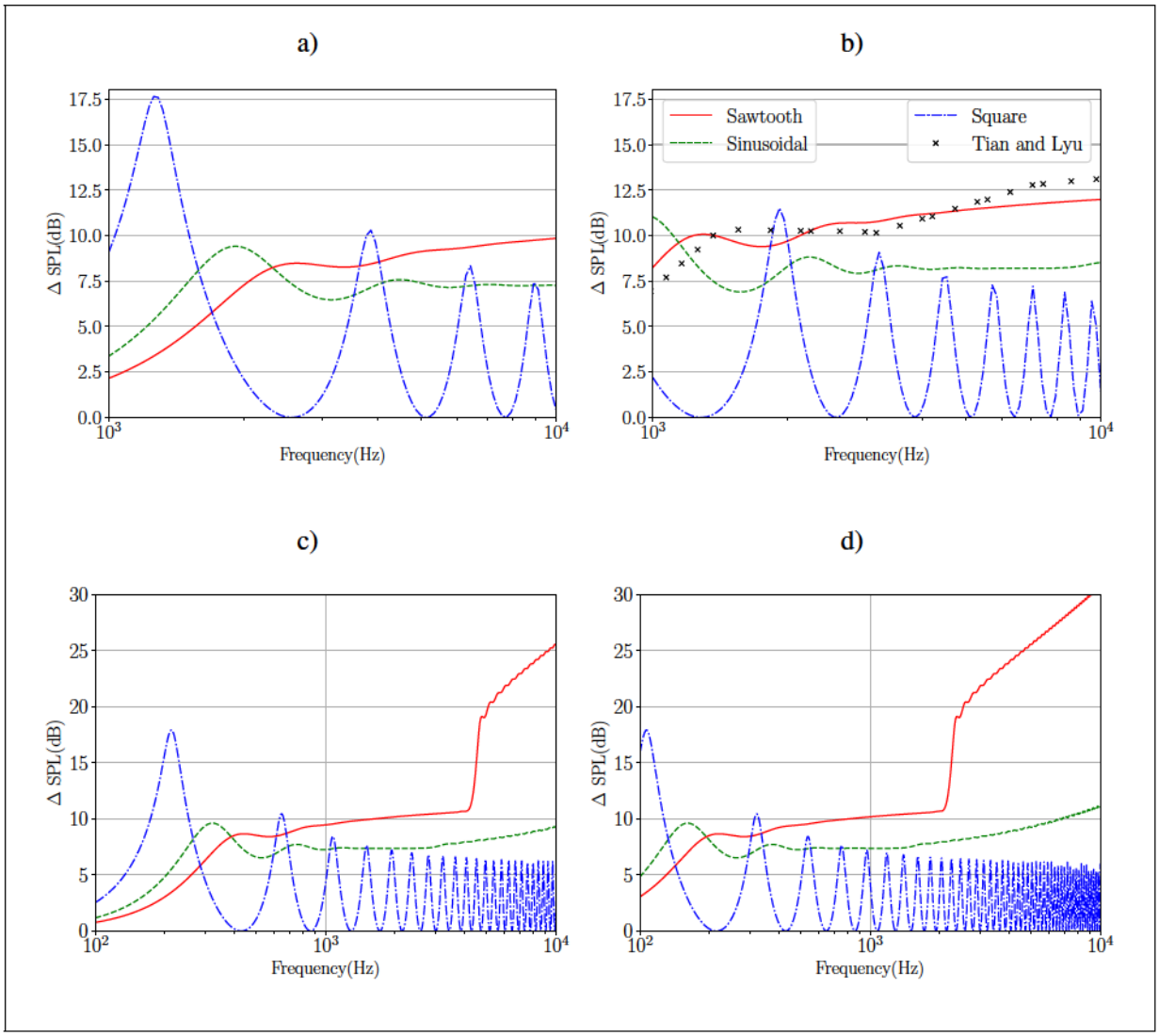

Figure 4.4 Noise reduction for different serration shapes for the cooling fan and wind turbine blade elements computed at an observer at $\theta = 0°$, except for configuration (b) where the location is at $\theta = 45°$. (a) Cooling fan ($2h = 0.1\,c$), (b) Cooling fan ($2h = 0.2\,c$), (c) Wind Turbine ($2h = 0.1\,c$)(d) Wind Turbine ($2h = 0.2\,c$)

for the wind turbine is due to the decay rate of the expansion coefficients. For large argument, it can be shown that the sawtooth coefficients fall as $\approx 1/x$ whereas the sinusoidal coefficients fall as $\approx 1/\sqrt{x}$. Finally, the noise reductions for the wind turbine grow as $\log(2hk)$ in perfect agreement with the original model by Ayton (2018). These results also show a fundamental

limitation of the serrated models available in the literature as they do not account for the noise increase due to the flow through the serrations as reported experimentally Gruber *et al.* (2010).

Li and Lee's model validation for blades ——————————-Summary

- Li and Lee's model can be used for blades, but its frequency range is application-dependent.
- It is in reasonable agreement with the more complex Lyu's sawtooth model.
- The model shows that each serration geometry performs better at different conditions.

4.3 NACA0012 Propeller

Having verified the frequency range and the directivity limitations of Li and Lee's model, this section presents a comprehensive methodology for predicting trailing edge noise for a representative drone propeller. The two-bladed rotor[1] has a 0.25 m diameter ( ), constant pitch (10°), and a constant chord (0.025 m) based on the NACA0012 airfoil. Experimental data from Gojon *et al.* (2021) and Santamaria, Sanjose, Gojon, Belliot & Moreau (2024) are available for validation.

The propellers were tested in the ISAE-SUPAERO anechoic chamber. This facility is acoustically treated in the 80–16 000 Hz frequency range and has dimensions of 5.02 m long, 5.24 m wide, and 5.34 m high from wedge-tip to wedge-tip. The isolated rotors are placed in the center of the chamber and are driven by a Faulhaber 3274G024BP4 3692 electric brushless motor, which has low noise emissions as compared to conventional off-the-shelf motors. Far-field noise is measured with a directivity antenna comprising 13, 1/4" GRAS microphones. The microphones are placed at a distance of 1.62m from the rotor center and spaced every 10 from 60 to 60 with the rotor plane at 0 as shown in Figure 4.5.

Acoustic data are acquired at a sampling frequency of 51.2 kHz for 16 s. Acoustic narrowband spectra are obtained from time signals using Welch's periodogram method with a Hanning

[1] While rotor is a term exclusively used to refer to helicopters main and tail rotors, the term is used here interchangeably with propeller. This practice is common in the small-propeller community

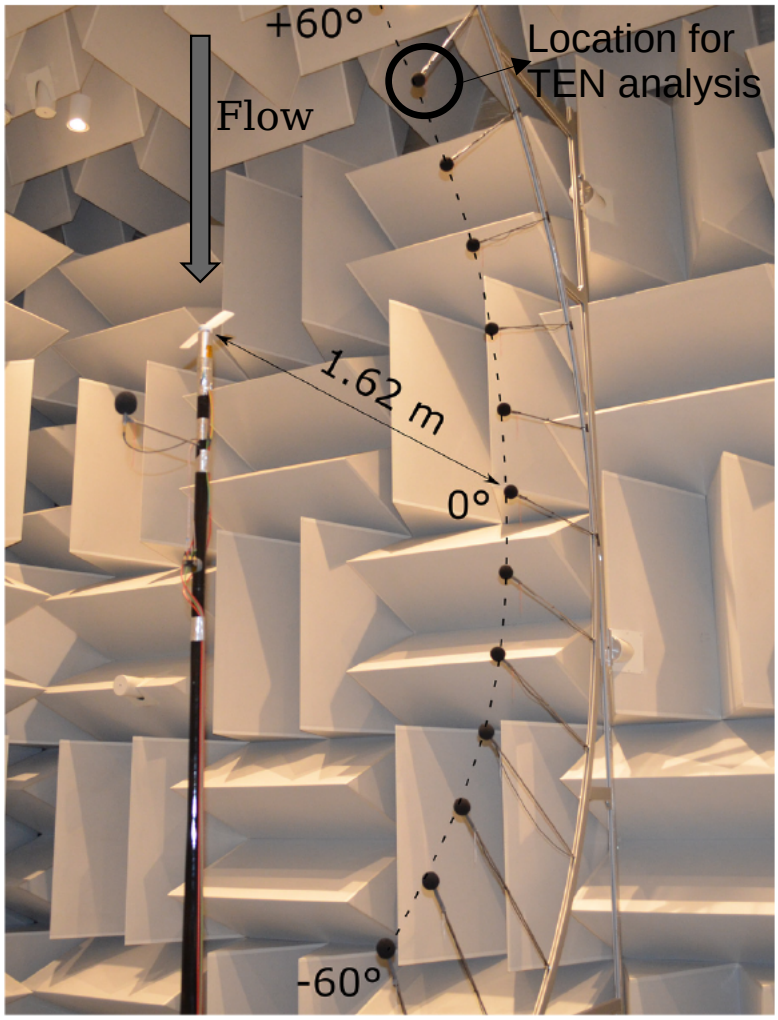

Figure 4.5 Experimental set-up with the baseline propeller

window applied on 50 segments, using a 50% overlap and an amplitude correction factor. The frequency resolution is 3.125 Hz. Following Zawodny & Boyd (2020) the random SPL uncertainty is 0.45 dB.

The far-field acoustics are calculated following the methodology in Sanjosé & Moreau (2018). First, a single-passage RANS simulation of the rotor is performed. After the convergence of mean aerodynamic quantities, the blade is divided into strips, and boundary layer parameters are

extracted. These parameters are used in the in-house broadband turbomachinery noise code PyFanNoise to model the wall-pressure spectrum and to calculate the far-field acoustic pressure using the models introduced and validated in Chapter 2 for each strip. Lastly, the complete rotor far-field acoustic pressure at a given observer location is calculated using Eq.(4.1). The methodology is summarized in Figure 4.6.

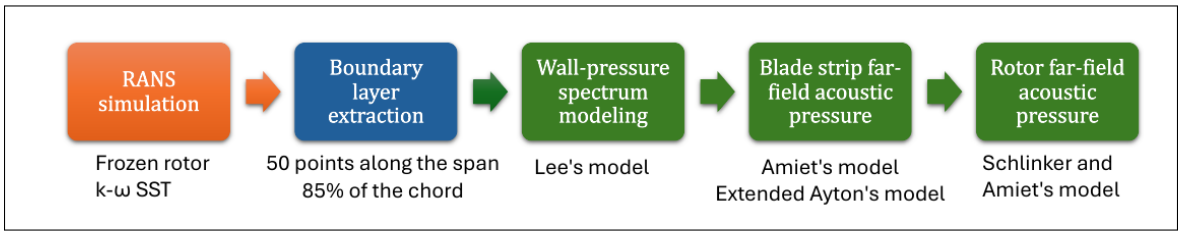

Figure 4.6 Methodology for propeller trailing edge noise calculation

4.3.1 RANS simulations set-up

The RANS simulations were run in the commercial software ANSYS CFX. The computational domain is divided into two regions: a large stationary domain and a rotating domain, as shown in terms of the propeller radius in Figure 4.7. The RANS equations are solved in a moving reference frame (MRF) in the rotating domain, introducing the Coriolis and centripetal components of the acceleration in the momentum equations. In both cases the air is modeled as an incompressible medium with constant temperature, using the CFX default physical and transport properties for air at 25 .

The experimental RPM range is between 4000 and 8000, yielding a chord-based Reynolds number range between 88000 and 176000 using the blade tip speed. The corresponding tip Mach numbers are 0.15 and 0.3 respectively. It is expected, then, that transitional effects play an essential role in aerodynamic performance, whereas compressibility effects can be disregarded.

The simulations are performed with the *High Resolution* advection scheme. For closure of the RANS equations, the SST model is used. Given the low-Reynolds number, the simulations

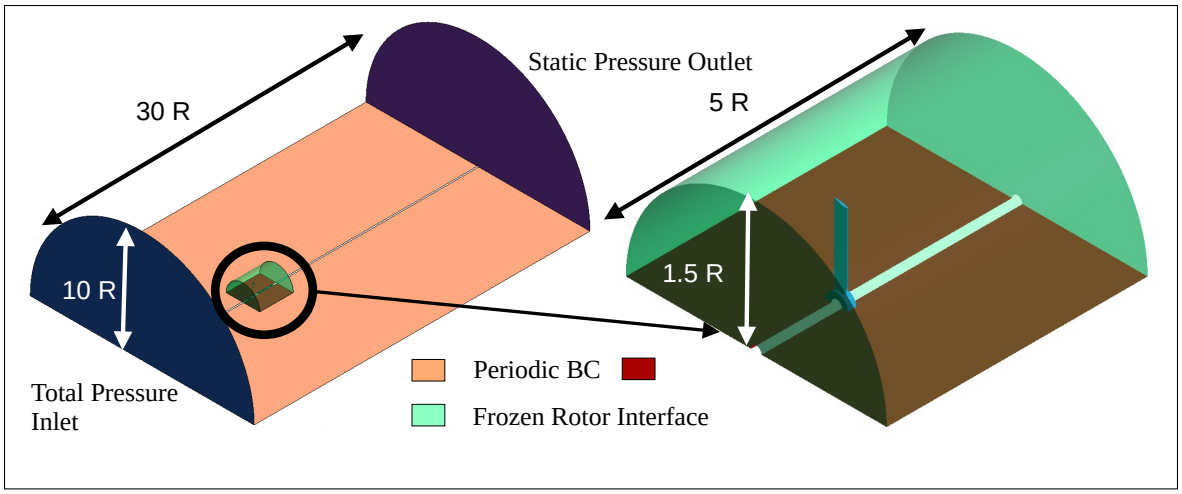

Figure 4.7 Single-passage stationary and rotational domain for RANS simulations

are performed twice for all RPM, first using the fully developed turbulence model, then the transitional modeling by activating the model based on the Langtry-Menter model.

The Langtry & Menter (2009) is a two-equation local correlation-based transition model (LCTM) that is used in conjunction with the SST model . The first equation is for the intermittency , and the second one is for the transition onset momentum thickness Reynold number . The intermittency is zero for laminar boundary layers where the production of turbulence kinetic energy is inhibited, and it is one for turbulent boundary layers where evolves according to its transport equation. The transport equation for connects empirical correlations to the onset criteria in the equation. It accounts for non-local effects due to changes in the freestream turbulence and in the pressure gradient at the edge of the boundary layer. A standard diffusion term in the equation propagates this information towards the wall. Due to its empirical nature, the model does not aim to reproduce the complex physics of transition but rather to model the consequences of the transition in the flow. The transition physics are thus entirely contained in the empirical correlations.

An unstructured mesh was generated using the software CentaurSoft and consisted of a surface mesh with an associated prismatic layer, and tetrahedral mesh for the rest of the domain. The

surface mesh parameters are the same as the ones used in Chapter 3 for the NACA0012 airfoil simulations and are discussed in Appendix IV. The key zone for the tetrahedral mesh is the region where the tip-vortices evolve downstream from the propeller as shown in red in Figure4.8.

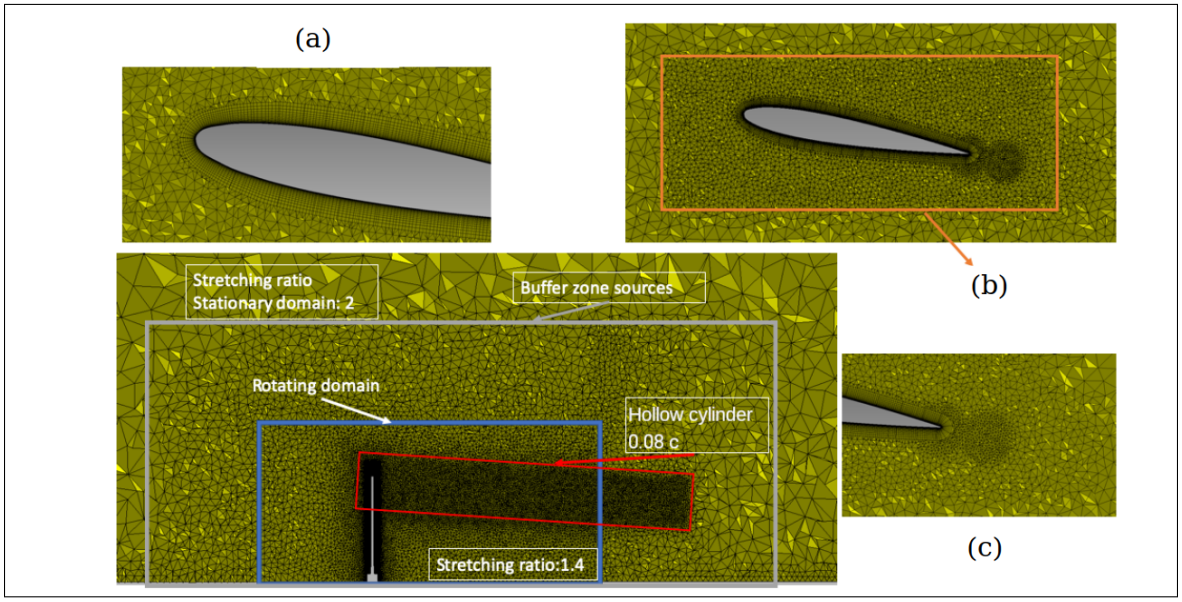

Figure 4.8 Mesh strategy for the propeller: (a) leading edge, (b) blade near-field, (c) blade wake

Poor resolution of the tip-vortices has a detrimental effect on the RANS aerodynamics predictions. Since a global convergence study is not practical from the computational time point of view, local refinements in key areas were made, and evaluated in terms of the thrust coefficient( ), Eq. (1.8) and the figure of merit (FM), Eq. (1.10). The convergence results as a function of mesh element size are shown in Figure 4.9 for the tip-vortex region.

While convergence is not reached in a strict sense, the results with the smallest tetrahedron size are seen not to vary significantly (less than 1.5% for the) with respect to the next tetrahedron size tested. Therefore, the smallest tetrahedron size shown in Figure 4.9 was deemed sufficient.

A similar study was performed to set the maximum element size in the stationary domain mesh, but it is not shown here for brevity. On average the largest elements in the stationary domain are on the order of the propeller chord. Having set the mesh maximum size in the stationary domain

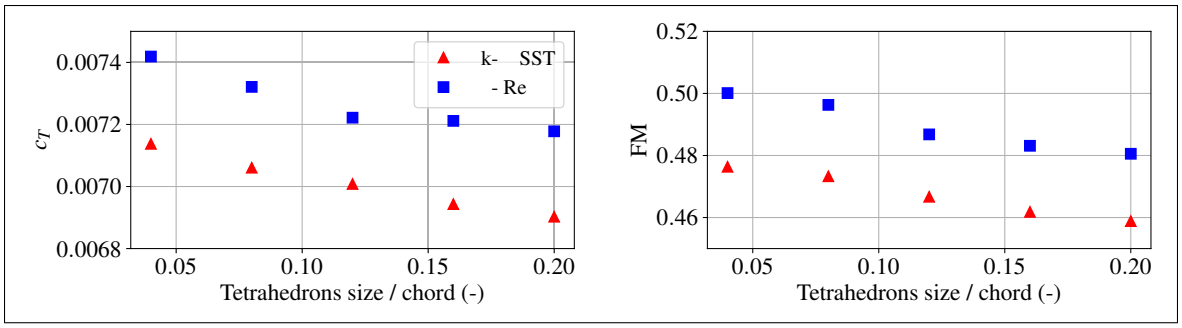

Figure 4.9 Convergence of mesh refinement for the region around the tip vortices (a) thrust coefficient and (b) figure of merit

and the refinement zones in the rotational domain, a grid convergence study is performed by scaling down the tetrahedron size in the rotational domain (blue rectangle in Figure 4.8) in a global manner. This results in an exponential increase in the tetrahedron number. Note that this does not affect the surface and the prismatic regions close to the blade. As seen in Figure 4.10 the thrust coefficient and Figure of Merit tend to an asymptotic value with an increasing number of elements. A rational polynomial fit is shown to highlight the trend and the shaded regions represent a region within 1% of the asymptotic value.

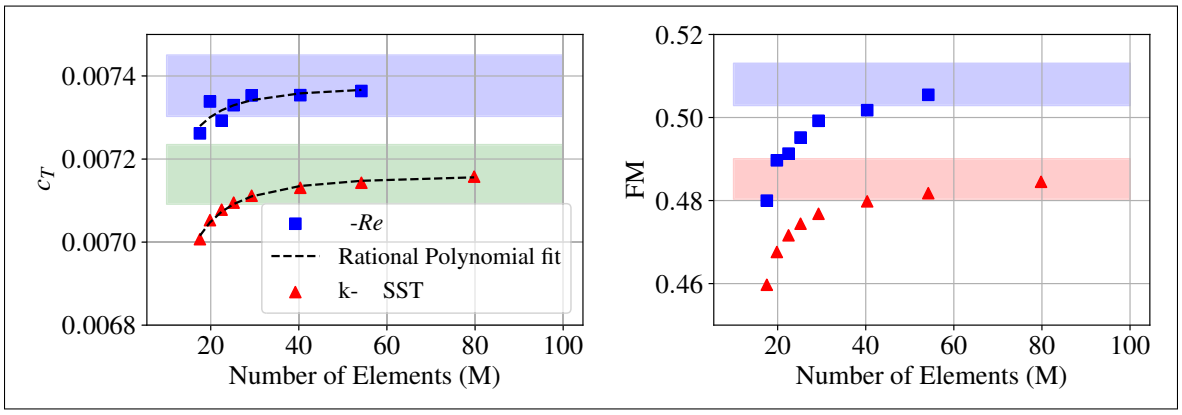

Figure 4.10 Grid convergence for (a) thrust coefficient and (b) figure of merit

Figure 4.11 shows isosurfaces of Q-criterion colored by vorticity superimposed on (left) axial velocity and (right) turbulence kinetic energy contours. Note that the black arrow denotes the positive direction in the axial direction. The tip vortices are adequately captured for the final

mesh used, and their trace is visible in the axial velocity contours as well. The Figure also illustrates the slipstream contraction downstream the propeller.

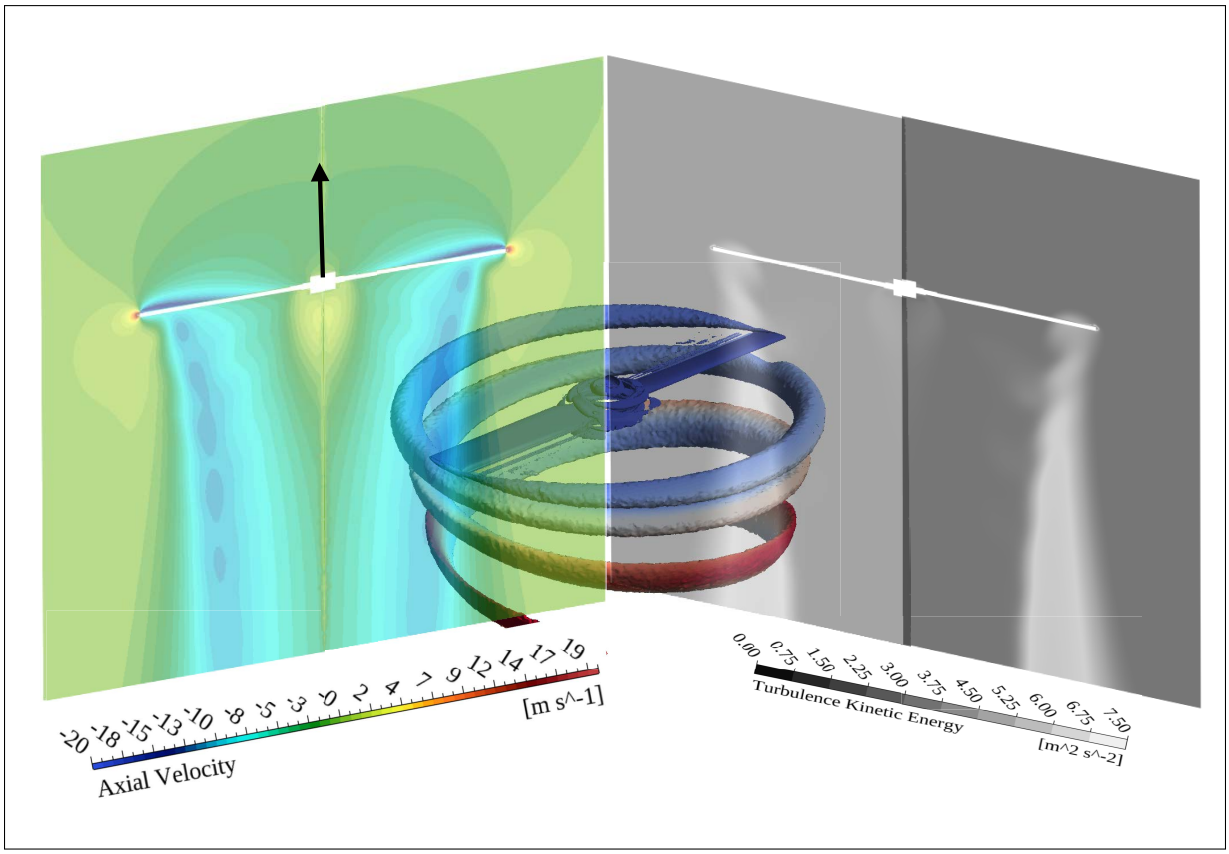

Figure 4.11 Isosurfaces of Q-criterion colored by vorticity superimposed on (left) axial velocity and (right) turbulence kinetic energy contours.

4.3.2 Aerodynamic results

Figure 4.12 compares the thrust coefficient and the Figure of Merit calculated from the RANS simulations with two data sets. The first data set is from Gojon *et al.* (2021) obtained using two 10 N S100 load cells from Strain Measurement Devices (SMD) (Wallingford, CT), while the second data set comes from Santamaria *et al.* (2024) using a six-axis ATI (Apex, NC) Nano 17 load cell. The latter data set was obtained in the anechoic room in Figure 4.5 while the former was obtained in a different test rig. Furthermore, the second data set also includes a propeller with tripping cylinders at 10% from the leading edge to force transition to turbulence

on the blade suction side. Details of the trip sizing and distribution can be found in Gowree, Jaroslawski, Mellot & Gojon (2023). The manufacturing subtleties of the 3D printer propeller are deferred to Chapter 5. Note that in Figure 4.12, the error bars represent the experimental uncertainty as reported in Li Volsi *et al.* (2024). The results from the first data set are labelled "JASA", and those from the second data set are labelled "AIAA".

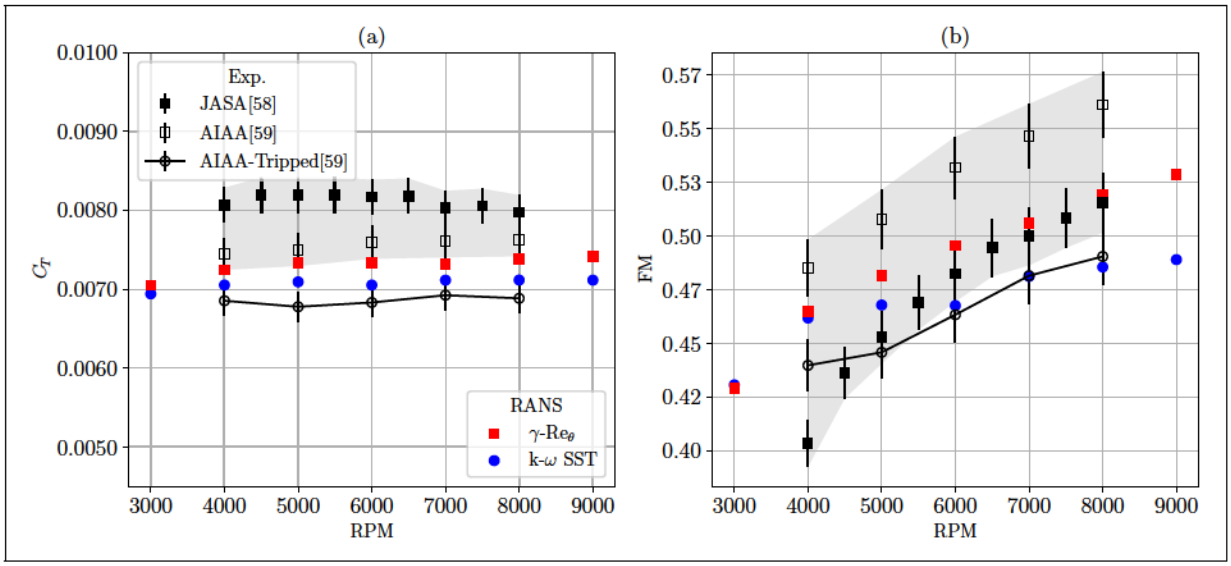

Figure 4.12 Comparison of the thrust coefficient (a) and the Figure of Merit (b) calculated from RANS with experimental data.

Note the considerable variation in measurements on the same clean propeller, as highlighted by the shaded areas. The prediction of static thrust remains challenging, even for high-fidelity simulations, where discrepancies between 5-12% have been observed (Thurman *et al.*, 2024; Romani, Grande, Avallone, Ragni & Casalino, 2022; Casalino, Romani, Pii & Colombo, 2023). Therefore, the RANS simulations are overall in good agreement with the experimental data. Both the transitional $\gamma - \mathrm{Re}_\theta$ and the fully turbulent models are within the 95% confidence interval of the measured thrust and Figure of Merit values.

To better understand the flow topology over the blade, the wall-shear stress streaklines are presented in Figure 4.13. The blade is colored by intermittency contours that identify the regions where the flow is laminar (red) or turbulent (blue). The contours range is selected based on

recommendations in ANSYS turbulence-modeling best practices guide. In the tip region of the blade (0 75), the boundary layer is in a transitional state and the transition position moves closer to the leading edge along the span. This is consistent with the increasing Reynolds number as the entrainment velocity increases with radius. Similarly, the percentage of blade span in the transitional regime increases with increasing RPM. The transition line (white) obtained experimentally from Infrared Thermography (IRT) (Jaroslawski, Forte, Moschetta & Gowree, 2023) in a similar, albeit 3-bladed, propeller at 6500 RPM is shown for a qualitative comparison.

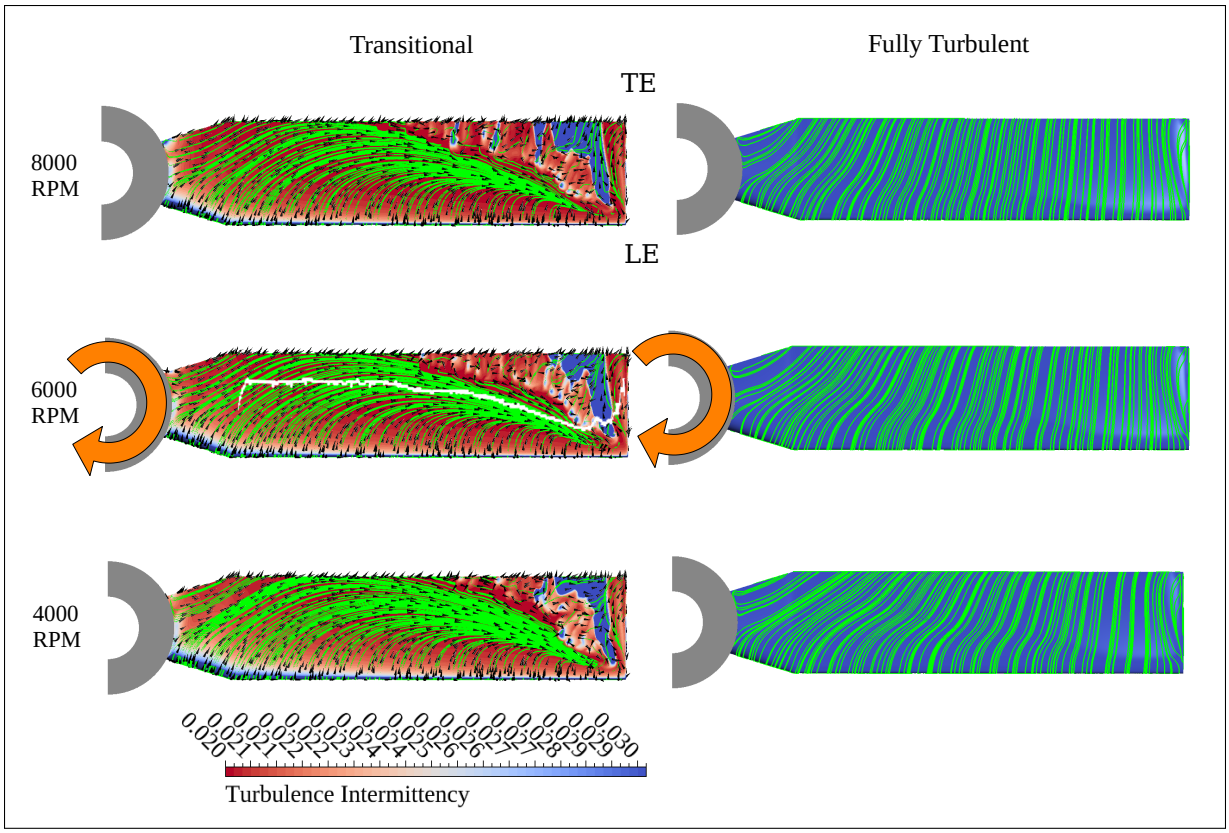

Figure 4.13 Suction side Wall-shear streaklines over contours of intermittency for the transitional and turbulent solutions at 8000, 6000 ,and 4000RPM. The white line at the 6000 RPM transitional case comes from IRT measurements.

The streaklines reveal the existence of strong radial flow close to the hub, affecting the whole suction side for the lowest RPM and less portions of the blade as the rotational velocity increases. For the transitional results, the streaklines show much more radial flow on the suction side

consistent with previous LES results (Shenoy, Gojon, Jardin & Jacob, 2024). They also show the location of the transition to turbulence along the span as a result of laminar flow separation.

The latter triggers the transition to turbulence at mid-chord in the outermost part of the blade and thus the state of the boundary layer at the trailing edge is close to the fully turbulent case. Additionally, the influence of the tip vortex is noticed in all cases on the suction side as it disturbs the flow from the chordwise direction. Lastly, the streaklines in the fully turbulent cases show no evidence of flow detachment or recirculation.

The is below 3 for most of the blade span in all cases and has maximum values at the leading edge of about 3, 4, and 5 for the 4000, 6000, and 8000 RPM cases respectively. Additionally, Figure 4.14 shows the Turbulence Kinetic Energy (TKE) contours at mid-span and at 90% span for the same RPMs. For the fully turbulent results, the maximum TKE location is shown to be within the prismatic layer for all cases. These two results assure that the inputs for the wall-pressure models are accurate.

Additionally, note that the boundary layer of the 4000 RPM case presents very low levels of turbulence, and it develops from the mid-chord, unlike the other two cases where the development starts around the quarter chord. Similarly, the transitional case remains laminar at mid-span, and the transition triggered by the LSB at 90% span results in a sharp increase of TKE and a thicker build-up all the way to the trailing edge.

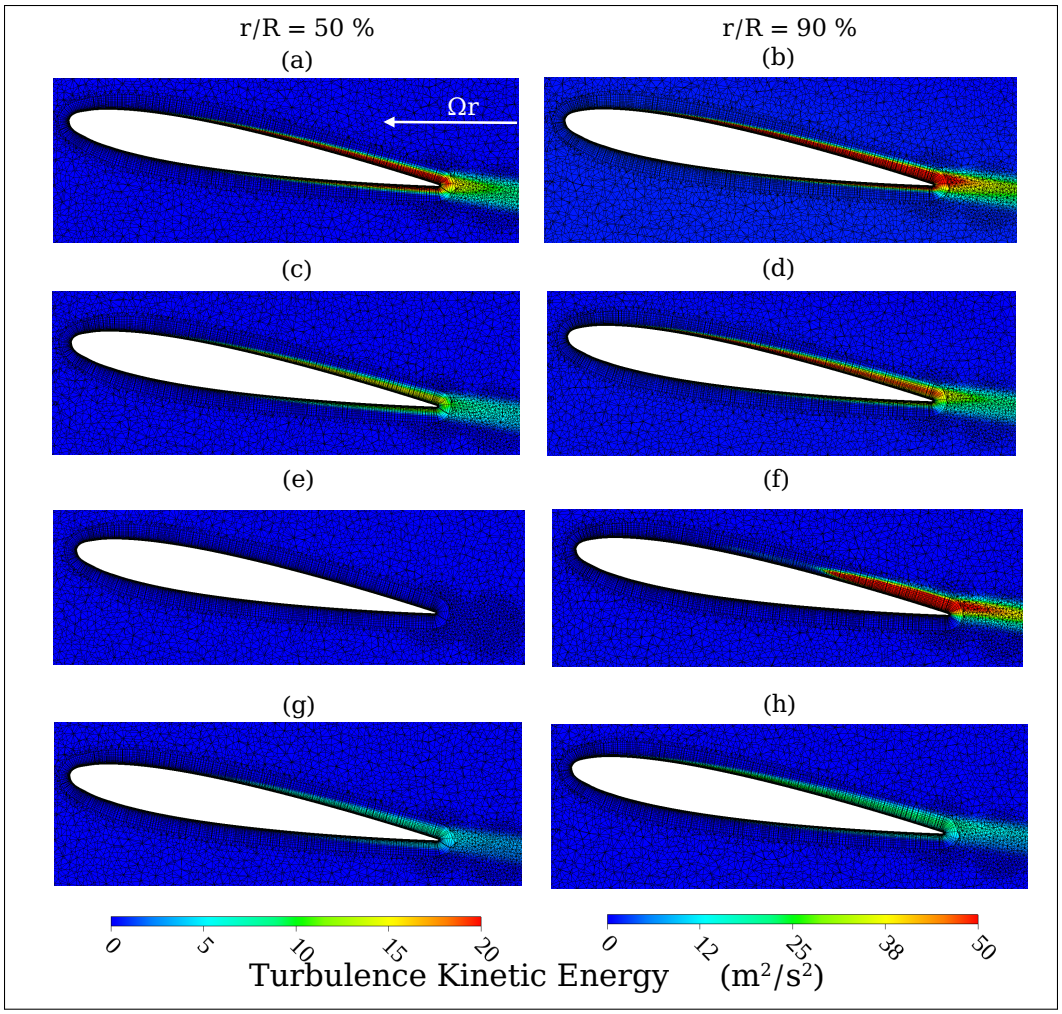

Figure 4.14 Turbulence kinetic energy at 50% of the span [(a),(c),(e) and(g)] and 90% of the span [(b),(d),(f) and(h)] for various simulations: [(a),(b)] 8000 RPM, [(c),(d)] 6000 RPM, and [(g),(h)] 4000 RPM for fully turbulent cases, and [(e),(f)] 6000 RPM for the transitional case.

With the results from the RANS simulations validated, the next step is the extraction of the boundary layer parameters to model the wall-pressure fluctuations spectrum. The extraction follows the same methodology based on the relative total pressure, as discussed in Chapter 3 (Sec.3.3.2) for the detection of the boundary layer edge as described by Sanjosé & Moreau (2018), and it is performed at 85% of the chord. The evolution of some parameters required to model the wall-pressure spectrum is shown in Figure 4.15 for different RPMs. The displacement thickness decreases as the speed increases as a direct consequence of increasing the Reynolds

number. The curves for Clauser's parameter, , tend to collapse for all rotational speeds along the midspan and diverge close to the blade tip, showing thus the independence of the Reynolds number in the midspan given that the chord at all radial positions is the same. Lastly, the wall shear stress, increases with Reynolds number as expected.

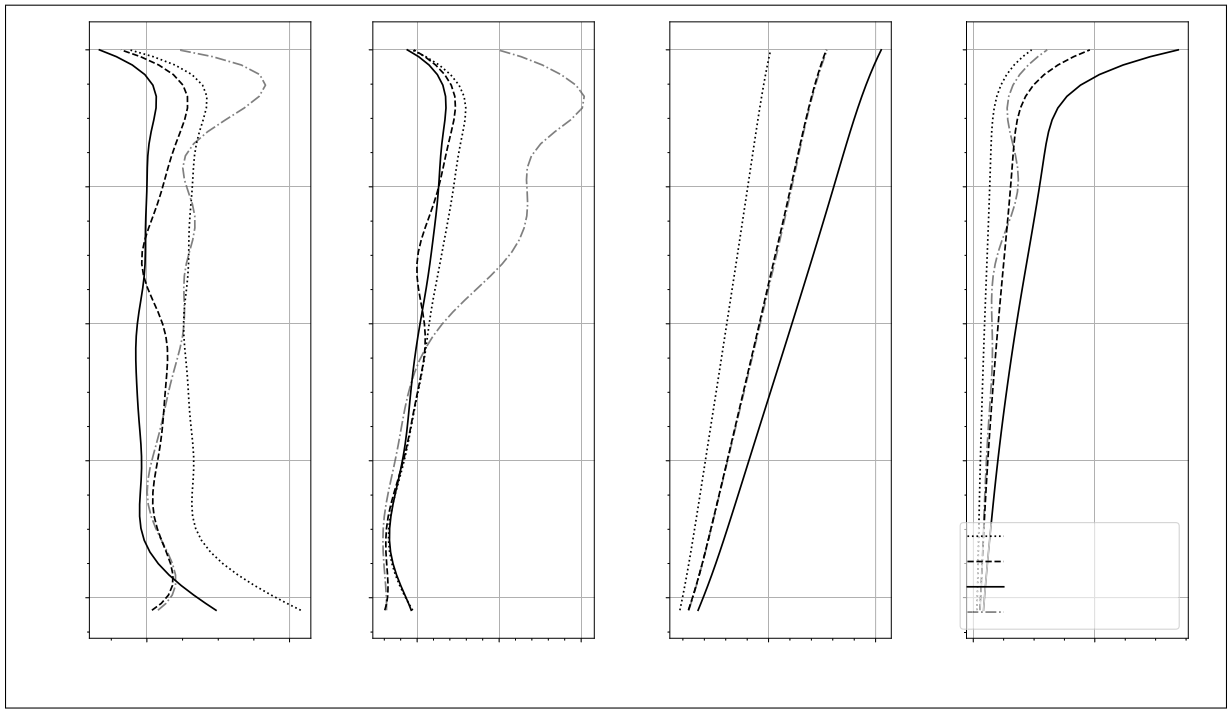

Figure 4.15 Evolution of the boundary layer displacement thickness (a), Clauser's parameter (b), external velocity (c), and wall shear stress (d) along the span for different RPMs.

4.3.3 Acoustic predictions for straight edge

Following the extraction of the mean flow quantities along the span, the wall-pressure fluctuations spectrum, , and the far-field acoustic pressure PSD are calculated in PyFanNoise. Unless otherwise noted, Lee's wall pressure spectrum, Eq. (2.22) is used in all calculations. After calculating the wall-pressure fluctuations spectrum and the blade strip acoustic pressure, the rotor acoustic Sound Power Level (SWL) is computed from Eq. (4.8). The results for the propeller rotating at 6000 RPM obtained with the methodology described in Figure 4.6 are

shown in Figure 4.16 and compared with experimental measurements from the clean and tripped propellers.

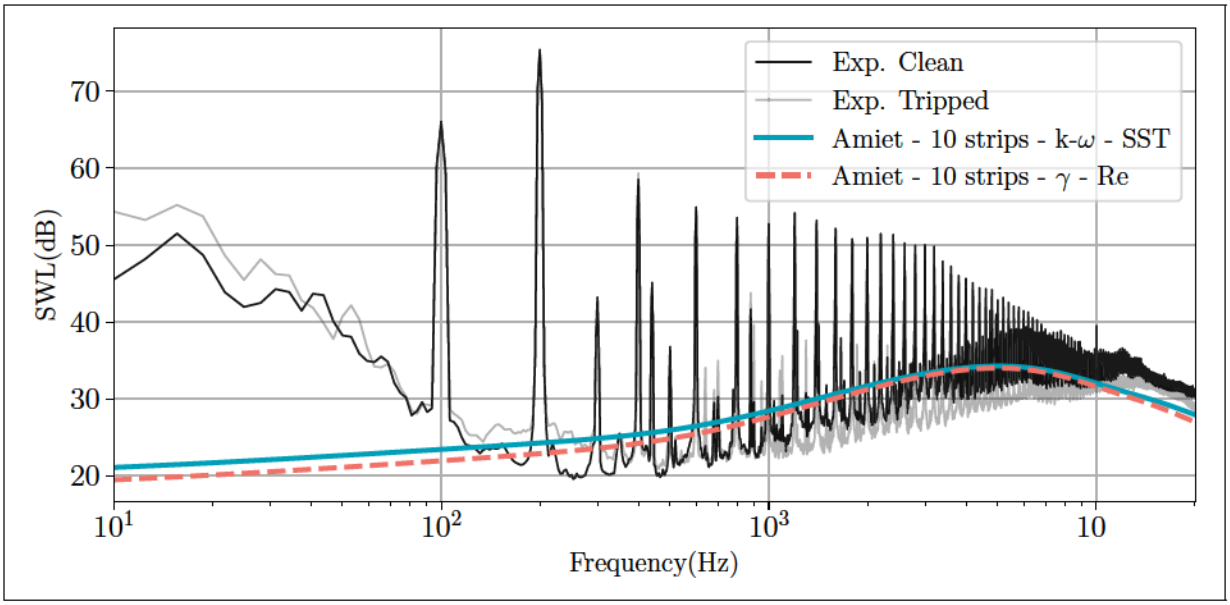

Figure 4.16 Comparison of SWL from RANS-PyFanNoise using Amiet's model with experimental data from clean and tripped propellers at 6000 RPM.

First, the impact of the turbulence modeling is assessed in Figure 4.16 by investigating the results obtained with Amiet's model using fully turbulent (blue line) and transitional (green dashed line) results. Note that despite the different flow topology shown in Figs. 4.13 and 4.14 the far-field noise predictions are almost identical with minor differences in the low-frequency range as also observed experimentally. Second, there is a good agreement for the broadband component of the noise between 100 and 10000 Hz, particularly with the clean results. This is due to the fact that turbulent flow is obseverved in the outermost part of the blade (Figure 4.13). Since the wall-pressure spectrum and correlation length models have been based on experimental data from fully developed turbulent boundary layers, only the results from the k-ω SST model will be used in the rest of the study.

Figure 4.17 compares Amiet's model and Li and Lee's model in the limit of zero serration amplitude. Both computations were made using 10 strips. Li and Lee's model is seen to over-predict the sound power levels at low frequencies but matches Amiet's model at around

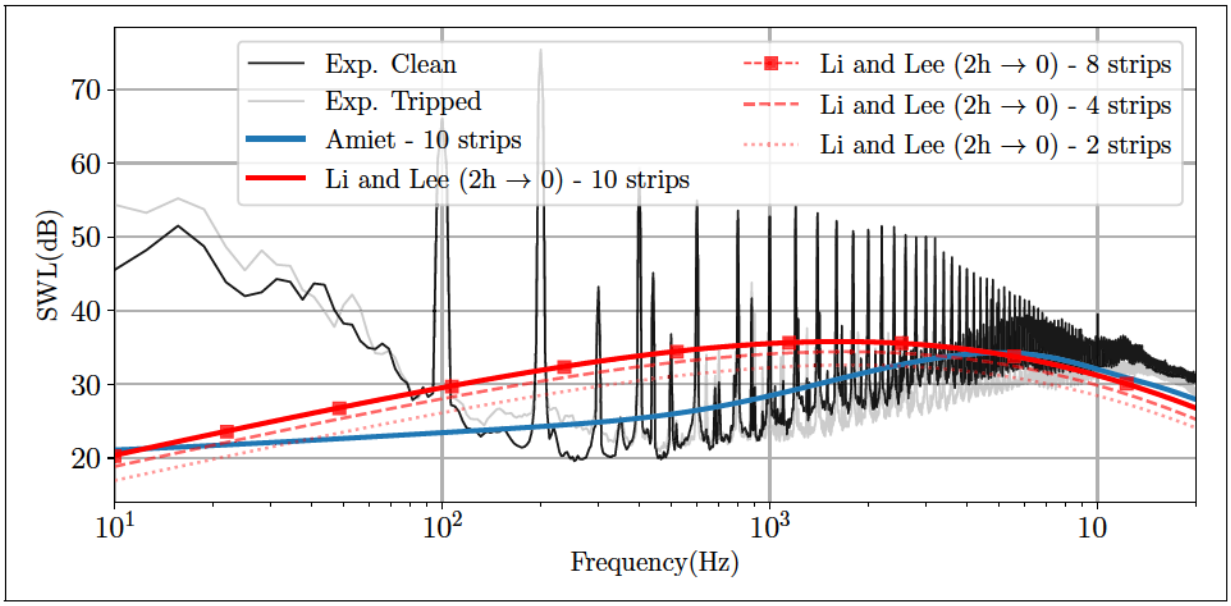

Figure 4.17 Comparison of SWL from RANS-PyFanNoise using Amiet's and the extended Ayton's model with experimental data from clean and tripped propellers at 6000 RPM.

4 kHz, making the model valid in the frequency range where trailing-edge noise dominates. This is also consistent with the directivity analysis of Section 4.2. Furthermore, note that both models underpredict the sound power levels for frequencies beyond 10 kHz. This is most likely caused by an additional noise source from a laminar boundary layer instability on the pressure side as will be demonstrated in the next Chapter. Moreover, Montoya-Ospina, Simon, Gojon & Parisot-Dupuis (2024) demonstrated for a similar propeller based on a NACA0018 section, that by tripping the pressure side only the high-frequency hump was removed and an early spectral roll-off around 4-5 kHz similar to the current prediction was observed. In the present study, only the noise caused by the scattering of fully turbulent boundary layers is considered.

The calculated noise levels can be influenced by the number of strips selected to discretize the blade response. The calculation for the extended Ayton's model becomes independent of the number of strips at around 10 strips, similar results are obtained with Amiet's model as well (not shown here). It is important to note that while using more strips may seem to improve the

matching with experimental data, the strip length cannot be arbitrarily small. The smallest strip length is limited by the spanwise correlation length, . Additionally, even though ten strips are used for the noise calculation, it is worth noting that approximately 95% of the acoustic power is radiated from the 2 outermost strips. Figure 4.18 shows that strips 9 and 10 contribute the most to the total radiated acoustic power for a straight trailing edge, regardless of the model used.

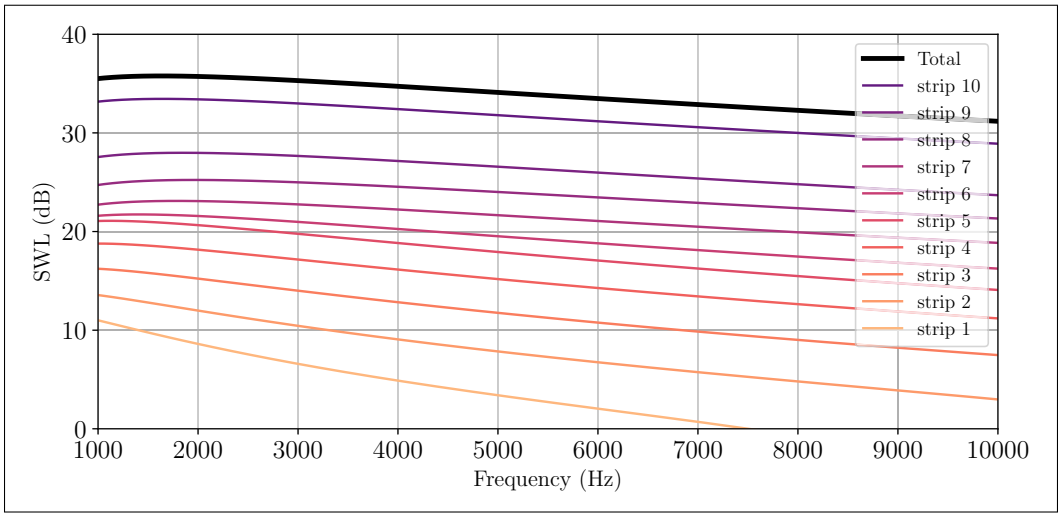

Figure 4.18 Acoustic power radiated from each blade strip using Li and Lee's model

Finally, a comparison of the directivity patterns obtained with Amiet's and Ayton's models with the experimental data from the tripped propeller is presented. The frequency range considered is 1-16 kHz as in the experimental campaign. Figure 4.19 shows the overall sound pressure level (OASPL) directivity for the 4000, 6000, and 8000 RPM cases. The flow is from top to bottom with the rotational plane at 0 . On the one hand, Amiet's model captures the expected dipolar pattern due to trailing edge noise while the extended Ayton's model matches Amiet's model at high elevation angles from the rotor plane in agreement with the results of Sec. 4.2. On the other hand, the results from both models are in better agreement with the experimental data as the rotational speed increases; this follows the findings of the development of the boundary layer as shown in Figure 4.14.

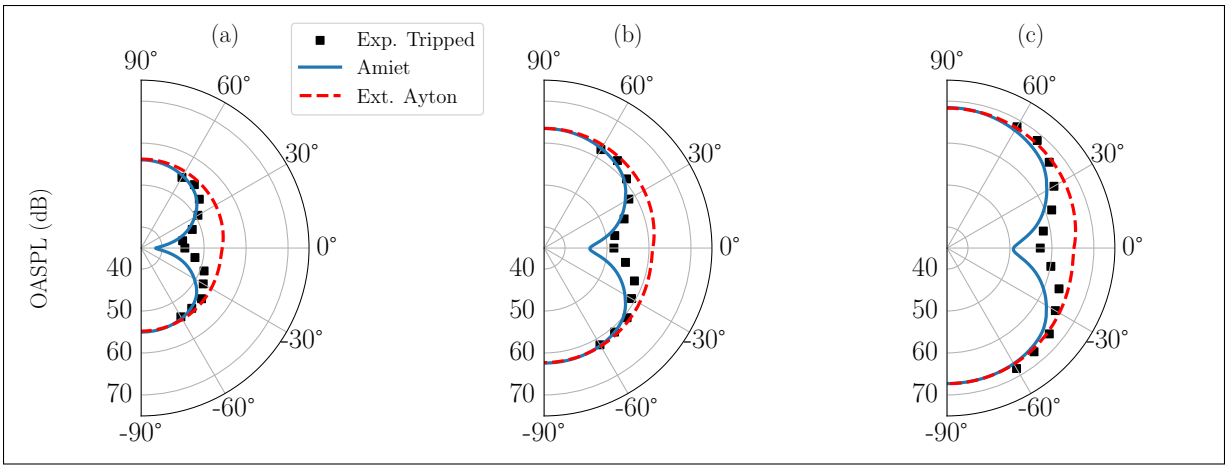

Figure 4.19 OASPL directivity at 4000 (a), 6000 (b), and 8000 (c) RPM for a straight edge propeller with tripping using Amiet's and the extended Ayton's model. The flow is from top to bottom.

4.3.4 Acoustic predictions for serrated edge

In this section, the performance of different serration shapes on the NACA0012 drone propeller is investigated. According to Gruber, Joseph & Chong (2011) and Lee *et al.* (2021), a serration becomes effective for amplitudes on the order of the boundary layer thickness (2 . Without loss of generality, the 6000 RPM case is chosen as the baseline. At this rotational speed, the boundary layer close to the tip is about 2.5 mm; thus, the serration amplitude, unless otherwise noted, is 5 mm (20% of the chord). The serration amplitude-to-wavelength ratio 2 is fixed to 2, in this case, following the optimal ratio found both experimentally and numerically (Gruber *et al.*, 2011; Kholodov & Moreau, 2021) and for consistency with the airfoil serration parameters in Chapter 3.

First, the noise levels of the propeller with sawtooth, sinusoidal, slitted-V, and square wave trailing edges are compared in Figure 4.20 with the noise levels of the propeller with a straight edge. Note that the spectra are zoomed in the frequency range of 1 kHz to 10 kHz, where the attenuation occurs and where the models were in good agreement with the experimental data. A linear scale is used for this decade. The slitted-V shape has the worst acoustic performance and the square wave the best with the sawtooth and sinusoidal shapes radiating almost equally across

the spectrum. Given that all other inputs are identical, the difference in the spectrum for each shape is only caused by the modal expansion coefficients E_n.

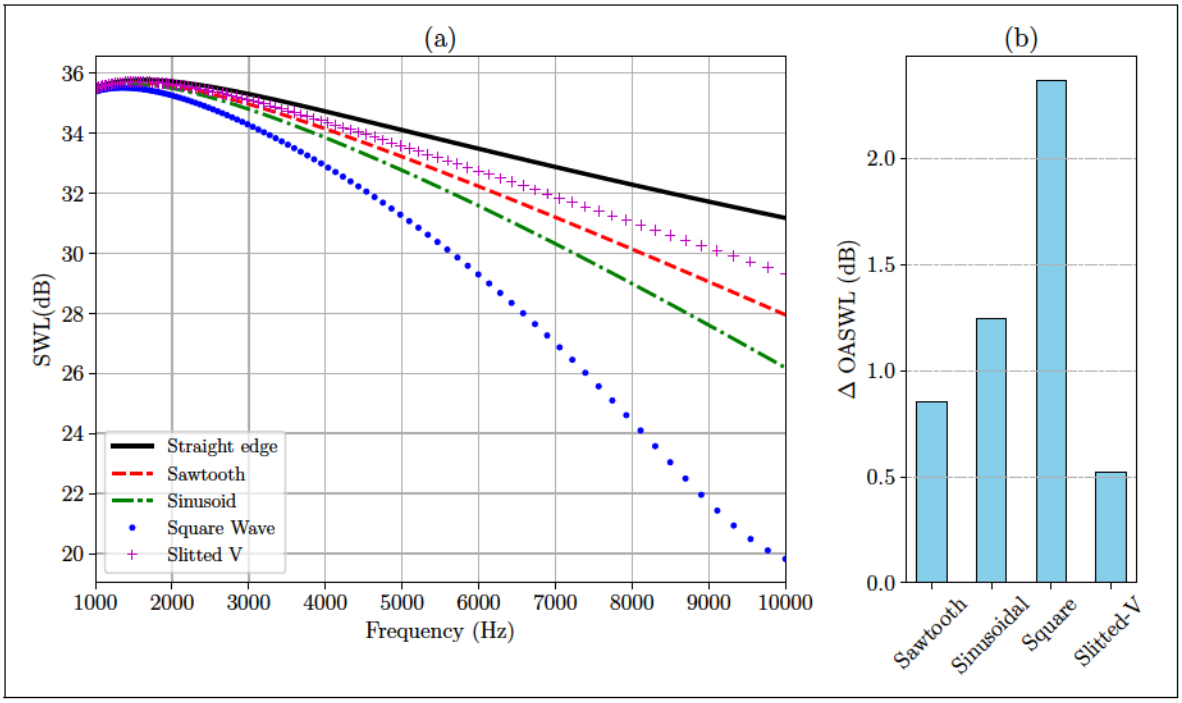

Figure 4.20 (a) Acoustic power radiated from the drone propeller with different serration shapes and (b) OASWL reduction between straight edge and serrated edge configurations.

The fact that the square wave performs better than the other serrations for the NACA0012 propeller is consistent with the airfoil analytical and experimental results from Chapter 3. More insight into why the square wave outperforms all the other shapes for the NACA0012 propeller, it is necessary to look in depth at the expansion coefficients, $E_n(\Lambda)$ (Eq. (2.93)).

Figure 4.21 shows the magnitude of the zeroth-mode expansion coefficient as a function of frequency for different shapes and an observer above the trailing edge. The Mach number and velocity values are taken from the propeller outermost strip since it contributes the most to the far-field. The curves follow the trend shown in the acoustic power spectrum (Figure 4.20) and demonstrate that the square wave shape indeed outperforms the other ones. The zeroth-mode coefficient for the square wave is given by a cosine function, and thus it can be shown that it will have maxima/minima for values of $\Lambda = n\pi$, for $n \in \mathbb{N}$. For low Mach numbers and

an observer above the trailing edge, this is in perfect agreement with the experimental results from Woodhead, Chong, Joseph & Wissink (2019) where the peaks/troughs were measured at frequencies $f = U_c/(2h)St$ for an airfoil with square-wave-type (slits) serrations and where St is the Strouhal number. Physically, this behavior comes from the constructive/destructive interference between the scattered waves from the root and the tip.

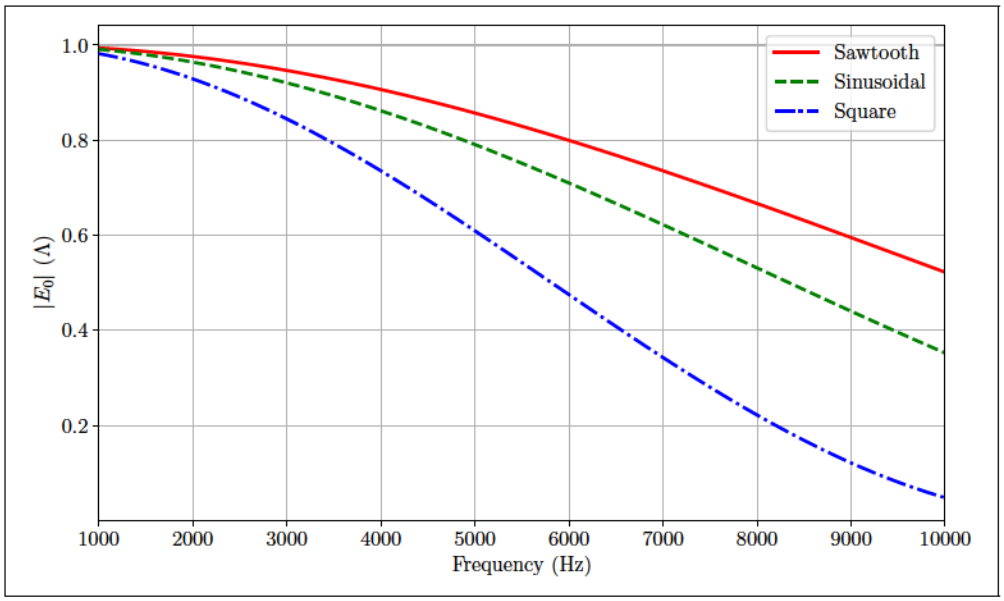

Figure 4.21 Zeroth-mode expansion coefficient for different shapes for the NACA0012 propeller case.

Contrary to the straight-edge case, the radiated acoustic power for serrated propellers might depend on more than the outermost strips. Figure 4.22 shows the acoustic power radiated from each strip with square wave serrations. It can be seen that the local minimum at 10 kHz is due to the contribution from strips 4-8; thus how strips overlap is fundamental to understanding the shape of the total spectrum.

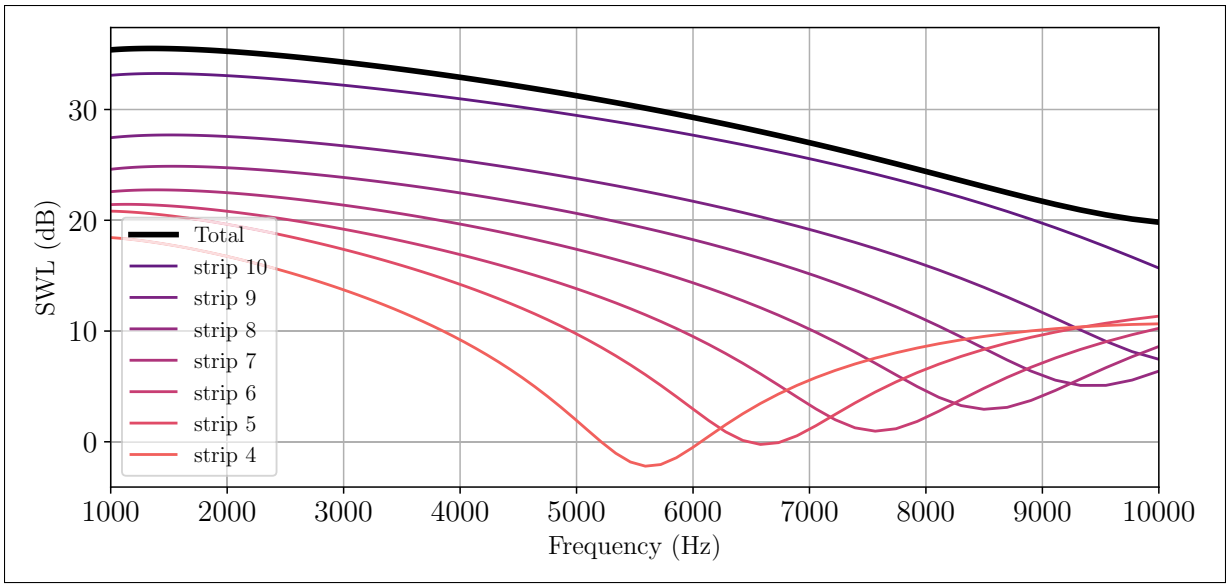

Figure 4.22 Acoustic power radiated from each strip for a propeller with square wave serrations.

Since the serration height for a given propeller may be a fixed parameter once the blade is manufactured, it is important to calculate the noise reductions over the whole operational range of the propeller. This is even more important if square wave serrations are to be used since a change in RPM could trigger a phase shift close to or at the constructive interference region. Figure 4.23 shows the directivity of the OASPL in the frequency range of 1-10 kHz for different serration shapes at different RPMs. It is clear that the serration height of 5 mm is effective over the whole operating points and for all observer angles. Additionally, it is noted that no lobes are present in any case, this is in good agreement with the original results in Ayton (2018) where lobes appeared for values of 2 4 for the square wave and 2 8 for the sawtooth. In the present calculations, 2 was always less than unity for the NACA0012 drone propeller.

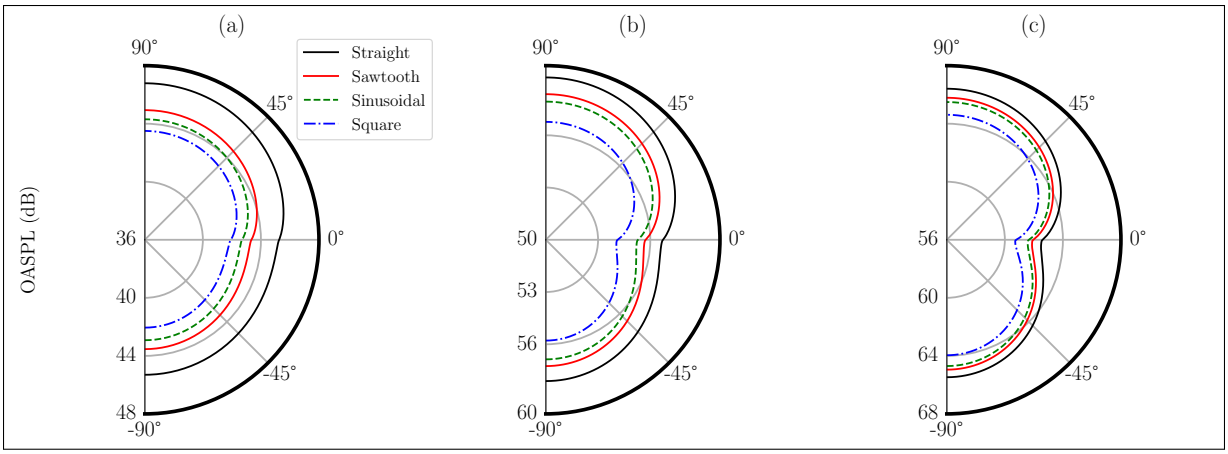

Figure 4.23 OASPL directivity for different serration shapes at 4000 (a), 6000 (b), and 8000 RPM (c).

NACA0012 propeller serration design————————-Summary

- The mesh region for the tip-vortices is critical for the RANS-simulation of hovering propellers.
- RANS transitional modeling is essential to accurately predict the thrust and Figure of Merit.
- Amiet's model is in good agreement with the experimental results for frequencies up to 10 kHz.
- Li and Lee's model matches Amiet's model for frequencies beyond 4 kHz.
- For straight edge propellers, the outermost strips contribute the most to the far-field acoustics.
- The square wave serration shows greater noise mitigation potential for small-scale propellers.

4.4 General serration shape design considerations

Given the limited range of applicability of the square wave type serration to small propellers, it is worth investigating alternatives for larger chord propellers, such as those found in ducted fans UAVs where diameter size constraints may play a key role and low-aspect ratio blades

would be more appropriate (Deng, Wang & Zhang, 2020). For such designs, the chord length is necessarily larger than for the drone propellers discussed in the previous section, to achieve the required thrust. This allows longer serrations to be used without compromising aerodynamic performance.

First, a design where only the chord length is increased four-fold compared to the previous NACA0012 drone propeller is considered. Thus, a similar blade but with a larger chord, such that the serration height-to-chord ratio remains the same, is analyzed. The tip Mach number is also preserved, but the tip Reynolds number based on the chord length is now four times higher, which makes the previous fully turbulent RANS flow field simulation even more relevant. As for the NACA0012 propeller case, the noise levels for different serrated trailing edges are first compared in Figure 4.24 with the noise levels of the same rotor with a straight edge (solid black line).

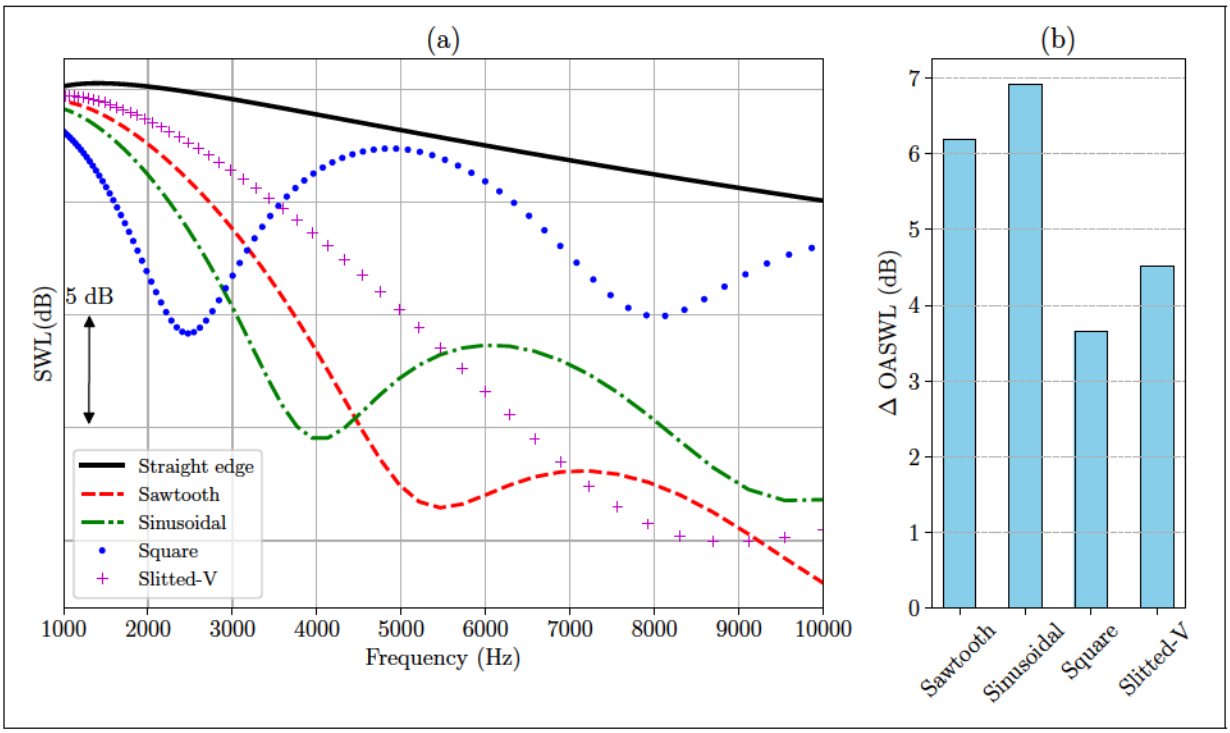

Figure 4.24 (a) Acoustic power radiated from large-planform UAVs with different serration shapes and (b) OASWL reduction between straight edge and serrated edge configurations.

Compared to Figure 4.20 for the drone propeller, a very different picture emerges in the frequency range of interest and more significant noise reductions are observed. On the one hand, the square wave presents strong oscillations and no longer provides any benefit beyond 3 kHz. On the other hand, both the sawtooth and sinusoidal serrations effectively reduce noise levels on the whole frequency range, by up to 8 dB at high frequencies. However, the frequencies at which they do so differ. The sawtooth outperforms the sinusoidal serration shape at frequencies greater than 5 kHz, whereas the opposite is true at lower frequencies. Given that all other inputs are identical, this effect is only caused by the modal expansion coefficients E_n. Moreover, an alternating pattern can be used along the span to obtain the best from both. Given that the last strip is expected to contribute the most to the far-field acoustics, as shown for the drone propeller case in Figure 4.18, two configurations, one ending with sinusoidal serrations and the other with sawtooth serration for the outermost strip, are considered in Figure 4.25

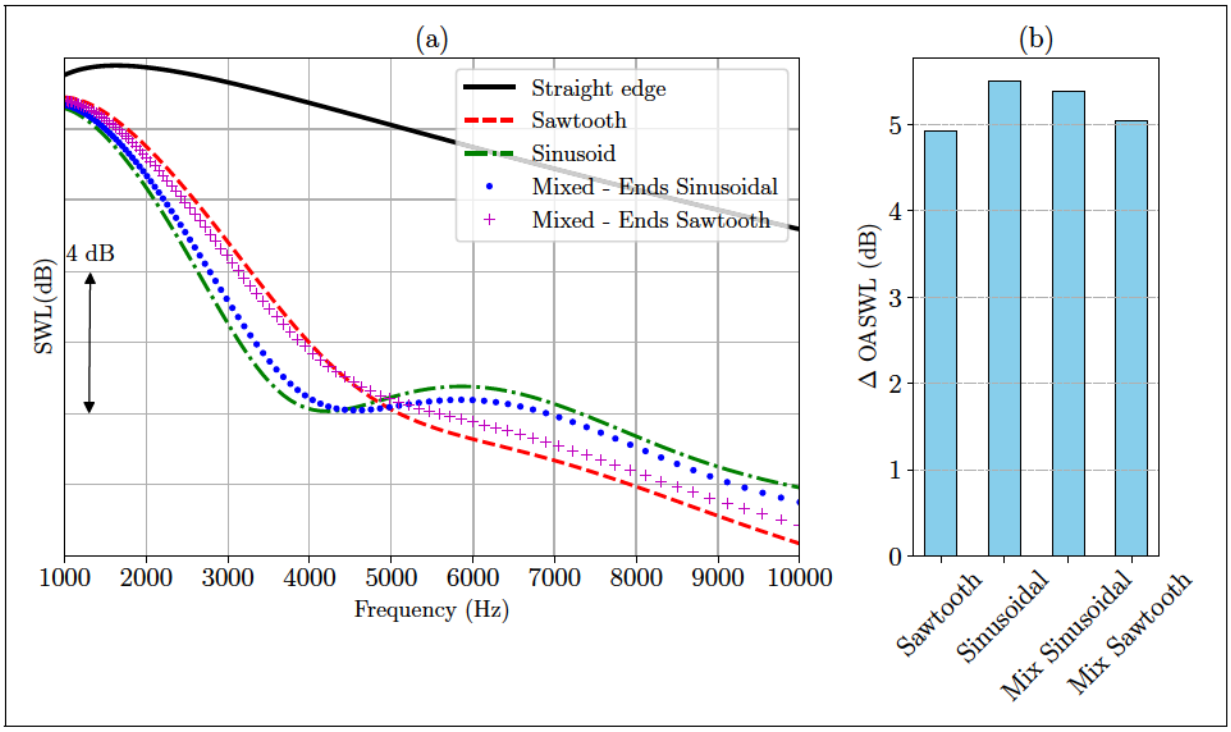

Figure 4.25 (a) Acoustic power radiated from large-planform UAVs with different serration shapes and (b) OASWL reduction between straight edge and serrated edge configurations.

By blending the serrations, the noise reductions are seen to be slightly modified from the single-shape cases, and the shift to higher frequency can be subjectively beneficial and exploited to tailor the spectrum around the dominant trailing edge noise frequency.

Turning to more general design considerations where not only the chord length but also the diameter and the rotational speed can change, both the tip Mach number and Reynolds number based on the chord will vary. Considering that the design conditions will correspond to attached flow with flow features similar to Figs. 4.13 and 4.15, the noise reduction achieved by serrations are expected to be driven again by their diffraction effect and therefore by the modal expansion coefficients . Contours of the magnitude of the zeroth-mode expansion coefficients of the sawtooth, sinusoidal, and square-wave serrations are therefore presented in Figure 4.26 as a function of the serration length 2 (in meter) and the tip Mach number , at selected frequencies of interest.

In Figure 4.26 the symbols represent the applications considered in this paper. For the wind turbine and cooling fan case, a serration height of 10% of the chord is used. These contours for the square wave clearly show that it outperforms the other shapes at moderate tip Mach number and for serration heights less than 1 cm. As soon as the latter is beyond 1 cm, the sawtooth and sinusoidal serrations outperform the square wave (or slit), with either one providing the largest noise reduction depending on the frequency range. As shown above, this suggests a possible combination of these two serration types to achieve the broadest noise reduction over the whole frequency range of interest. Finally, an augmentation of the tip Mach number significantly reduces the effect of all serration designs for a given serration height. The latter needs to be doubled when the Mach number goes from 0.1 (small drones) to 0.4 (large UAM propeller),

4.5 Conclusion

This chapter presented a low-order methodology showing potential noise reductions for a representative drone propeller. Following single-blade passage RANS simulations of a small propeller with constant chord and pitch based on the NACA0012 airfoil, the wall-pressure

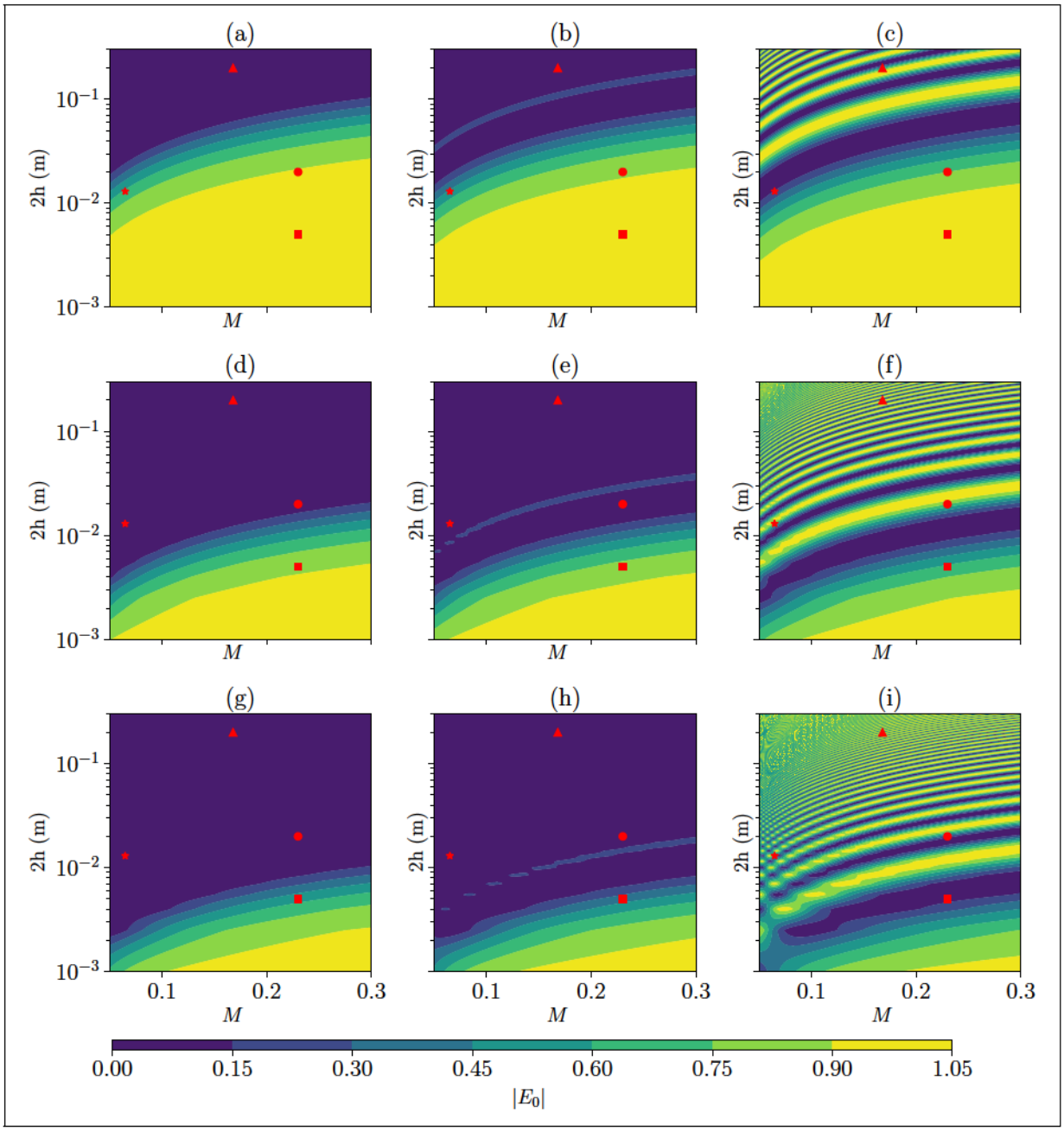

Figure 4.26 Magnitude of the zeroth-mode expansion coefficient for the sawtooth [(a),(d) and (g)], sinusoidal [(b),(e) and (h)], and square wave [(c),(f) and (i)] serrations for 1000 Hz,[(a)-(c)], 5000 Hz, [(d)-(f)]and 10000 Hz[(g)-(i)]. Wind turbine (△), cooling fan(*), drone propeller (□) and ducted fan(○).

fluctuations spectrum is modeled and the propeller far-field acoustics are calculated with the turbomachinery broadband noise in-house code PyFanNoise. Li and Lee's model was used

to assess potential trailing-edge noise reductions. It was shown that different serration shapes perform better at different non-dimensional frequencies. The often-overlooked square wave was shown to outperform the more traditional sawtooth and sinusoidal serrations when used in the NACA0012 drone propeller, over the whole operational range.Larger noise reductions and a larger design space for the serrations can be obtained by increasing the blade planforms, allowing longer, more efficient serrations. Indeed, a mix of sinusoidal and sawtooth serrations can then be tuned to achieve significant noise reduction over the entire audible frequency range of interest between 100 Hz and 10 kHz

CHAPTER 5

INSTALLATION AND MANUFACTURING EFFECTS OF TRAILING EDGE SERRATIONS

"Clouds are not spheres, mountains are not cones, coastlines are not circles, and bark is not smooth, nor does lightning travel in a straight line"

— Benoit Mandelbrot

This final chapter puts to test the findings of previous Chapter for the NACA0012 propeller. Several 3D printed propellers were manufactured to assess the impact of the serration installation method. That is, the acoustic and aerodynamic effect of "cutting" the serrations directly onto the blade compared to the use of add-on appendices, like in the case of the NACA0012 airfoil in Chapter 3. Following the presentation of the test matrix, the broadband filtered spectra is used to separate noise sources from transitional and turbulent boundary layers. Then, results for cut-in and add-on serrations are presented. Lastly, the noise reduction predictions using the RANS-based methodology from Chapter 4 are compared with the experimental ones.

5.1 Serrated propeller design and manufacturing

In the previous Chapter, Amiet's and Li and Lee's models were used to predict trailing edge noise with and without serrations. Both models result from solving a BVP with mixed boundary conditions for the convection of a pressure gust over a flat plate that represents an airfoil or a blade strip. The flat plate is assumed to be infinitesimally thin. Additionally, the methodology of the previous Chapter used a wall-pressure fluctuations spectrum model based on fully turbulent boundary layers. These two assumptions are not met in practice as blades have a finite thickness and small-scale propellers operate in transitional regimes. Another concern arising from the use of trailing-edge serrations is their impact on aerodynamic performance. Given the finite thickness at the trailing edge, the cutting or addition of serrations could result in modification

of the aerodynamic performance. Therefore, a complete experimental campaign was then conducted to assess the validity of the analytical models assumptions and to investigate the impact of serrations on aerodynamic performance

5.1.1 Propeller test matrix

Several CAD models of serrated propellers were generated. The serration types are divided into three categories: add-on (A), cut-in sharp (C-SH), and cut-in smooth (C-SM). The first case is a flat plate appendix where the serration patterns are carved. The division between sharp and smooth serrations for the cut-in case is necessary since blunt edges could result in vortex-shedding noise as noted by Chong *et al.* (2013) and must be considered at early design stages. Note that the smooth teeth in the case of the serrated controlled-diffusion (CD) airfoil were shown to add no extra noise sources and provided very similar aerodynamic performance compared to the straight edge (Sanjose *et al.*, 2014; Moreau *et al.*, 2019). The detail of cut-in and add-on teeth is shown in Figure 5.1. Note that to make a fair comparison, two baseline propellers are proposed. The original propeller (B) without any modification will serve as the baseline for the propellers with cut-in serrations, whereas a modified propeller with a flat plate add-on (BP) will be used to assess the add-on serrations.

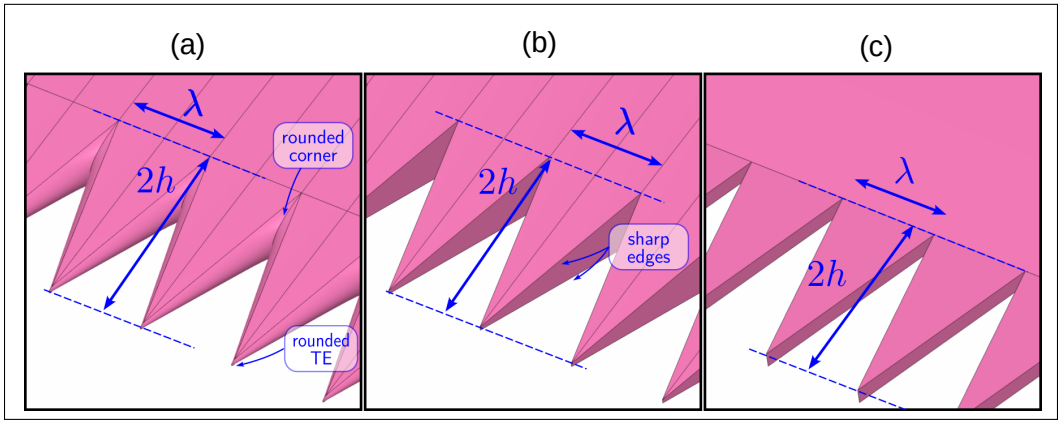

Figure 5.1 Serrations types: (a) cut-in smooth, (b) cut-in sharp and (c) add-on

Based on the RANS simulations in Chapter 4 (Sec. 4.3.4) the serration tip-to-root amplitude was set to 2h=5 mm and the wavelength to =2.5 mm. The thickness at the trailing edge was the

main manufacturing constraint and was initially set at a minimum of 0.1 mm. For propellers with cut-in serrations, the teeth are thicker at the root (1.4 mm), and the minimum thickness of 0.1 mm can be obtained at the tip. For the add-on cases, the tapered NACA 0012 profile end is replaced with a flat plate of constant thickness and sufficient length to allow for serration printing. The flat plate thickness was set to 0.4 mm, as lower values resulted in loss and/or detachment of teeth during printing. The resulting mean chords are the same as the baseline for the propellers with cut-in serrations. For the add-on cases, the NACA0012 profile is truncated at 96% of the chord and the resulting mean chord is 6% longer than the baseline.

Table 5.1 Serrated propeller test matrix

		Clean	**Tripped(T)**	**Designation**
Baseline	Straight edge	x	x	B-(T)
	Flat plate add-on	x	x	BP-(T)
Cut-in sawtooth	Sharp	x		C-ST-SH
	Smooth	x		C-ST-SM
Add-on	Square	x	x	A-SQ-(T)
	Sawtooth	x	x	A-ST-(T)

Additionally, given the fully turbulent assumption of the analytical models, the propellers with add-on serrations were manufactured in two configurations: a "clean" one and one with tripping cylinders at 10% of the chord. Following Gowree *et al.* (2023) design on a similar, albeit 3-bladed, NACA0012 propeller, the tripping height and diameter were set to 140 m and 1.37 mm, respectively, with a distance between cylinders of 2.54 mm. The complete test matrix is shown in Table 5.1. Figure 5.2 and Figure 5.3 show the baseline and serrated propeller tips and some blade planforms, respectively.

5.1.2 Propeller manufacturing

The propellers were manufactured using stereolithography (SLA) with the Form-3L 3D printer using the Formlabs RIGID 4000 resin. Several experimental campaigns (Gojon *et al.*, 2021; Gowree *et al.*, 2023; Li Volsi *et al.*, 2024) required manufacturing similar propellers and helped validate this process. SLA-printed objects are continuous and highly isotropic, enabling the

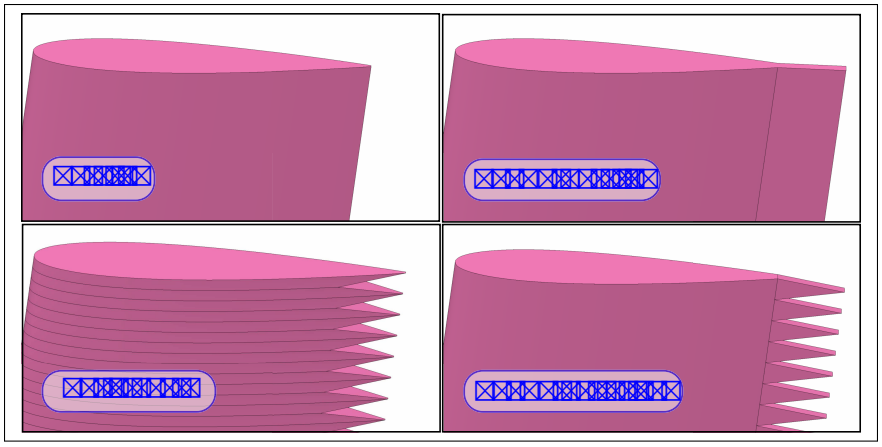

Figure 5.2 Tip view of baseline and serrated propellers

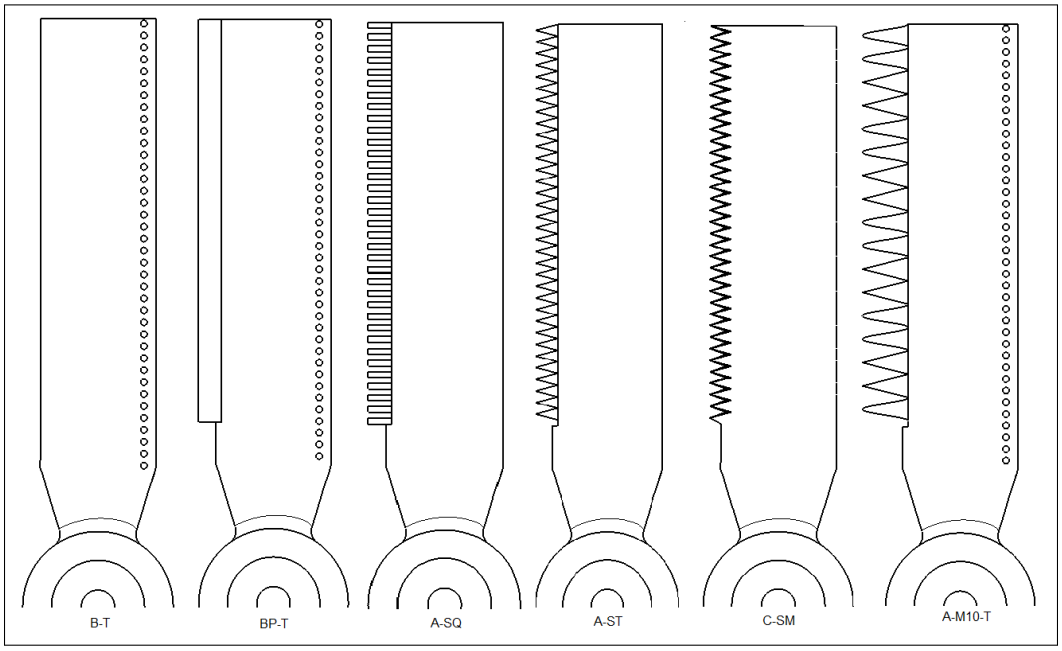

Figure 5.3 Planforms of some tested propellers: (a)straight-edge with trip (B-T) ,(b) add-on flat plate with trip (BP-T) ,(c) add-on square wave (A-SQ), (d) add-on sawtooth (A-SQ), (e), cut-in smooth serration (C-SM) and (f) Mixed sinousidal serrations with double amplitude and wavelength (A-M10-T)

creation of parts with smooth surface finishes and fine features. The precision is on the order of 0.1 to 0.3 mm for fine features and within 0.5% for larger dimensions.

As serrations are rather thin appendages (0.4 mm) and relatively long (5 mm), their manufacturing is challenging. The automatic algorithms of the printing software define the layout, orientation, and support of the print, but they yield excessive support on the serrations. Therefore, the support distribution was manually modified, by seeking a balance between supporting the part and placing supports on fragile parts. Finally, with a layer thickness of 0.1 mm, the printing time was around 20 hours for 4 propellers.

Following the printing, the rotors were washed with isopropyl alcohol to remove any resin remaining on the rotor surface. Then, they were UV-treated to finalize the polymerization process, and to improve part strength. The support structures required for the printing process were cut out, and lastly the propellers were hand-sanded, as it has been shown that surface roughness can impact rotor aerodynamics and acoustics (Gowree *et al.*, 2023; Pettingill, Zawodny, Thurman & Lopes, 2021). The final step was the static balancing of the rotors. Figure 5.4 shows the propeller with cut-in sharp serrations (C-SH). Figure 5.5 shows the propeller with an add-on plate (BP) during static balancing.

Figure 5.4 3D printed propeller with sawtooth cut-in sharp serrations (C-SH)

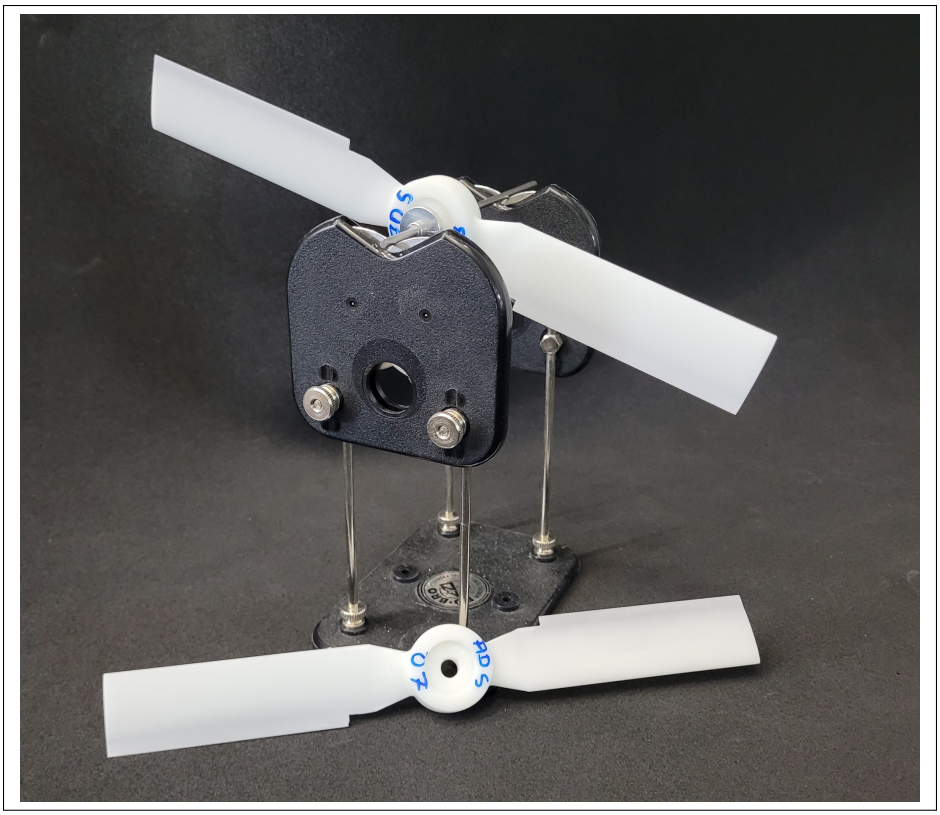

Figure 5.5 3D printed propeller with flat plate add-on (BP) during static balancing.

Serration design and manufacturing——————————————————————-Summary

- The serrations are sized based on the RANS-estimated boundary layer thickness of 5 mm from Chapter 4 at 6000 RPM. The wavelength is set such that the amplitude-to-wavelength ratio is 2.
- Cut-in (3D) and add-on(2d, flat-plate like) serrations are manufactured, with the trailing edge thickness being the main manufacturing constraint.
- The serrated propellers are manufactured with SLA in clean and tripped configurations. The latter only for add-on cases.

5.2 Experimental set-up and signal processing

The propellers were tested in the ISAE-SUPAERO anechoic room described in the previous Chapter (Figure 4.5) using the same motor and the same microphone array. Thrust and torque measurements were done with a six-axis ATI (Apex,NC) Nano 17 load cell.

5.2.1 Signal processing

Following the measurements, time-averaged thrust, torque, and power results were calculated and are presented in a dimensionless form for the thrust coefficient and the Figure of Merit , as defined in Eqs. (1.8) and (1.10) respectively.

For the acoustic results, the broadband component of the spectrum is necessary to assess the serration effect. The broadband component is obtained using a Savitzky-Golay filter (Savitzky & Golay (1964)), as implemented in the open-source signal processing library SciPy. The filter requires two parameters: the window length and the polynomial order. Tuning these two parameters results in filtering out the shaft and BPF harmonics, leaving the broadband signal.

The application of the Savitzky-Golay filter with a window spanning 500 samples and a polynomial order of 6 on the straight-edge propeller is shown in Figure 5.6 for different RPMs. The broadband signal shown in black in Figure 5.6 consists of two overlapping humps. The first one is between 1-10 kHz without any clear peaks (highlighted in grey zones), while the second one has several peaks, and their frequency depends on the RPM.

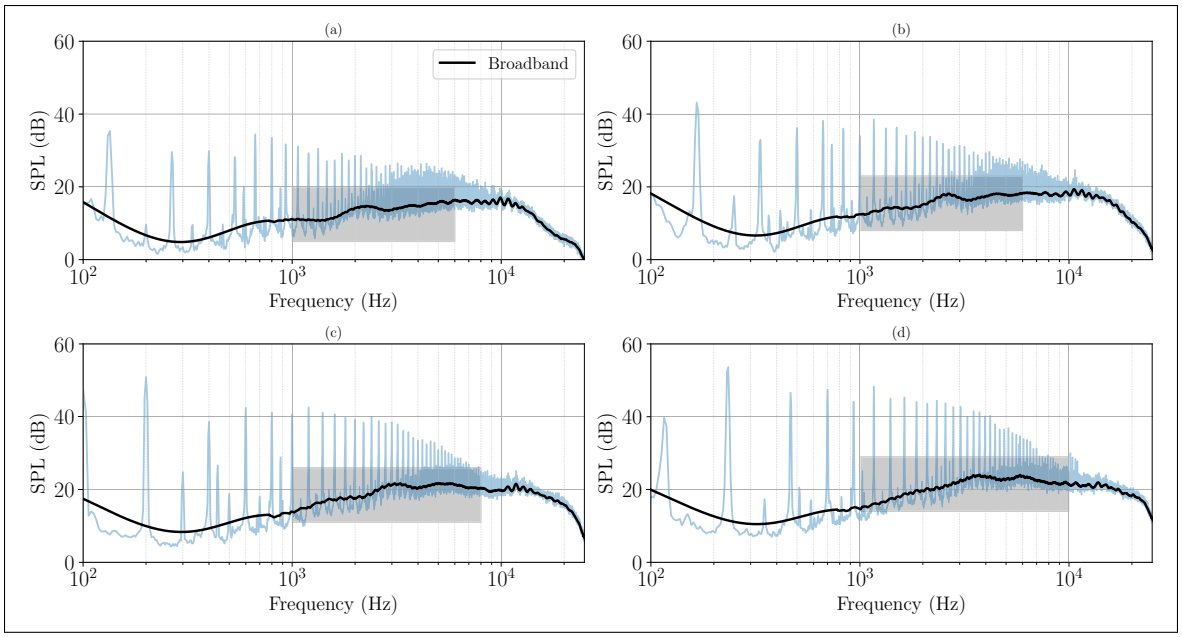

Figure 5.6 SPL and extracted broadband signal at 60 from the rotor plane for straight edge propeller at (a) 4000 RPM, (b) 5000 RPM, (c) 6000 RPM, and (d) 7000 RPM. The gray zones correspond to trailing edge noise from the turbulent boundary layer scattering.

When scaled with the fifth power of the blade velocity at 75% of span $_{75}$, the spectra at all RPM collapse as shown in Figure 5.7. This stresses the non-compact dipole nature of the source, and this hump can be attributed to trailing-edge noise. The second hump, however, does not follow this scaling, as it is the consequence of laminar boundary layer instability tones, as demonstrated next.

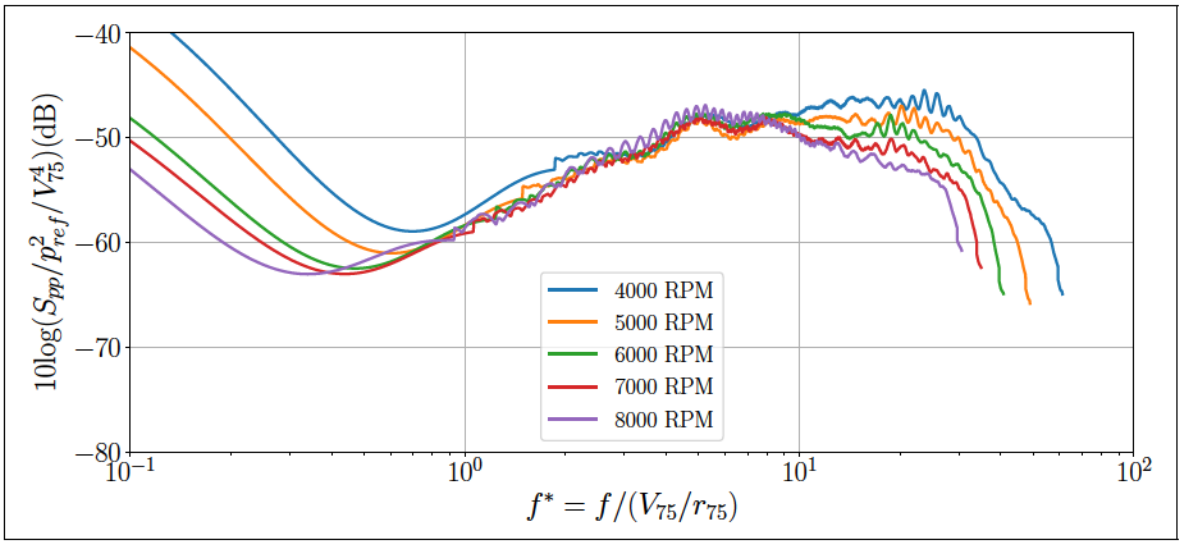

Figure 5.7 Scaled baseline broadband extracted spectra as a function of Strouhal number based on the blade velocity at 75% span (V_∞).

5.2.2 Baseline laminar boundary layer instability tones

The filtered spectra in Figure 5.6 and Figure 5.7 reveal well-defined peaks for most RPMs. These peaks are better visualized in Figure 5.8 (a), where a vertical offset has been added to the individual spectra to aid visualization. The number of peaks and their prominence decrease as the rotational speed increases, demonstrating a Reynolds number dependency. The identified tones are then scaled with the chord-based Reynolds number (top scale) in Figure5.8 (b). The tones follow the well-known ladder-type pattern, and a power fit reveals a dependency of $V_\infty^{0.8}$, in good agreement with the initial findings by Paterson *et al.* (1973a) and Tam (1974).

The good agreement with the scaling, along with the low Reynolds number, suggests that the tones are the consequence of an aeroacoustic feedback loop between the instabilities in the transitional boundary layer and the acoustic waves radiated from the trailing edge. The frequency between consecutive peaks at each RPM is almost constant and can be used to infer the feedback-loop length from the following relationship for the n^{th} tone (Yakhina *et al.* (2020); Arbey & Bataille (1983)):

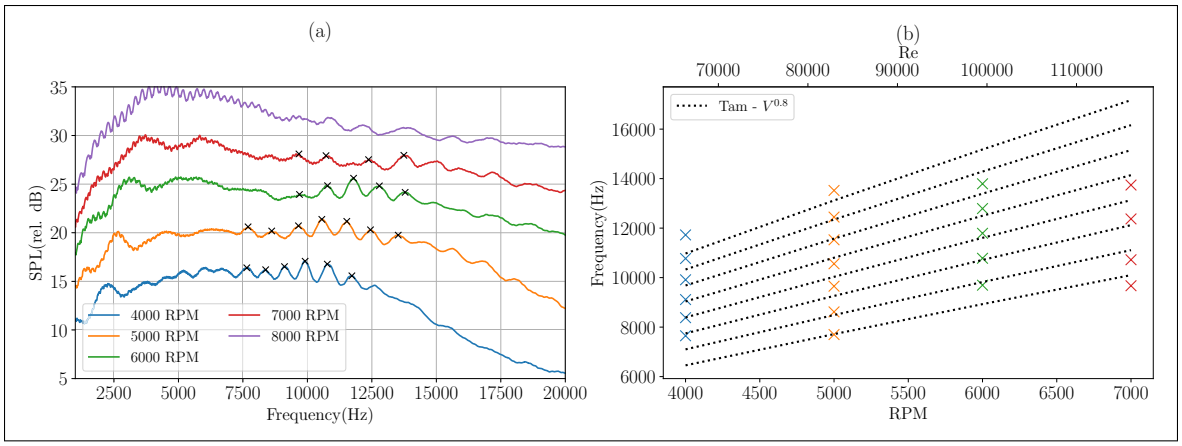

Figure 5.8 (a) Filtered spectra and laminar boundary layer tones at different RPM (with arbitrary SPL offset) and (b) tone scaling with Reynolds number.

$$\frac{1}{2} \quad \frac{1}{1} \qquad (5.1)$$

where , the ratio of the average instability convection speed to , is fixed to 0.4 Yakhina *et al.* (2020). By subtracting the equations between two consecutive tones, the following expression is obtained:

$$\frac{1}{1} \qquad (5.2)$$

Using the average distance between peaks in Figure5.8, the feedback-loop length, , is estimated to be 18.5, 19.7, and 22.2 mm for the 4000, 5000, and 6000 RPM cases, respectively. Note that all these values are lower than the propeller chord and increase with the Reynolds number, which suggests that the transition location moves upstream with increasing RPM.

Moreover, Pröbsting *et al.* (2015) identified different regimes of tonal noise on a NACA0012 airfoil depending on whether the tones come from the suction or pressure side, or both, as shown in Figure5.10. Since the airfoil section of the propellers used in the present study is NACA0012, an estimate of the effective angle of attack and Reynolds number along the span is required to use the regime chart.

In order to obtain an estimate of the effective angle of attack the RANS results from Chapter 4 are used. The first step in the calculation is to perform a meridional average of the flow through the propeller. Secondly, a line at a distance of 10% chord upstream of the propeller is chosen for the extraction of the velocities in the relative reference frame. The upstream velocity triangle then provides the angle δ as shown in Figure 5.9 (a). Since the blade pitch β is constant along the span, the effective angle of attack, α_{eff}, is easily calculated.

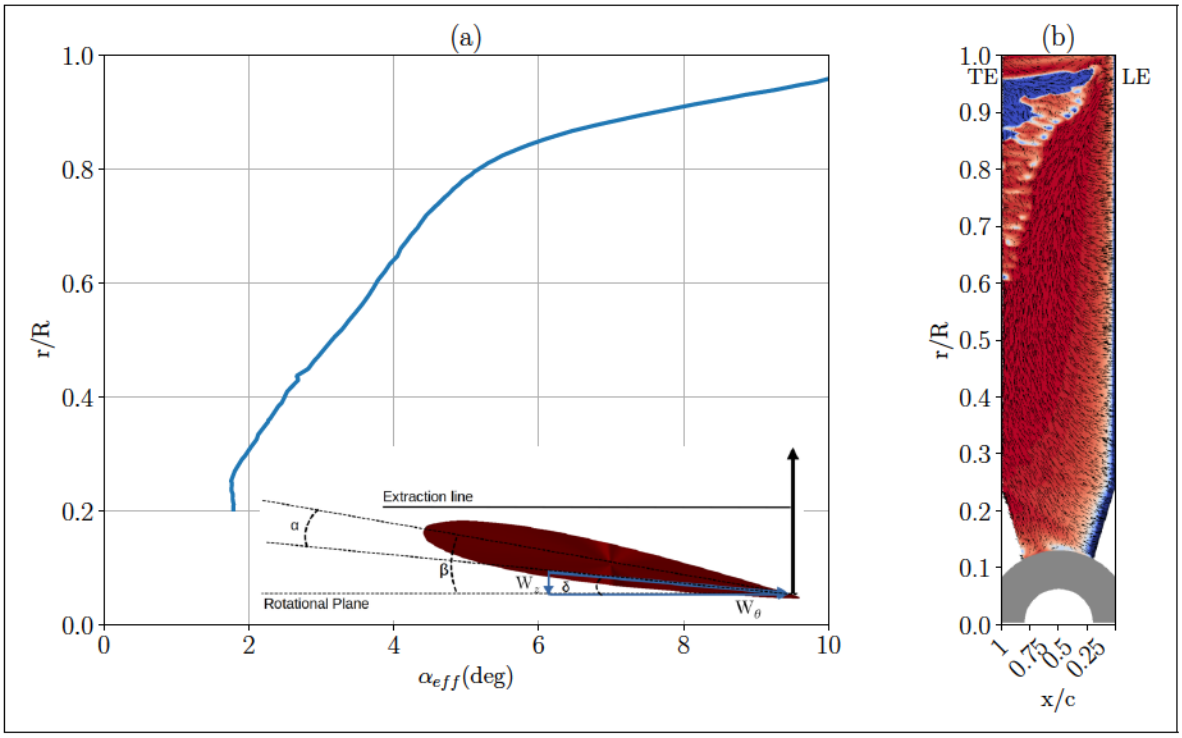

Figure 5.9 Effective angle of attack along the span. Miniature shows velocity triangle (a). Wall-shear stress streaklines imposed over contours of turbulence intermittency at 6000 RPM. Blue regions indicate turbulent flow, whereas red marks laminar flow (b).

The regions of transitional flow along the span are identified with the intermittency contours in Figure 5.9 (b). For r/R below 0.6, the boundary layer remains laminar; the region between 0.6 and 0.8 exhibits transitional flow; and the outermost part of the blade is fully turbulent. Therefore, the zones where the instabilities in the boundary layer might occur correspond to the region between 0.6 and 0.8. In this region, the effective angle of attack is between 3.5° and

5 . The effective angle of attack and Reynolds number are extracted and marked in green in Figure 5.10

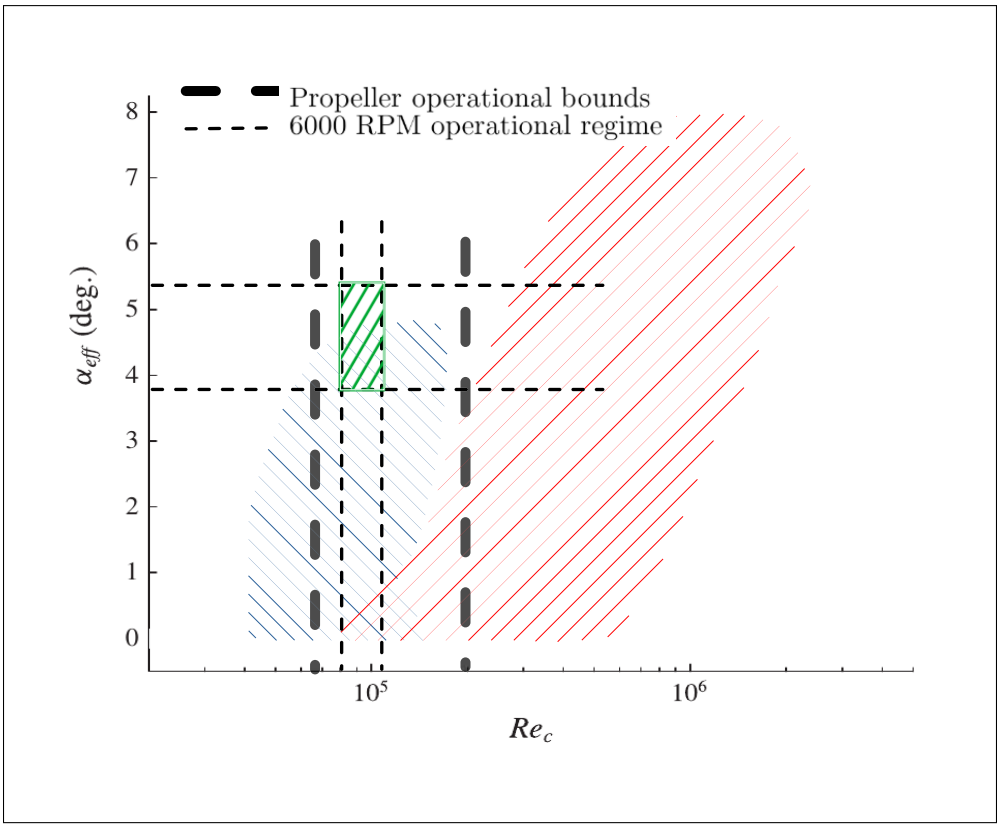

Figure 5.10 Regimes of tonal noise generation. Suction (blue, hatched) and pressure (red, hatched) side dominated.(Adapted from Pröbsting *et al.* (2015)). Zones of transitional flow in the propeller (green, hatched)

The green zone matches the suction-dominated regime, thus adding further evidence that the tones identified in the baseline spectrum come from instabilities in the transitional boundary layer on the suction side. Furthermore, as shown later, the filtered spectra for the suction side tripped propeller do not display these tones.

The frequency and levels of this noise source are highly dependent on the manufacturing process as noted by Thurman *et al.* (2024). To show the reproducibility of this phenomenon, the data set from three identically designed rotors in Gojon *et al.* (2021) will be used and designated JASA. The propellers materials, manufacturing details, and assembly method are summarized in Table

5.2. In the present study, the propeller was printed as a single piece, whereas the blades and hub were individually printed and assembled for the other propellers. Furthermore, as shown later, the filtered spectra for the suction side tripped propeller do not display these tones.

Table 5.2 Test matrix and designation for NACA0012 airfoil

Propeller	**Material**	**Printing direction**	**Assembly**
JASA 1	Rigid resin	1	3 pieces
JASA 2	Rigid resin	2	3 pieces
JASA 3	Grey resin	1	3 pieces
Present study	Rigid resin	NA	1 piece

Using the same filtering techniques described in the previous section, the filtered spectra and identified tones for the JASA propellers and the baseline propeller of the present study are shown in Figure 5.11 where the SPL of each propeller has been arbitrarily shifted to avoid cluttering. While all the propellers display peaks, their prominence differ. For example, the JASA-3 propeller peaks are well-defined, with an easily identifiable central peak. In contrast, the peaks from the JASA-1 propeller are of lower amplitude. Additionally, the peaks for all the JASA propellers are identified at similar frequencies, whereas the peaks in the present study's propeller occur at higher frequencies. Despite the frequencies not matching, the average peak separation of all identified peaks is on the same order of magnitude. Lastly, note that the hump peak shifts from propeller to propeller. Given that the geometry is identical, this can be attributed primarily to material, printing, and assembly methods, all of which can directly impact the blade's surface finish and, consequently, the evolution of the transitional regions along the blade.

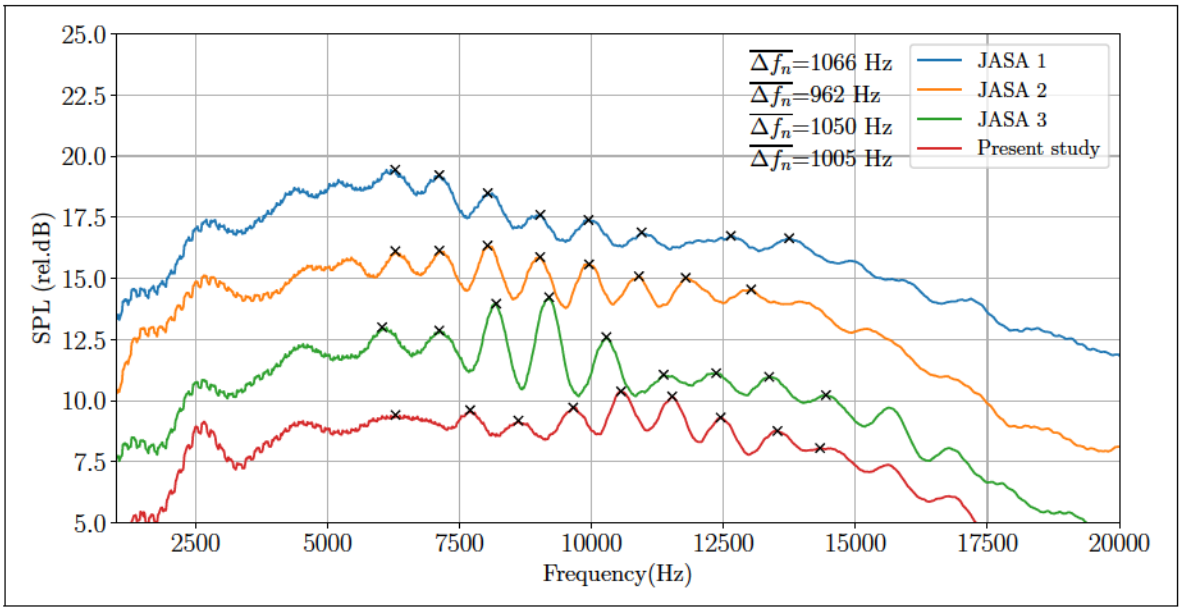

Figure 5.11 Filtered spectra and peaks for JASA propellers and present NACA0012 propeller.

Baseline noise sources——————————————————-Summary

- The broadband component of the NACA0012 baseline rotor comprises two humps.
- The first one, due to the scattering of the turbulent boundary layer dominant in frequencies between 1-10 kHz.
- The second one, due to instabilities in laminar boundary layer dominates beyond 10 kHz.
- The humps contain tones that scale as $V^{0.8}$ in good agreement with the airfoil observations.
- small differences in manufacturing method or material have an impact in the hump frequency content.

5.3 Experimental results

The results for the cut-in serrations are presented first, followed by the add-on ones. Then, the effects of the tripping cylinders on the baselines and the add-on serrated propellers are discussed. Lastly, a comparison with the theoretical noise reductions is made for all cases.

5.3.1 Cut-in serrations

In this section, the aerodynamics and acoustic effects of cut-in trailing edge serration are discussed. The serrations are either sharp or smooth as summarized in Table 5.1. To investigate the impact of the 3D printing method, two samples of each serrated rotor have been manufactured and compared here.

Figure 5.12 shows the thrust coefficient and the Figure of Merit for straight-edge (B), sharp (C-SH), and smooth (C-SM) cut-in serrated propellers. Two sets of results are shown for the sharp and smooth serrated propellers, corresponding to data obtained for each sample. Li Volsi *et al.* (2024) performed an uncertainty quantification analysis on the same test stand and on a similar propeller by repeating aerodynamics measurements at the same RPM. Using their measured mean and standard deviations, the aerodynamic loads relative uncertainties were calculated and scaled by the present results for the straight-edge propeller. The results of this linear scaling are presented with error bars corresponding to a confidence interval of 95%.

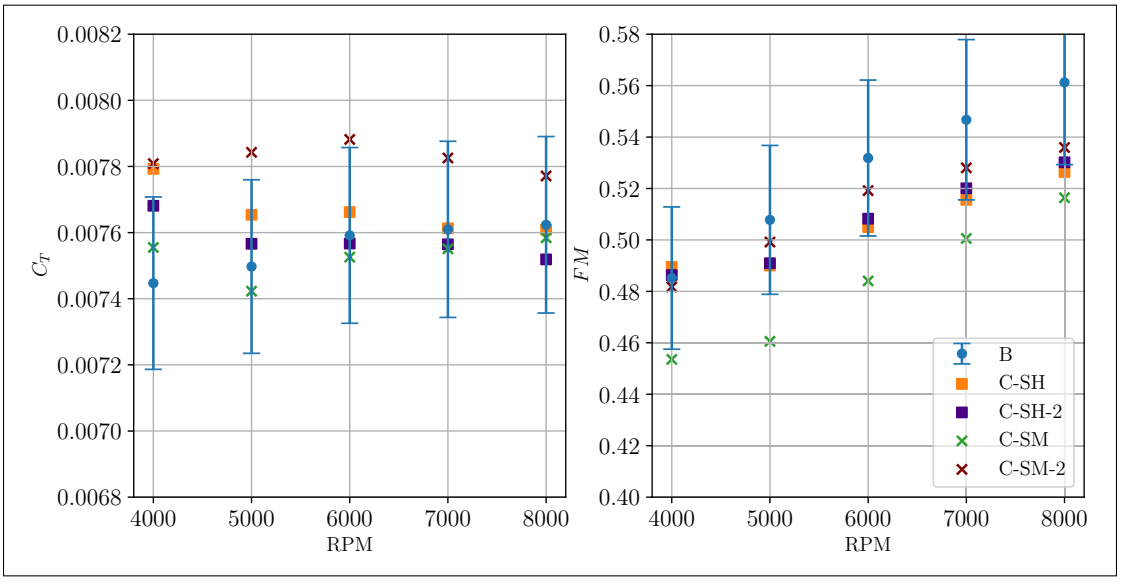

Figure 5.12 (a) Thrust coefficient and (b) Figure of Merit for propellers with a straight edge (B), sharp (C-SH), and smooth (C-SM) cut-in serrations.

In terms of repeatability, the differences between the sharp-teeth propellers are found to be less than the ones between the smooth-teeth ones, with an average relative difference of less than 2%

for the former and 4% for the latter. The geometrical complexity of the smooth teeth may explain this trend. Below 6000 RPM, all the serrated propellers are seen to fall within the baseline uncertainty range, except for one of the smooth cases. At the highest RPM, the sharp and smooth cases have a 5% and an 8% decrease in the FM, respectively, for the worst-performing samples. These results highlight the importance of assessing the repeatability of the manufacturing method for serrated propellers, as minor changes in the teeth geometry may give large uncertainties in performance estimates.

To assess the impact of the manufacturing method on the far-field acoustics, the sound pressure levels (SPL) or spectra at 60 from the rotor plane of the two samples are compared in Figs. 5.13 and 5.14 for sharp and smooth cut-in designs, respectively. Note that this observer position will be used for all spectrum comparisons since trailing edge noise is expected to contribute more to the overall spectrum compared to positions closer to the rotational plane.

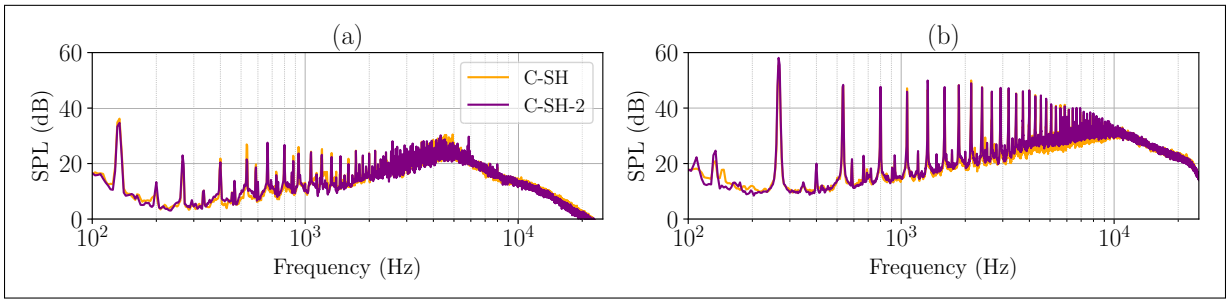

Figure 5.13 SPL at 60 from the rotor plane for propellers with sharp cut-in serration (a) 4000 RPM and (b) 8000 RPM.

Unlike the aerodynamic performances, the relative SPL differences between samples of the same geometry are less pronounced, particularly at high RPM. In the following analysis, the C-SH and C-SM samples are used to compare with the straight edge case.

The spectra at 60 from the rotor plane at four rotational speeds between 4000 and 7000 RPM are shown in Figure 5.15 for the same geometries. Overall, the broadband noise levels are increased for both serration designs compared to the baseline. Only at high frequencies can both the sharp and smooth serrations reduce broadband noise levels, and the frequency at which they

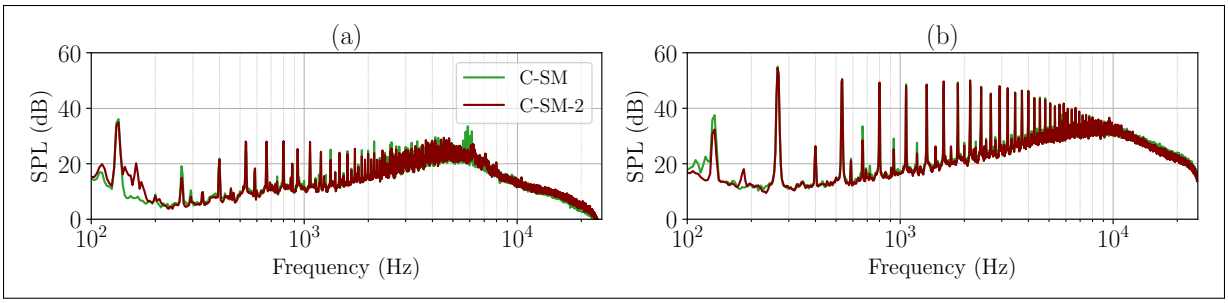

Figure 5.14 SPL at 60 from the rotor plane for propellers with smooth cut-in serration (a) 4000 RPM and (b) 8000 RPM.

do so depends on the RPM, which is in good agreement with the findings in Pang *et al.* (2018); Yang *et al.* (2020). Additionally, the serrated rotors radiate less than the baseline case at the BPF harmonics at lower speeds.

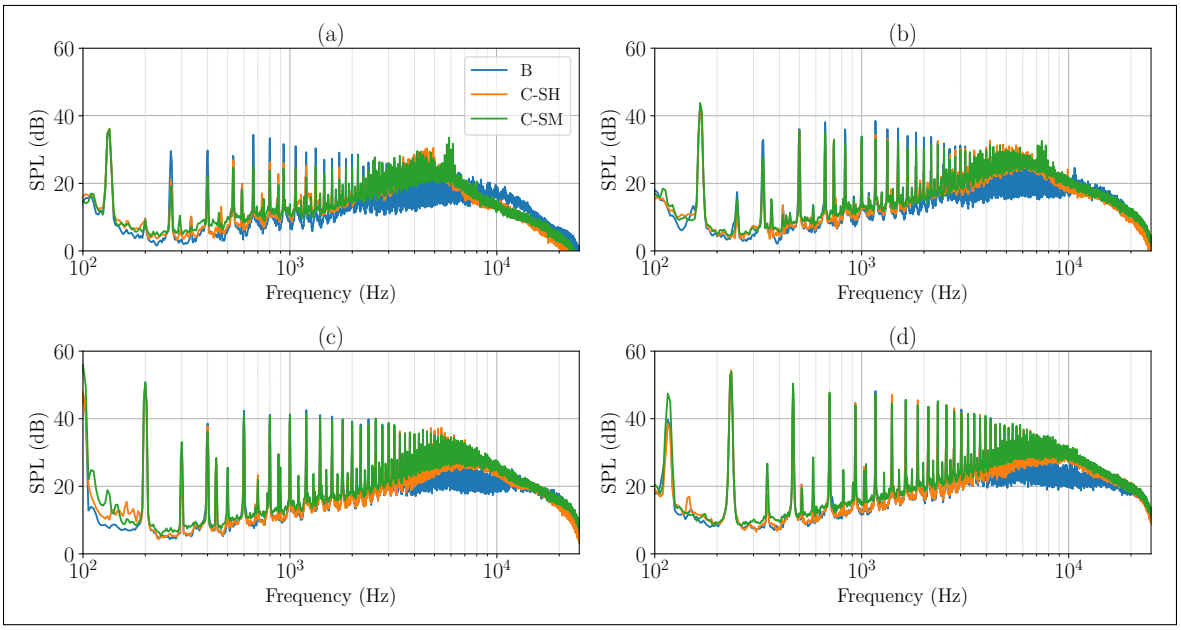

Figure 5.15 SPL at 60 from the rotor plane for straight edge propeller(B) and cut-in sharp (C-SH) and smooth (C-SM) serrations for (a) 4000 RPM; (b) 5000 RPM, (c) 6000 RPM; and (d) 7000 RPM.

Noise increase due to cut-in serrations in airfoils was measured by Chong *et al.* (2013) and ascribed to vortex-shedding noise emanating from the serration root. Given the three-dimensionality and considerable bluntness (5%) of the serrations for the cut-in cases, the filtered spectra of

the propellers are analyzed next to confirm if the noise increase is indeed due to vortex-shedding. Figure 5.16 (a) shows the extracted broadband signal for the straight, cut-in sharp, and cut-in smooth propellers with varying RPM. An arbitrary offset between each curve has been added for better visualization. The humps peak frequency changes with RPM, and it is slightly shifted for the sharp and smooth serrations. The Strouhal number ( ) is computed from the peak frequencies, the serration root thickness , and the blade speed at 75% of the span and plotted as a function of the Reynolds number and RPM, as shown in Figure 5.16 (b).

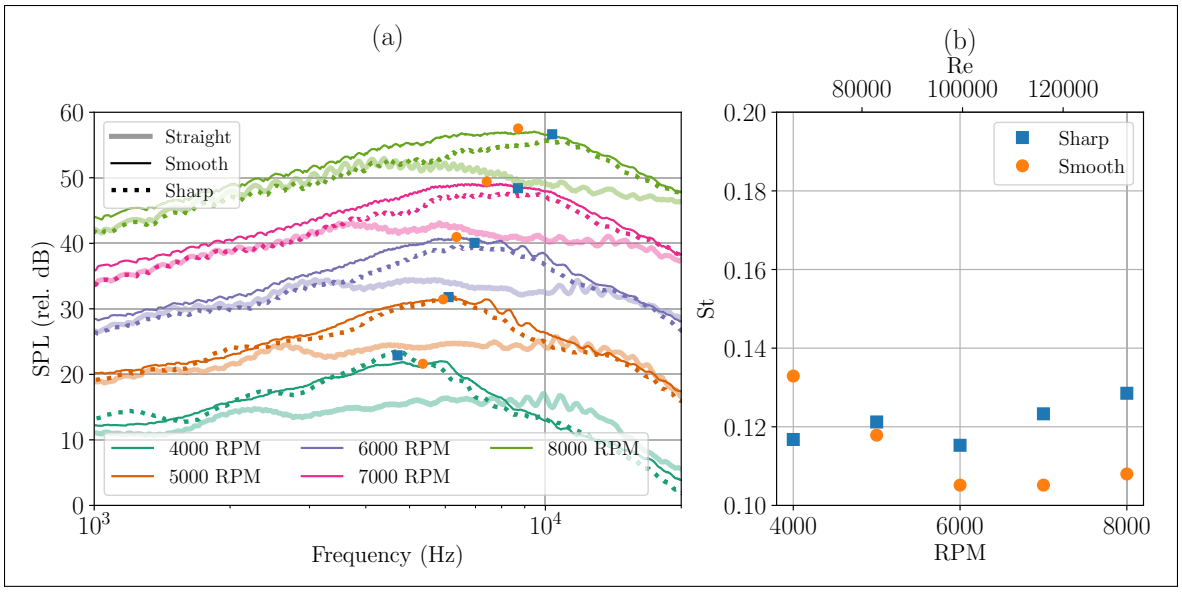

Figure 5.16 (a) Filtered spectra for straight, cut-in sharp and cut-in smooth propellers at different RPMs (with arbitrary SPL offset) .(b) Strouhal number for the peak frequency as a function of Reynolds number

The scaling reveals two different behaviors for each serration type. In the case of sharp serrations, the values are in the neighborhood of 0 12 with a slight tendency to increase with Reynolds number, whereas the smooth serrations do not have a discernible trend. The behavior in the latter case is attributed to the more complicated geometry of the smooth teeth as the current rotor scale could not fully alleviate the sharp or blunt edges as in the previous CD airfoil (Sanjose *et al.*, 2014; Moreau *et al.*, 2019). Note that for the sharp serrations, the values are in fair agreement with the values reported by Chong *et al.* (2013) for airfoils, with the caveat that their serrations were sharper (i.e. smaller serration wavelength) and the lowest tested Reynolds number was

200,000. Therefore, the cut-in serrations increase noise mainly caused by vortex-shedding phenomena.

Moreover, the results in Figure 5.16 (a) suggest that at low RPMs, the cut-in serrations can eliminate the laminar boundary-layer instability tones. This serration effect is in good agreement with the experimental and numerical results by Chong *et al.* (2013), Moreau *et al.* (2016) and Gelot & Kim (2020) on an airfoil. In the latter study, the authors suggested that the serrations weaken the aeroacoustic feedback loop at the source via two mechanisms: first, a reduction of the wall-pressure fluctuations close to the trailing edge, and second, an early breakdown of the spanwise coherence length.

Directivity patterns for the BPF, the extracted broadband noise, and the overall sound pressure level (OASPL) are shown in Figure 5.17. The broadband noise is calculated between 1000-16000 Hz, and the OASPL is calculated between 80-16000 Hz following Gojon *et al.* (2021) and Gowree *et al.* (2023). The same trend as above is seen for all angular positions: an overall increase of the broadband noise component at all speeds. At the BPF, the serrated propellers produce similar noise levels, whereas the baseline propeller radiates less at lower RPM, with all curves collapsing as the RPM increases. A similar trend is observed for the OASPL, noting that the directivity pattern changes as the RPM increases, signaling a change in the dominant noise source from tonal to broadband (mostly TEN).

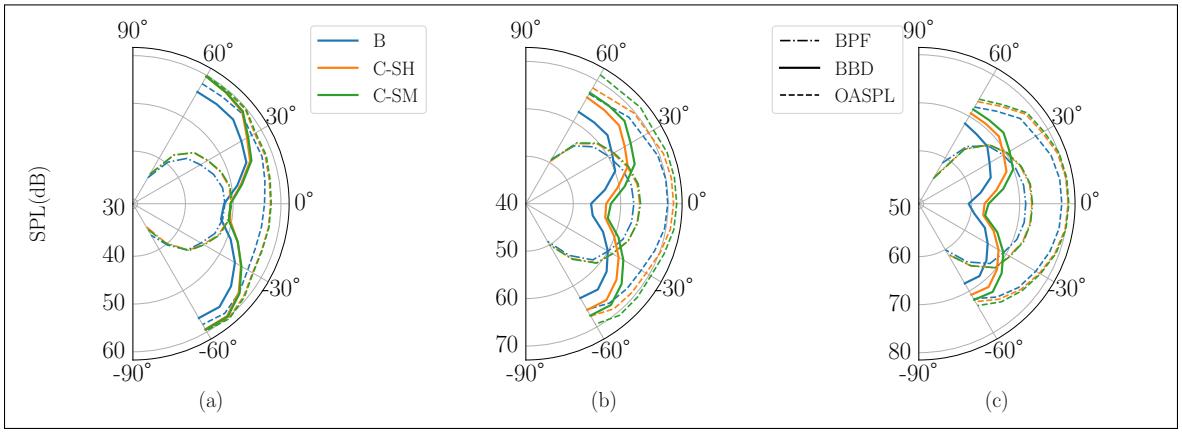

Figure 5.17 BPF, Broadband and OASPL directivity for straight edge (B), sharp (C-SH) and smooth (C-SM) cut-in serrations at (a) 4000 RPM; (b) 6000 RPM and (c) 8000 RPM.

5.3.2 Add-on serrations

The add-on serrations required a significant modification of the airfoil profile by adding the flat plate at the trailing edge with sufficient thickness to be 3D printed. Therefore, it is necessary to consider the aerodynamic and acoustic effects of the plate itself. Figure 5.18 shows the thrust coefficient and figure of merit for the baseline (B), the baseline with flat plate appendix (BP), and the add-on serrations (A-ST). The discontinuity in the profile shape tangent at the rear of the airfoil results in a reduction of aerodynamic performance, as seen by a lower figure of merit at all RPMs. Since the serrated plate has less surface area than the original flat plate appendix, the figure of merit is slightly improved for the serrated propeller (A-ST) compared to the flat plate add-on (BP), while the thrust coefficient is unchanged.

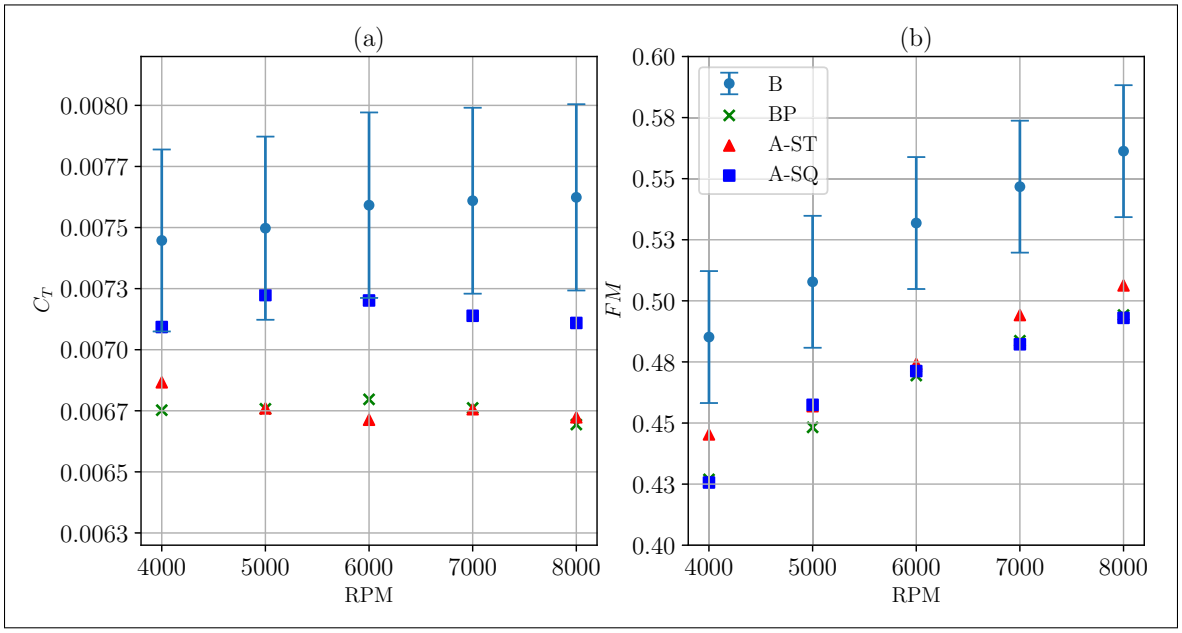

Figure 5.18 (a) Thrust coefficient and (b) Figure of Merit for propellers with a straight edge (B), add-on flat plate (BP), add-on sawtooth serrations (A-ST) and add-on square wave serrations

The acoustic effects of the add-on plate and serrations are shown in Figure 5.19 for an observer at 60 from the rotor plane and at different RPMs.

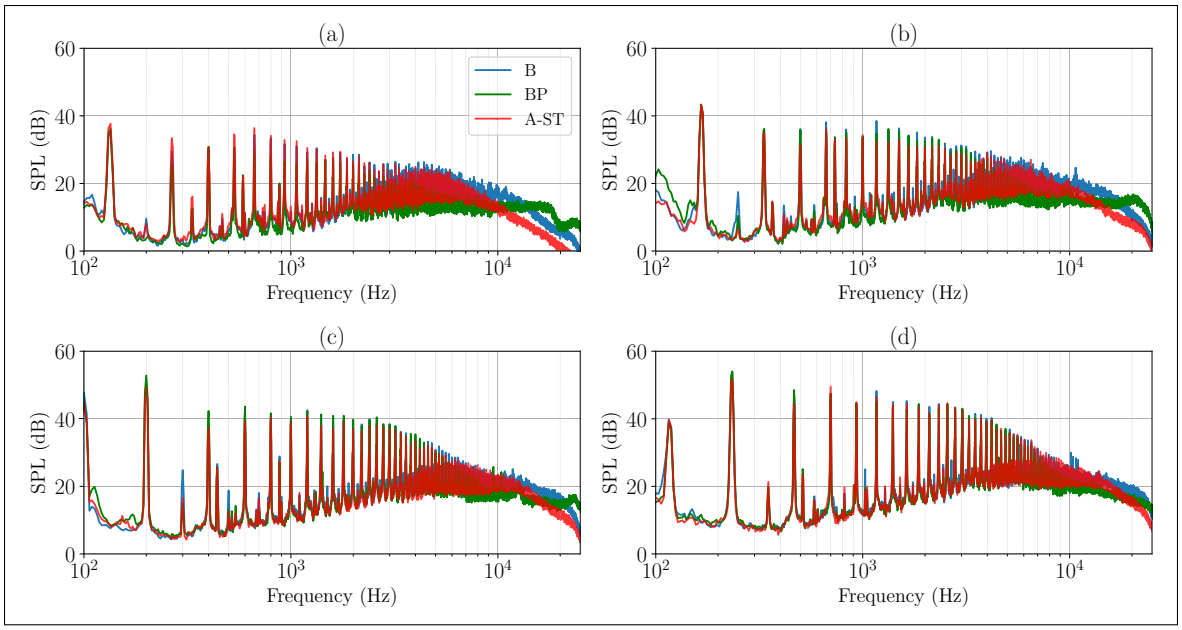

Figure 5.19 SPL at 60 from the rotor plane for propellers with a straight edge(B), add-on flat plate (BP), and add-on serrations (A-ST) for (a) 4000 RPM; (b) 5000 RPM; (c) 6000 RPM; and (d) 7000 RPM.

The presence of the flat plate alone reduces broadband noise below 10 kHz at all RPM and seems to be more effective than the serrated propeller for most frequencies of interest, albeit with some significant noise increase at very high frequencies. The reason behind the good acoustic performance of the propeller with the add-on plate could be attributed to an improved pressure recovery along the suction side, thanks to the add-on flat plate. The adverse pressure gradient indeed has a strong influence on the wall-pressure spectra, hence resulting in the observed beneficial acoustic effect. The frequency range at which the serrations are effective depends on the RPM, as it did for the cut-in serrations. Additionally, the propeller with the add-on serrations (A-ST) eliminates the noise caused by the laminar boundary layer instabilities on the baseline (B), again in agreement with the airfoil results (Chong *et al.*, 2013; Moreau *et al.*, 2016; Gelot & Kim, 2020).

The BPF directivity is shown in Figure 5.20 for the same propellers. It is noted that the propeller with the add-on plate, radiates less at positions below the rotor plane for the 4000 and 6000

RPM cases. The serrated propeller increases the BPF noise by a small amount at certain angles for some RPM and vice versa, without any discernible trend.

Both the propeller with the add-on plate and the add-on serrations reduce broadband noise at low RPMs as shown in Figure 5.20. The reduction is larger at higher elevation angles and decreases with increasing RPM. Notice that the reduction in broadband noise from add-on propellers is larger than the one from cut-in serrations when compared to their respective baselines. Thus, how the serrations are installed is crucial and must be assessed during the design phase.

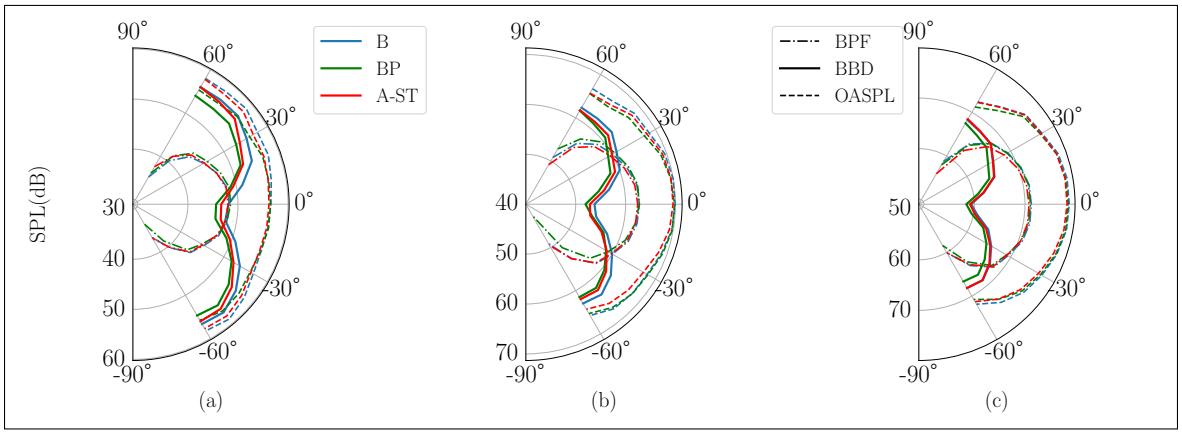

Figure 5.20 BPF, Broadband, and OASPL directivity for propellers with a straight edge(B), add-on flat plate(BP), and add-on serrations(A-ST) for (a) 4000 RPM; (b) 6000 RPM, and (c) 8000 RPM.

5.3.3 Effect of serration shape

The effect of serration shape on the far-field acoustics is shown in Figure 5.21 for the sawtooth and square wave serrations. While both shapes increase broadband noise compared to the case of the plate, the sawtooth performs better than the square wave. This is in contrast to the expected benefits from the square wave serrations, as demonstrated experimentally in Chapter 3, on the one hand, and from the theoretical predictions in Chapter 4, on the other. The reasons for this disagreement are hypothesized to be related to the difficulties during the manufacturing process of the square wave. Several attempts were required to guarantee the integrity of the teeth, and even after a successful print, some teeth were damaged during the detachment process. Further

research is required to leverage the potential noise mitigation from the square wave when applied for propellers.

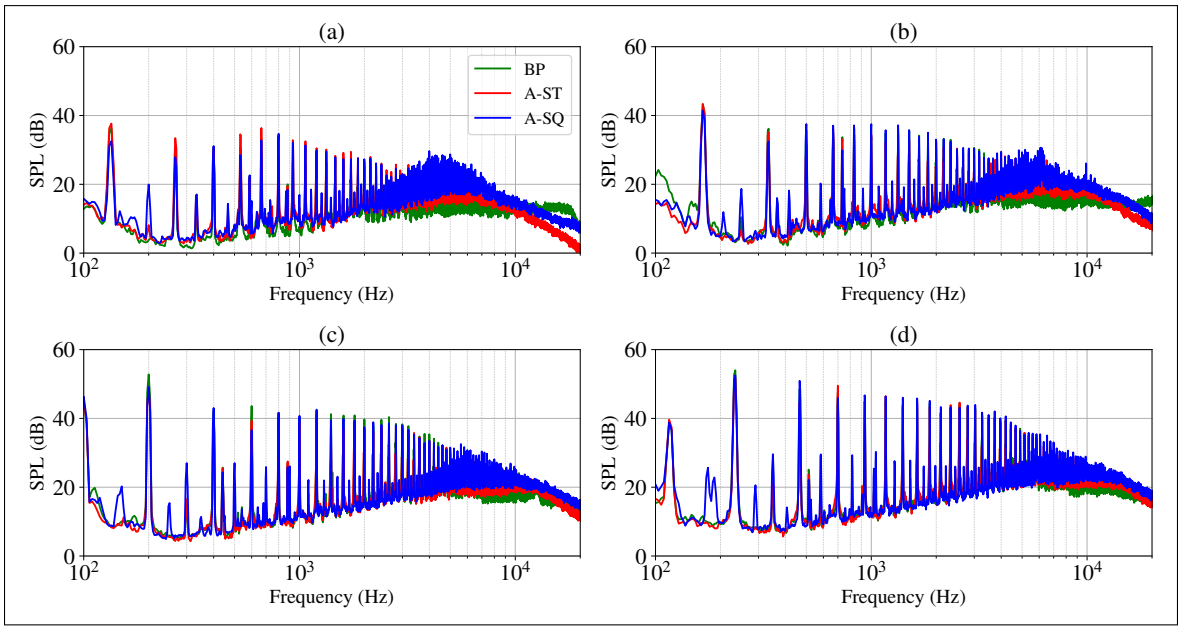

Figure 5.21 SPL at 60 from the rotor plane for propellers with add-on flat plate (BP), and add-on sawtooth serrations (A-ST) and add-on square wave serrations (A-SQ) for (a) 4000 RPM; (b) 5000 RPM; (c) 6000 RPM; and (d) 7000 RPM.

5.3.4 Effects of forced transition

First, the original baseline propellers (with and without add-on plate) are compared with their tripped counterparts. From an aerodynamics point of view, the presence of the cylinders has two effects: first, they create excrescence drag, and second, they force turbulent flow over the blade. These two effects combined yield lower aerodynamic performance. This is confirmed in Figure 5.22, where both the thrust and the figure of merit are lower for the tripped case (B-T) at all RPMs when compared to the baseline (B). This is in good agreement with the original results from Gowree *et al.* (2023). Interestingly, this trend is not followed for the add-on plate tripped (BP-T) case, which generates the most thrust and has the second-best Figure of Merit from all the baselines. Additionally, it is noted that while the relative difference between the

baseline (B) and its tripped twin (B-T) is constant throughout the RPM range, the gap between the clean and tripped baseline with the plate reduces with increasing RPM.

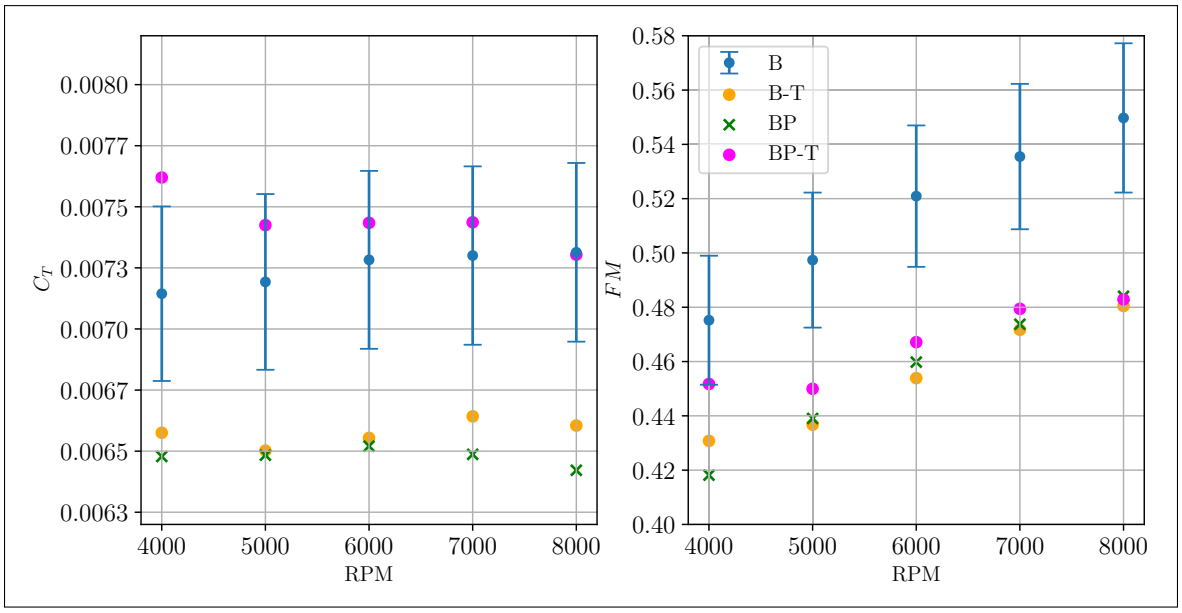

Figure 5.22 (a) Thrust coefficient and (b) Figure of Merit for clean and tripped propellers with a straight edge (B, BT) and add-on plate (BP, BPT)

The impact of the tripping cylinders on the far-field acoustics is shown in Figs. 5.23 and 5.24 for the baseline and for the propeller with an add-on flat plate, respectively. For the former, the forced transition is seen to reduce broadband noise, particularly at low RPM. As demonstrated in the previous section, this is due to the elimination of laminar boundary layer instability tones; the same explanation was suggested by Gowree *et al.* (2023). Note that the presence of a laminar separation bubble (LSB) around mid-chord has also been confirmed recently by high-fidelity simulations (Vittal-Shenoy, Gojon, Jardin & Jacob, 2022; Rendon *et al.*, 2024)

The spectra for the clean and tripped propeller with the add-on plate show a different behavior. At 4000 RPM, the tripped case reduces broadband noise below 8 kHz, then there is a noise increase between 8-15 kHz due to a hump centered at 12 kHz and a reduction beyond this range. Similar trends are observed at different RPMs. It is hypothesized that the junction modifies the boundary layer and thus its scattering at the plate edge deviates from a fully turbulent boundary layer. Future numerical simulations will investigate such effects in detail.

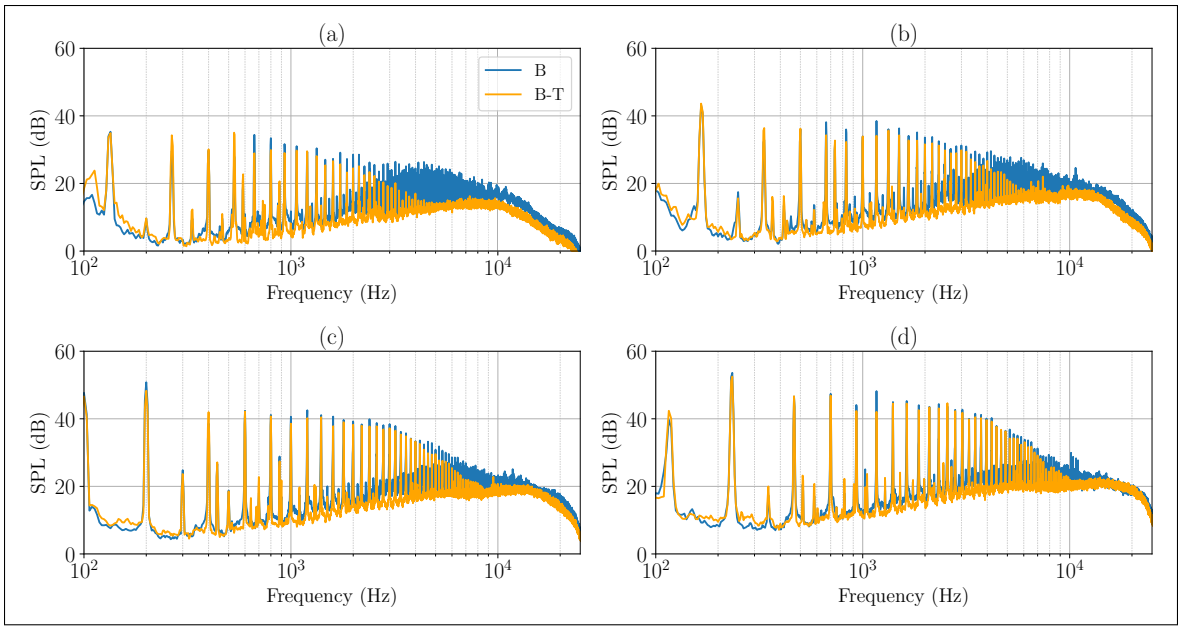

Figure 5.23 SPL at 60 from the rotor plane for clean (B) and tripped (BT) propellers with a straight edge (a) 4000 RPM, (b) 5000 RPM, (c) 6000 RPM, and (d) 7000 RPM.

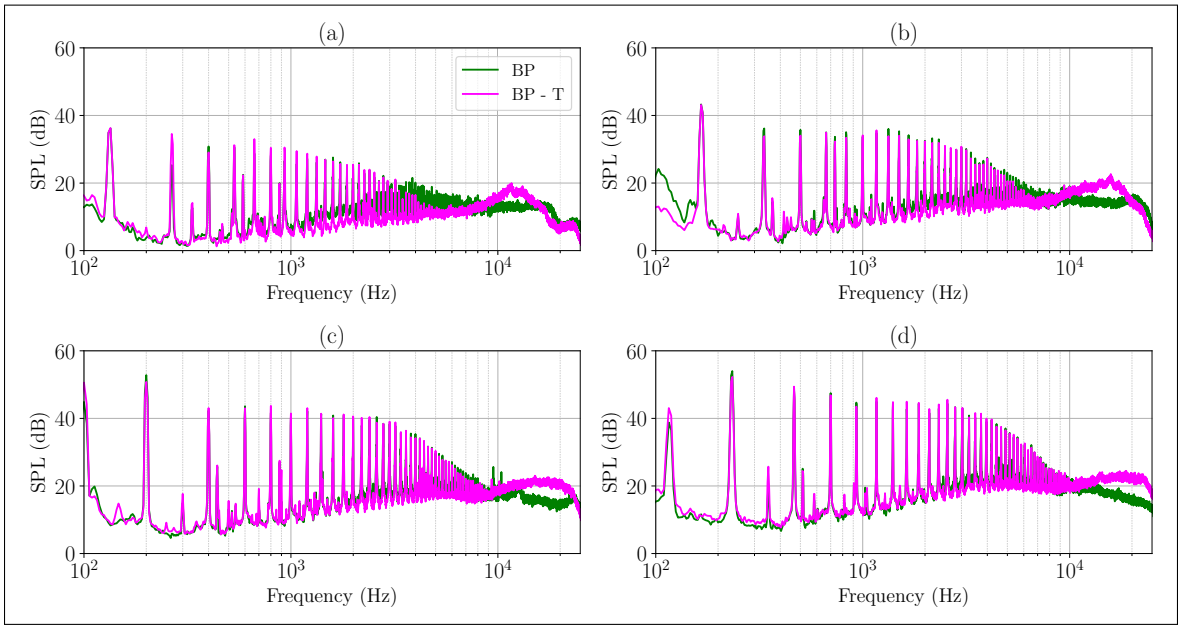

Figure 5.24 SPL at 60 from the rotor plane for clean (BP) and tripped (BP-T)propellers with an add-on flat plate (a) 4000 RPM, (b) 5000 RPM, (c) 6000 RPM, and (d) 7000 RPM.

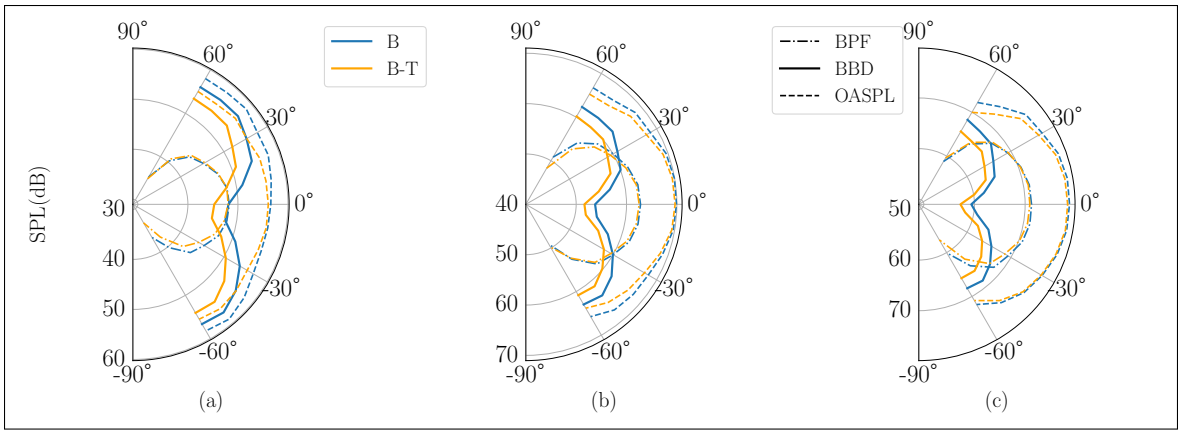

Figure 5.25 BPF, Broadband, and OASPL directivity for clean(B) and tripped(BT) propellers with a straight edge (a) 4000 RPM, (b) 6000 RPM and (c) 8000 RPM.

While the forced transition reduces broadband noise, its effect on the BPF is almost negligible for both the baseline and the propeller with the add-on plate as shown in Figures 5.25 and 5.26 respectively. Regarding the OASPL, the tripped baseline (B-T) has the lowest noise levels at 4000 RPM closely followed by the baseline with the add-on plate. The noise reductions from the add-on plate with the trip at lower frequencies are almost outweighed by the aforementioned secondary hump and match the levels of the baseline for observers close to the rotational plane.

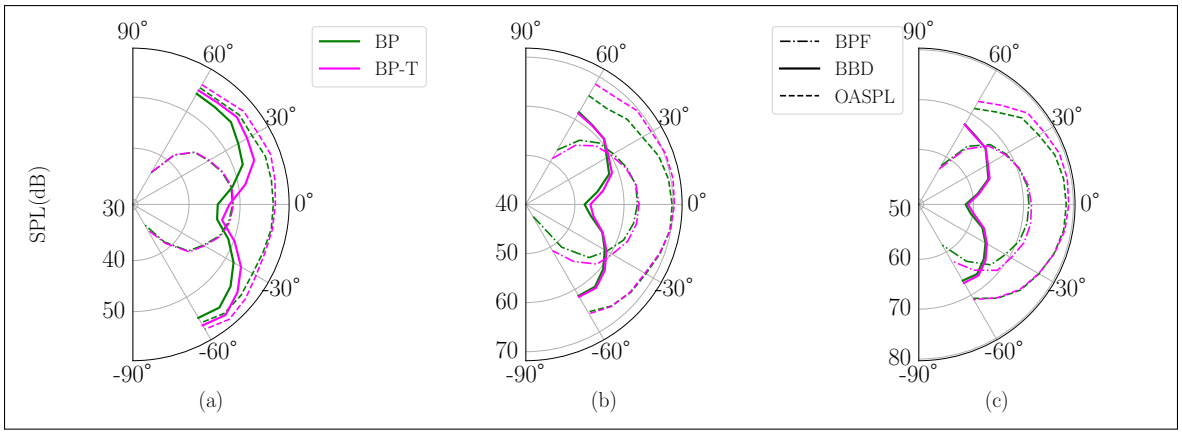

Figure 5.26 BPF, Broadband, and OASPL directivity for clean(BP) and tripped (BP-T) propellers with an add-on flat plate (a) 4000 RPM, (b) 6000 RPM, and (c) 8000 RPM.

5.3.5 Effects of forced transition and serrations

This section presents the effects of adding tripping cylinders to the propeller with add-on serrations. Starting with the aerodynamics in Figure 5.27, it is noticed that the propeller with the add-on flat plate and the trip (BP-T) generates more thrust at all RPMs, while the values for the rest of the propellers tend to collapse at higher RPMs.

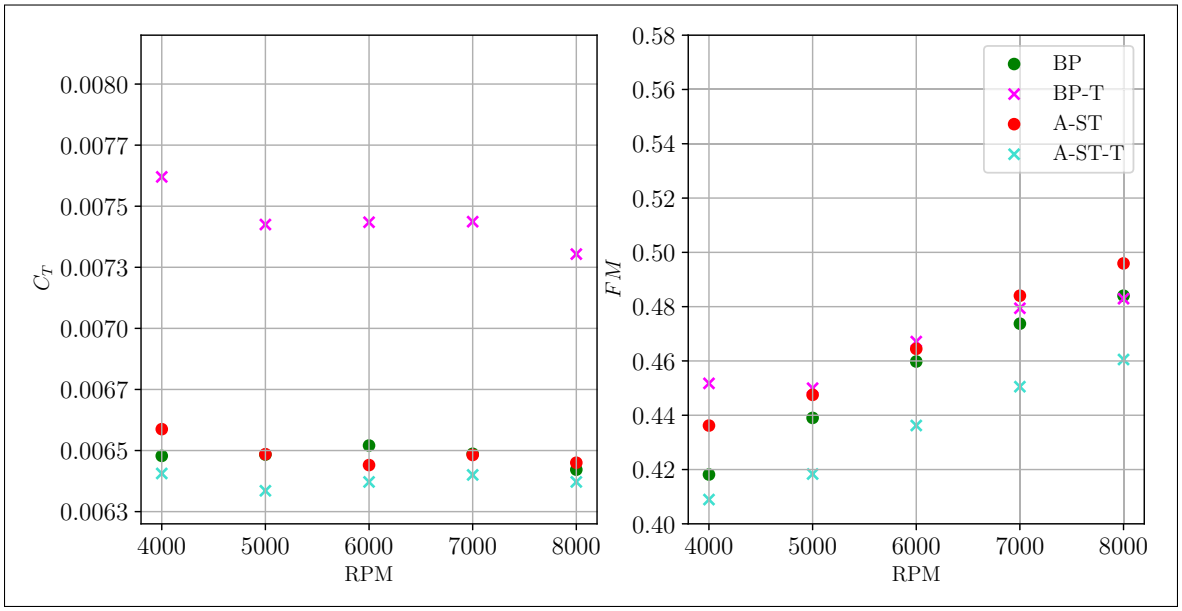

Figure 5.27 (a) Thrust coefficient and (b) Figure of Merit for clean and tripped propellers with an add-on plate (BP, BP-T) and add-on serrations(A-ST, A-ST-T)

For the Figure of Merit, the tripped propeller with the serrations (A-ST-T) has the worst performance. The tripped propeller outperforms the rest for RPMs below 6000 after which the serrated propeller (A-ST) attains higher values.

The spectra in Figure 5.28 show that the compound effect of the trip and the serrations (A-ST-T) results in noise reductions over the whole frequency range at all RPMs, noting that the tripped propeller with the add-on plate (BP-T) slightly outperforms the rest in the low-frequency range. Additionally, the humps beyond 10 kHz in the add-on tripped case are not present in either of the serrated cases, suggesting that the serrations eliminate the LSB as mentioned in the previous section.

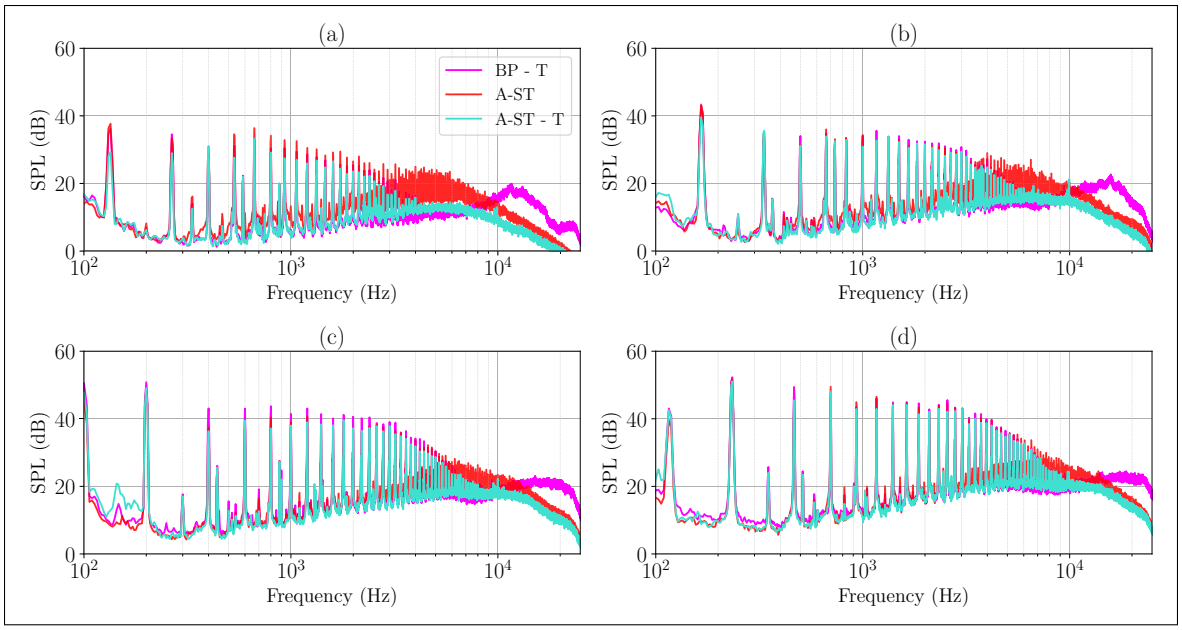

Figure 5.28 SPL at 60 from the rotor plane for clean and tripped propellers with add-on serrations (A-ST, A-ST-T) and for the tripped propeller with add-on flat plate(BP-T) at (a) 4000 RPM, (b) 5000 RPM, (c) 6000 RPM, and (d) 7000 RPM.

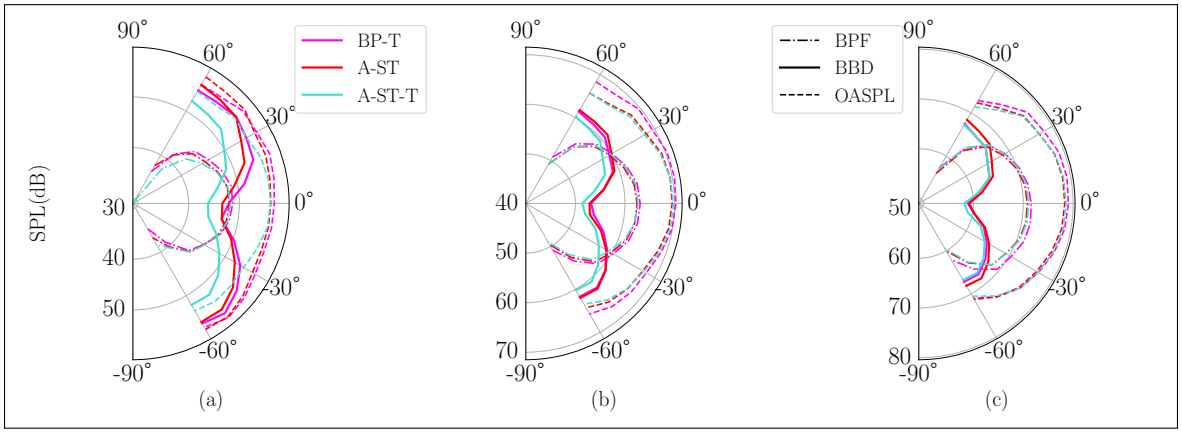

Figure 5.29 BPF, broadband, and OASPL directivity for clean and tripped propellers with add-on serrations (A-ST, A-ST-T) and for the tripped propeller with add-on flat plate(BP-T) at (a) 4000 RPM, (b) 6000 RPM, and (c) 8000 RPM.

The propeller with add-on serrations and forced transition also outperforms the rest in terms of radiated tonal noise as shown in Figure 5.29 and consistently reduces noise over the frequency range of interest particularly at high elevation angles. Overall, with an aerodynamic penalty of

about 4% in the Figure of Merit, the propeller with add-on serrations and with the trip (A-ST-T) can reduce tonal and broadband noise at all RPMs, although such reductions decrease with increasing rotational speed.

To conclude this experimental result section, it is important to contrast the noise reduction benefits due to the trip and the serrations with the imposed aerodynamic penalties. Figure 5.30 shows the Overall Sound Pressure Levels for the extracted broadband noise levels at 6000 RPM and for an observer at 60 with their corresponding Figure of Merit. Note that to include all potential effects of the serrations, the broadband noise levels are integrated from 1 to 16 kHz, as done in the directivity plots of this section.

While the trade-off between noise reduction and aerodynamic performance is evident, it is worth considering the relative large uncertanties involved in the static measurements of small propellers, as shown with the errorr bars in Figure 5.12. With the exception of the propellers with cut-in serrations (C-SH and C-SM), all other configurations reduce the noise compared with the baseline propeller. These results show that further noise reductions studies involving serrations must include their detrimental effect in aerodynamic performance and are a preliminary step for optimization methodologies.

Experimental results on serrated propellers ——————————-Summary

- Tripping and serrations can mitigate trailing edge noise.
- While cut-in serrations can reduce trailing edge noise, they increase overall noise due to vortex-shedding at the serration root.
- The sawtooth serration is more effective at reducing trailing edge noise than the square wave at all frequencies. This is in contrast to the results on airfoils.
- There is a clear trade-off between noise reduction and aerodynamic performance when using trailing edge serrations.
- Up to 5 dB in broadband noise reduction for a 4% Figure of Merit reduction for the add-on serrations with trip.

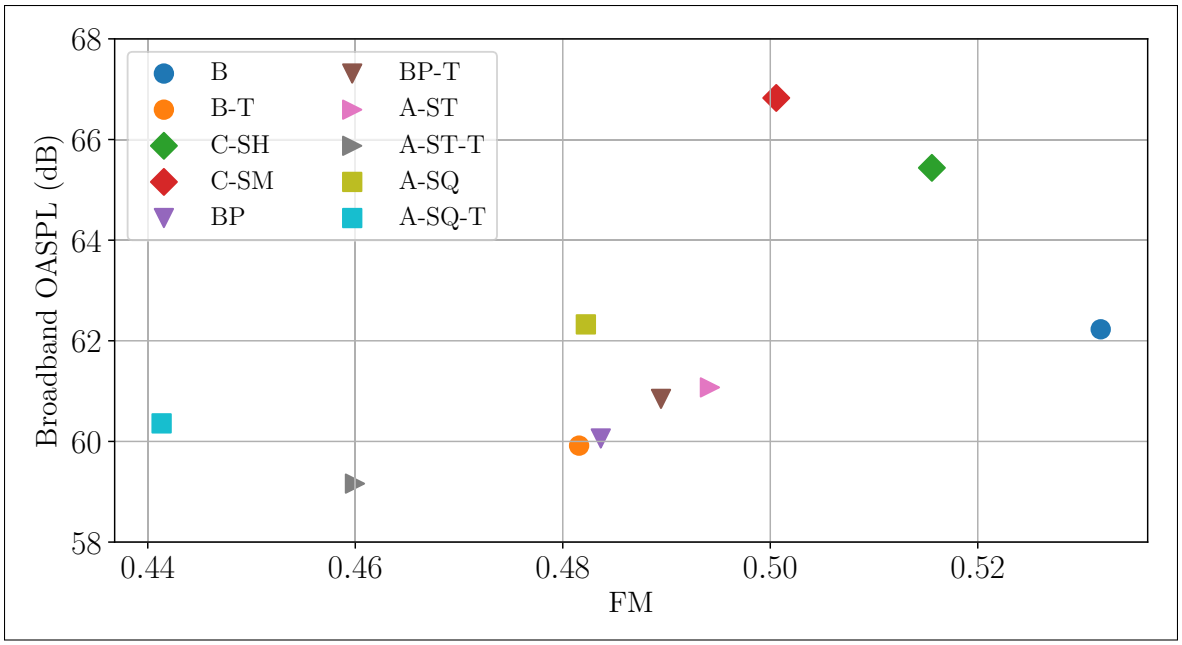

Figure 5.30 OASPL vs FM for all the propellers at 6000 RPM and for an observer at 60

5.4 Comparison with semi-analytical predictions

The noise reductions from the different propellers are compared with results obtained in the in-house code PyFanNoise with the RANS-based semi-analytical method presented in Chapter 4. Note that each serration type was compared with its respective baseline. Thus, the cut-in serrations (C-SH, C-SM) were compared with the Baseline (B) and the add-on serrations (A-ST, A-ST-T) with the baseline with the add-on plate (BP, BPT) in clean and tripped configurations. Figure 5.31 shows the broadband noise levels reductions
from the different serrated propellers and compares them with the theoretical predictions for an observer at 60 from the rotor plane. The frequency range used to calculate the difference is between 1 and 20 kHz.

At 4000 RPM, all the serrated propellers increase broadband noise, except for the add-on tripped case. At this RPM, there are significant differences between the cut-in sharp and smooth cases, with the latter yielding lower reductions beyond 12 kHz. Notably, the add-on trip and the sharp case yield similar noise reductions of 3 dB past 12.5 kHz. At this RPM, the add-on tripped case gives more than 5 dB noise reduction close to 10 kHz.

For the 6000 RPM case, the frequency range at which noise reductions occur moves to higher frequencies, with the add-on (clean) and cut-in cases decreasing noise only past 16 kHz. The add-on tripped case shows around 1 dB noise increase below 5 kHz and yields noise reductions up to 5 dB beyond this frequency.

At the highest RPM, only the add-on tripped serration reduces noise, being effective beyond 12.5 kHz. The cut-in cases perform almost equally, yielding a 7 dB noise increase at 10 kHz. There are a few takeaways regarding the theoretical predictions based on the extended Ayton's model, given that its assumptions (infinite flat plate, fully turbulent flow) mainly correspond to the A-ST-T case only. First, the model cannot predict any noise increase since this is related to manufacturing and secondary flow effects. Secondly, the model over-predicts the maximum noise reduction at all RPMs by 3- 4 dB. Thirdly, the model captures the trend of decreasing serration benefit with increasing RPM for the add-on tripped case, meeting the model assumptions more

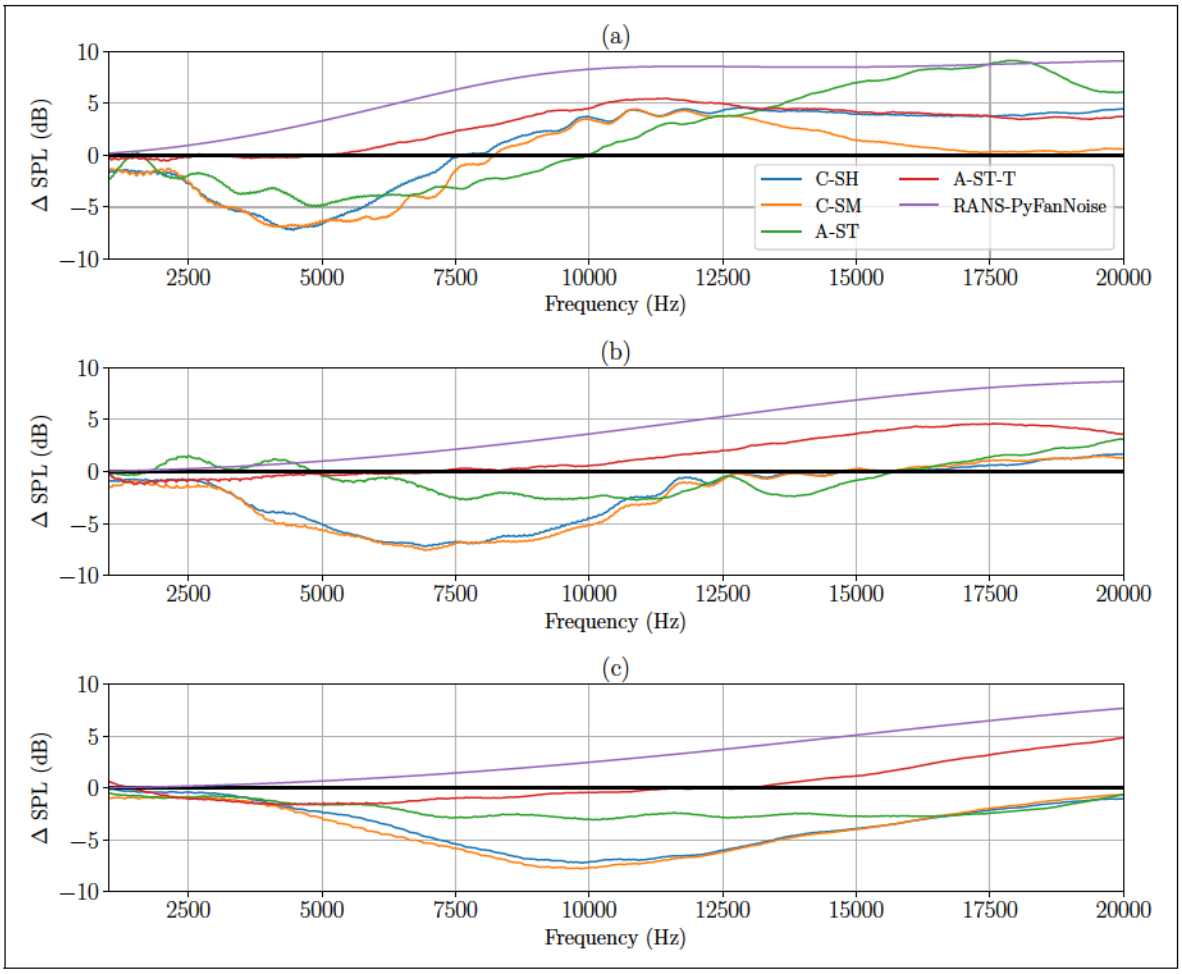

Figure 5.31 Broadband noise reductions for serrated propellers and comparison with analytical predictions (a) 4000 RPM, (b) 6000 RPM, and (c) 8000 RPM.

closely. Lastly, it accurately predicts the spectral shape of the noise reduction and the location of the maximum noise reductions, roughly 10, 15, and 20 kHz for 4000, 6000, and 8000 RPM, respectively. Thus, the model and the methodology presented may be used during the early propeller design, particularly at low RPM, to get an insight into the frequency range and theoretical noise reductions.

5.5 Conclusion

In this Chapter, theoretical noise reductions using serrations have been assessed. Realistic serration design has been considered by taking into account manufacturing methods constraints such as minimum thickness and tolerances. Different propellers based on a NACA0012 airfoil section with add-on, cut-in sharp, and cut-in smooth serrations have been built with SLA rapid prototyping. Two baselines corresponding to the original propeller and a modified one with an add-on flat plate have been manufactured for better comparison. The spectra of these baseline rotors show equidistant narrow-band humps at almost all tested rotational speeds that have been identified to laminar boundary-layer instability noise on the blade suction sides, matching previous experiments on the NACA0012 airfoil. Additional prototypes with tripping elements at 10% from the leading edge have been manufactured to study the impact of forced transition on the baselines and add-on serrated propellers. As previously found on airfoils, tripping alleviates the laminar boundary-layer instability noise.

It is demonstrated that with SLA it is possible to obtain similar samples for the cut-in serrations, for which small deviations have been found, particularly for the propeller with smooth teeth. The present study stresses the importance of considering how serrations are installed in the design. The propellers with cut-in serrations show noise reductions for different frequencies at different RPMs. Below those frequency ranges, noise increase was measured. Some of the noise increase has been attributed to vortex shedding characterized by a Strouhal number based on the serration root thickness and the relative velocity at 75% span of 0.12, very close to what was previously found on airfoils. The tripped propeller with the add-on serrations was the most effective at reducing broadband noise with an aerodynamic penalty of 5% in the Figure of Merit.

The theoretical model, the assumptions of which are close to the tripped propeller with add-on serrations (A-ST-T), correctly predicts the noise reduction frequency range for this case. Additionally, the analytical results capture the noise reduction decrease with increasing RPM trend. However, the predictions for cut-in serrations do not agree with the experimental data, as these serrations deviate significantly from the idealized one. The results show that both cut-in

and add-on serrations are valid methods to reduce TEN. However, in both cases, the serrations are most effective at low RPMs, where broadband noise dominates the spectra. Overall, although the noise reductions are over-predicted by 3-4 dB, the method can provide initial guidelines for serration design

CONCLUSION AND RECOMMENDATIONS

"The first principle is that you must not fool yourself, and you are the easiest to fool."

— Richard P. Feynman

6.1 Conclusions

A low-order methodology for the design of propellers with serrated trailing edges has been proposed, applied, and validated to a representative drone propeller based on the NACA0012 airfoil, featuring a constant pitch and chord along the span. The methodology leverages low-fidelity RANS simulations to model the single-point wall-pressure fluctuations spectrum. The latter is then used in conjunction with Amiet's model for straight edges, Li and Lee's extension of Ayton's model for serrated edges, and a newly derived model for the square-wave serration presented in Chapter 2. The new model combines Ayton's formulation, based on the Wiener-Hopf method, to obtain the scattered pressure, which is later used in Curle's analogy to derive the far-field acoustic pressure Power Spectral Density (PSD). The new model alleviates Ayton's model 2D nature and includes finite-chord effects. All analytical models assume a frozen turbulent field convecting along an infinitesimally thin flat plate at zero angle of attack.

Two experimental datasets were used to validate the acoustic models. The first one is for an industrial controlled-diffusion (CD) airfoil with and without sawtooth serrations, for which the experimental wall-pressure spectra were available. A good agreement is found for the straight-edge case using Li and Lee's model in the limit of zero serration amplitude. Limitations at low frequencies due to the semi-infinite chord are observed. For the serrated edge case, the predicted noise reductions are within 3-4 dB of the experimental values in the frequency range

where noise reductions were measured. Outside this range, the model overpredicts the noise reductions.

The second validation dataset is the result of an experimental campaign presented in Chapter 3 on a NACA0012 airfoil at operational conditions typical of drone propellers. The airfoil was fitted with add-on sawtooth and square wave serrations. Laminar Boundary Layer (LBL) instability noise was identified at almost all operating conditions, and it was necessary to add a trip to force a fully turbulent boundary layer on both sides. The serrations were then tested for clean and tripped configurations. In the former case, the two serration geometries reduce noise levels, with the square wave serration achieving the best performance, reducing noise by up to 10 dB. For the tripped airfoil, the serrations can also reduce noise levels, though to a lesser extent, up to 4 dB. The square wave serration again outperforms the sawtooth, particularly at low frequencies. The newly developed square wave model recovers Amiet's straight-edge solution and is thus valid over the entire frequency range. Both models fail to predict noise reductions at low Reynolds numbers, with agreement with experiments improving with increasing Reynolds number. for the square wave, the new model better predicts trends across all operational conditions and is within 3 dB of the measured noise reductions. Li and Lee's model captures the noise-reduction trends across different serration shapes. Further validation for the new square model is required to provide uncertainty margins.

The methodology was then extended to propellers by coupling the airfoil models with Schlinker and Amiet's method. The extension was verified with wind turbine and cooling fan blade elements available in the literature. Li and Lee's model matches Amiet's model at high frequencies and at high elevation angles relative to the rotor plane. Single-blade passage RANS simulations of the NACA0012 propeller were performed, and aerodynamic and acoustic validation was made with experimental data. The propeller operates in the Reynolds number range between 80,000 to 160,000, based on the chord and the blade relative velocity, and thus transitional effects play

an important role. There are two essential considerations for accurate low-Reynolds-number performance prediction with RANS. On the one hand, the tip vortex region must be finely discretized to obtain the correct loading. On the other hand, modeling the transition with the -Re is emphasized, as the thrust coefficient and Figure of Merit are in better agreement with the experimental dataset. The two aerodynamic performance metrics falling within the 95% confidence interval across the operating range.

The wall-pressure fluctuations spectrum was modeled from the RANS results, and the propeller far-field acoustics were calculated using the in-house turbomachinery noise code PyFanNoise. Little to no difference was found in the acoustic predictions between the transitional and fully turbulent models, and the latter was used throughout Chapter 4. Amiet's model matches the measured Sound Power Levels (SWL) for frequencies between 1 and 10 kHz, while Li and Lee's model matches Amiet's results at frequencies beyond 4 kHz. Overall, the acoustic results agree fairly well with experimental measurements, especially at high rotational speeds, where secondary flows are weaker and the onset of turbulence matches more favorably with the fully turbulent k- SST model used in the RANS. This finding aligns with the results of Chapter 3 on airfoils. Li and Lee's model was used to assess potential reductions in trailing-edge noise. It was shown that different serration shapes perform better at different non-dimensional frequencies. The often-overlooked square wave was shown to outperform the more traditional sawtooth and sinusoidal serrations when used in the NACA0012 drone propeller across its entire operational range.

The OASPL directivity plots showed no deviation from the dipole pattern for any of the shapes considered, and potential reductions of up to 10 dB are possible with the square wave at high frequencies. Larger noise reductions and a larger design space for the serrations can be obtained by increasing the blade planforms, allowing longer, more efficient serrations. Indeed, a mix of sinusoidal and sawtooth serrations can be tuned to achieve significant noise reduction across

the entire audible frequency range of interest, from 100 Hz to 10 kHz. This could also change the classical propeller design paradigm, in which the blade chord distribution and planform are no longer primarily driven by aerodynamic considerations but by passive noise-reduction constraints.

In Chapter 5, several propellers based on a NACA0012 airfoil section with add-on, cut-in sharp, and cut-in smooth serrations were manufactured using stereolithography (SLA) rapid prototyping to validate the theoretical results presented in Chapter 4. Two baselines corresponding to the original propeller and a modified one with an add-on flat plate have been manufactured for better comparison. Additional prototypes with tripping elements at 10% from the leading edge have been manufactured to study the impact of forced transition on the baselines and add-on serrated propellers. The spectra of these baseline rotors exhibit equidistant, narrow-band humps at nearly all tested rotational speeds, which have been identified as laminar boundary-layer instability noise on the blade suction sides, matching previous experiments on the NACA0012 airfoil. As previously observed on airfoils, tripping or serrations alleviate the noise from laminar boundary-layer instability.

A repeatibility test for the cut-in serrations was made and demonstrates that identical acoustics are obtained from different samples. This thesis emphasizes the importance of considering how serrations are incorporated into the design. The propellers with cut-in serrations show broadband noise reductions at different frequencies and RPMs. Below those frequency ranges, noise levels increased. Some of the noise increase has been attributed to vortex shedding characterized by a Strouhal number based on the serration root thickness and the relative velocity at 75% span of 0.12, very close to what was previously found on airfoils. Overall, there is a clear trade-off between noise reduction and aerodynamic performance. The propellers with cut-in serrations have a lesser impact on aerodynamics but increase noise due to vortex shedding. The tripped propeller with the add-on serrations was the most effective at reducing broadband noise, with

measured noise reductions of up to 5 dB at the lowest RPM and an aerodynamic penalty of 4% in the Figure of Merit across the operational envelope.

The theoretical model, whose assumptions closely match those of the tripped propeller with add-on serrations (A-ST-T), accurately predicts the noise-reduction frequency range for this case. Additionally, the analytical results capture the decrease in noise reduction with increasing RPM trend. However, the predictions for cut-in serrations do not agree with the experimental data, as these serrations deviate significantly from the idealized one. The results show that both cut-in and add-on serrations are effective methods for reducing TEN. However, in both cases, the serrations are most effective at low RPMs, where broadband noise dominates the spectra. Overall, although the noise reductions are over-predicted by 3-4 dB, the method can provide initial guidelines for serration design and clear guidance of where to expect the noise reductions.

6.2 Recommendations

Extension of the present work may come from different fronts. From a theoretical perspective, it would be ideal to further validate the new square wave model and extend it to the rotating case. In the former case, Finite Element Method (FEM) frequency-domain simulations can be used to model a flat plate with serrated edges to obtain the near-field scattered pressure (Lyu *et al.*, 2016; Zhang & Lyu, 2024) and compare the results with those obtained in Chapter 2. On a more ambitious scale, new acoustic models that account for the three-dimensionality of cut-in serrations may be developed, as has been done for cambered, finite-thickness airfoils at a non-zero angle of attack (Ayton & Peake, 2013).

From the numerical perspective, high-fidelity numerical simulations could contribute in two ways. On the one hand, they will allow validation of the noise-reduction mechanisms of the square wave and, at the same time, establish the limitations of the assumptions presented in this thesis, e.g., frozen turbulence and an infinitesimally thin flat plate. On the other hand, the

high-fidelity simulation of serrated propellers could be used to study in detail the trade-off between noise reduction and aerodynamic performance. Moreover, the simulation could shed light on the performance disparity between the square wave in the airfoil and propeller cases. On a similar vein, a reduced-order model that can account for the aerodynamic penalties induced by the serrations would serve as a stepping stone towards a complete optimization method and ultimately, a design where little to no penalties are introduced. Further noise reduction could be achieved by introducing optimal serration shapes based on the serration wavelength (Kholodov & Moreau, 2021).

Finally, different aspects of the overall methodology can also be improved. For example, extraction of the boundary layers on both sides of the blade could further improve agreement with experimental data. Moreover, further investigation into transitional boundary-layer wall-pressure spectrum modeling would be beneficial, as new models (Arroyo Ramo *et al.*, 2025) would easily integrate into the framework. This approach might require redefining or changing the model inputs compared to the fully turbulent case. Additionally, the common assumption of frozen turbulence can be relaxed for serrated-edge cases. Recent studies have shown that better agreement between models and experiments is found by considering a non-frozen turbulent field (Tian & Lyu, 2025, 2024).

APPENDIX I

BACK-SCATTERING CORRECTION DERIVATION

Equation (2.37) does not allow calculating airfoil self-noise unless severe restrictions on the geometry are made. A correction proposed by Roger and Moreau (2005) considers the effects of a finite chord by taking into account the back-scattering from the leading edge. In this section the derivation of the full solution for the pressure jump is presented. The velocity potential of an irrotational fluid generally lacks physical meaning, nonetheless, it's a powerful mathematical tool in the study of acoustic waves. Therefore,the relationship between pressure disturbance and potential is given by:

$$0 \frac{\quad}{\quad}$$

With and , Substituting and making non-dimensional by the semi-chord gives

$$\frac{\quad}{0} \quad \frac{\quad}{\quad} \quad - \qquad \text{(A I-1)}$$

Equation (A I-1) is actually a first order ODE that can be solved using an integrating factor such that the following general type of ODE

Has the following solution

Which gives the potential

$$0 \quad \frac{\quad}{0} \quad 0 \quad -$$

Substituting (2.37) in the above equation gives the potential for 0 as:

$$_1 \quad 0 \quad \frac{}{_0} \quad - \quad 1 \quad 1 \quad - \qquad \text{(A I-2)}$$

The preceding integral is done by parts, with the exponential functions as and the Fresnel function as . The derivative of the Fresnel function is evaluated using Leibniz rule

— — — —

Since the limits of the integral are fixed and noting that 1 1 gives the potential:

$$_1 \quad 0 \quad \frac{-}{_0 \quad 1 \; -} \quad {}^{1\,-} \quad 1 \quad {}_1 \quad 1 \quad 1 \quad 1$$

(A I-3)

With

$$\frac{}{\frac{1}{}} \quad {}_1 \quad {}^{-}_1 \quad 1 \quad - \quad {}^{-} \quad 1 \quad -$$

This potential must now be canceled upstream of the leading edge by adding a second potential as a correction, corresponding to the back-scattering. The following change of variables is done to get another canonical Schwarzschild problem:

$$_1 \quad _1 \quad {}^{-} \qquad 2$$

This allows to define a potential $_2$ such that $_2 \quad 0 \quad {}_1 \quad 0$ for 0. In other words, the potential for 2 is set to zero. Above's transformations along with the no-flow boundary condition allows to find the potential as

$$_2 \quad 0 \quad \frac{1}{} \quad {}_0 \quad \frac{}{} \; \frac{-}{} \; {}_1 \quad 0$$

Which is solved using the equivalence between the Fresnel integral and the complementary error function, since the original integral cannot be computed directly. Details are omitted for brevity

and can be found in Roger and Moreau. The back-scattering potential is then:

$$_{2} \quad 0 \quad \frac{}{_{0}} \quad \frac{1}{2\,\bar{} \qquad 1\,\bar{}} \,\overset{4\,\bar{}}{}\, \frac{1}{\bar{}\;_{1}}\,^{2} \qquad ^{1\,\bar{}} \qquad \text{(A I-4)}$$

$$^{2\,\bar{}} \quad ^{2}\,1 \quad 1 \qquad 2\,\bar{} \qquad 2$$

Where the notation stands for an imaginary part multiplied by the correction factor $1 \quad \frac{1}{4\,\bar{}} \quad ^{1\;2}$ substitution of (A I-4) into (A I-1) allows to find the back-scattering disturbance pressure, such that:

$$_{2} \quad 0 \quad \frac{1}{2\,\bar{} \qquad 1\,\bar{}} \,\overset{4\,\bar{}}{}\, \frac{1}{\bar{}\;_{1}}\,^{2} \qquad ^{1\,\bar{}} \qquad \text{(A I-5)}$$

$$\bar{} \qquad 1\,\bar{} \qquad \frac{}{}$$

Where

$$^{2\,\bar{}} \quad ^{2}\,1 \quad 1 \qquad 2\,\bar{} \qquad 2$$

$$\frac{}{} \quad ^{2\,\bar{}} \quad ^{2}\,2\,\bar{}\,1 \quad 1 \qquad 2\,\bar{} \qquad 2 \qquad 1 \qquad \overline{2\,\bar{} \qquad 2} \;\; ^{2\,\bar{}} \quad ^{2}$$

APPENDIX II

SQUARE WAVE STREAMWISE RADIATION INTEGRAL

The integrals for the radiation integral in Eq. (2.115) are calculated here. For convenience, the calculation is shown for an indefinite integral

$$\text{erfc} \quad 1 \qquad \frac{\sqrt{\qquad\qquad 2}}{2} \tag{A II-1}$$

Let which gives:

$$\text{erfc} \quad 1 \qquad \frac{\sqrt{\qquad\qquad 2}}{2} \qquad 2 \tag{A II-2}$$

and let 2 which gives

$$\text{erfc} \quad 1 \qquad \frac{\sqrt{\quad}}{2} \qquad ^{2} \tag{A II-3}$$

Substitute erfc 1 $\frac{}{2}$ 1 erf 1 $\frac{}{2}$ to obtain two integrals:

$$^{2} \qquad \text{erf} \quad 1 \qquad \frac{\sqrt{\quad}}{2} \qquad ^{2} \tag{A II-4}$$

The integral on the left is straightforward. The integral on the right can be computed via integration by parts with erf 1 $\frac{\sqrt{\quad}}{2}$ and ^{2} . The derivative of follows from Leibniz integral rule:

$$\frac{}{} \text{erf} \quad 1 \qquad \frac{\sqrt{\quad}}{2} \qquad \frac{}{} \frac{2}{=} \int_{0}^{} \qquad ^{2} \qquad \frac{2}{=} \frac{}{2 \sqrt{\quad}}$$

which yields:

$$\frac{}{}^{2} \quad \text{erf} \quad 1 \quad \frac{}{2} \quad \frac{}{}^{2} \quad \frac{2}{} \frac{}{2 \;\; \overline{\;\;}} \frac{}{}^{2} \tag{A II-5}$$

After regrouping the exponentials, the remaining integral is:

$$\frac{}{}^{2} \frac{2}{} \quad \frac{}{2 \;\; \overline{\;\;}} \tag{A II-6}$$

Substitute $\overline{\;\;}$ to get:

$$\frac{}{}^{2} \frac{2}{} \quad \frac{}{}^{2} \tag{A II-7}$$

Then, substitute $\overline{\;\;}$ to obtain:

$$\frac{}{}^{2} \frac{\overline{\;\;}}{} \frac{2}{} \quad ^{2} \tag{A II-8}$$

The last integral is by definition erf 1 $\frac{}{2}$, substituting back for and gives:

$$\frac{}{}^{2} \frac{\overline{\;\;}}{} \text{erf} \quad 1 \quad \frac{\overline{\;\;}}{2} \tag{A II-9}$$

The complete integral thus reads:

$$\frac{1}{} \frac{}{}^{2} \quad \text{erf} \quad 1 \quad \frac{}{2} \frac{}{}^{2} \quad \frac{}{}^{2} \frac{\overline{\;\;}}{} \text{erf} \quad 1 \quad \frac{\overline{\;\;}}{2} \tag{A II-10}$$

The first two terms are grouped using the definition of erfc 1 $\frac{}{2}$. Additionally, using

2 gives:

$$\frac{}{} \operatorname{erfc}\left(1 \sqrt{\frac{2}{2}}\right) \quad \frac{}{}^{2} \sqrt{\frac{}{}} \frac{}{} \operatorname{erf}\left(1 \sqrt{\frac{2}{2}}\right)$$

(A II-11)

The final result is obtained by substitution of and factoring the common terms:

$$\frac{}{} \operatorname{erfc}\left(1 \sqrt{\frac{2}{2}}\right) \quad {}^{2} \sqrt{\frac{}{}} \frac{}{} \operatorname{erf}\left(1 \sqrt{\frac{2}{2}}\right)$$

(A II-12)

APPENDIX III

TRIP THICKNESS SELECTION FOR NACA0012 AIRFOIL

Selection of the trip thickness to force transition to turbulence over the NACA0012 airfoil was done by systematically changing the thickness on each airfoil side for an arbitrarily chosen geometric angle of attack of 4 degrees. Note that at higher angles of attack, particularly larger than 6 degrees, the low frequency humps decrease in magnitude. Figures III-1, III-2 and III-3 show the result for V_∞ = 12 m/s, 16 m/s and 20 m/s respectively.

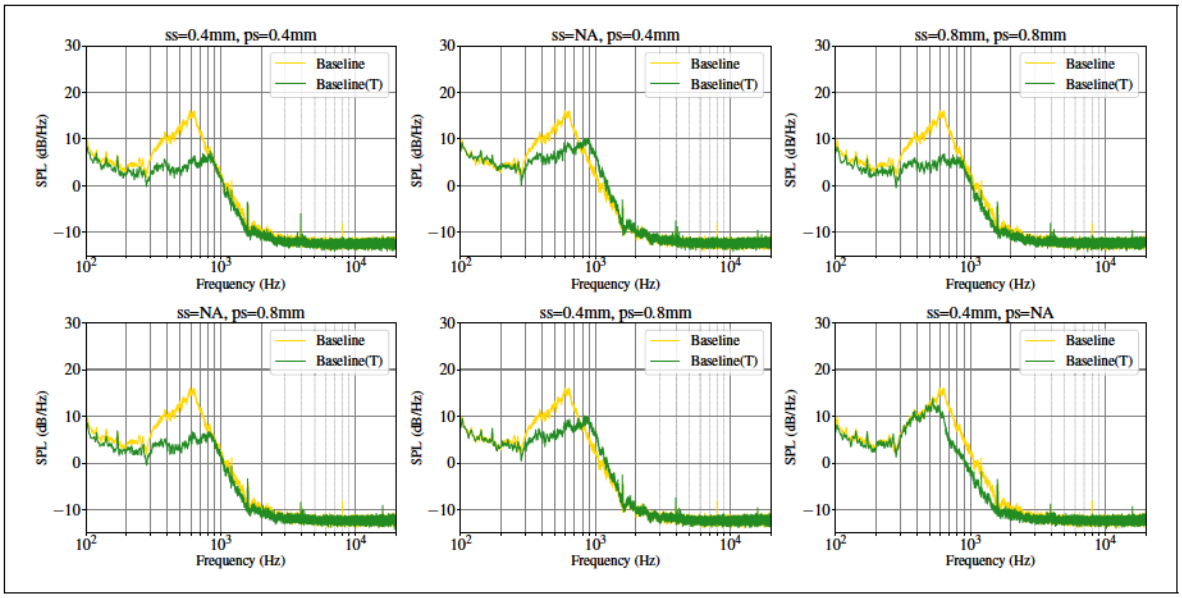

Figure-A III-1 Baseline and Baseline with trip for different trip thicknesses combinations in the pressure (ps) and suction (ss) sides. NA indicates not applied

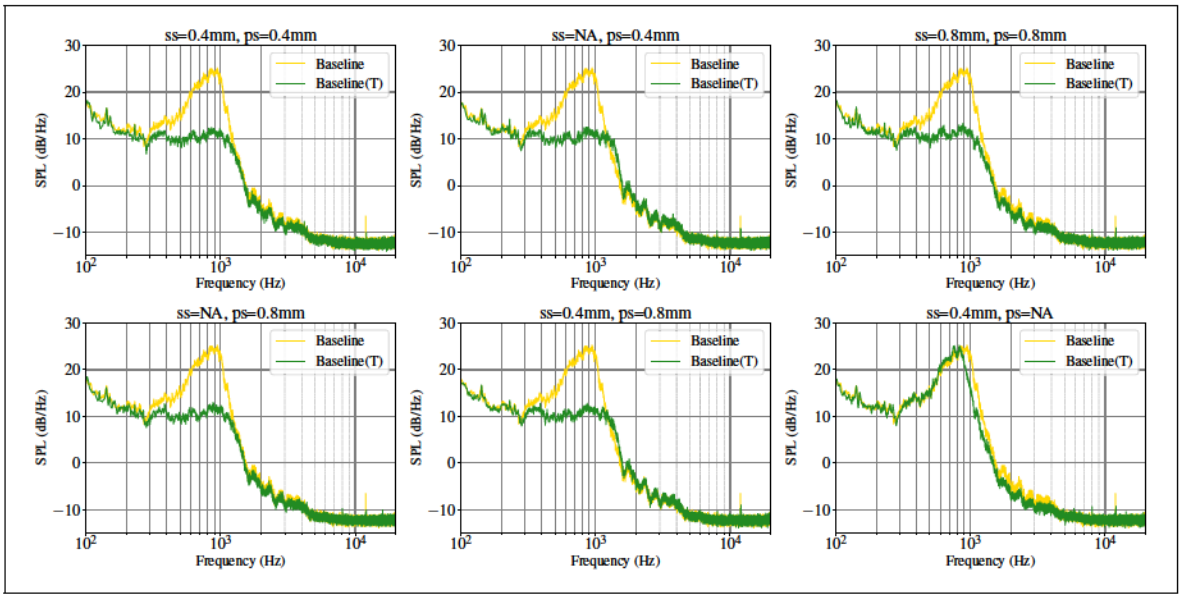

Figure-A III-2 Baseline and Baseline with trip for different trip thicknesses combinations in the pressure (ps) and suction (ss) sides. NA indicates not applied

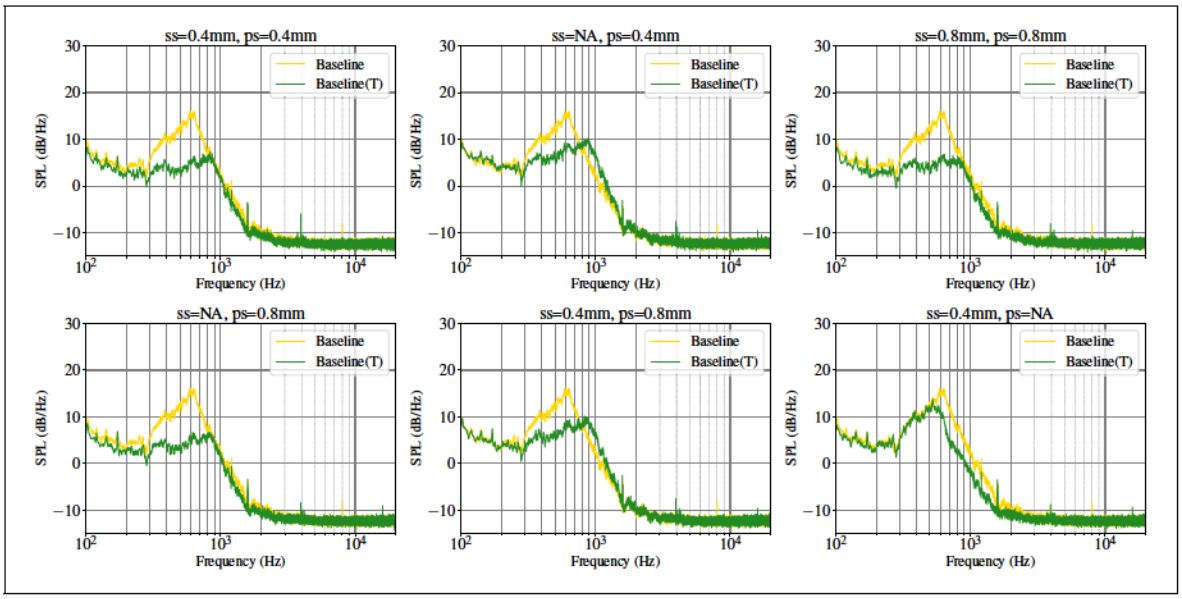

Figure-A III-3 Baseline and Baseline with trip for different trip thicknesses combinations in the pressure (ps) and suction (ss) sides. NA indicates not applied

APPENDIX IV

RANS MESH GENERATION

The airfoil grid, created using the CentaurSoft grid generator, consists of a hybrid mesh with quadrilaterals close to the wall and triangles everywhere else. The airfoil simulations objective is to define the first layer thickness, number of layers and aspect and stretching ratios for the quadrilaterals. These parameters play a key role in accurately capturing the boundary layer and, thus, are critical for trailing edge noise prediction. The stretching ratio and the number of prismatic layers are fixed to 1.15 and 25, respectively, based on the ANSYS CFX transition modeling guide recommendations. Thus, the variable parameters are the first layer thickness and the cell aspect ratio, as shown in Table IV-1 for a total of fifteen meshes. The velocity components on the inlet conditions of the airfoil domain are extracted at 50% of the blade span from a prior simulation of the propeller spinning at 6000 rpm yielding a Reynolds number of 66000. The simulations are then run for fully turbulent (SST) and transitional ( ) models.

Table-A IV-1 Mesh prismatic layer test matrix

Aspect ratio	**First layer thickness(%c)**	**Number of prismatic layers**	**Stretching ratio**
10	0.01,0.015,0.02,0.03,0.04	25	1.15
20	0.01,0.015,0.02,0.03,0.04	25	1.15
40	0.01,0.015,0.02,0.03,0.04	25	1.15

In terms of convergence, all the fully turbulent cases except for the case with the smallest first layer thickness reached RMS values below 10^{-6}, while for the transitional model, only the cases with the largest aspect ratio and thicker first layer reached the threshold. The skin friction coefficient distribution is shown in Figs. IV-1 and IV-2 for the transitional and turbulent cases, respectively. The fully turbulent results tend to collapse except for the smallest first layer thickness. In contrast, the transitional results show greater variation. The transition location can be inferred from the change in curvature in the curves. The laminar-turbulent transition takes place around 50% for the cases with a smooth distribution. The effect of the

aspect ratio is marginal for the turbulent results, while it can significantly impact the skin friction distribution for the transitional cases. Similar sensitivity of the model to grid parameters has been reported in the case of a helicopter rotor in hover. (Richez, 2024)

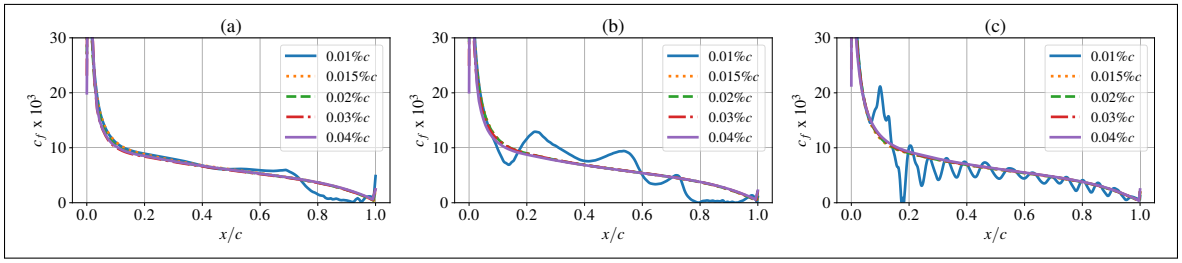

Figure-A IV-1 Suction side skin friction coefficient distribution as a function of first layer thickness for an aspect ratio of (a) 40, (b) 20, (c) 10 using the k- SST model

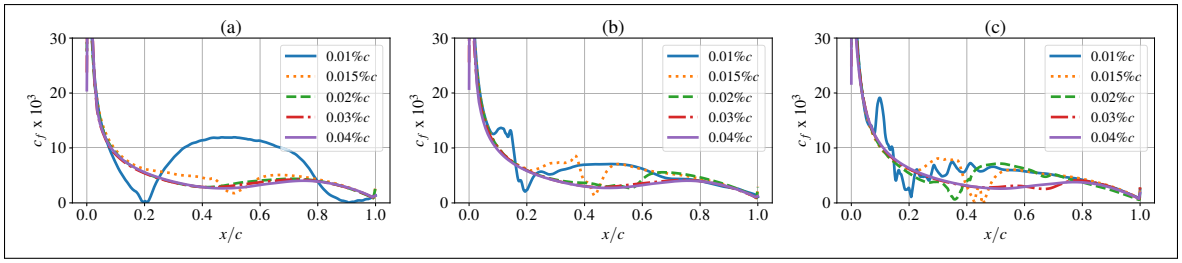

Figure-A IV-2 Suction side skin friction coefficient distribution as a function of first layer thickness for an aspect ratio of (a) 40, (b) 20, (c) 10 using the model

Overall, larger aspect ratios produce smoother skin friction coefficient distributions and improve convergence. It is important to note that for transitional simulations, it is recommended to have a finer discretization in the streamwise direction to capture laminar separation bubbles. Therefore, for this particular configuration, a trade-off between solution smoothness and accurate modelling must be made. The averaged values measured in the different simulations are reported in Table IV-2 for the suction side and at 10%.

Table-A IV-2 Suction side y values at 10% of the chord for the different first layer thickness tested.

First layer thickness	0 01%	0 015%	0 02%	0 03%	0 04%
y at 10%	0.5	0.7	1.0	1.5	2.0

The effects of the first layer thickness and the aspect ratio on the airfoil drag coefficient are shown in Fig. IV-3. The transitional results (right in Fig. IV-3) show a lower drag coefficients compared to the turbulent solution as a result of the laminar region. The results highlight the marginal impact of the grid on the turbulent drag predictions and the high sensitivities for the transitional ones. The latter can be associated to the shifting location of the transition on the different grids as highlighted in the distribution in Fig. IV-2. As the value increases, the transition is delayed downstream, resulting in lower on a larger portion of the airfoil surface, yielding a lower drag coefficient. The aspect ratio influence is unclear for transitional simulations. On the contrary, increases as the aspect ratio increases and the first layer thickness for fully turbulent simulations (left in Fig. IV-3). The unstable distribution seen for the first layer thickness of 0 01% in Figs. IV-1 and IV-2 are associated to the too low value of 0.5.

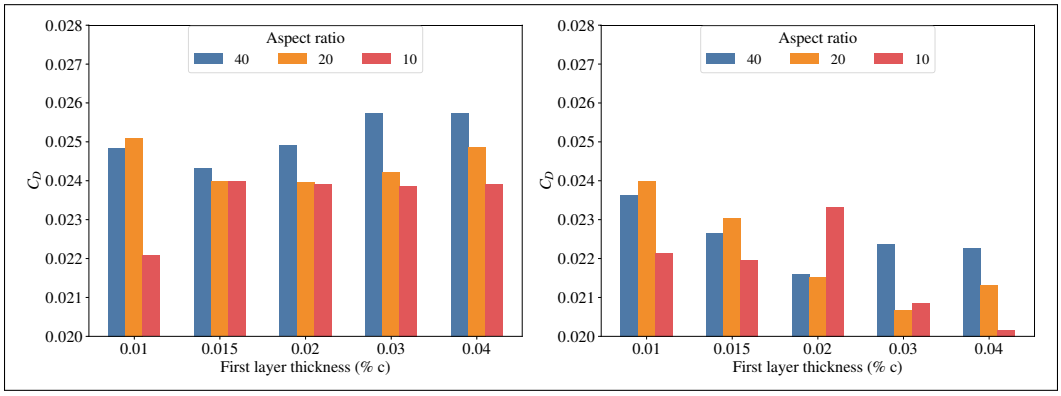

Figure-A IV-3 Drag coefficient with varying first layer thickness and aspect ratio with (a) k- SST and (b)

In order to design a mesh that is suitable for both fully turbulent and transitional simulations at the lowest computational cost, a balance must be struck between the two parameters. To reduce the possibilities of oscillatory solutions, the first layer thickness will be set to 0.03% of the chord and the aspect ratio to 20 for the propeller surface mesh. With these parameters, 324 points around the airfoil are obtained, and ensure a below 1 for 15%.

BIBLIOGRAPHY

Akila, H., Marinus, B. G. & Larbi, S. (2018). Trailing Edge Noise of Innovative Mini-RPA Propeller Blade Geometry. *2018 AIAA/CEAS Aeroacoustics Conference*, (AIAA AVIATION Forum). doi: 10.2514/6.2018-3451.

Amiet, R. K. (1975). Acoustic Radiation from an Airfoil in a Turbulent Stream. *Journal of Sound and Vibration*, 41(4), 407–420. doi: 10.1016/S0022-460X(75)80105-2.

Amiet, R. K. (1976). Noise Due to Turbulent Flow Past a Trailing Edge. *Journal of Sound and Vibration*, 47(3), 387–393. doi: 10.1016/0022-460X(76)90948-2.

Arbey, H. & Bataille, J. (1983). Noise Generated by Airfoil Profiles Placed in a Uniform Laminar Flow. *Journal of Fluid Mechanics*, 134, 33–47. doi: 10.1017/S0022112083003201.

Arce León, C., Ragni, D., Pröbsting, S., Scarano, F. & Madsen, J. (2016). Flow Topology and Acoustic Emissions of Trailing Edge Serrations at Incidence. *Experiments in Fluids*, 57(5), 91. doi: 10.1007/s00348-016-2181-1.

Arroyo Ramo, A., Moreau, S., Sandberg, R. D., Bauerheim, M. & Jacob, M. C. (2025). The Effect of the Leading-Edge Separation Bubble Vortex Shedding on the Far Field Noise of a Controlled Diffusion Airfoil: A DNS Study. *Journal of Sound and Vibration*, 618, 119336. doi: 10.1016/j.jsv.2025.119336.

Avallone, F., Pröbsting, S. & Ragni, D. (2016). Three-Dimensional Flow Field over a Trailing-Edge Serration and Implications on Broadband Noise. *Physics of Fluids*, 28(11), 117101. doi: 10.1063/1.4966633.

Ayton, L. J. (2018). Analytic Solution for Aerodynamic Noise Generated by Plates with Spanwise-Varying Trailing Edges. *Journal of Fluid Mechanics*, 849, 448–466. doi: 10.1017/jfm.2018.431.

Ayton, L. J. & Peake, N. (2013). On High-Frequency Noise Scattering by Aerofoils in Flow. *Journal of Fluid Mechanics*, 734, 144–182. doi: 10.1017/jfm.2013.477.

Ayton, L. J., Gill, J. & Peake, N. (2016). The Importance of the Unsteady Kutta Condition When Modelling Gust–Aerofoil Interaction. *Journal of Sound and Vibration*, 378, 28–37. doi: 10.1016/j.jsv.2016.05.036.

Bertagnolio, F., Fischer, A., Appel, C., Herr, M., Seel, F., Lutz, T., Boorsma, K., Schepers, G., Botero, M., Casalino, D., van der Velden, W., Sucameli, C. & Bortolotti, P. (2023). Wind Turbine Noise Code Benchmark: A Comparison and Verification Exercise. *10th International Conference on Wind Turbine Noise*.

Blake, W. K. (2017). *Mechanics of Flow-Induced Sound and Vibration, Volume 2: Complex Flow-Structure Interactions*. Academic Press.

Blandeau, V. P. & Joseph, P. F. (2011). Validity of Amiet's Model for Propeller Trailing-Edge Noise. *AIAA Journal*, 49(5), 1057–1066. doi: 10.2514/1.J050765.

Brooks, F., Stuart, D. & Marcolini, A. (1989). *Airfoil Self-Noise and Prediction*.

Bull, M. K. (1996). Wall-Pressure Fluctuations beneath Turbulent Bondary Layers: Some Reflectations on Forty Years of Research. *Journal of Sound and Vibration*, 190(3), 299–315. doi: 10.1006/jsvi.1996.0066.

Candeloro, P., Nargi, R. E., Grande, E., Ragni, D. & Pagliaroli, T. (2021). Experimental Fluid Dynamic Characterization of Serrated Rotors for Drone Propulsion. *Journal of Physics: Conference Series*, 1977(1), 012007. doi: 10.1088/1742-6596/1977/1/012007.

Carreño Ruiz, M., Scanavino, M., D'Ambrosio, D., Guglieri, G. & Vilardi, A. (2022). Experimental and Numerical Analysis of Hovering Multicopter Performance in Low-Reynolds Number Conditions. *Aerospace Science and Technology*, 128, 107777. doi: 10.1016/j.ast.2022.107777.

Casalino, D., Grande, E., Romani, G., Ragni, D. & Avallone, F. (2021). Definition of a Benchmark for Low Reynolds Number Propeller Aeroacoustics. *Aerospace Science and Technology*, 113, 106707. doi: 10.1016/j.ast.2021.106707.

Casalino, D., Romani, G., Pii, L. M. & Colombo, R. (2023). Flow Confinement Effects on sUAS Rotor Noise. *Aerospace Science and Technology*, 143, 108756. doi: 10.1016/j.ast.2023.108756.

Catlett, M. R., Anderson, J. M., Forest, J. B. & Stewart, D. O. (2016). Empirical Modeling of Pressure Spectra in Adverse Pressure Gradient Turbulent Boundary Layers. *AIAA Journal*, 54(2), 569–587. doi: 10.2514/1.J054375.

Chase, D. M. (1980). TURBULENT BOUNDARY LAYER WALL PRESSURE. *Journal of Sound and Vibration*.

Chong, T. P., Vathylakis, A., Joseph, P. F. & Gruber, M. (2013). Self-Noise Produced by an Airfoil with Nonflat Plate Trailing-Edge Serrations. *AIAA Journal*, 51(11), 2665–2677. doi: 10.2514/1.J052344.

Colonius, T. & Lele, S. K. (2004). Computational Aeroacoustics: Progress on Nonlinear Problems of Sound Generation. *Progress in Aerospace Sciences*, 40(6), 345–416. doi: 10.1016/j.paerosci.2004.09.001.

Corcos, G. M. (1964). The Structure of the Turbulent Pressure Field in Boundary-Layer Flows. *Journal of Fluid Mechanics*, 18(03), 353. doi: 10.1017/S002211206400026X.

Crighton, D. G. (1985). The Kutta Condition in Unsteady Flow. *Annual Review of Fluid Mechanics*, 17(Volume 17, 1985), 411–445. doi: 10.1146/annurev.fl.17.010185.002211.

Curle, N. (1955). The Influence of Solid Boundaries upon Aerodynamic Sound. *Proceedings of the Royal Society of London. Series A. Mathematical and Physical Sciences*, 231(1187), 505–514. doi: 10.1098/rspa.1955.0191.

Deming, A. F. (1938). *Noise from Propellers with Symmetrical Sections at Zero Blade Angle, II*.

Deng, S., Wang, S. & Zhang, Z. (2020). Aerodynamic Performance Assessment of a Ducted Fan UAV for VTOL Applications. *Aerospace Science and Technology*, 103, 105895. doi: 10.1016/j.ast.2020.105895.

Dominique, J., Van den Berghe, J., Schram, C. & Mendez, M. A. (2022). Artificial Neural Networks Modeling of Wall Pressure Spectra beneath Turbulent Boundary Layers. *Physics of Fluids*, 34(3), 035119. doi: 10.1063/5.0083241.

Drela, M. (1988). Low-Reynolds-number Airfoil Design for the M.I.T. Daedalus Prototype- A Case Study. *Journal of Aircraft*, 25(8), 724–732. doi: 10.2514/3.45650.

Ernsthausen, W. (1937). *The Source of Propeller Noise*.

F. Farassat & Brentner, K. (1994). Helicopter Noise Prediction: Current Status and Future. *Journal of Sound and Vibration*. doi: 10.1006/jsvi.1994.1047.

Fabre, B., Gilbert, J., Hirschberg, A. & Pelorson, X. (2012). Aeroacoustics of Musical Instruments. *Annual Review of Fluid Mechanics*, 44(Volume 44, 2012), 1–25. doi: 10.1146/annurev-fluid-120710-101031.

Farassat, F. (1976). *Theory of Noise Generation From Moving Bodies With an Application to Helicopter Rotors* (Report n R-451). Langley Research Center.

Ffowcs Williams, J. E., Hawkings, D. L. & Lighthill, M. J. (1969). Sound Generation by Turbulence and Surfaces in Arbitrary Motion. *Philosophical Transactions of the Royal Society of London. Series A, Mathematical and Physical Sciences*, 264(1151), 321–342. doi: 10.1098/rsta.1969.0031.

Fritsch, D. J., Vishwanathan, V., Roy, C. J., Todd Lowe, K., Devenport, W. J., Croaker, P., Tkachenko, O., Pook, D., Lane, G., Shubham, S. & Sandberg, R. D. (2023). Modeling the Surface Pressure Spectrum Beneath Turbulent Boundary Layers in Pressure Gradients. *AIAA Journal*, 61(5), 2002–2021. doi: 10.2514/1.J062074.

Froude, W. (1889). On the Part Played in Propulsion by Differences of Fluid Pressure. *Trans. Inst. Naval Architects*, 30, 390.

Gelot, M. B. R. & Kim, J. W. (2020). Effect of Serrated Trailing Edges on Aerofoil Tonal Noise. *Journal of Fluid Mechanics*, 904, A30. doi: 10.1017/jfm.2020.724.

Glegg, S. & Devenport, W. (2024). *Aeroacoustics of Low Mach Number Flows: Fundamentals, Analysis, and Measurement* (ed. Second edition). London San Diego, CA Cambridge, MA Kidlington, Oxford: Academic Press.

Gojon, R., Jardin, T. & Parisot-Dupuis, H. (2021). Experimental Investigation of Low Reynolds Number Rotor Noise. *The Journal of the Acoustical Society of America*, 149(6), 3813–3829. doi: 10.1121/10.0005068.

Gojon, R., Parisot-Dupuis, H., Mellot, B. & Jardin, T. (2023). Aeroacoustic Radiation of Low Reynolds Number Rotors in Interaction with Beams. *The Journal of the Acoustical Society of America*, 154(2), 1248–1260. doi: 10.1121/10.0020672.

Goody, M. (2004). Empirical Spectral Model of Surface Pressure Fluctuations. *AIAA Journal*, 42(9), 1788–1794. doi: 10.2514/1.9433.

Gowree, E., Jaroslawski, T., Mellot, B. & Gojon, R. (2023). Noise Reduction on Low Reynolds Number Rotors by Boundary Layer Transition. *Applied Acoustics*, 210, 109446. doi: 10.1016/j.apacoust.2023.109446.

Gradštejn, I. S., Ryžik, J. M., Jeffrey, A. & Zwillinger, D. (2009). *Table of Integrals, Series and Products* (ed. 7. ed., [3. Nachdr.]). Amsterdam: Elsevier Acad. Press.

Graham, R. R. (1934). The Silent Flight of Owls. *The Journal of the Royal Aeronautical Society*, 38(286), 837–843. doi: 10.1017/S0368393100109915.

Gruber, M. (2012). *Airfoil Noise Reduction by Edge Treatments*. (Ph.D. thesis, University of Southampton, Institute of Sound and Vibration).

Gruber, M., Joseph, P. & Chong, T. P. (2010). Experimental Investigation of Airfoil Self Noise and Turbulent Wake Reduction by the Use of Trailing Edge Serrations. *16th AIAA/CEAS Aeroacoustics Conference*. doi: 10.2514/6.2010-3803.

Gruber, M., Joseph, P. & Chong, T. (2011). On the Mechanisms of Serrated Airfoil Trailing Edge Noise Reduction. *17th AIAA/CEAS Aeroacoustics Conference (32nd AIAA Aeroacoustics Conference)*. doi: 10.2514/6.2011-2781.

Gutin. (1936). On the Sound Field of a Rotating Propeller.

Gwak, D. Y., Han, D. & Lee, S. (2020). Sound Quality Factors Influencing Annoyance from Hovering UAV. *Journal of Sound and Vibration*, 489, 115651. doi: 10.1016/j.jsv.2020.115651.

Hales, A. D. G. (2024). *Mathematical Modelling of Acoustic Diffraction Noise Embracing Diverse Boundary Conditions*. (Ph.D. thesis, University of Cambridge (United Kingdom), England).

Hanson, D. B. & Parzych, D. J. (1993). *Theory for Noise of Propellers in Angular Inflow With Parametric Studies and Expeimental Verification* (Report n 4499).

Hobbs, D. E. & Weingold, H. D. (1984). Development of Controlled Diffusion Airfoils for Multistage Compressor Application. *Journal of Engineering for Gas Turbines and Power*, 106(2), 271–278. doi: 10.1115/1.3239559.

Howe, M. S. (1978). A Review of the Theory of Trailing Edge Noise. *Journal of Sound and Vibration*, 61(3), 437–465. doi: 10.1016/0022-460X(78)90391-7.

Howe, M. S. (1991). Aerodynamic Noise of a Serrated Trailing Edge. *Journal of Fluids and Structures*, 5(1), 33–45. doi: 10.1016/0889-9746(91)80010-B.

Howe, M. S. (1998). *Acoustics of Fluid-Structure Interactions* (ed. Online-Ausg). Cambridge: Cambridge University Press. doi: 10.1017/CBO9780511662898.

Howe, M. S. (2001). Edge-Source Acoustic Green's Function for an Airfoil of Arbitrary Chord, with Application to Trailing-Edge Noise. *Quarterly Journal of Mechanics and Applied Mathematics*, 54(1), 139–155. doi: 10.1093/qjmam/54.1.139.

Howe, M. S. & McGowan, R. S. (2005). Aeroacoustics of [s]. *Proceedings of the Royal Society A: Mathematical, Physical and Engineering Sciences*. doi: 10.1098/rspa.2004.1405.

Hu, N. & Herr, M. (2016). Characteristics of Wall Pressure Fluctuations for a Flat Plate Turbulent Boundary Layer with Pressure Gradients. *22nd AIAA/CEAS Aeroacoustics Conference*. doi: 10.2514/6.2016-2749.

Huang, X. (2017). Theoretical Model of Acoustic Scattering from a Flat Plate with Serrations. *Journal of Fluid Mechanics*, 819, 228–257. doi: 10.1017/jfm.2017.176.

Hwang, Y. F., Bonness, W. K. & Hambric, S. A. (2009). Comparison of Semi-Empirical Models for Turbulent Boundary Layer Wall Pressure Spectra. *Journal of Sound and Vibration*, 319(1), 199–217. doi: 10.1016/j.jsv.2008.06.002.

Intaratep, N., Alexander, W. N., Devenport, W. J., Grace, S. M. & Dropkin, A. (2016). Experimental Study of Quadcopter Acoustics and Performance at Static Thrust Conditions. *22nd AIAA/CEAS Aeroacoustics Conference*. doi: 10.2514/6.2016-2873.

Jaroslawski, T., Forte, M., Moschetta, J.-M. & Gowree, E. R. (2023). Boundary Layer Forcing on a Rotating Wing at Low Reynolds Numbers. *Experiments in Fluids*, 64(3), 58. doi: 10.1007/s00348-023-03597-9.

Jaworski, J. W. & Peake, N. (2020). Aeroacoustics of Silent Owl Flight. *Annual Review of Fluid Mechanics*, 52(1), 395–420. doi: 10.1146/annurev-fluid-010518-040436.

Jo, Y., Jardin, T., Gojon, R., Jacob, M. C. & Moschetta, J.-M. (2019). Prediction of Noise from Low Reynolds Number Rotors with Different Number of Blades Using a Non-Linear Vortex Lattice Method. *25th AIAA/CEAS Aeroacoustics Conference*. doi: 10.2514/6.2019-2615.

Jones, D. S. (1989). *Acoustic and Electromagnetic Waves* (ed. Repr.). Oxford: Clarendon Press.

Jones, L. E. & Sandberg, R. D. (2012). Acoustic and Hydrodynamic Analysis of the Flow around an Aerofoil with Trailing-Edge Serrations. *Journal of Fluid Mechanics*, 706, 295–322. doi: 10.1017/jfm.2012.254.

Kholodov, P. & Moreau, S. (2021). Optimization of Trailing-Edge Serrations with and without Slits for Broadband Noise Reduction. *Journal of Sound and Vibration*, 490, 115736. doi: 10.1016/j.jsv.2020.115736.

Kim, Y. N. & George, A. R. (1982). Trailing-Edge Noise from Hovering Rotors. *AIAA Journal*, 20(9), 1167–1174. doi: 10.2514/3.51176.

Kroeger, R. A. & Helvey, T. C. (1971). *LOW SPEED AERODYNAMICS FOR ULTRA-QUIET FLIGHT* (Report n AFFDL-TR-71-75).

Kücükcoskun, K. (2012). *Prediction of Free and Scattered Acoustic Fields of Low-Speed Fans*. (Ph.D. thesis, Ecole Centrale de Lyon ; Institut von Karman de dynamique des fluides (Rhode-Saint-Genèse, Belgique)).

Lallier-Daniels, D., Bolduc-Teasdale, F., Moreau, S., Guilleminot-Simon, P., Lévesque-Leduc, M., Rancourt, D. & Sanjosé, M. (2020). Predictive Acoustic Modeling of Open Propellers Using Analytical Tools and RANS Simulations. *VFS International Powered Lift Conference*, pp. 66–77.

Langtry, R. B. & Menter, F. R. (2009). Correlation-Based Transition Modeling for Unstructured Parallelized Computational Fluid Dynamics Codes. *AIAA Journal*, 47(12), 2894–2906. doi: 10.2514/1.42362.

Le Prell, C. G. (2019). Effects of Noise Exposure on Auditory Brainstem Response and Speech-in-Noise Tasks: A Review of the Literature. *International Journal of Audiology*, 58(sup1), S3-S32. doi: 10.1080/14992027.2018.1534010.

Lee, H. M., Lu, Z., Lim, K. M., Xie, J. & Lee, H. P. (2019). Quieter Propeller with Serrated Trailing Edge. *Applied Acoustics*, 146, 227–236. doi: 10.1016/j.apacoust.2018.11.020.

Lee, J. H., Kwon, Y. S., Hutchins, N. & Monty, J. P. (2012). Spatially Developing Turbulent Boundary Layer on a Flat Plate. arXiv:1210.3881.

Lee, S. (2018). Empirical Wall-Pressure Spectral Modeling for Zero and Adverse Pressure Gradient Flows. *AIAA Journal*, 56(5), 1818–1829. doi: 10.2514/1.J056528.

Lee, S., Ayton, L., Bertagnolio, F., Moreau, S., Chong, T. P. & Joseph, P. (2021). Turbulent Boundary Layer Trailing-Edge Noise: Theory, Computation, Experiment, and Application. *Progress in Aerospace Sciences*, 126, 100737. doi: 10.1016/j.paerosci.2021.100737.

Leishman, J. G. (2023). *Introduction to Aerospace Flight Vehicles*. Embry-Riddle Aeronautical University.

Li, S. K. & Lee, S. (2022). Extensions and Applications of Lyu and Ayton's Serrated Trailing-Edge Noise Model to Rotorcraft. *28th AIAA/CEAS Aeroacoustics 2022 Conference*. doi: 10.2514/6.2022-2916.

Li Volsi, P., Brogna, G., Gojon, R., Jardin, T., Parisot-Dupuis, H. & Moschetta, J.-M. (2024). Analysis of MAV Rotors Optimized for Low Noise and Aerodynamic Efficiency with Operational Constraints. *Fluids*, 9(4), 96. doi: 10.3390/fluids9040096.

Lighthill, M. J. (1952). On Sound Generated Aerodynamically I. General Theory. *Proceedings of the Royal Society of London. Series A. Mathematical and Physical Sciences*, 211(1107), 564–587. doi: 10.1098/rspa.1952.0060.

Lilley, G. (1998). A Study of the Silent Flight of the Owl. *4th AIAA/CEAS Aeroacoustics Conference*. doi: 10.2514/6.1998-2340.

Lima Pereira, L. T., Avallone, F., Ragni, D. & Scarano, F. (2023). A Parametric Study of Serration Design for Trailing–Edge Broadband Noise Reduction. *Applied Acoustics*, 211, 109470. doi: 10.1016/j.apacoust.2023.109470.

Longhouse. (1977). Vortex Shedding Noise of Low Tip Speed, Axial Flow Fans. *Journal of Sound and Vibration*, 53(1), 25–46. doi: 10.1016/0022-460X(77)90092-X.

Lyu, B. (2023). Analytical Green's Function for the Acoustic Scattering by a Flat Plate with a Serrated Edge. *Journal of Fluid Mechanics*, 961, A33. doi: 10.1017/jfm.2023.256.

Lyu, B., Azarpeyvand, M. & Sinayoko, S. (2016). Prediction of Noise from Serrated Trailing Edges. *Journal of Fluid Mechanics*, 793, 556–588. doi: 10.1017/jfm.2016.132.

Lyu, B. & Ayton, L. J. (2020). Rapid Noise Prediction Models for Serrated Leading and Trailing Edges. *Journal of Sound and Vibration*, 469, 115136. doi: 10.1016/j.jsv.2019.115136.

Lyu, B., Ayton, L. J. & Chaitanya, P. (2019). On the Acoustic Optimality of Leading-Edge Serration Profiles. *Journal of Sound and Vibration*, 462, 114923. doi: 10.1016/j.jsv.2019.114923.

Merino Martinez, R. (2018). *Microphone Arrays for Imaging of Aerospace Noise Sources*. (Dissertation (TU Delft)).

Montoya-Ospina, S., Simon, F., Gojon, R. & Parisot-Dupuis, H. (2024). Passive Noise Control for Low Reynolds Number Rotors. *30th AIAA/CEAS Aeroacoustics Conference (2024)*. doi: 10.2514/6.2024-3112.

Moreau, S. & Roger, M. (2005). Effect of Airfoil Aerodynamic Loading on Trailing Edge Noise Sources. *AIAA Journal*, 43(1), 41–52. doi: 10.2514/1.5578.

Moreau, S., Henner, M., Iaccarino, G., Wang, M. & Roger, M. (2003). Analysis of Flow Conditions in Freejet Experiments for Studying Airfoil Self-Noise. *AIAA Journal*, 41(10), 1895–1905. doi: 10.2514/2.1905.

Moreau, S., Laffay, P., Idier, A. & Atalla, N. (2016). Several Noise Control of the Trailing-Edge Noise of a Controlled-Diffusion Airfoil. *22nd AIAA/CEAS Aeroacoustics Conference*. doi: 10.2514/6.2016-2816.

Moreau, S., Sanjosé, M., Lyu, B. & Ayton, L. J. (2019). Analytical, Numerical and Experimental Investigation of Trailing-Edge Noise Reduction on a Controlled Diffusion Airfoil with Serrations. *25th AIAA/CEAS Aeroacoustics Conference*. doi: 10.2514/6.2019-2450.

Mueller, T. J. & DeLaurier, J. D. (2003). AERODYNAMICS OF SMALL VEHICLES. *Annual Review of Fluid Mechanics*, 35(Volume 35, 2003), 89–111. doi: 10.1146/annurev.fluid.35.101101.161102.

Neal, D. R. (2010). *The Effects of Rotation on the Flow Field over a Controlled-Diffusion Airfoil*. (Ph.D. thesis, Michigan State University, United States – Michigan).

Nigro, D. (2017). *Prediction of Broadband Aero and Hydrodynamic Noise: Derivation of Analytical Models for Low Frequency*. (Ph.D. thesis, The University of Manchester (United Kingdom), England).

Ning, Z., Wlezien, R. W. & Hu, H. (2017). An Experimental Study on Small UAV Propellers with Serrated Trailing Edges. *47th AIAA Fluid Dynamics Conference*. doi: 10.2514/6.2017-3813.

Noble, B. (1958). *Methods Based on the Wiener-Hopf Technique for the Solution of Partial Differential Equations*. New York, Pergamon Press.

Oerlemans, S., Fisher, M., Maeder, T. & Kögler, K. (2009). Reduction of Wind Turbine Noise Using Optimized Airfoils and Trailing-Edge Serrations. *AIAA Journal*, 47(6), 1470–1481. doi: 10.2514/1.38888.

Padois, T., Laffay, P., Idier, A. & Moreau, S. (2015). Detailed Experimental Investigation of the Aeroacoustic Field around a Controlled-Diffusion Airfoil. *21st AIAA/CEAS Aeroacoustics Conference*, (AIAA AVIATION Forum). doi: 10.2514/6.2015-2205.

Pagliaroli, T., Candeloro, P., Duchetto, F. D., Rossignol, K.-S. & Yin, J. (2025). On Rotor Noise Interference. *Journal of Fluid Mechanics*, 1013, A43. doi: 10.1017/jfm.2025.10294.

Panda, J., Roozeboom, N. H. & Ross, J. C. (2019). Wavenumber-Frequency Spectra on a Launch Vehicle Model Measured via Unsteady Pressure-Sensitive Paint. *AIAA Journal*, 57(5), 1801–1817. doi: 10.2514/1.J057449.

Pang, E., Cambray, A., Rezgui, D., Azarpeyvand, M. & Showkat Ali, S. A. (2018). Investigation Towards a Better Understanding of Noise Generation from UAV Propellers. *2018 AIAA/CEAS Aeroacoustics Conference*. doi: 10.2514/6.2018-3450.

Pargal, S., Yuan, J. & Moreau, S. (2024). A Generalized Wall-Pressure Spectral Model for Non-Equilibrium Boundary Layers. *Journal of Fluid Mechanics*, 996, A27. doi: 10.1017/jfm.2024.665.

Passchier-Vermeer, W. & Passchier, W. F. (2000). Noise Exposure and Public Health. *Environmental health perspectives*, 9.

Paterson, R. W., Vogt, P. G., Fink, M. R. & Munch, C. L. (1973a). Vortex Noise of Isolated Airfoils. *Journal of Aircraft*, 10(5), 296–302. doi: 10.2514/3.60229.

Paterson, R. W., Vogt, P. G., Fink, M. R. & Munch, C. L. (1973b). Vortex Noise of Isolated Airfoils. *Journal of Aircraft*, 10(5), 296–302. doi: 10.2514/3.60229.

Patterson, A., Schiller, N. H., Ackerman, K. A., Gahlawat, A., Gregory, I. M. & Hovakimyan, N. (2020). Controller Design for Propeller Phase Synchronization with Aeroacoustic Performance Metrics. *AIAA Scitech 2020 Forum*. doi: 10.2514/6.2020-1494.

Pettingill, N. A., Zawodny, N. S., Thurman, C. S. & Lopes, L. V. (2021). Acoustic and Performance Characteristics of an Ideally Twisted Rotor in Hover. *AIAA SCITECH 2021 FORUM*.

Powell, A. (1959). On the Aerodynamic Noise of a Rigid Flat Plate Moving at Zero Incidence. *The Journal of the Acoustical Society of America*, 31(12), 1649–1653. doi: 10.1121/1.1907674.

Pröbsting, S. & Yarusevych, S. (2015). Laminar Separation Bubble Development on an Airfoil Emitting Tonal Noise. *Journal of Fluid Mechanics*, 780, 167–191. doi: 10.1017/jfm.2015.427.

Pröbsting, S., Scarano, F. & Morris, S. C. (2015). Regimes of Tonal Noise on an Airfoil at Moderate Reynolds Number. *Journal of Fluid Mechanics*, 780, 407–438. doi: 10.1017/jfm.2015.475.

Rankine, W. (1865). On the Mechanical Principles of the Action of Propellers. *Transactions of the Institute of Naval Architects*, 6.

Rendon, J., Moreau, S., Gojon, R. & Bauerheim, M. (2024). LBM and iLES Comparison for the Aaerodynamic and Acoustic Characteristics of a Low-speed Rotor. *30th AIAA/CEAS Aeroacoustics Conference (2024)*, (Aeroacoustics Conferences). doi: 10.2514/6.2024-3046.

Richez, F. (2024). Numerical Investigation of Turbulence Transition Models for the Prediction of Helicopter Rotor Performance in Hover. *Vertical Flight Society 80th Forum*.

Rizzi, S. A. (2020). *Urban Air Mobility Noise: Current Practice, Gaps, and Recommendations* (Report n TP-2020-5007433). Langley Research Center.

Roger, M. & Moreau, S. (2005). Back-Scattering Correction and Further Extensions of Amiet's Trailing-Edge Noise Model. Part 1: Theory. *Journal of Sound and Vibration*, 286(3), 477–506. doi: 10.1016/j.jsv.2004.10.054.

Roger, M. & Moreau, S. (2012). Addendum to the Back-Scattering Correction of Amiet's Trailing-Edge Noise Model. *Journal of Sound and Vibration*, 331(24), 5383–5385. doi: 10.1016/j.jsv.2012.06.019.

Roger, M., Moreau, S. & Guedel, A. (2006). Broadband Fan Noise Prediction Using Single-Airfoil Theory. *Noise Control Engineering Journal*, 54(1), 5–14. doi: 10.3397/1.2888773.

Roger, M., Schram, C. & Santana, L. D. (2013). Reduction of Airfoil Turbulence-Impingement Noise by Means of Leading-Edge Serrations and/or Porous Material. *19th AIAA/CEAS Aeroacoustics Conference*. doi: 10.2514/6.2013-2108.

Romani, G., Grande, E., Avallone, F., Ragni, D. & Casalino, D. (2022). Performance and Noise Prediction of Low-Reynolds Number Propellers Using the Lattice-Boltzmann Method. *Aerospace Science and Technology*, 125, 107086. doi: 10.1016/j.ast.2021.107086.

Rozenberg, Y., Roger, M. & Moreau, S. (2010). Rotating Blade Trailing-Edge Noise: Experimental Validation of Analytical Model. *AIAA Journal*, 48(5), 951–962. doi: 10.2514/1.43840.

Rozenberg, Y., Robert, G. & Moreau, S. (2012). Wall-Pressure Spectral Model Including the Adverse Pressure Gradient Effects. *AIAA Journal*, 50(10), 2168–2179. doi: 10.2514/1.J051500.

Sandberg, R. D. & Sandham, N. D. (2008). Direct Numerical Simulation of Turbulent Flow Past a Trailing Edge and the Associated Noise Generation. *Journal of Fluid Mechanics*, 596, 353–385. doi: 10.1017/S0022112007009561.

Sanjosé, M. & Moreau, S. (2018). Fast and Accurate Analytical Modeling of Broadband Noise for a Low-Speed Fan. *The Journal of the Acoustical Society of America*, 143(5), 3103–3113. doi: 10.1121/1.5038265.

Sanjose, M., Meon, C., Moreau, S., Idier, A. & Laffay, P. (2014). Direct Numerical Simulation of Acoustic Reduction Using Serrated Trailing-Edge on an Isolated Airfoil. *20th AIAA/CEAS Aeroacoustics Conference*. doi: 10.2514/6.2014-2324.

Santamaria, J., Sanjose, M., Gojon, R., Belliot, S. & Moreau, S. (2024). Installation and Manufacturing Effects of Propeller Trailing Edge Serrations. *30th AIAA/CEAS Aeroacoustics Conference (2024)*, (Aeroacoustics Conferences). doi: 10.2514/6.2024-3322.

Sarradj, E., Fritzsche, C. & Geyer, T. (2011). Silent Owl Flight: Bird Flyover Noise Measurements. *AIAA Journal*, 49(4), 769–779. doi: 10.2514/1.J050703.

Savitzky, Abraham. & Golay, M. J. E. (1964). Smoothing and Differentiation of Data by Simplified Least Squares Procedures. *Analytical Chemistry*, 36(8), 1627–1639. doi: 10.1021/ac60214a047.

Schäffer, B., Pieren, R., Heutschi, K., Wunderli, J. M. & Becker, S. (2021). Drone Noise Emission Characteristics and Noise Effects on Humans—A Systematic Review. *International Journal of Environmental Research and Public Health*, 18(11), 5940. doi: 10.3390/ijerph18115940.

Schlinker, R. & Amiet, R. (1981). Helicopter Rotor Trailing Edge Noise. *7th Aeroacoustics Conference*. doi: 10.2514/6.1981-2001.

Schwarzschild, K. (1901). Die Beugung und Polarisation des Lichts durch einen Spalt. I. *Mathematische Annalen*, 55(2), 177–247. doi: 10.1007/BF01444971.

Shenoy, D. V., Gojon, R., Jardin, T. & Jacob, M. C. (2024). Aerodynamic and Acoustic Study of a Small Scale Lightly Loaded Hovering Rotor Using Large Eddy Simulation. *Aerospace Science and Technology*, 150, 109219. doi: 10.1016/j.ast.2024.109219.

Sinayoko, S., Kingan, M. & Agarwal, A. (2013). Trailing Edge Noise Theory for Rotating Blades in Uniform Flow. *Proceedings of the Royal Society A: Mathematical, Physical and Engineering Sciences*, 469(2157), 20130065. doi: 10.1098/rspa.2013.0065.

Smol'yakov, A. V. & Tkachenko, V. M. (1983). *The Measurement of Turbulent Fluctuations*. Berlin, Heidelberg: Springer. doi: 10.1007/978-3-642-81983-4.

Sommerfeld, A. (1896). Mathematische Theorie der Diffraction. *Mathematische Annalen*, 47(2), 317–374. doi: 10.1007/BF01447273.

Stephenson, J. H., Weitsman, D. & Zawodny, N. S. (2019). Effects of Flow Recirculation on Unmanned Aircraft System (UAS) Acoustic Measurements in Closed Anechoic Chambers. *The Journal of the Acoustical Society of America*, 145(3), 1153–1155. doi: 10.1121/1.5092213.

Stepniewski, W. Z. & Keys, C. N. (1984). *Rotary-Wing Aerodynamics*. Courier Corporation.

Szőke, M., Fiscaletti, D. & Azarpeyvand, M. (2020). Influence of Boundary Layer Flow Suction on Trailing Edge Noise Generation. *Journal of Sound and Vibration*, 475, 115276. doi: 10.1016/j.jsv.2020.115276.

Tam, C. K. W. (1974). Discrete Tones of Isolated Airfoils. *The Journal of the Acoustical Society of America*, 55(6), 1173–1177. doi: 10.1121/1.1914682.

Thurman, C., Boyd Jr., D., Buning, P., Reboul, G. & Benoit, C. (2024). NASA/ONERA Collaboration on Small Hovering Rotor Broadband Noise Prediction Using Lattice-Boltzmann Method and Structured Navier-Stokes Solvers. *30th AIAA/CEAS Aeroacoustics Conference (2024)*. doi: 10.2514/6.2024-3106.

Tian, H. & Lyu, B. (2024). The Impact of Non-Frozen Turbulence on the Modelling of the Noise from Serrated Trailing Edges. *Journal of Fluid Mechanics*, 990, A4. doi: 10.1017/jfm.2024.495.

Tian, H. & Lyu, B. (2022). Prediction of Broadband Noise from Rotating Blade Elements with Serrated Trailing Edges. *Physics of Fluids*, 34(8), 085109. doi: 10.1063/5.0094423.

Tian, H. & Lyu, B. (2025). Numerical Study on the Wall Pressure Fluctuations of Airfoils with Straight and Serrated Trailing Edges. *AIAA AVIATION FORUM AND ASCEND 2025*. doi: 10.2514/6.2025-3421.

Tian, Y. & Cotté, B. (2016). Wind Turbine Noise Modeling Based on Amiet's Theory: Effects of Wind Shear and Atmospheric Turbulence. *Acta Acustica united with Acustica*, 102(4), 626–639. doi: 10.3813/AAA.918979.

Tinney, C. E. & Sirohi, J. (2018). Multirotor Drone Noise at Static Thrust. *AIAA Journal*, 56(7), 2816–2826. doi: 10.2514/1.J056827.

Vittal-Shenoy, D. (2023). *Aeroacoustic Study of Low Reynolds Number Rotors Using Large Eddy Simulations*. (Ph.D. thesis, Institut Supérieur de l'Aéronautique et de l'Espace (ISAE)).

Vittal-Shenoy, D., Gojon, R., Jardin, T. & Jacob, M. C. (2022). Aeroacoustic Study of Low Reynolds/Low Mach Number Rotor Using LES. *56th 3AF International Conference on Applied Aerodynamics*.

Wang, M., Moreau, S., Iaccarino, G. & Roger, M. (2009). LES Prediction of Wall-Pressure Fluctuations and Noise of a Low-Speed Airfoil. *International Journal of Aeroacoustics*, 8(3), 177–197. doi: 10.1260/147547208786940017.

Watkins, S., Burry, J., Mohamed, A., Marino, M., Prudden, S., Fisher, A., Kloet, N., Jakobi, T. & Clothier, R. (2020). Ten Questions Concerning the Use of Drones in Urban Environments. *Building and Environment*, 167, 106458. doi: 10.1016/j.buildenv.2019.106458.

Wei, Y., Qian, Y., Bian, S., Xu, F. & Kong, D. (2021). Experimental Study of the Performance of a Propeller with Trailing-Edge Serrations. *Acoustics Australia*, 49(2), 305–316. doi: 10.1007/s40857-021-00221-w.

Wei, Z., Wang, S., Farris, S., Chennuri, N., Wang, N., Shinsato, S., Demir, K., Horii, M. & Gu, G. X. (2024). Towards Silent and Efficient Flight by Combining Bioinspired Owl Feather Serrations with Cicada Wing Geometry. *Nature Communications*, 15(1), 4337. doi: 10.1038/s41467-024-48454-3.

Williams, J. E. F. & Hall, L. H. (1970). Aerodynamic Sound Generation by Turbulent Flow in the Vicinity of a Scattering Half Plane. *Journal of Fluid Mechanics*, 40(04), 657. doi: 10.1017/S0022112070000368.

Willmarth, W. W. & Roos, F. W. (1965). Resolution and Structure of the Wall Pressure Field beneath a Turbulent Boundary Layer. *Journal of Fluid Mechanics*, 22(1), 81–94. doi: 10.1017/S0022112065000599.

Winslow, J., Otsuka, H., Govindarajan, B. & Chopra, I. (2018). Basic Understanding of Airfoil Characteristics at Low Reynolds Numbers (104–105). *Journal of Aircraft*, 55(3), 1050–1061. doi: 10.2514/1.C034415.

Wolko, H. & Anderson, J. D. J. (1987). *The Wright Flyer: An Engineering Perspective*. National Air and Space Museum.

Woodhead, P. C., Chong, T. P., Joseph, P. & Wissink, J. (2019). On the Double-Rooted Trailing Edge Serration. *25th AIAA/CEAS Aeroacoustics Conference*. doi: 10.2514/6.2019-2436.

Wright, S. E. (1976). The Acoustic Spectrum of Axial Flow Machines. *Journal of Sound and Vibration*, 45(2), 165–223. doi: 10.1016/0022-460X(76)90596-4.

Wu, H., Moreau, S. & Sandberg, R. D. (2020). On the Noise Generated by a Controlled-Diffusion Aerofoil at R e c = 1.5 × 10 5. *Journal of Sound and Vibration*, 487, 115620. doi: 10.1016/j.jsv.2020.115620.

Yakhina, G., Roger, M., Moreau, S., Nguyen, L. & Golubev, V. (2020). Experimental and Analytical Investigation of the Tonal Trailing-Edge Noise Radiated by Low Reynolds Number Aerofoils. *Acoustics*, 2(2), 293–329. doi: 10.3390/acoustics2020018.

Yang, Y., Wang, Y., Liu, Y., Hu, H. & Li, Z. (2020). Noise Reduction and Aerodynamics of Isolated Multi-Copter Rotors with Serrated Trailing Edges during Forward Flight. *Journal of Sound and Vibration*, 489, 115688. doi: 10.1016/j.jsv.2020.115688.

Zamponi, R., Gioli Torrione, G., Zůbek, V., Gallo, E., Zarri, A. & Schram, C. (2025). Maneuvering Drone Noise Investigation in a Reverberant Environmenta). *The Journal of the Acoustical Society of America*, 157(6), 4468–4481. doi: 10.1121/10.0036900.

Zawodny, N. S. & Boyd, D. D. (2020). Investigation of Rotor–Airframe Interaction Noise Associated with Small-Scale Rotary-Wing Unmanned Aircraft Systems. *Journal of the American Helicopter Society*, 65(1), 1–17. doi: 10.4050/JAHS.65.012007.

Zawodny, N. S., Boyd, D. D. & Burley, C. L. (2016). Acoustic Characterization and Prediction of Representative, Small-Scale Rotary-Wing Unmanned Aircraft System Components. *VFS International Powered Lift Conference*.

Zhang, S. & Lyu, B. (2024). A Rapid Three-Dimensional Serrated Trailing-Edge Noise Model Based on Analytical Green's Functions. *30th AIAA/CEAS Aeroacoustics Conference (2024)*. doi: 10.2514/6.2024-3126.

Zhao, K., Li, Y., Pei, R., Li, H. & Bennett, G. J. (2024). Review of Wavenumber-Frequency Spectrum Models of Turbulent Boundary-Layer Wall Pressure Fluctuations. *AIAA Journal*, 0(0), 1–27. doi: 10.2514/1.J064561.

Zhong, S., Zhou, P., Fattah, R. & Zhang, X. (2020). A Revisit of the Tonal Noise of Small Rotors. *Proceedings. Mathematical, Physical, and Engineering Sciences*, 476(2244), 20200491. doi: 10.1098/rspa.2020.0491.